Understanding Cathode Electrolyte Interfaces of Nickel-Rich $LiNi_xMn_yCo_zO_2$ Electrodes

A Dissertation Presented for the
Doctor of Philosophy
Degree
The University of Tennessee, Knoxville

Nathan Dale Phillip
December 2019

Dedication

To my mother, for teaching me patience;
to my father, for teaching me work ethic;
to my brother, for friendship when it was hard to come by;
and to my fiancée, for always being there for me.

Acknowledgements

This work could not have been done without my immense support network. I thank my family, friends, mentors, and colleagues for helping me throughout my graduate work and everything that led to it.

To all my group members in their innumerable projects at Oak Ridge National Laboratory, I say thank you for guiding me to become a scientist, collaborating with me on fascinating experiments, and teaching me how to use our countless instruments. I appreciate my group leader, Nancy Dudney, for welcoming me to the family she has set up and providing me with access to the people and resources I needed to excel. I am grateful for my office mates who provided a bottomless font of laughter to wash away the stress of the day, as well as for being gracious guinea pigs for my baking projects.

I thank my dissertation committee: Gabriel Veith, Claus Daniel, Thomas Zawodzinski, and Claudia Rawn, for mentoring me through the tortuous process of earning a PhD. Above all I thank Gabe for without his magnanimous patience and encouragement in the face of what was called, "an aggressive timeline," for finishing my research, this work simply would not have come to fruition. I am indebted to his wisdom and mentorship and look forward to repaying the favor in kind down the road. I also had many informal mentors: Andrew Westover, Beth Armstrong, Robert Sacci, Andrew Kercher, David Wood, Jianlin Li, Lee Riedinger, Tom Rogers, and Lynn Youngs all enriched my multi-faceted adventure through the Bredesen Center, and I appreciate their time and dedication to me beyond what their job titles required.

And to my fellow students in the Bredesen Center and other programs, it was my pleasure to work along side you and share stories on our journeys. I am particularly grateful to Jonathon Romero, Ashley Cliff, David Reeves, and David Garcia, who have remained my close friends ever since I first bumped into them in our first years of graduate school. Despite our different interests and paths, I have loved having a group to step away from it all and enjoy board games and movies with. Katie Browning and Landon Tyler, thank you for welcoming me to the lab group with open arms. You were the cornerstone of our happy office space with all the wonderful interns and post-bachelor's who joined us, and I am honored to call you friends.

My friends in Ohio also deserve praise here: Josh Godar, Jack Brinton, Max Pauly, Kevin Nicholson, Katherine Thomas, Maggie Perme, and Alex Merk, I know it was bittersweet when I left for Tennessee, so thank you all for giving me a second home to come back to for weekends and vacations.

And to my other Ohio friend who became my fiancée, climbing partner, backpacking partner, SCUBA buddy, gaming partner, and soon to be partner in life, Tori Delap, thank you. I love you for all the adventures we have had together and have planned together. You gave me an excuse to climb and backpack throughout the Southeast and explore more of Florida and Texas than I ever thought I would during my four years here. Thank you for making time for me despite your own hard-won journey through flight school and hanging out with us nerds instead of your cool pilot friends. Thank you for finding patience and sympathy even during journeys into uncut wilderness where you may have questioned my sanity and my definition of fun. I cannot wait to go on countless adventures with you in Washington and wherever else life may lead us.

And finally, I thank my family. Mom and Dad, thank you for raising me to be the man I am today and for supporting me even as my passions have drawn me further from home. You have always been my biggest fans and it warms my heart to share my experiences with you. Ty, you have always been my best friend and I do not know how I would get through it all without having you to talk with on the phone or through a headset when gaming. Thank you for visiting me in

Knoxville and going on road trips which I plan down to the half penny, and for keeping me grounded to Earth along the way. I could not have asked for a better older brother. To my cousins: few members of the broad Phillip family had ventured outside of the Chicagoland area before I went to Ohio and eventually Tennessee, and I know it was hard for us to be apart because most of us grew up within three blocks of each other. It has been one of my greatest pleasures in life to watch you all grow up despite Ty and me influencing you as troublesome older cousins. Ryan, Nick, Brad, Joe, Emily, Anna, Amira, and Sam, the more people I meet, the more I realize how fortunate we were to grow up as friends. A big part of that is due to my grandparents, so thank you Grandma Judy, Gramps, Grandma Pat, and Grandpa Jim for making sure we all played together nicely and had an awesome lake house to hang out at. I am grateful for this family and look forward to sharing these lessons as I expand my own branch of it.

Abstract

The rapid growth of the energy storage market has fueled demand for battery materials with higher energy densities, longer cycle lives, and better safety features. This necessitates pushing the limits of known structures such as Ni-rich LiNixMnyCozO2 (x + y + z = 1) cathodes which offer high energy densities (>200 mAh/g) at high cutoff voltages (≥ 4.5 V vs. Li/Li+). Pushing into this high voltage regime introduces challenges of structural rearrangement, electrolyte decomposition, and the formation of an unstable cathode/electrolyte interphase layer (CEI) comprised of decomposition products. The CEI is poorly understood at high voltages but considered critical for passivating these materials against continuous degradation.

This thesis addresses that knowledge gap through the development of thin film cathodes which were applied as a model system for studying interfacial modifications. Polymeric binders were deposited in various morphologies and found to reduce interfacial resistance by an order of magnitude compared to uncoated samples. The formation of a thin, LiF-rich passivation layer informs the selection of future binding agents as well as processing conditions for thin uniform coatings in commercial cells. Modification of the initial surface chemistry of the cathode by thin metal oxide coatings of varying isoelectric points demonstrated that an acidic surface is more effective for capacity retention and a stable CEI than more neutral or basic surfaces. This answered the question of how surface treatment of cathode materials influences electrolyte degradation at the surface and indicated that future efforts should focus on coatings which preferentially react with Li salts to form a fluorinated interphase.

The degradation mechanism of NMC622 was deconvoluted from challenges of liquid electrolytes which are unstable at high voltages through the construction of the first Ni-rich NMC/Lipon/Li solid state battery. It was determined that using a solid electrolyte which is proven at high voltages did not stabilize the NMC material with cycling, indicating that despite interest of the field, Ni-rich NMC cathodes are not viable for solid state batteries without structural modification. This also demonstrated that accessing additional Li inventory with high voltage operation of Ni-rich NMC is not enabled by a stable CEI alone.

Table of Contents

1. Why Study Ni-rich Lithium Ion Battery Interfaces? 1
    1.1 The Lithium-ion Battery 1
2. The State of the Art 3
    2.1 Cathode Structures 3
    2.2 Anode Structures 7
    2.3 Electrolyte Compositions 11
    2.4 The Solid Electrolyte Interphase 18
    2.5 The Cathode/Electrolyte Interphase 24
    2.6 Inactive Battery Components and their Influence on Interfaces 29
3. The Scope of this Thesis 33
4. Experimental Methods 34
    4.1 Core/Primary Techniques 34
    4.2 Materials Synthesis and Supplemental Characterization 38
5. Synthesis of Ni-Rich Thin-Film Cathode as Model System for Lithium Ion Batteries 39
    5.1 Abstract 39
    5.2 Introduction 40
    5.3 Methods 41
    5.4 Results & Discussion 43
    5.5 Conclusions 53
6. Influence of Binder Coverage on Interfacial Chemistry of Thin Film $LiNi_{0.6}Mn_{0.2}Co_{0.2}O_2$ Cathodes 54
    6.1 Abstract 54
    6.2 Introduction 54
    6.3 Methods 55
    6.4 Results & Discussion 57
    6.5 Conclusions 69
7. Controlling the Isoelectric Point of Ni-rich NMC Cathode Interfaces 70
    7.1 Abstract 70
    7.2 Introduction 70
    7.3 Methods 72
    7.4 Results & Discussion 73
    7.5 Conclusions 82
8. Structural Degradation of High Voltage NMC in Solid State Battery 83
    8.1 Abstract 83
    8.2 Introduction 83
    8.3 Methods 84
    8.4 Results & Discussion 85
    8.5 Conclusions 92
9. Conclusions 93

References 101

Vita 117

List of Tables

Table 1. Common Li salts used in carbonate electrolytes. Adapted from Ref.[84] 13
Table 2. Common carbonate solvents and selected physical properties[95] 13
Table 3. Common room temperature ionic liquid cation and anions with their melting points and electrochemical stability windows, adapted from Ref.[15] 16
Table 4. Aprotic Electrolytes for Li-ion Batteries (adapted from Ref.[118]) 19
Table 5. Common electrolyte additives for SEI formation in carbonate electrolytes 23
Table 6. Electrolyte additives for Ni-rich NMC CEI 28
Table 7. Selected physical properties of common separators: a) microporous polymer membrane, b) non-woven fabric mat, and c) an inorganic composite. Values collected from product brochures and Ref.[195] 30
Table 8. Relative integrated intensities of the primary diffraction lines of NMC622 powder and films on different substrates 46
Table 9. Specific capacity and coulombic efficiency of the first two cycles of uncoated and binder coated samples 64
Table 10. Surface charge for sputtered films on NMC622, Al_2O_3, pellets of pristine metal oxide powders and measured IEP of metal oxide powders used in this study 74

List of Figures

Figure 1. The interfaces of a lithium-ion battery: A) Al current collector/electrolyte, B) cathode/electrolyte, C) separator/electrolyte, D) cell casing/electrolyte, E) anode/electrolyte, F) Cu current collector/electrolyte. The general half redox reaction at each electrode is shown below each structure. 3
Figure 2. $LiCoO_2$ a) crystal structure[44] and b) typical voltage profile[45] with c) $LiNi_{0.8}Mn_{0.1}Co_{0.1}O_2$ voltage profiles at a range of upper cutoff voltages, reproduced with permission from Ref.[39] All crystal structures in this work were made in VESTA[46] with Li, Co, and O atoms shown in green, blue, and red, respectively. 5
Figure 3. $LiMn_2O_4$ a) crystal structure[62] and b) typical voltage profile reproduced with permission from Ref.[45] with c) $LiNi_{0.5}Mn_{1.5}O_{4-\delta}$ voltage profile (reproduced with permission from Ref.[59] Copyright 2004 American Chemical Society) where Li, Mn, and O are shown in green, purple, and red, respectively. 6
Figure 4. $LiFePO_4$ a) crystal structure[63] and b) typical voltage profile, reproduced with permission from Ref.[45] where Li, Fe, P, and O are shown in green, tan, grey, and red, respectively. 7
Figure 5. Schematic of a) LiC_6 graphite structure with inset of view down the *c* axis with Li and C atoms shown in green and grey, respectively and b) voltage profile of Li_xC_6 at various stages of Li^+ insertion, reproduced with permission from Ref.[66] 8
Figure 6. Schematic of a) $Li_4Ti_5O_{12}$ structure[70] and b) voltage profile, reproduced with permission from Ref[74] 9
Figure 7. a) Voltage profile of amorphous Si for the first 10 cycles reproduced with permission from Ref.[79] and top-down SEM images of the surface of Si films after b) 3 and c) 50 cycles, reproduced with permission from Ref.[82] 10
Figure 8. Schematic of a) $Li_{2.94}PO_{3.50}N_{0.31}$, Lipon reproduced with permission from Ref.[97] with Li in green, O in red, N in blue, P in gray and b) $Li_7La_3Zr_2O_{12}$, LLZO from Ref.[99] with Li in cyan and O in red. 14
Figure 9. Density functional theory molecular dynamics simulations of a) low concentration electrolyte (1:25 LiFSA/DMC) and b) salt-in-solvent (1:1.1 LiFSA:DMC) long-range ordering of charged species. Li^+ is shown in purple, free and coordinated DMC is shown in light blue and grey, respectively, with FSA^- in free or aggregate clusters shown in red and dark blue, respectively. Adapted from Ref.[110] 17
Figure 10. Schematics of a) mosaic SEI structure on Li metal,[16, 114] b) desolvation-driven SEI formation on graphite from Ref.[93], and c) continuous SEI formation due to the expansion of Si when cycling 19
Figure 11. Schematic of a) reduction of EC to alkyl carbonates and b) variable structure of Si SEI depending on salt composition, reproduced with permission from Ref.[127] 21
Figure 12. Schematic illustration of a) PVdF-based and b) PAA-based SiO composite anodes, reproduced with permission from Ref.[133] 22
Figure 13. Overview of processes at the cathode/electrolyte interface of Ni-rich NMC in $LiPF_6$ in EC/DMC electrolyte 24
Figure 14. a) Surface reconstruction from the R-3*m* layered structure of $LiNi_{0.4}Mn_{0.4}Co_{0.18}Ti_{0.02}O_2$ to a rock salt-type structure, reproduced with permission from Ref.[174], and b) gas evolution during charging for several NMC stoichiometries, LNMO, and conductive carbon C65, reproduced with permission from Ref.[13] 26

Figure 15. Schematic of a) full concentration gradient Ni-rich NMC reproduced with permission from Ref.,[188] b) improved cycling stability of NMC622 with Al_2O_3 coating reproduced with permission from Ref.[179], and c) rate capability of NMC811 with $LiAlO_2$ ("NCM-LAO"), $LiTi_2O_4$ ("NCM-LTO"), and combination $Li_xAlO_2/Li_xTi_2O_4$ coating ("NCM-LTAO") reproduced with permission from Ref.[189] 28
Figure 16. a) reported decomposition mechanism on conductive carbon and CEI of Ni-rich NMC, reproduced with permission from Ref.[208] and b) schematic of SEI (left) and CEI (right) species detected with synchrotron-based XPS, reproduced with permission from Ref.[211] 31
Figure 17. Schematic of a) RF magnetron sputtering system and b) principle of XRD for a layered crystal structure 35
Figure 18. XPS a) photoelectron emission (top) and Auger electron emission (bottom) with b) typical survey scan profile of PVDF-coated Au with Mg Kα source showing photoelectron lines F1s, O1s, C1s, and Au4f and F(KLL) Auger lines..... 36
Figure 19. Schematic of a) coin cell battery and b) Swagelok cell, and c) EIS curve with inset equivalent circuit reproduced with permission from Ref.[226] 37
Figure 20. Schematic of a) thin film NMC electrode prepared by magnetron sputtering with b) SEM surface view of thin film and c) traditional coating morphology schematic for d) SEM of composite NMC electrode with inset image of secondary particle 44
Figure 21. Li:(NMC) stoichiometric ratio of annealed and unannealed films deposited from various target stoichiometries and working plasma pressures. All error bars are two sigma. 44
Figure 22. XRD highlighting ordering of the (104) and (101) planes relative to the (003) plane for NMC622 powder and thin films on different substrates with the (104) region expanded on the right (* = substrate peaks). 46
Figure 23. a) XRD of NMC622 films on substrate with 200 nm Co layer reveals significant (104) preferential ordering over film on Pt-coated substrate, but b) EDS reveals significant Co migration on annealing substrates with a thick (200 nm) Co layer 47
Figure 24. 20 nm Co interlayer of substrate does not penetrate surface and thus does not influence stoichiometry of the active material. Co detected in annealed sample due to EDS beam penetration depth 47
Figure 25. Intensity of (104) orientation in pole figures of NMC622 films on a) $Pt:Al_2O_3$ and b) $Pt:Co:Al_2O_3$..... 48
Figure 26. HAADF STEM images of NMC622 films on a) $Pt:Al_2O_3$ and b) $Pt:Co:Al_2O_3$ with inset SAED patterns. HRTEM images of the NMC/Pt interface with crystal orientations highlighted for c) $Pt:Al_2O_3$ and d) $Pt:Co:Al_2O_3$..... 49
Figure 27. a) Rutherford Backscattering Spectroscopy plot of the $Pt:Co:Al_2O_3$ substrate before and after annealing with corresponding b) TEM image of substrate with SAED patterns of c) Pt, d) Co, and e) Al_2O_3 layers 49
Figure 28. XRD of $Pt:Co:Al_2O_3$ and $Pt:Al_2O_3$ substrates and reference data..... 51
Figure 29. Raman Principal Component Analysis of thin film NMC622 for first three components 51
Figure 30. a) Raman spectra of thin film and composite electrodes, b) film stoichiometry measured by ICP-OES, and c) EDS comparison of film and composite stoichiometry. All error bars are two sigma..... 51

Figure 31. a) Typical electrochemical cycling at C/20 and b) differential capacity of thin film and composite material. c) Nyquist plot of impedance of thin films and composite material after formation cycles (solid lines) and after cycling (dashed lines)..... 53
Figure 32. a) Ni2p XPS spectra for pristine (middle) and cycled thin films (top) and pristine composite NMC622 (bottom) with b) schematic of electrode configurations 58
Figure 33. Potential binder morphology in composite electrodes and thin film analogs for a) minimal surface coverage, b) sporadic globular coverage, and c) uniform thin coverage ... 58
Figure 34. Pristine and cycled NMC622 thin films extracted for XPS of a) C1s, b) O1s, c) F1s, d) P2p, and e) Ni2p spectra after 2 formation cycles between 3.0 – 4.5 V vs. Li/Li^+ with the intensity of the pristine O1s signal multiplied as labeled for clarity 59
Figure 35. 0.1 wt% PVDF spin coating on NMC622 thin film a) SEM top down image and EDS maps corresponding to b) C, c) O, d) F, e) Al, f) Pt, g) Mn, h) Co, and i) Ni 60
Figure 36. a) Chemical structure of binders used in this study and XPS of pristine coated samples b) C1s and c) O1s spectra 61
Figure 37. XPS spectra of stock binder powders for a) C1s, b) O1s, and c) F1s 61
Figure 38. Cycling data for a) the first cycle specific capacity, b) the second cycle specific capacity, and c) AC impedance of electrodes after cycle 2 of each binder coating morphology and composition 63
Figure 39. *Ex situ* XPS component spectra before and after cycling NMC622 films coated with PVDF (a,b), LiPAA (c,d), and CMC (e,f) for F1s and P2p with the intensity of some spectra multiplied as labeled for clarity 65
Figure 40. *Ex situ* XPS component spectra before and after cycling NMC622 films coated with PVDF (a,b), LiPAA (c,d), and CMC (e,f) for C1s and O1s with the intensity of some spectra multiplied as labeled for clarity 67
Figure 41. Ni2p spectra of pristine and cycled uncoated (a), PVDF-coated (b, c), LiPAA-coated (d, e), and CMC-coated (f, g) thin film electrodes..... 67
Figure 42. Relative composition of surface species measured after cycling by *ex situ* XPS for a) M-O, and b) Li_2CO_3 and polycarbonates (orange), $Li_xPO_yF_z$ (green), and LiF (purple) with discharge capacity retention overlaid..... 68
Figure 43. XPS spectra of pristine M-O coatings of a) Ti 2p, b) Cr 2p, and c) Zn 2p on NMC622 74
Figure 44. Ni2p spectra of pristine metal oxide coated NMC622 74
Figure 45. Surface zeta potential measurements in a) Brookhaven ZR5 and b) Brookhaven ZR6 probe particle solutions 75
Figure 46. Isoelectric point measurements through titration of solutions of a) NMC622, b) TiO_2, c) Cr_2O_3, and d) ZnO powders at immediately after titration and after 24 hours in suspension 76
Figure 47. Voltage profiles of a) second cycle at 10 mA/g (C/20) and 10 cycles at 40 mA/g for b) TiO_2:NMC, c) Cr_2O_3:NMC, and d) ZnO:NMC 77
Figure 48. Electrochemical cycling of metal oxide coated NMC622 vs. Li metal at constant current/constant voltage (CC/CV) for a) the first cycle at 10 mA/g (~C/20), b) the specific capacity during 40 mA/g (~C/5) cycles with solid and hollow symbols for charge and discharge capacity, respectively, c) impedance measurements before cycling (inset) and after formation cycles and 40 mA/g cycles, and d) growth of CEI impedance with cycling 78

Figure 49. XPS spectra of pristine and cycled metal oxide-coated NMC622 electrodes of a) C1s, b) O1s, c) F1s, d) P2p, and e) Ti2p, Cr2p, and Zn2p with certain spectra multiplied as indicated for clarity and uncoated NMC622 data included in black from Ref.[306] 80
Figure 50. Specific capacity of a) liquid carbonate electrolyte cell and b) solid state cell with a constant current/constant voltage cycling protocol at ±5 mA/g (~C/40) and ±17 mA/g (~C/12) current densities for the first and second cycles, respectively with c) differential capacity for the liquid and solid cells at 5 mA/g and d) extended cycling at 17 mA/g until cycle 98 where the current density was returned to 5 mA/g. All cells were cycled in duplicate. 86
Figure 51. Charge and discharge profile of liquid cell cycle 23 at ± 17 mA/g 88
Figure 52. AC impedance data of liquid electrolyte cell for a) high frequency, b) medium frequency, and c) low frequency from uncycled through cell failure during cycle 14 88
Figure 53. AC impedance of uncycled and cycled a) liquid carbonate electrolyte cell and b) solid state cell with insets showing the high frequency regimes for each sample and the equivalent circuit model used 88
Figure 54. AC impedance data of solid state battery for a) high frequency and b) medium frequency and low frequency region from uncycled through cycle 97 when cell was removed for XRD 89
Figure 55. XRD of pristine 1.5 µm solid state NMC622 electrode and after 96 cycles at 10 mA/g. The cycled cell had a 1.7 µm layer of Lipon, 3 µm of Li, and Kapton tape on top of the NMC622. The pristine data was normalized to the Al_2O_3 substrate peak at 57.6^o for comparison. 91
Figure 56. XRD of pristine 1.5 µm solid state NMC622 electrode without Kapton covering and Pt:Co:Al2O3 substrate with Kapton covering. 91
Figure 57. a) XPS signal is less attenuated for solid thin films compared to composite electrodes, (b) schematically depicted 94
Figure 58. CEI compositions measured by XPS where a) PVDF-coated cathodes had LiF-rich surfaces and b) acidic metal oxide surfaces formed metal fluoride species after cycling but basic ZnO did not. XPS and specific capacity trends were verified in duplicate samples. .. 95
Figure 59. Schematic of EC oxidation on $Li_{0.5}CoO_2$ with potential energy diagram with EC chemisorbing by nucleophilic attack to form a $C_{EC} - O_{surface}$ bond before transferring H in the transition state 2 (TS2) ring opening reaction which forms an oxygen vacancy in the surface. Reproduced with permission from Ref.[325] 95
Figure 60. Interfaces with simple metal fluorides demonstrated a) lower interfacial resistance for PVDF-coated samples and b) acidic surfaces whereas c) a stable high voltage electrolyte had the lowest interfacial impedance and minimal growth with cycling. Trends were confirmed with replicate cells. 97
Figure 61. An oxygen redox plateau was detected at ~4.4 V vs. Li/Li^+ for a) uncoated NMC622 films cycled at 5 mA/g (C/40), which was suppressed in b) binder-coated samples cycled at 10 mA/g (C/20), and c) metal oxide coatings had an oxygen redox plateau of similar magnitude whereas d) solid state batteries with a Lipon electrolyte had no 4.4 V plateau. All data was reproduced in duplicate. 98
Figure 62. XRD of pristine and cycled NMC622 cathodes extracted from liquid carbonate electrolyte or solid state cells. All samples were coated with Kapton tape to prevent reaction with atmosphere during data acquisition. 99

1. WHY STUDY NI-RICH LITHIUM ION BATTERY INTERFACES?

In the transportation sector, the United States is overwhelmingly dependent on petroleum, accounting for 92% of US transportation energy use in 2017.[1] This broad reliance is reflected on a consumer level, as well, given that an average household in the US spends 15.8% of its income on transportation.[1] Considering these two points, diversification of the transportation energy portfolio would be wise to improve affordability and mitigate the high energy risk of this dependence due to influences of trade disputes, armed conflicts, and natural resource accessibility. Electric vehicles offer a path forward in this effort, as they are agnostic to the source of electricity, allowing for optimization of supply from local energy sources rather than a sole source, be it foreign or domestic. Indeed, nearly all of the electricity used in the US is generated domestically[2] and those electricity sources vary widely across the country with 34.2% from coal, 25.7% from natural gas, 22.7% from nuclear, 7.4% from hydro, 6.3% from wind, and 3.7% total from solar, geothermal, and biomass of the 97.7 quadrillion BTU consumed in the US in 2017.[2, 3]

To realize this shift to lower risk sources of energy for transportation, energy storage for electric vehicles must progress to the point of competitiveness with standard internal combustion engine (ICE) vehicles for smooth integration into the transportation sector. The most likely candidate to satisfy that need in the near term (<10 years) is the lithium-ion battery. As identified by US DRIVE (Driving Research and Innovation for Vehicle efficiency and Energy sustainability), an electric vehicle which is comparable to standard ICE vehicles must be able to economically travel 300 miles on a single charge of its battery at $75/kWh and 350 Wh/kg at the cell level with a 15-year calendar life for at least 1000 deep discharge cycles.[4, 5] One deep discharge cycle corresponds to withdrawal of 80% of the rated capacity of a battery. These metrics correspond to approximately 235 Wh/kg and 500 Wh/L at the pack level, as compared to current battery packs available on the market from 130-140 Wh/kg and 210 Wh/L.[6] These economic and performance metrics must be balanced with environmental and political considerations. While lithium has a low supply risk score due to the primary sources in Chile and Australia,[7] another common battery material, cobalt, has a rather high supply risk due to political instability in the Democratic Republic of Congo,[8] which supplied 64% of the world's cobalt in 2018 .[7, 9] As a result, recent research of lithium-ion battery materials has focused on both improving overall performance and reducing the amount of cobalt used in the cathode.

This thesis focuses on one of those low-cobalt cathode materials, $LiNi_{0.6}Mn_{0.2}Co_{0.2}O_2$ (NMC622) which is a promising candidate for next-generation lithium-ion batteries.[10, 11] At conventional operating voltages (i.e. 3 – 4.3 V *vs.* Li/Li^+), NMC622 has good stability, but increased energy density can be achieved by cycling to higher voltages ($\geq$ 4.5 V).[12] The increased voltage causes degradation of the electrolyte and cathode material at the cathode/electrolyte interface which is poorly understood,[13] so this work investigates those challenges by isolating different physical, chemical, and electrochemical environments at this interface. These findings help understand the limitations of NMC622 as well as inform approaches for stabilizing other cathode materials by controlling surface chemistry.

1.1 The Lithium-ion Battery

The modern lithium-ion battery supplies and stores energy by transferring positively charged lithium-ions between the positive electrode – the cathode, typically a layered transition

metal oxide such as $LiCoO_2$ – and the negative electrode – the anode, which in most cases is graphite. This is shown schematically in Figure 1: Li^+ transfers from their sites between the metal oxide layers of the cathode (Figure 1B) to intercalate between layers of the graphite (Figure 1E), the structures of which are detailed in Sections 2.1 and 2.2, respectively. The driving force for this transport of lithium between electrodes is an electrical potential across the cell established by an external load (circuit) which allows electrons to pass between terminals of the electrodes, shown in Figure 1A and B as aluminum and copper.

While electrons may pass through the external circuit, Li^+ transfers between electrodes through an ion-conducting but electronically resistive electrolyte, which will be discussed in Section 2.3. This is shown in Figure 1C as solvated Li^+ diffusing through a microporous membrane, or separator, which is soaked with electrolyte and prevents direct contact of the electrodes which would result in a short circuit. The charge of the system is balanced in the general redox reaction shown below each electrode material in Figure 1 by oxidation of the transition metal when Li^+ is extracted from the cathode (charging the cell), and reduction when Li^+ is reinserted (discharge).[14]

While this simplified view suggests that Li^+ transfers directly into the bulk of each electrode material, the greatest challenges of lithium-ion battery research exist at the transition between each component of the cell: the interfaces.[15] Perhaps the best studied among these is the anode/electrolyte interface (Figure 1E) where the Li^+ desolvates to enter the anode during charging and in many systems forms a solid electrolyte interphase (SEI) comprised of electrolyte degradation products (discussed in Section 2.4).[16] An analogous environment is present at the cathode/electrolyte interface (CEI),[17] seen in Figure 1B, although it has received comparably less investigation than the SEI despite its importance in understanding certain cathode materials, discussed in Section 2.5. Passivation of the current collectors in electrolyte raises concerns of adhesion and good electrical contact between $LiCoO_2$ and aluminum (Figure 1A) and the copper current collector and graphite (Figure 1F),[18] which will be discussed in Section 2.6 along with the reactivity of the electrolyte with other inactive cell components (separator and cell casing: Figure 1C and D, respectively). Given the plethora of interfaces to consider, what follows in Section 2 is a review of these materials (Section 2.1-2.3) with a focus on the challenges at their interfaces (Section 2.4-2.6).

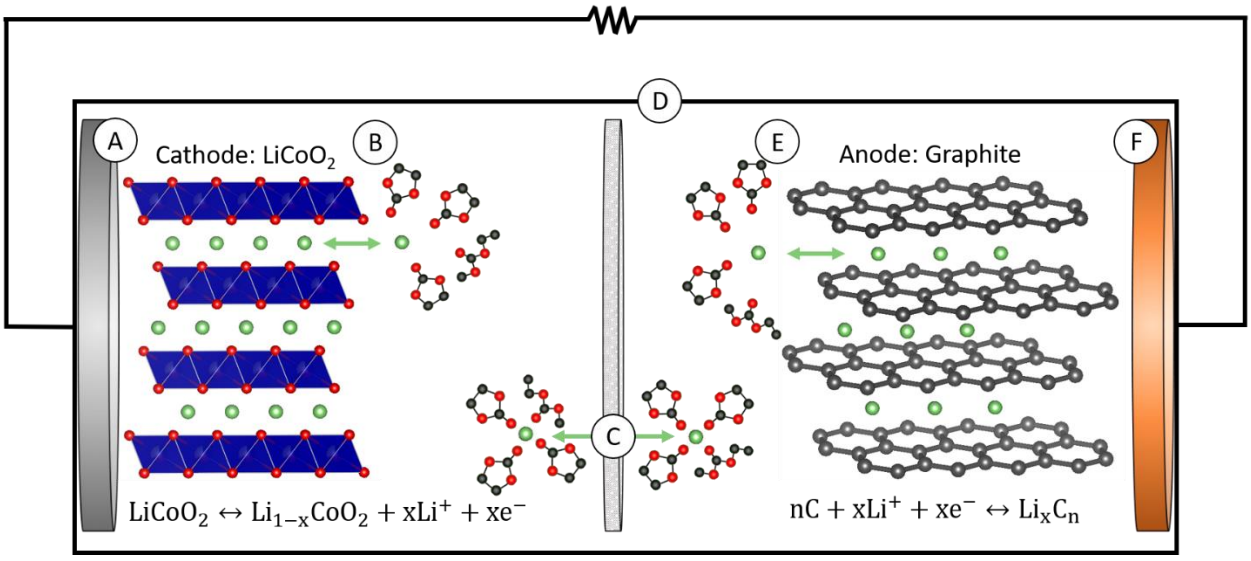

Figure 1. The interfaces of a lithium-ion battery: A) Al current collector/electrolyte, B) cathode/electrolyte, C) separator/electrolyte, D) cell casing/electrolyte, E) anode/electrolyte, F) Cu current collector/electrolyte. The general half redox reaction at each electrode is shown below each structure.

2. THE STATE OF THE ART

2.1 Cathode Structures

The cathode of a lithium ion battery provides the Li source for the system. The crystal structure and composition of these materials dictate their relevant properties for energy storage including the ionic conductivity, extent of Li extraction before the structure degrades, and reactivity with the electrolyte. Among these, layered structures with one or more transition metals providing charge compensation to Li extraction have proved dominant.

2.1.1 Layered Rock Salt

$LiCoO_2$ was used in the overview of Section 1.1 due to its historical significance to the commercialization of lithium-ion batteries[14] and exemplary behavior of the class of layered rock salt cathode materials of the general formula $LiMO_2$, where M is a transition metal such as Co, Ni, Mn, V, Fe, etc. The crystal structures of these materials can be seen in Figure 2a and have rhombohedral symmetry (space group R-3*m*), with Li^+ and the M ions residing in alternating interstitial sites of the cubic close-packed oxygen framework. This is also known as an O3-type layered oxide by the Delmas notation, which categorizes oxides of the general formula A_xMO_2 by whether the alkali atoms (A) are inserted between $(MO_2)_n$ sheets with octahedral (O), tetrahedral (T), or prismatic (P) coordination.[19] The layers filled by M ions form sheets of MO_6 edge-sharing octahedra with Li^+ able to intercalate between those sheets.[20] This allows for two-dimensional transport of Li^+ along *ab* planes but not in the *c* direction of the lattice.

The physical motion of Li^+ into/out of a structure can be examined quantitatively by recording the cell potential versus the charge (or discharge) capacity such as in Figure 2b. In this representation, the voltage of a $LiCoO_2$ half cell is plotted as a function of Li in the structure

because, according to the Nernst equation, the potential of the host structure is a function of the composition of ions (Li^+, in this case) in the structure.[21] Several plateaus are visible in the voltage profile, which correspond to two-phase regions, as explained by Gibbs' phase rule, where a two-phase region has zero degrees of freedom and thus voltage is independent of composition in that region. The length of the plateau indicates the miscibility gap of the two phases, and the adjacent regions (x approaches 0 or 1), are single phase regions.[21] In this case, the plateau of interest in LCO occurs around 3.9 V *vs.* Li/Li^+ where much of the Li^+ intercalates with the Co^{3+}/Co^{4+} redox couple.[22]

When charged to 4.85 V *vs.* Li/Li^+, nearly all of the Li^+ may be extracted from the host $LiCoO_2$ structure.[14] Not all of this capacity is reversibly accessible because once 50% of the Li^+ has been extracted (x = 0.5 in Figure 2b), excessive lattice distortion causes a phase transformation from hexagonal to monoclinic (C2/*m*) around 4.15 V *vs.* Li/Li^+. [23] This is accompanied by a reduction in the *c* lattice parameter by 1.7%,[23-25] causing differential stress within the cathode particles which can result in mechanical failure of the material.[26] As such, cycling of $LiCoO_2$ is typically limited to <50% Li extraction – corresponding to an upper cutoff voltage around 4.2 V *vs.* Li/Li^+ in Figure 2b – resulting in a practical capacity of ~140 mAh/g.

$LiNiO_2$ is isostructural with $LiCoO_2$ but suffers from a different structural challenge: it is difficult to synthesize because a portion of the Ni ions reside within the Li layers due to their similar ionic radii (Ni^{2+} is 0.69 Å and Li^+ is 0.76 Å, while Co^{3+} is smaller at 0.54 Å).[27] This impedes Li (de)intercalation as well as renders Ni within the Li layers and adjacent Ni atoms electrochemically inactive,[28] resulting in a poor stability with cycling and a reversible capacity of ~160 mAh/g.[29] To mitigate these structural problems, solid solutions of this family of materials have been iterated through to culminate with the modern analog: $LiNi_xMn_yCo_zO_2$ ("NMC," where x + y + z = 1), which reduces the amount cation mixing to 1-6%[30, 31] while preserving the hexagonal crystal structure when charging below 50% Li. In this configuration, Ni is divalent, Mn is tetravalent, and Co is trivalent in the pristine material, with the practical capacity of NMC333 limited to ~160 mAh/g when cycled to a typical upper cutoff voltage of 4.3 V *vs.* Li/Li^+.[32, 33] This capacity is similar to that of $LiCoO_2$ at the same upper cutoff voltage (reported to be 164 mAh/g on first discharge[34]), but NMC333 can be cycled reversibly whereas $LiCoO_2$ experiences degradation due to extracting >50% of the Li in its structure, as discussed above. In the case of NMC333, the voltage window is selected to avoid decomposition of carbonate electrolytes and structural decomposition while still accessing the Ni^{2+}/Ni^{4+} redox couple over 3.0-4.3 V *vs.* Li/Li^+.[33, 35] The Co^{3+}/Co^{4+} redox couple, in this case, is observed at ~4.2-4.5 V *vs.* Li/Li^+,[36] higher than that of $LiCoO_2$ (~3.9 V) due to the inductive effect: the strength of anion-cation covalence in a structure can be modulated by its nearest neighbor cations, resulting in a shift in redox potential.[37]

Increasing the relative amount of Ni in NMC allows for increased specific capacity in a given voltage window (*e.g.* 3.0 – 4.3 V *vs.* . Li/Li^+) due to some of the Ni entering the trivalent state to balance the charge of the structure, as is the case in $LiNiO_2$.[11, 12, 38] These Ni-rich (>50% Ni) NMCs have exhibited reversible specific capacities up to 200 mAh/g for NMC811,[39-41] but suffer from increased Li^+/Ni^+ cation mixing with increasing Ni content.[39] This can be mitigated somewhat by synthesis at adequate partial pressures of oxygen to suppress the reduction of Ni^{3+}. Lu *et al.* found that operating at a minimum oxygen flow rate of 1000 mL/min is required to overcome the diffusion barrier of Ni^{2+} from NiO precursors into melted Li species, forming Ni^{3+} while Li^+ diffuses into the octahedral sites vacated by the Ni^{2+} ions in NiO,[42] although this process is dependent on precursors and temperature.[43] As seen in Figure 2c, further specific capacity increases are available at higher upper cutoff voltages thanks to additional Ni^{3+} contributing to

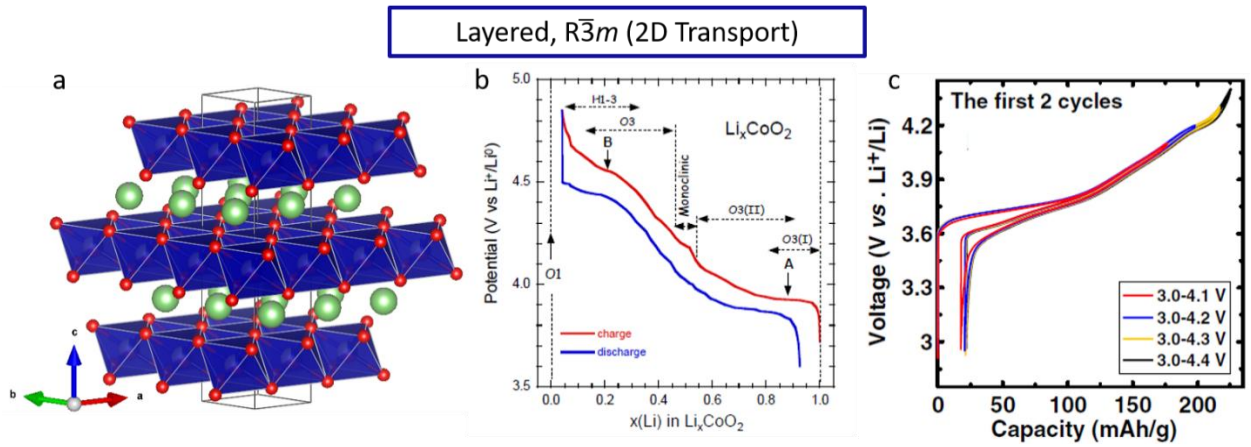

Figure 2. $LiCoO_2$ a) crystal structure[44] and b) typical voltage profile[45] with c) $LiNi_{0.8}Mn_{0.1}Co_{0.1}O_2$ voltage profiles at a range of upper cutoff voltages, reproduced with permission from Ref.[39] All crystal structures in this work were made in VESTA[46] with Li, Co, and O atoms shown in green, blue, and red, respectively.

charge compensation (via Ni^{3+}/Ni^{4+}) and eventually Co^{3+}/Co^{4+} as more Li^+ is removed from the cathode layers. The rate capability of these materials is favorable as well, as increasing Ni content is attributed to high electronic conductivity (1.6×10^{-6} S/cm) and Li^+ diffusivity ($\sim 1 \times 10^{-9}$ cm^2/S), meaning high charge transfer rates and rapid ion transport within the bulk.[32] Unfortunately, this trend correlates to a release of oxygen from the lattice which decreases the thermal stability of the system because oxygen may react with the electrolyte in a combustion reaction, potentially triggering thermal runaway – a catastrophic failure of the cell due to a self-propagating exothermic reaction cycle of increasing temperatures.[32, 47-49]

Oxygen release from the lattice also lowers capacity retention due to concomitant surface structural rearrangement[50, 51] and electrolyte decomposition at the CEI.[52, 53] This tradeoff between performance and stability makes Ni-rich NMC an intriguing material to study, and it offers a promising means to reduce the Co supply risks discussed in Section 1, so efforts to understand and mitigate these challenges will be discussed in subsequent sections.

2.1.2 Spinel

Spinel oxides of the general formula LiM_2O_4, such as $LiMn_2O_4$, have also proved to be attractive cathode materials due to their comparatively low material cost and structural stability at modest charge potentials. The structure consists of cubic close-packed oxygen with 75% of the metal cations in the alternating layers between oxygen planes with the remaining 25% residing in adjacent planes.[54] In the case of $LiMn_2O_4$, this forms a network of edge-sharing MnO_6 octahedra with Li in face-sharing tetrahedral sites, depicted as green spheres in Figure 3a. This structure allows for three-dimensional Li^+ transport along perpendicular channels in the *ac* and *ab* planes thanks to octahedral vacancies in the spinel framework.[54] The cubic *Fd3m* host structure remains stable in the voltage range ~3.5 – 4.5 V *vs.* Li/Li^+ shown in Figure 3b $0 \leq x \leq 1$, for $Li_xMn_2O_4$), where with Li^+ extracted in a two-stage process visible in the two primary plateaus at ~4.0 and 4.15 V.[55] Full Li^+ extraction is difficult at practical voltages, however, so $LiMn_2O_4$ is typically limited to an accessible capacity of 120 mAh/g.[54]

Additional Li content may be inserted into $LiMn_2O_4$ at ~3 V *vs.* Li/Li^+, but this forms a two-phase electrode of cubic $LiMn_2O_4$ and tetragonal $Li_2Mn_2O_4$.[54] This is accompanied by Jahn-Teller distortion of the crystal structure due to an increased concentration of Mn^{3+} ions, inducing a strain on the system which is too great to maintain structural stability over sustained electrochemical cycling.[55]

Unfortunately, there is gradual capacity loss in spinel cathodes due to dissolution of Mn^{2+} into the electrolyte following the disproportionation reaction:[55]

$$2\ Mn^{3+}\ (s) \rightarrow Mn^{4+}\ (s) + Mn^{2+}\ (sol.)$$

This can be triggered by acidic attack of the particle surface due to trace protons in the electrolyte (such as a few ppm of H_2O), but could be suppressed by the partial substitution of Mn with another transition metal to increase the oxidation state of Mn to Mn^{4+}.[56] While some transition metals reduced overall capacity in exchange for improved cycle life,[57] the substitution of 25% of the Mn with Ni – forming $LiNi_{0.5}Mn_{1.5}O_4$ – allows for the good cycling performance shown in Figure 3c at 3.5 – 5.0 V *vs.* Li/Li^+ .[58] The Jahn-Teller distortion of $LiMn_2O_4$ is also suppressed in $LiNi_{0.5}Mn_{1.5}O_4$ due to the oxidation state of Ni^{2+} balanced with Mn^{4+} rather than the Jahn-Teller active Mn^{3+} state in the base spinel.[56] In this variant, charge compensation is provided by the $Ni^{2+/4+}$ redox couple shown in Figure 3c at ~4.7 V *vs.* Li/Li^+. The non-stoichiometric, disordered version of this material, $LiNi_{0.5}Mn_{1.5}O_{4-\delta}$, was found to exhibit lower impedance and higher discharge capacity at high rates than the stoichiometric material, with a capacity of 147 mAh/g.[59] Unfortunately, high voltage operation induces unwanted side reactions at the CEI, and so significant effort has been made toward understanding these interfaces.[49]

2.1.3 Olivine

Olivo-phosphates, namely $LiFePO_4$, have been commercialized for high power applications (*e.g.* power tools) thanks to their long cycle life, material abundance, and low toxicity relative to Co.[60, 61] The orthorhombic (*Pnma*) structure shown in Figure 4a consists of a distorted hexagonal close-packed oxygen array with Li and Fe in half of the octahedral sites and P in one eighth of the tetrahedral sites.[60]

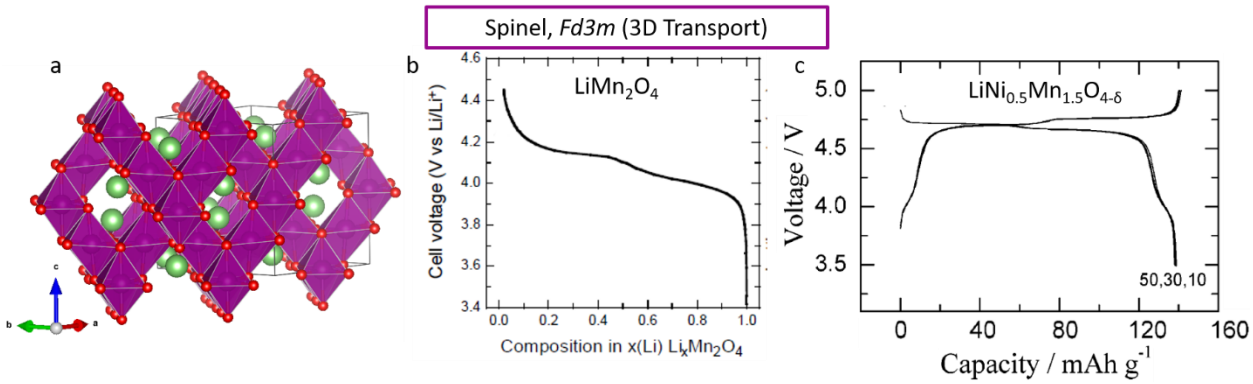

Figure 3. $LiMn_2O_4$ a) crystal structure[62] and b) typical voltage profile reproduced with permission from Ref.[45] with c) $LiNi_{0.5}Mn_{1.5}O_{4-\delta}$ voltage profile (reproduced with permission from Ref.[59] Copyright 2004 American Chemical Society) where Li, Mn, and O are shown in green, purple, and red, respectively.

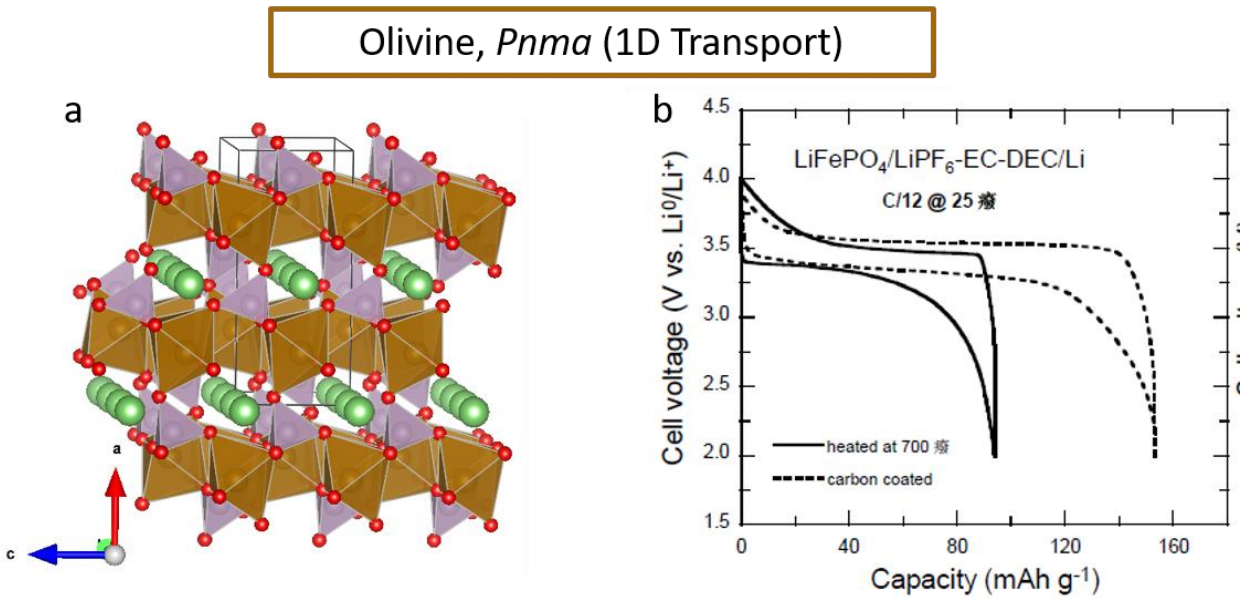

Figure 4. $LiFePO_4$ a) crystal structure[63] and b) typical voltage profile, reproduced with permission from Ref.[45] where Li, Fe, P, and O are shown in green, tan, grey, and red, respectively.

Corner-sharing FeO_6 octahedra form in the *bc* plane, with Li^+ able to (de)intercalate from edge-sharing octahedra along the *b*-axis in one-dimensional transport from alternating *a*-*c* planes.[60] Li^+ insertion occurs the ~3.5 V *vs.* Li/Li^+ plateau in Figure 4b with the Fe^{3+}/Fe^{2+} redox couple providing charge compensation.[60, 64] In practice, the structure was stable throughout cycling due to a modest unit cell volume change (6.8%),[60] but with limited capacity (<100 mAh/g) seen in the solid line of Figure 4b due to poor electronic conductivity and Li^+ diffusivity (<10^{-9} S/cm and ~10^{-14} cm^2/S, respectively).[45] The electronic conductivity of these materials is commonly improved by the addition of a carbon coating seen as the dashed line on the voltage profile of Figure 4b.

2.2 Anode Structures

Anode materials in lithium ion batteries provide a host structure for lithium storage when charging a cell. Graphite and other carbon frameworks have long dominated the field, but recently interest has shifted on alloying compounds such as Si which offer the potential for much higher specific capacity than the intercalation chemistry of graphite.

2.2.1 Graphite

By far the most ubiquitous of the anode materials used in commercial lithium-ion batteries is graphite. As seen in Figure 5a, graphite is comprised of sheets of hexagonally bonded carbon atoms with adjacent layers connected by van der Waals forces.[65] The comparatively weak van der Waals forces allow for Li^+ to intercalate between graphene layers up to 1 Li for every 6 C when a cell is charged to 0.1 V *vs* Li/Li^+. This atomic ratio provides a theoretical specific capacity of 372 mAh/g for graphite. When considering the voltage profile of Figure 5b, the Li^+ storage capacity is achieved in a staging process of voltage plateaus indicating two-phase regions, where two phases coexist in a mixture during a transition between those phases according to the stoichiometry of

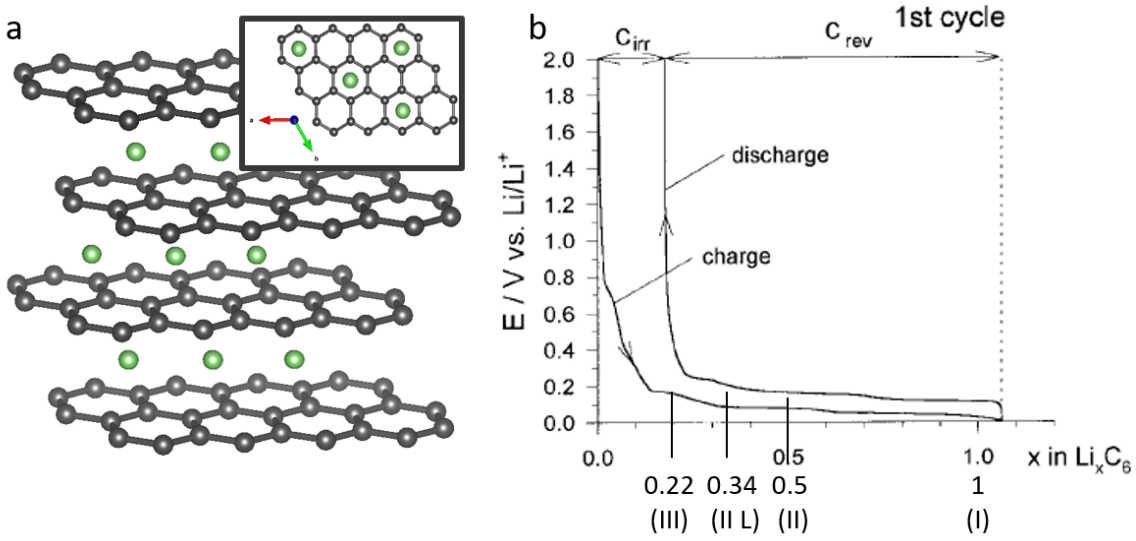

Figure 5. Schematic of a) LiC_6 graphite structure with inset of view down the *c* axis with Li and C atoms shown in green and grey, respectively and b) voltage profile of Li_xC_6 at various stages of Li^+ insertion, reproduced with permission from Ref.[66]

Li_xC_6: x = 0.22 (Stage III), 0.34 (II L), 0.5 (II), 1 (I).[66, 67] The stage index (I, II, III) corresponds to the number of graphene layers between two guest lithium layers. A guest lithium layer can be seen in the inset of Figure 5a, with the repulsive interactions of Li^+ preventing adjacent site occupancy. These stages occur due to the thermodynamics of expanding the van der Waals gap during intercalation and repulsion between guest Li^+.[66]

The final plateau resides just 100 mV above the Li/Li^+ potential, making graphite attractive as an anode material, but its true value resides in its stability over the lifetime of a cell.[68] This stability is attributed to the modest volume change on charge/discharge of ~10% and the passivation layer which forms near 0.8 V during the first cycle[66] in Figure 5b: the SEI, which will be discussed in Section 2.4. The stability of this passivation layer during cycling was essential for enabling graphite anodes, as one of the original favorable electrolyte solvents, propylene carbonate (PC), decomposes at 0.8 V during each cycle when it co-intercalates with Li^+ and causes disintegration of graphite through exfoliation.[69] Electrolyte blends including ethylene carbonate (EC) form a more stable SEI which prevents ongoing decomposition of the electrolyte, thus enabling graphite anodes for commercial applications.[67] These electrolyte systems and the SEI will be discussed further in Sections 2.3 and 2.4, respectively.

2.2.2 $Li_4Ti_5O_{12}$

Another common insertion-based anode is lithium titanate (LTO). As seen in Figure 6a, LTO has the same *Fd3m* space group as the spinel cathodes discussed in Section 2.1, but takes the form of a defect spinel due to 1/6 of the octahedral sites (16d) being occupied by Li^+, with the remaining 5/6 filled by Ti^{4+}, with the remaining Li^+ in tetrahedral (8a) sites (blue and green spheres in Figure 6a, respectively).[70] The spinel notation, in this case, would be $Li[Ti_{0.67}Li_{0.33}]O_4$. As such, the Li^+ storage mechanism differs from spinel cathodes in that LTO follows the reaction: $3Li + Li_4Ti_5O_{12} \rightarrow Li_7Ti_5O_{12}$, where Li^+ insertion displaces tetrahedrally-coordinated Li into octahedral

sites, forming the rock salt-type $Li_7Ti_5O_{12}$.[54] The voltage profile in Figure 6b reflects this in the single flat plateau at ~1.55 V *vs.* Li/Li^+ which corresponds to the two-phase region of the intercalation reaction, where the $Li_4Ti_5O_{12}$ and $Li_7Ti_5O_{12}$ phases coexist as a mixture.

Notably, this intercalation process has a single two-phase region rather than the multiple two-phase regions of graphite's staging process, making LTO attractive as an anode material because it has a consistent voltage across the operation of the battery which allows for more predictable power output.[71] This operating potential is higher than that of graphite and thus does not operate through the same 0.8 V region attributed to organic electrolyte reduction on graphite, which will be further discussed in Section 2.4. This makes LTO a useful anode for model studies of batteries without concerns of electrolyte decomposition at the anode and for pairing with high voltage cathodes which allow for a reasonable average cell voltage ($V_{cathode} - V_{anode} = V_{cell}$).[72] Conversely, common cathode materials such as NMC333 coupled with LTO form a ~2.7 V battery, making it less practical than graphite (V_{cell} = 3.7 V) for commercial cells due to the relatively low operating voltage (and therefore, lower cell power). The low electronic conductivity (~10^{-13} S/cm^{-1} when fully delithiated)[73] also limits rate performance (the amount of capacity which can be extracted at a given current) but mitigation strategies for this will be discussed in Section 2.4. The specific capacity is relatively low compared to other anode options, at 175 mAh/g,[71] but LTO remains relevant in the field due to its excellent cyclability thanks to its minimal volume change (<1%) upon cycling and minimal electrolyte decomposition.[54, 74]

2.2.3 Alloying Anodes

Metals and metalloids which alloy with Li offer significantly higher specific capacities than graphite and insertion-based anodes (potentially 4200 mAh/g for $Li_{22}Si_5$ and or 994 mAh/g for $Li_{22}Sn_5$[75] if the materials are stabilized). Of these materials, silicon has been the subject of intense study lately due to its high specific capacity, material abundance, and low discharge potential (~0.4 V *vs.* Li/Li^+).[76]

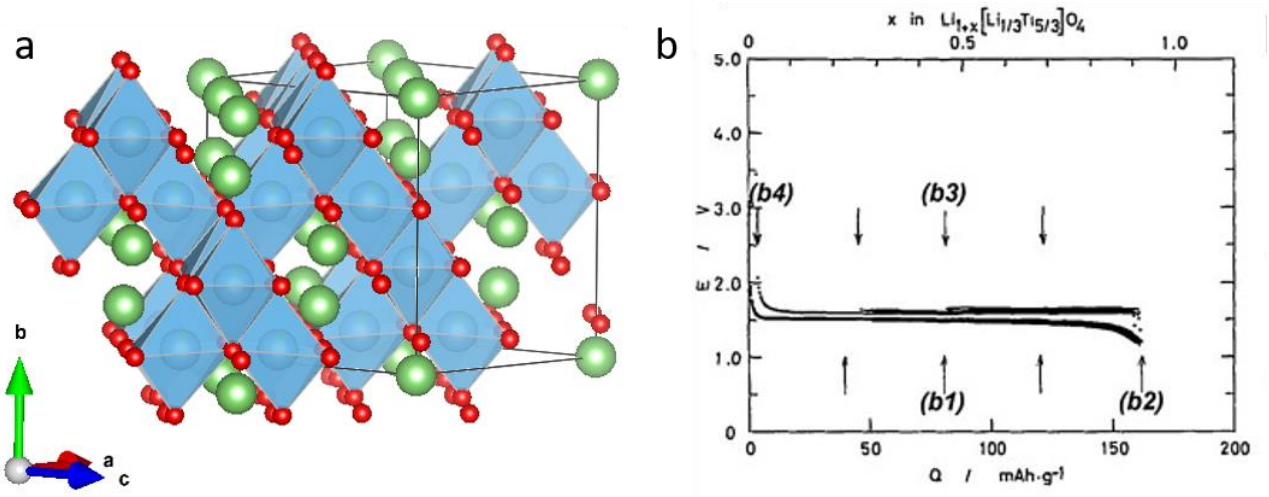

Figure 6. Schematic of a) $Li_4Ti_5O_{12}$ structure[70] and b) voltage profile, reproduced with permission from Ref[74]

The voltage profile of amorphous Si shown in Figure 7a contains a single plateau around ~0.15 V *vs.* Li/Li^+ when charging (alloying), indicating a single two-phase addition reaction.[76, 77] The lower cutoff voltage is 0 V *vs.* Li/Li^+, which causes crystallization of the amorphous phase to $Li_{15}Si_4$.[78] The two-phase dealloying reaction on discharge can be seen at ~0.4 V *vs.* Li/Li^+ in Figure 7a. This voltage curve hysteresis of 0.3 V is attributed to the activation energy required for bond breaking on discharge (dealloying) and is characteristic of alloying anodes.[78]

Unfortunately, amorphous Si suffers from rapid capacity fading due to the nature of the alloying process: Li uptake in such quantities is necessarily associated with volume expansion – on the order of 300% for Si[78] – the consequences of which can be seen between Figure 7b (cycle 3) and Figure 7c (cycle 50) as sizable cracks are formed. The massive expansion and contraction on cycling induces catastrophic strain on the Si particles, resulting in fracturing of material.[79] This causes loss of capacity may be due to i) active material becoming electronically disconnected and therefore inaccessible for electrochemistry and ii) fractures exposing fresh Si surfaces to the electrolyte, which provides additional opportunities for electrolyte decomposition and SEI formation. The net effect is a continual capacity loss between cycles as seen in Figure 7a and limits the practical application of the material.[75, 79] To minimize this effect, small particles of amorphous Si are preferred to crystalline Si due to the mechanical stability of spherical amorphous particles relative to the higher surface area per volume of crystalline Si.[80]

The primary mitigation strategy is blending a modest amount of Si (~15%) with graphite and carbon black to allay some of the volume expansion while bolstering the specific capacity of the anode.[80] This Si blend typically consists of Si particles which are on the order of a hundred nanometers because lower volume particles have proportionally lower surface area and thus lower surface strain upon alloying with Li.[81] This approach is taken to further extremes with nanomaterials engineering, which will be discussed alongside interfacial strategies in Section 2.4.

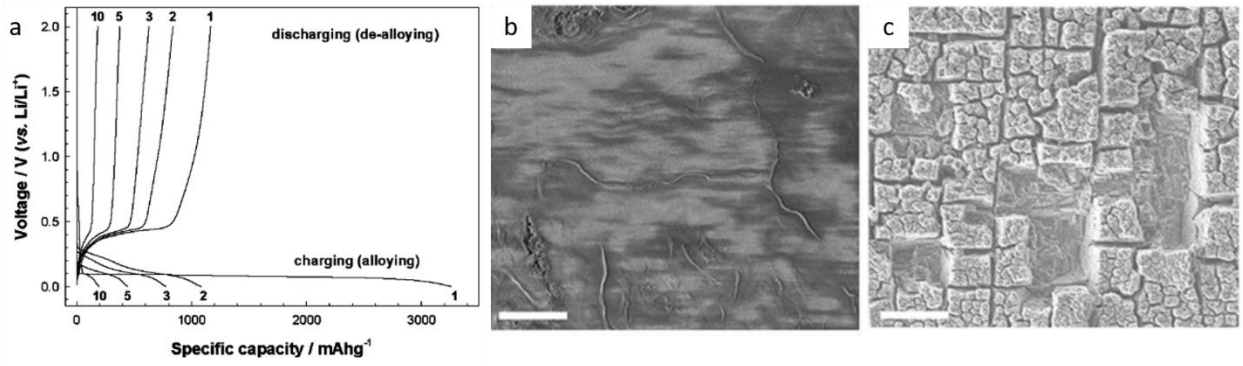

Figure 7. a) Voltage profile of amorphous Si for the first 10 cycles reproduced with permission from Ref.[79] and top-down SEM images of the surface of Si films after b) 3 and c) 50 cycles, reproduced with permission from Ref.[82]

2.2.4 Li Metal

In terms of theoretical values, pure Li metal is the ideal anode for a lithium-based battery because it forgoes the need for a host structure, providing high gravimetric (3860 mAh/g) and volumetric capacity (2061 Ah/L).[83] This encouraged substantial research efforts toward commercialization of Li batteries in the 1970s and 1980s, with several primary (nonrechargeable) Li batteries brought to market.[84] Li metal proved to be more challenging to implement safely in secondary (rechargeable) batteries, and following battery fires in cell phones based on the technology in the late 1980s, Li metal battery research retreated from mainstream research.[83, 85] The causes of these catastrophic battery failures were the high reactivity of Li (due to its high reduction potential) and its tendency to crystallize in branching nanowires known as dendrites. A Li metal anode stores and delivers Li by plating and stripping Li from its surface during charge and discharge cycles, with dendrites and other morphologies of Li (i.e. "mossy Li") preferentially forming at nucleation points and growing into the electrolyte. The high surface area of these structures provides more opportunities for the electrolyte to react with the surface, often forming an SEI in nonaqueous solvents,[16] as well as puncturing the separator and causing the cell to short.[85]

The causes of these catastrophic battery failures remain a challenge for modern studies of Li metal anodes, but there has been a resurgence of interest lately due to batteries approaching the theoretical energy density limits of intercalation materials used today and the cumulative knowledge from decades of studying Li-ion systems.[83] Among the most promising of these efforts are for solid-state batteries, which contain both electrodes and an electrolyte in the solid phase. Solid electrolytes with a shear modulus greater than twice that of Li metal (3.4 GPa at room temperature[86]) are expected to inhibit dendrite formation, and this is observed in the case of Lipon.[87] Dendrites may still form along grain boundaries of crystalline electrolytes such as $Li_{6.75}La_3Zr_{1.75}Ta_{0.25}O_{12}$,[88] but this progress has been made in stabilizing the interface of solid-state batteries as well as liquid cells through electrolyte engineering,[89] which will be discussed in the next section.

2.3 Electrolyte Compositions

Electrolytes are the final active component of a lithium-ion battery, providing the medium through which Li^+ may transfer between electrodes. This core function is accomplished today through a balance of properties including: 1) electrochemical stability at the anode and cathode (often through a passivating layer), 2) inert to cell casing components and the separator with 3) a high ionic conductivity, and electronically insulating for facile Li^+ diffusion and minimal self-discharge while remaining 4) low cost and 5) stable across a wide temperature range.[84] In practice, these parameters are difficult to achieve with simple systems, so electrolyte research to date has sought mixtures which achieve a good combination of these properties. Pioneering electrolyte development for lithium-based batteries was based on the demonstration in 1958 of Li electrodeposition from $LiClO_4$ in PC,[90] which was long favored for its wide liquid temperature range and high dielectric constant which allows it to dissolve a variety of lithium salts. Solvents with active protons can dissolve salts more readily, but the reduction of protons occurs at 3.05 V *vs.* Li/Li^+[91] which is well within the operating potential of most lithium-ion batteries, limiting solvent options to aprotic chemistries.[84] The favoritism of PC over other solvents continued for decades due to a lack of understanding of the complexities at the anode/electrolyte interface, and perhaps also due to a common assumption that PC and EC should function similarly due to their difference of one methyl group.[83] It was eventually determined that PC co-intercalates with Li^+ in

graphite which causes exfoliation of the anode, whereas other carbonates stabilize the interface,[69] which enabled commercialization of lithium-ion batteries.[83]

2.3.1 Carbonates

The most common electrolyte used in lithium-ion batteries today consists of a lithium salt dissolved in a mixture of carbonate solvents. The salt is typically $LiPF_6$, $LiBF_4$, or $LiClO_4$ in a blend of acyclic carbonate esters such as dimethyl carbonate (DMC), ethyl methyl carbonate (EMC), or diethyl carbonate (DEC) and a cyclic carbonate ester such as EC or PC.[84] Common salts are listed in Table 1 with several physical properties such as ion conductivity at 25°C, the temperature of thermal decomposition in solution, and whether it corrodes Al commonly found in current collectors and cell casing. An ideal salt would have excellent solubility in nonaqueous solvents at room temperature, have an anion which is stable against the solvent, and be inert toward other cell components such as the cell casing, separator, current collectors.[84] Practical Li salt options are rather limited because of the intrinsic requirement of remaining soluble and stable over the broad working range found in many battery systems (0 – 5 V *vs.* Li/Li^+).[84, 89] This requirement excludes halides (LiX, where X = F, Cl, etc.) which have low solubility carbonate electrolytes and $LiAlX_4$, which are common in primary lithium batteries but not suited in secondary cells due to corrosion of other cell components.[84] The most common salt used in commercial cells, $LiPF_6$, is not the ideal choice but is a compromise of good physical properties with somewhat low thermal and chemical stability.

Mixed solvent systems are necessary because no viable single solvent has been found which balances the desired properties of high dielectric permittivity (to dissolve the salt), low viscosity (for facile Li^+ transport), and stability at the electrode interfaces.[15] Examples of common solvents are included in Table 2 along with their ionic conductivity, dielectric constant, viscosity, melting point, and boiling point. Among the aprotic solvents, EC is ubiquitous with the weight ratio of these components was optimized by experimental trial and error to be 20 – 40 wt.% before Kang Xu and coworkers verified the benefit of this ratio on interfacial passivation and Li^+ transport into electrodes.[92, 93]

The role of EC in electrolyte decomposition and the SEI will be discussed in the next section, but the solvation sheath around Li^+ can be considered for the bulk, as it directly influences the ion conductivity of the electrolyte. Ionic conductivity, σ, is a function of solvation and dissociation of ionic compounds by polar solvents and the subsequent migration of those complexes:

$$\boldsymbol{\sigma = \sum_i n_i \mu_i Z_i e} \quad \textbf{(1)}$$

Where n_i is the number of free ions in solution, μ_i is the ionic mobility, Z_i is the valence order of the ionized species *i*, and *e* is the charge of an electron.[94] In the case of most lithium-ion battery electrolytes with one salt species, this equation accounts for the only two charged species present: the anions and cations. As such, the measured ionic conductivity represents both species, but the mobility of the cation, μ_{Li}, determines the rate at which the battery operates. This useful portion of the conductivity can be accounted for by the Li^+ transference number:

$$\boldsymbol{t_{Li} = \frac{\mu_{Li}}{\sum_i \mu_i}} \quad (2)$$

Table 1. Common Li salts used in carbonate electrolytes. Adapted from Ref.[84]

Salt	Structure	M. Wt	T_m/ °C	$T_{decomp.,}$ / °C in solution	Al-corrosion	σ /mScm^{-1} (1.0 M, 25 ° C)	
						in PC	in EC/DMC
$LiBF_4$		93.9	293 (d)	> 100	N	3.4 [a]	4.9 [c]
$LiPF_6$	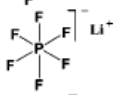	151.9	200 (d)	~ 80 (EC/DMC)	N	5.8 [a]	10.7 [d]
$LiAsF_6$	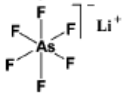	195.9	340	> 100	N	5.7 [a]	11.1 [c]
$LiClO_4$	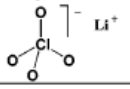	106.4	236	>100	N	5.6 [a]	8.4 [d]
Li Triflate	$Li^+ CF_3SO_3^-$	155.9	>300	>100	Y	1.7 [a]	
Li Imide	$Li^+ [N(SO_2CF_3)_2]^-$	286.9	234 [b]	>100	Y	5.1 [a]	9.0 [e]
Li Beti	$Li^+ [N(SO_2CF_2CF_3)_2]^-$				N		

Table 2. Common carbonate solvents and selected physical properties[95]

Solvent	Ionic Conductivity at 20.0°C, mS/cm	Dielectric Constant	Viscosity, cP	Melting Point, °C	Boiling Point, °C
Propylene Carbonate (PC)	5.2	64.4	2.5	-48	242
Ethylene Carbonate (EC)	6.9	89.6 (40°C)	1.86 (40°C)	39	248
Diethyl Carbonate (DEC)	2.9	2.82	0.75	-43	126
Ethyl Methyl Carbonate (EMC)	4.3	2.9	0.65	-55	109
Dimethyl Carbonate (DMC)	6.5	3.12	0.59	4	90

Given this relationship, it is important to consider the Li^+ transference number when discussing electrolytes, which for most dilute aprotic systems ranges from 0.20 – 0.40.[84] This low fraction is thought to originate from the high surface charge density of Li^+ encouraging greater solvation than its anions and thus having lesser mobility due to their solvation sheath.[84] The solvation sheath is a function of the viscosity of the solvent and determines how much "drag" a solvated species experiences as it migrates through an electrolyte.[84] Typically, no more than four solvent molecules may coordinate with each Li^+ in carbonate solvents. The structure of this solvation sheath has implications for the initial structure of the SEI and will be discussed in the next section.[93]

2.3.2 Solid-State Inorganics

A route toward non-flammable, higher energy density batteries, and enabling the reliable Li metal anode sought after in Section 2.2 is a solid-state electrolyte whose electrochemical stability window is broad enough to avoid decomposition at the Li anode and physical properties which are robust enough to prevent a short due to Li dendrites. Common solid-state electrolytes are either amorphous (for example lithium phosphorus oxynitride, Lipon, seen in Figure 8a) and crystalline (such as $Li_7La_3Zr_2O_{12}$, LLZO in Figure 8b). Li^+ mobility is intrinsically different in the solid phase than for liquid carbonate electrolytes described above. Good ionic conductivity in crystalline electrolytes (10^{-5} – 10^{-3} S/cm for oxides such as LLZO) relies on the concentration of sites for Li^+ migration, typically formed by crystallographic site vacancies (Schottky defect), interstitial defects (Frenkel defect), or cation substitution. These influence the local energy required for Li^+ motion in the solid (termed migration energy) but must be balanced to avoid structural distortion which can have an adverse effect on Li^+ mobility.[96]

Glassy electrolytes such as Lipon have a somewhat lower ionic conductivity (10^{-6} S/cm) but exhibit a similar diffusion process to crystalline electrolytes. In these amorphous materials, short and medium-range order still exist,[97] with Li^+ excited from local sites to neighboring sites, resulting in Li^+ motion on a macroscopic level.[98]

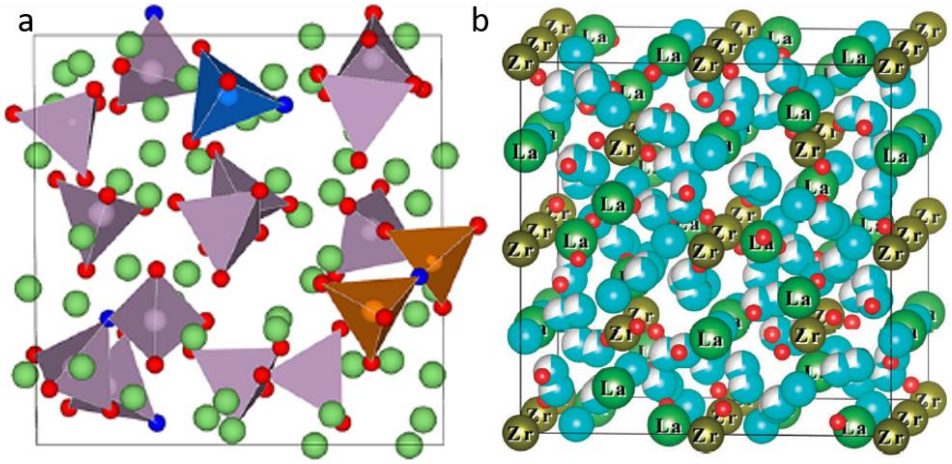

Figure 8. Schematic of a) $Li_{2.94}PO_{3.50}N_{0.31}$, Lipon reproduced with permission from Ref.[97] with Li in green, O in red, N in blue, P in gray and b) $Li_7La_3Zr_2O_{12}$, LLZO from Ref.[99] with Li in cyan and O in red.

A primary benefit of Lipon and other glassy electrolytes is that they prevent the growth of Li dendrites, which crystalline electrolytes often experience along grain boundaries.[100]

Besides ionic conductivity and mechanical stability, solid-state electrolytes should have low electronic conductivity, chemical compatibility with both electrodes, and a wide electrochemical window in order to compete with liquid electrolytes.[98] Meeting these metrics does not guarantee widespread commercial implementation, however, as certain methods of manufacturing do not scale as economically as others. Physical vapor deposition (PVD) techniques such as radio frequency magnetron sputtering can deposit high-quality thin films of Lipon but are more expensive to scale up than comparable slurry coating of β-Li_3PS_4.[101] Different processing techniques also influence the solid-solid interface between the electrolyte and electrode materials. Intimate contact is necessary to minimize losses in ionic conductivity at these interfaces throughout the lifetime of a battery. Electrodes may experience volume changes during Li^+ insertion and extraction, as mentioned previously, but in an all solid-state configuration this can result in partial delamination at the interface, which reduces the effective area available for Li^+ diffusion and drives up impedance.[96]

2.3.3 Highly Viscous Electrolytes

Several families of electrolytes with high viscosities (an order of magnitude greater than water, 0.89 cP at 25 °C) exhibit interesting physiochemical properties. Ionic liquids, in the most literal sense of the term, are comprised solely of disassociated ions in a molten state and the absence of a solvent.[15] Of this family, salts with low melting points are referred to as room temperature ionic liquids (RTIL) and are of interest because the lack of a volatile solvent enables a high flash point (typically >260 °C),[102] and their broad electrochemical stability window (>4 V) makes them viable systems for high voltage systems such as Ni-rich NMC.[103] In order to be a Li^+ conducting electrolyte for any system, a significant portion of a Li salt (>0.5 M) must be dissolved.[84] Common RTIL combinations are listed in Table 3, with an imidazolium or pyrrolidinium (PYR) cation paired with an anion such as bis(trifluoromethanesulfonyl)imide (TFSI, also known as NTf_2[103, 104]) or $B(CN)_4$. Imidazolium-based RTILs exhibit ionic conductivities from 0.1 – 18 mS/cm, but suffer from low Li^+ transference numbers (<0.1).[103] Pyrrolidinium-based RTILs have been of increasing interest lately, with the ionic conductivity of PYR-TFSI reported as high as 1 mS/cm at 25 °C[105] with generally high Li^+ transference numbers (~0.4).[15]

The reduction and oxidation potentials of these combinations are also included in Table 3, with most imidazolium-based systems having a reduction potential above the intercalation potential of common anodes such as graphite at ~0.3 V *vs.* Li/Li^+, so electrolyte decomposition is observed at the anode. A protective SEI forms in carbonate systems to inhibit continuous degradation with cycling, but ionic liquids generally do not efficiently form an SEI so additives such as vinylene carbonate (VC) are often included as sacrificial electrolyte elements to form an SEI.[104] Pyrrolidinium-based RTILs have a lower reduction potential but still suffer from an unstable SEI unless an anode with a higher operating voltage such as LTO is selected. This limits the commercial practicality of an RTIL-based battery due to lower overall energy density, and so research remains focused on answering interfacial challenges.[104]

Table 3. Common room temperature ionic liquid cation and anions with their melting points and electrochemical stability windows, adapted from Ref.[15]

Cation	Anion	T_m (°C)	E_{red} (V vs. Li)	E_{ox} (V vs. Li)
 imidazolium	TFSI	0.8 (R_1=Me; R_2=H, R_3=Et)	1.0 (R_1=Me; R_2=H, R_3=Et)	5.3 (R_1=Me; R_2=H, R_3=Et)
	BF_4^-	15 ($R_{1,3}$=Me)		
	PF_6^-	58~62 ($R_{1,3}$=Me)		
	TFSI	15 ($R_{1,2}$=Me; R_3=Pr)	0.64 (R_1=Me; R_2=H, R_3=Hex)	5.73 (R_1=Me; R_2=H, R_3=Hex)
	FSI	-12 (R_1=Me; R_2=H, R_3=Et)	0.7	5.3
	$B(CN)_4^-$	12.6 (R_1=Me; R_2=H, R_3=Et)		
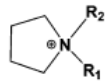 pyrrolidinium	TFSI		0.2 (R_1=Me; R_2=Pr)	5.6 (R_1=Me; R_2=Pr)
	FSI	-9 (R_1=Me; R_2=Pr)		
		-18 (R_1=Me; R_2=Bu)		
	TFSI	-7.9 (R_1=Et; R_2=Bu)		

Sulfones are another highly viscous electrolyte with high oxidation potentials (>5.0 V) and dielectric permittivity. Similar to RTILs, sulfones have low flammability but have been limited in practical applications due to their inability to passivate graphite anodes and average ionic conductivity (~3 mS/cm[106]) and wettability due to their high viscosity (~6 cP for ethyl methyl sulfone).[84, 107] The stability and viscosity challenges have been somewhat mitigated with the addition of carbonate cosolvents for a stable graphite SEI.[15] Recently, fluorinated ethers were shown to stabilize the Li metal interface[108] and improve ionic conductivity up to 10 mS/cm at 55 ^{o}C,[107] opening a potential avenue for the application of high voltage cathodes paired with Li metal anodes for high energy density cells.

"Quasi-ionic liquids," also known as "solvent-in-salt" electrolytes are the transition case between dilute (~1.0 M) carbonate electrolytes and entirely salt ionic liquids.[15] These mixtures have salt to solvent molar ratios which approach or exceed 1, resulting in unique solution structures and properties such as ionic conductivity >10 mS/cm[109]. For example, Al dissolution from the cathode current collector was observed to decrease with an increasing salt concentration in a study of lithium bis(fluorosulfonyl)amide (LiFSA) in DMC, to the point of complete inhibition at a ratio of 1:1.1 LiFSA:DMC in an LMNO half cell.[110] Interfacial studies of the system were inconclusive, but the high salt ratio effectively stabilized cycling in the range 3.5 – 5.2 V *vs.* Li/Li^{+}. Raman spectroscopy coupled with molecular dynamics simulations supported the argument that there were no free anions (FSA^{-}) nor solvent molecules, due to each species coordinating with multiple other species. The net result can be seen in Figure 9 as long-range three-dimensional ordering of the electrolyte.[110] This complex coordination is thought to be the primary factor that extends the reduction potential of electrolytes and enables novel systems such as ~3 V battery using a "water-in-salt" electrolyte of LiTFSI and a $LiMn_2O_4$ cathode paired with a Mo_6S_8 anode.[111]

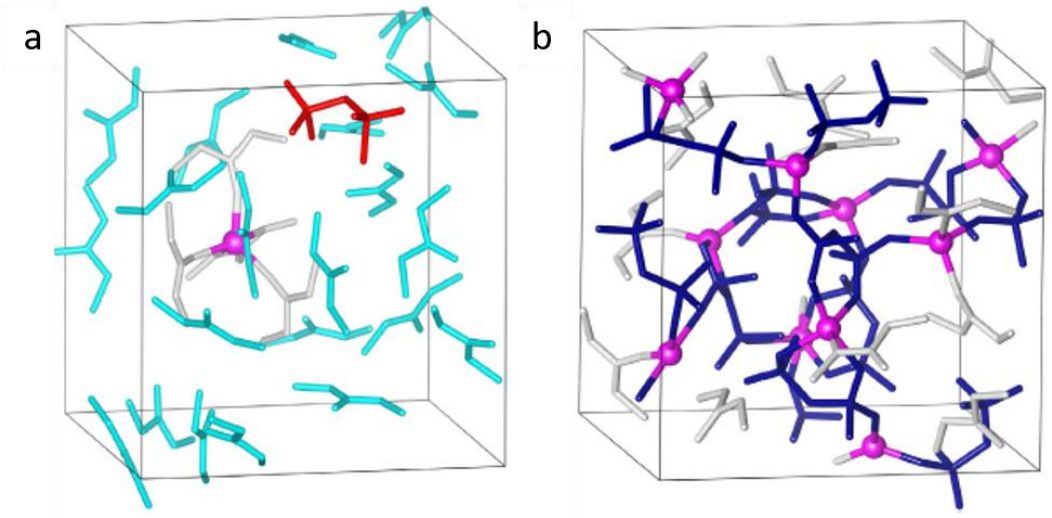

Figure 9. Density functional theory molecular dynamics simulations of a) low concentration electrolyte (1:25 LiFSA/DMC) and b) salt-in-solvent (1:1.1 LiFSA:DMC) long-range ordering of charged species. Li^{+} is shown in purple, free and coordinated DMC is shown in light blue and grey, respectively, with FSA^{-} in free or aggregate clusters shown in red and dark blue, respectively. Adapted from Ref.[110]

Combinations and variations on the chemistries described here have been developed over the long history of electrolyte development. These mixtures often possess one or more improved characteristics from the base materials at the cost of added complexity. Some of these combinations are listed in Table 4, which includes the ionic conductivity and electrochemical stability window of the electrolytes. Included in the table are the polymer class of electrolytes, which are often combined with other electrolytes to take advantage of their mechanical flexibility and ease of manufacturing. Polymer electrolytes such as poly(ethylene oxide) (PEO) have good ionic conductivity on the order of 10^{-4} S/cm at elevated temperatures (65-78 ^{o}C), so ceramic fillers are often added to lower the glass transition temperature, improving conductivity at room temperature.[98] Another approach is combining RTILs with polymer electrolytes to boost ionic conductivity at room temperature, as was recently demonstrated for a high voltage (2.5 – 4.8 V *vs.* Li/Li^+) Li-rich NMC system with 80% capacity retention after 1200 cycles at 1C rate.[105] Given the promise of these combinations and the essential function of the electrolyte in lithium-ion batteries, this area of research continues to grow alongside new materials discoveries.

2.4 The Solid Electrolyte Interphase

Passivation of the battery materials discussed above against continuous decomposition reactions with the electrolyte has been an enabling phenomenon of lithium ion batteries.[112] This thesis focuses on the passivation and ongoing reactions of those interfaces for high voltage batteries, so it is important to understand what is known with regards to the solid electrolyte interphase (SEI) and cathode electrolyte interphase (CEI). It is an open question as to how best to passivate high voltage cathodes such as NMC622 and whether the material can be stabilized, so lessons from other interfaces are considered here.

As mentioned in Section 1.1 and 2.3, stabilizing the anode/electrolyte interface against continuous electrolyte decomposition was integral to the commercialization of lithium-ion batteries. Central to this was the formation of the SEI: a protective surface layer on most anode materials formed by electrolyte decomposition products which passivate the surface from further electrolyte degradation while allowing Li^+ transport and insulating against electrons. The importance of this interphase is inextricably linked with modern electrochemistry, as the discoveries of nonaqueous electrolytes which were stable against Li metal made pioneers of Li battery research suspect such a passivating layer.[83, 112, 113] Peled coined the term SEI[16] for alkali and alkaline earth metals, but any anode with a lithiation potential close to the reduction potential of Li/Li^+ requires a stable SEI to prevent continuous electrolyte decomposition.[15, 114] This is because the reduction potential of most nonaqueous electrolytes are above the reduction potential of the anode. The SEI on Li metal is thought to form upon contacting a carbonate electrolyte solvent such as PC or EC in a single electron pathway followed by radical termination, eventually forming Peled's mosaic structure seen in Figure 10a due to the amalgam of species.[115, 116] The precise structure remains a subject of debate,[15, 114, 116] and has variable composition depending on bulk electrolyte composition, as Dedryvere *et al.* observed by studying the SEI formed in electrolytes with different salts ($LiPF_6$, $LiBF_4$, LiTFSI, LiBETI).[117] The graphite SEI is thought to have a similar structure, although Xu *et al.* found that its formation is dependent on how Li^+ desolvates at the interface (seen in Figure 10b) as influenced by electrolyte composition.[92, 93]

Carbonate electrolyte reduction occurs between 0.8 – 0.2 V *vs.* Li/Li^+ on graphite, although if the layer is not fully developed, solvent molecules may co-intercalate with Li^+. This can cause exfoliation of graphene layers and continuous electrolyte decomposition due to an incomplete passivation layer, as is the case for PC as a single solvent electrolyte.[69] EC does form a complete

Table 4. Aprotic Electrolytes for Li-ion Batteries (adapted from Ref.[118])

Electrolyte	Example of Chemistry	Ionic Conductivity (x 10^{-3} S/cm) at room temperature	Electrochemical Window (V) *vs.* Li/Li^+		Safety Remarks
			Reduction	Oxidation	
Liquid Organic	1 M $LiPF_6$ in EC:DEC (1:1)	7	1.3	4.5	Flammable
	1 M $LiPF_6$ in EC:DMC (1:1)	10	1.3	>5.0	
Ionic Liquids	1M LiTFSI in EMI-TFSI	2.0	1.0	5.3	Non-flammable
	1 M $LiBF_4$ in EMI-BF_4	8.0	0.9	5.3	
Polymer	LiTFSI-P(EO/MEEGE)	0.1	<0.0	4.7	Flammable
	$LiClO_4$-PEO_8 + 10 wt% TiO_2	0.02	<0.0	5.0	
Inorganic Solid	$Li_{4-x}Ge_{1-x}P_xS_4$ (x=0.75)	2.2	<0.0	>5.0	Non-flammable
	0.05Li_4SiO_4 + 0.57Li_2S + 0.38SiS_2	1.0	<0.0	>8.0	
Inorganic Liquid	$LiAlCl_4$ + SO_2	70	-	4.4	Non-flammable
Liquid Organic + Polymer	0.04$LiPF_6$ + 0.2EC + 0.62DMC + 0.14PAN $LiClO_4$ + EC + PC + PVdF	4.2	-	4.4	Flammable
		3.0	-	5.0	
Ionic Liquid + Polymer	1 M LiTFSI + P_{13}TFSI + PVdF-HFP	0.18	<0.0	5.8	Less Flammable
Ionic Liquid + Polymer + Liquid Organic	56 wt% LiTFSI-Py_{24}TFSI + 30 wt% PVdF-HFP + 14 wt% EC/PC	0.81	1.5	4.2	Less Flammable
Polymer + Inorganic Solid	2 vol% $LiClO_4$-TEC-19 + 98 vol% 95 (0.6Li_2S + 0.4Li_2S) + 5Li_4SiO_4	0.03	<0.0	>4.5	Non-flammable

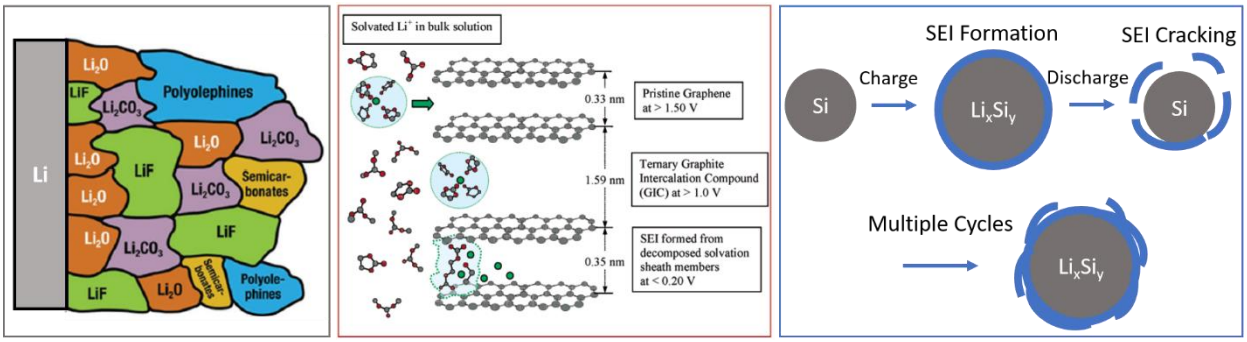

Figure 10. Schematics of a) mosaic SEI structure on Li metal,[16, 114] b) desolvation-driven SEI formation on graphite from Ref.[93], and c) continuous SEI formation due to the expansion of Si when cycling

SEI and is generally accepted as an indispensable cosolvent for nonaqueous electrolytes.[15] Since the inception of lithium-ion batteries, the SEI has received intense scrutiny, particularly for Li metal and graphite anodes,[119, 120] but here the focus will lie on composite Si anodes because their high specific capacity makes them attractive to pair with high voltage cathodes such as Ni-rich NMC for the next generation of high energy density batteries.

2.4.1 Formation and Structure of Si SEI

SEI formation on Si anodes and whether a stable interphase can be formed in conventional electrolytes is a controversial field of active research but offers a useful example of a system which is not fully understood. A prevailing theory is that Si SEI formation is a dynamic process due to volume changes during alloying causing the surface film to break off and reform.[78] As depicted in Figure 10c, when charging (alloying), a given Si particle expands in volume, providing additional surface area for forming an SEI, which can fracture over successive cycles as particles expand and contract. On each cycle, fresh Si surfaces are exposed, providing additional sites for SEI formation which results in rapid cell failure due to the consumption of the available Li and electrolyte inventory.[75] The chemistry and evolution of this layer on Si composite (80 wt% Si, 12 wt% carbon black, 8 wt% carboxymethyl cellulose, CMC) was studied by Edström *et al.* using hard (2000 – 7000 eV) and soft (100 – 800 eV) X-rays for depth profiling at different states of charge.[121] The consumption of the native layer of SiO_x and Si-OH during the first dealloying cycle observed by others[122, 123] was proposed by their group based on synthetic standards to follow the reactions:

$$SiO_2 + 4Li \rightarrow Si + 2Li_2O$$

$$2SiO_2 + 4Li \rightarrow Si + Li_4SiO_4$$

This argument was supported by the observation of Li_2O and Li_4SiO_4 in their O1s XPS spectra for their highest energy photons (deepest penetration depth) but diminished at lower photon energies.[121] Carbonates (Li_2CO_3 and/or lithium alkyl carbonates) and residual $LiPF_6$ were observed as the dominant component at shallower depths, in the upper layers of the SEI by their group and others,[121, 122, 124] whereas LiF was detected throughout, likely according to:

$$LiPF_6\ (sol.) \leftrightarrow LiF\ (s) + PF_5^-\ (sol.)$$

Alkyl carbonates are thought to form from the reduction of the organic carbonate-based electrolytes discussed in Section 2.3. Of these, EC is ubiquitous in electrolyte mixtures due to the formation of a stable SEI layer on graphite by forming alkyl carbonates via the single electron pathway seen in Figure 11a[125, 126] which is the same mechanism attributed to carbonate SEI components on Si.

While carbonate solvent additives are common targets for SEI control (discussed below), there is evidence that the choice of salt affects the long-term composition of the SEI. As seen in Figure 11b, a comparison of Si cycled in an $LiPF_6$-based or LiFSI-based electrolyte yielded different surface chemistry, as detected by synchrotron XPS.[127] Specifically, Si/C/CMC electrodes with a native SiO_2 layer (top of Figure 11b) were either soaked or cycled in a 1 M $LiPF_6$ EC:DEC (2:1 v/v) electrolyte which produced a SEI comprised of Li_2O, Li_4SiO_4, and SiO_xF_y species (Figure 11b, left). Electrodes soaked or cycled in 1 M LiFSI EC:DEC (2:1 v/v) avoided fluorination of Si, as evidenced by the lack of SiO_xF_y observed in the XPS spectra on the right of Figure 11b, possibly due to the lower sensitivity of LiFSI to hydrolysis compared to $LiPF_6$.[127]

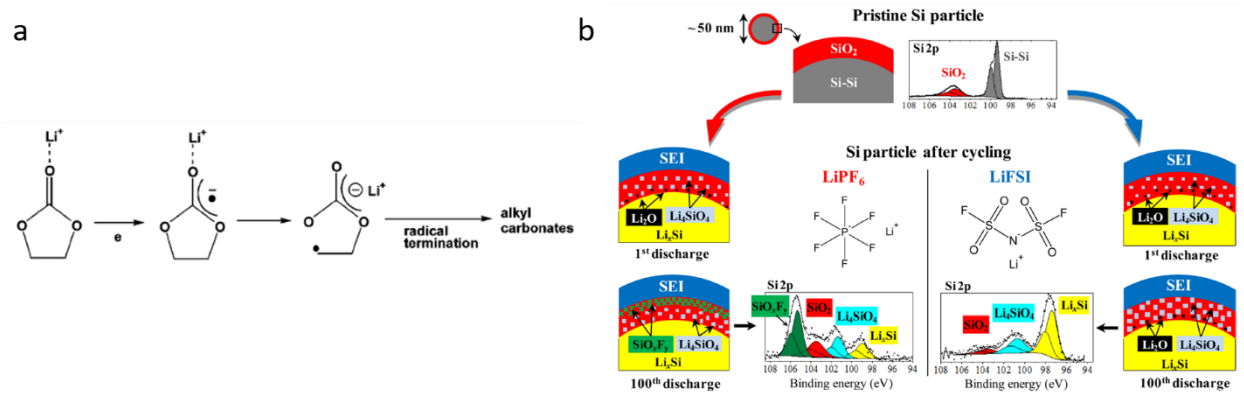

Figure 11. Schematic of a) reduction of EC to alkyl carbonates and b) variable structure of Si SEI depending on salt composition, reproduced with permission from Ref.[127]

Many studies focus on composite Si electrodes but preparing the active material in a fully dense thin film allows for isolated examination of processes without contributions by conductive carbon or the binder (to be discussed in Section 2.6). Studies of Si and SiO_x thin films enabled quantification of initial surface species.[122] Vaughey *et al.* deposited thin films of Si on an electrochemical quartz microbalance to track the initial consumption of the native SiO_x layer,[128] while Lucht *et al.* deposited binder-free Si anodes on a TEM grid for detailed structural observation of the Si SEI.[124] Their group observed an SEI primarily composed of LiF, Li_xSiO_y, and lithium ethylene dicarbonate for anodes cycled in an $LiPF_6$/EC electrolyte, and found that Si cycled in an $LiPF_6$/FEC electrolyte had improved cycle life as well as an SEI with more LiF and polymeric species than the baseline electrolyte.

Additionally, nanoscale structures were found to reduce the impact of the massive alloying volume change thanks to the lower proportion of volume to the surface area.[82, 129] This premise led to the development of various nanostructured Si (*e.g.* Si nanowires[130]) to achieve good cycle life, but the low amount of material limits their application for large format cells due to low overall cell capacity. A solution to the problem of volume expansion and subsequent SEI cracking has been explored in the realm of changing the binder used in composite Si electrodes. Compared to common binders like PVDF and CMC, polyacrylic acid (PAA) stabilized the cyclability of Si nanopowder to 100 cycles with >99% coulombic efficiency.[131] The prevailing failure theory of PVDF-based Si composites is that fine network of PVDF polymer threads (<30 nm) leaves much of the Si surface exposed, allowing for substantial SEI formation on Si as well as allowing alloying particles to disconnect from the bulk and become unavailable for further reactions.[132] PAA is thought to mitigate this according to the schematic illustrated in Figure 12, where the PAA coating may chemically cross-link to provide better coverage of Si particles, allowing elastic-like deformation of the polymer during alloying which suppresses cracking of the SEI.[133] The robust polymer network also reduced the amount of active material which lost electrical contact during cycling due to volume expansion inducing particle migration, which improved the effective capacity over the lifetime of the cell. [133]

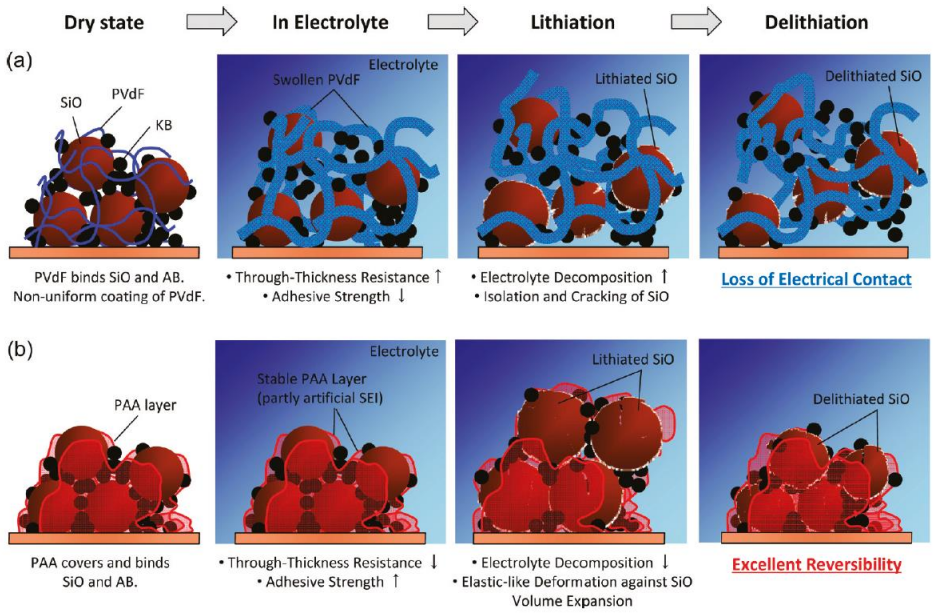

Figure 12. Schematic illustration of a) PVdF-based and b) PAA-based SiO composite anodes, reproduced with permission from Ref.[133]

2.4.3 Controlling the SEI

Beginning with the first efforts aimed at understanding the nature of the SEI, researchers have attempted to alter its makeup in hopes of extending battery lifetime and performance.[69, 134] Adding small amounts (≤10 wt. %) of additional solvents or salts – commonly referred to as additives – are the most popular means to influence the SEI chemistry and formation. Additives are often included as a sacrificial component of the electrolyte, with a higher reduction potential than the bulk electrolyte species so that the additives are consumed first to form the passivation layer, preserving the bulk electrolyte for continued battery operation. Other additives are designed to improve the ionic conductivity of the electrolyte (*e.g.* crown ethers) and improve battery safety by preventing overcharging and being flame retardant.[135] Numerous additive blends have been studied and will not all be discussed here, but some of the most effective ones are included in Table 5. While studies of individual additives can determine their physical properties, it is often useful to directly compare multiple additives in the same system and lab to determine trends, such as the work done by Dahn *et. al* for NMC||Graphite in carbonate electrolytes.[136-138] In addition to altering the SEI chemistry, these additives often have a dual purpose such as impeding exothermic reactions or scavenging reactive species such as HF, which can form from trace water present in a cell.[135] Others can provide benefits for the SEI at the anode as well as stabilize the cathode electrolyte interface, which will be discussed in the next section. The latter is particularly useful for reducing cross-talk: species such as metal fluorides evolving on one electrode and diffusing through the electrolyte to interfere with the opposite electrode.[139]

While the mechanisms of SEI formation and composition with additives for Si systems are still an area of intense research, it is generally accepted that fluoroethylene carbonate (FEC) can improve cyclability of Si anodes.[132] Aurbach *et al.* studied the mechanism of SEI formation with FTIR and XPS of cycled Si nanowires in three $LiPF_6$-based carbonate solutions with up to 10 wt%

Table 5. Common electrolyte additives for SEI formation in carbonate electrolytes

Additive	Structure	Anode SEI Studied
Vinylene Carbonate (VC)		Li metal,[140] Graphite,[141] Si[142]
Fluorethylene Carbonate (FEC)	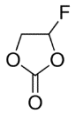	Li metal,[143] Graphite,[144] Si[145]
CO_2	O=C=O	Li metal,[146] Graphite[147]
Succinic Anhydride (SA)	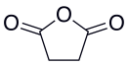	Li metal,[148] Graphite,[149] Si[150]
Tris(trimethylsilyl)phosphite (TTSPi)	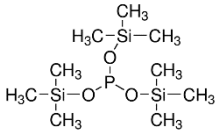	Graphite[151]
1,3-propane sultone (PS)		Graphite[149]
Lithium bis(oxalate) borate (LiBOB)	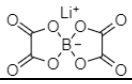	Li metal,[152] Graphite,[153] Si[154]

FEC.[155] They proposed a mechanism of FEC forming vinylene carbonate (VC) by an HF elimination reaction followed by polymerization of VC into surface polycarbonates.[155] Others observed similar polycarbonate and LiF-rich SEI on Si, but suggested a ring opening mechanism forming an unstable organic radical which polymerizes at the surface in a 3 or 4 electron pathway, yielding additional Li_2CO_3.[124, 156, 157] The latter route was supported by recent work by Gasteiger *et al.* in which OEMS and NMR were used to track the reductive decomposition of FEC into CO_2, H_2, LiF, Li_2O, Li_2CO_3, and a partially cross-linked polymer.[158] Despite the complexity of electrolyte additive formulations, intensive research continues toward understanding how to further stabilize the SEI on Si..

2.5 The Cathode/Electrolyte Interphase

Similar to the SEI on graphite, understanding the CEI is crucial for broad implementation of new cathode materials. While the layer is analogous to the SEI, there are several key differences: 1) it is often referred to as an interface rather than an interphase because it is not as ubiquitous to stable battery operation across multiple battery chemistries as the SEI is because 2) the nature of the CEI varies significantly depending on the cathode material through 3) unique modes of electrolyte and cathode changes including electrolyte decomposition, crystal structure rearrangement, metal leaching, and gas evolution. This complexity, as well as the comparatively vast and recent array of cathode materials studied compared to anodes, has resulted in less knowledge on the CEI, which drives the interest of this thesis. An overview of processes and reactions that govern the CEI can be seen in Figure 13, with the bottom of the image showing the bulk layered cathode material (*e.g.* NMC622) oriented in the (101) crystal orientation. This layered bulk can transition to spinel-like and rock salt phases at high voltages, releasing lattice oxygen during structural rearrangement. This can spur electrolyte degradation, releasing gas and forming a layer on the surface while residual water in the electrolyte may react to form HF and leach metal species. These interrelated processes will be discussed in the coming sections.

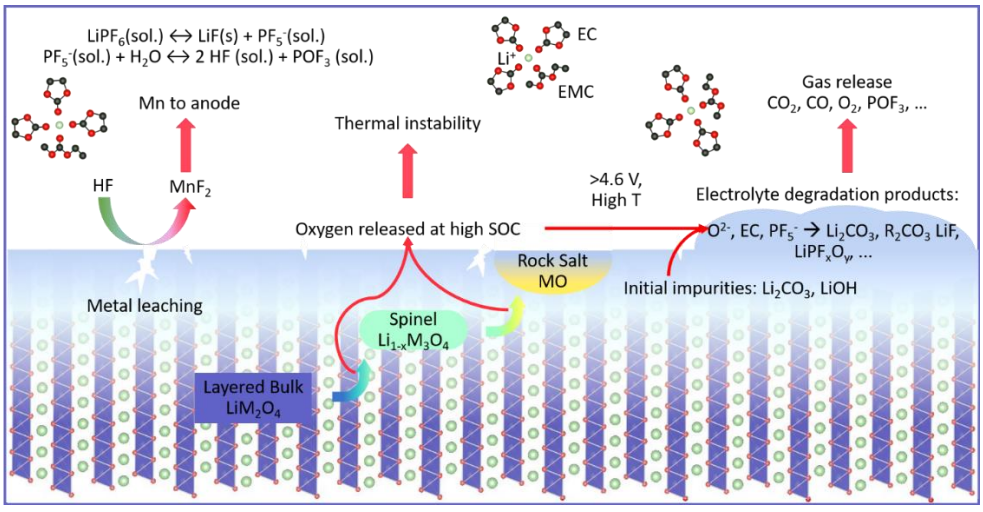

Figure 13. Overview of processes at the cathode/electrolyte interface of Ni-rich NMC in $LiPF_6$ in EC/DMC electrolyte

2.5.1 Formation and Structure

Perhaps the first observation of a surface film formed on lithium cathode materials was in a report by Goodenough *et. al* on AC impedance analysis of LCO.[159] They argued that the AC impedance evolution observed could be explained by a surface layer element included in their equivalent circuit model. While that model has evolved over time, the basic tenants which developed from it remain relevant: a desirable interfacial layer would be a good Li+ conductor while remaining electronically insulating so as not to hinder kinetics but still prevent side reactions. Additionally, it should be mechanically robust enough to withstand minor volume changes during (de)lithiation of the cathode without cracking and exposing fresh surfaces for continuous reactions.

The CEI forms through several interdependent reaction pathways. Residual Li_2CO_3 forms on the surface of layered metal oxide cathode materials during manufacturing and reaction with atmosphere:[17, 160]

$$Li(M)O_2\ (s) + ½\ xCO_2\ (g) + ¼\ xO_2\ (g) \rightarrow Li_{1-x}(M)O_2\ (s) + ½\ xLi_2CO_3\ (s)$$

LiOH may also be present on the initial cathode surface due to active surface oxygen (O^{2-}) reacting with CO_2 and moisture:[161]

$$3\ O^{2-}\ (sol.) + 2\ CO_2\ (sol.) + H_2O\ (l) \rightarrow 2\ CO_3^{2-}\ (sol.) + 2\ OH^-\ (sol.)$$

$$Li^+\ (s) + CO_3^{2-}\ (sol.) + 2\ OH^-\ (sol.) \rightarrow Li_2CO_3\ (s) + 2\ LiOH\ (s) + 2e^-$$

Upon contacting the electrolyte, LiF develops on the surface, likely due to trace amounts of moisture present in carbonate electrolytes forming HF:

$$LiPF_6\ (sol.) \leftrightarrow LiF\ (s) + PF_5^-\ (sol.)$$

$$PF_5^-\ (sol.) + H_2O\ (l) \leftrightarrow 2\ HF\ (sol.) + POF_3\ (sol.)$$

$$HF\ (sol.) + Li_2CO_3\ (s) \leftrightarrow 2\ LiF\ (s) + H_2O\ (l) + CO_2\ (g)$$

The evolution of these species is dependent on the materials involved so the following discussion will focus on NMC622 in typical carbonate electrolytes (*e.g.* $LiPF_6$ in EC/EMC), as it is the primary material of interest in this thesis. There is some disagreement in the literature as to whether electrolyte degradation at the CEI is strictly electrochemically driven or whether there is a chemical oxidation pathway. The former suggests that salt anions in the electrolyte (*e.g.* PF_6^-) form complexes with solvent molecules which spur nucleophilic attack of the cathode surface.[162, 163] The latter argument stems from the fact that some cathode materials undergo crystal structure rearrangement at the surface during cycling, which can cause oxygen release from the lattice.[12]

Delithiation of the cathode (or increased temperature) causes progressively structural rearrangement of transition metal oxides from the layered compound to spinel (LiM_2O_4, then M_3O_4) and finally MO-type rock salts, as seen in Figure 14a as a distinct surface layer. [12, 50, 164-167] The reduction of metal oxides by the proposed scheme (layered structure > spinel > rock salt) is necessarily accompanied by oxygen loss, causing thermal instability due to potential combustion with the electrolyte and an environment for chemical oxidation of the electrolyte at the CEI within the voltage range for which the standard carbonate electrolyte is stable in isolation.[15, 53, 168] This hypothesis was well-supported recently by Doeff *et al.*[50] who traced redox behavior in NMC622 from the bulk to the surface with synchrotron X-ray absorption spectroscopy (XAS), electron energy loss spectroscopy (EELS) and *in situ* X-ray Diffraction (XRD), finding that while the bulk crystal structure and electronic changes were reversible, the surface structural rearrangement and reduction was not. They attributed this difference to Ni not being the only species to contribute to charge compensation during (de)lithiation, but Co and O as well due to transition metal-oxygen hybridization. Gasteiger *et al.* directly investigated this chemical *vs.* electrochemical oxidation of the electrolyte for NMC622, 811, and 111 using On-Line Electrochemical Mass Spectrometry (OEMS).[13] The onset of gas evolution (CO_2 and CO) can be seen in Figure 14b at 4.2 V *vs.* Li/Li^+

for NMC622, which is lower than the typical oxidative stability limit for carbonate electrolytes. There was also a sharp rise in CO_2 and CO detected with the onset of O_2 generation at ~4.6 V, supporting the hypothesis of surface reactions initiated by the release of lattice oxygen from NMC rather than the oxidation of carbon, which was only observed about 5.0 V *vs.* Li/Li^+ on the C65 trace in Figure 14b.

Novák *et al.* demonstrated in an *in situ* study of NMC333 using OEMS to trace carbonate solvent oxidation in the common electrolyte 1 M $LiPF_6$ in 3:7 (w/w) mixture of EC and DEC.[53] They found that conductive carbon cathode can catalyze the oxidation of an ethylene carbonate electrolyte into protic species that can go on to react with PF_5^- from the electrolyte salt, forming POF_3 and highly acidic HF, which can corrode the cathode and leach transition metal ions. The role of so-called "inactive" components like conductive carbon will be discussed further in Section 2.6. Winter *et al.* carried out several related studies on the same NMC material, finding that the degradation products at the NMC CEI could not account for all of the irreversible capacity loss observed.[33, 169, 170] Interestingly, they found that despite the identification of species such as LiF, Li_2CO_3, RCO_3, and $LiPF_xO_y$ with XPS,[170] the addition of a constant potential step on discharge could recover up to 61% of the initial capacity loss even after 50 cycles from 3.0 – 4.6 V *vs.* Li/Li^+.[33] This suggests that much of the available capacity loss is through kinetic limitations on lithiation of NMC, rather than parasitic reactions.

Additional capacity losses in the cell can be attributed to an unstable CEI not preventing metal dissolution. In the case of Mn, a disproportionation reaction may occur from Mn^{3+} formed due to defects or oxygen vacancies in the NMC lattice:[171]

$$2\ Mn^{3+}\ (s) \rightarrow Mn^{4+}\ (s) + Mn^{2+}\ (sol.)$$

At higher states of charge, when Mn is oxidized to Mn^{4+}, dissolution has been proposed to follow Hunter's reaction, forming the spinel-like structure, λ-Mn_2O_4:[17, 171-173]

$$Li_{1-x}Mn_2O_4 + 2(1-x)\ HF \rightarrow ((3 + x)/4)\ \lambda\text{-}Mn_2O_4 + (1-x)LiF + (1-x)\ H_2O + ((1-x)/2)\ MnF_2$$

In either case, Mn^{2+} may diffuse through the electrolyte and oxidize Li from the anode, effectively removing available Li^+ for energy storage, thus lowering the capacity of the cell:

$$Mn^{2+}\ (sol.) + 2\ LiC_6\ (s) \rightarrow Mn\ (s) + 2\ Li^+\ (sol.) + graphite\ (s)$$

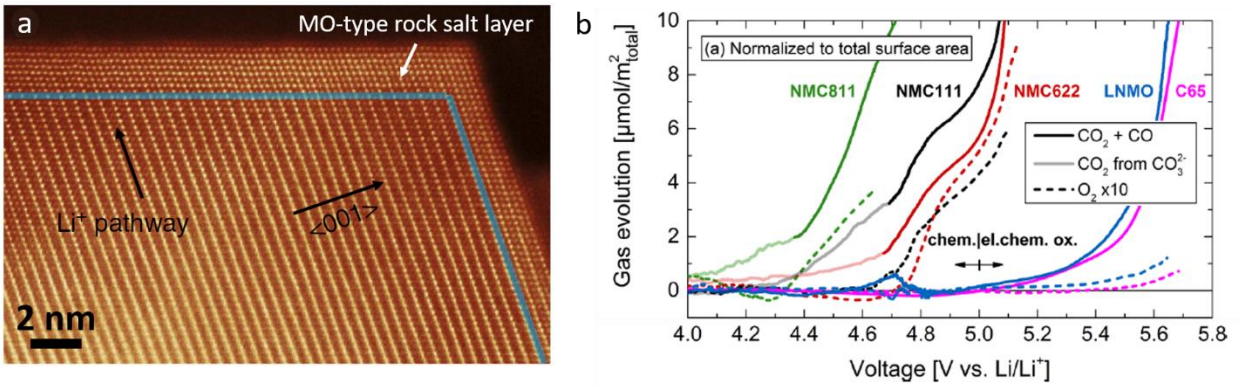

Figure 14. a) Surface reconstruction from the R-3*m* layered structure of $LiNi_{0.4}Mn_{0.4}Co_{0.18}Ti_{0.02}O_2$ to a rock salt-type structure, reproduced with permission from Ref.[174], and b) gas evolution during charging for several NMC stoichiometries, LNMO, and conductive carbon C65, reproduced with permission from Ref.[13]

The Mn ions can form species such as MnO, Mn_2O_3, or $MnCO_3$ which catalyze further electrolyte decomposition at the SEI.[175] In the case of an NMC622 half cell cycled between 4.6 – 3.0 V *vs.* Li/Li^+ in 1 M $LiPF_6$ in EC/EMC (1:1, w/w) for 53 cycles, ~1.4 µg of dissolved transition metals (Ni, Mn, and Co) were detected for every 1 mg of transition metals in the pristine electrode.[176] These challenges are exacerbated at higher temperatures and upper cutoff voltages (≥ 4.5 V *vs.* Li/Li^+) for Ni-rich NMCs,[12, 32] but the ability to access additional lithium content at higher upper cutoff voltages (as discussed in Section 2.1) encourages researchers to find ways to stabilize the CEI.

2.5.2 Efforts to Control the CEI of Ni-rich NMCs

As with the SEI, a common route for designing a stable CEI is through the addition of electrolyte additives, although relatively few have been studied for Ni-rich NMC systems. Common electrolytes additives studied in that context are included in Table 6. Additives are selected such that they oxidize before solvent molecules of the bulk electrolyte, ideally passivating the cathode surface such that no further degradation occurs over the lifetime of the cell. In practice, there is often a balance of desired properties (*e.g.* continuous CEI layer, suppressed metal dissolution, scavenging HF) and undesirable impedance rise, which can inhibit rate capability and lower practical cell capacity, as is the case for glutaric anhydride, for example.[177] VC is a common additive for the anode SEI (Table 5), but has been demonstrated by Dahn *et. al* to suppress the growth of the surface rock salt layer of NMC811.[178] Prop-1-ene-1,3-sultone (PES) also suppressed surface rock salt layer growth in the same study, but those cells failed faster than the control NMC811, [178] although it was found to improve capacity retention for NMC622.[179] This suggests the necessity to balance failure mechanisms of structural rearrangement with electrolyte oxidation in order to achieve long-lasting batteries. Several groups address this through additive blends of three components or more,[137, 180] but another approach is surface modification.

Surface pretreatment of cathode materials by doping, coating, etching, or other surface modifications can influence the formation and evolution of the CEI on Ni-rich NMCs. Doping is a particularly useful strategy for Ni-rich materials which suffer from irreversible structural changes (Figure 14a). This refers to partially replacing transition metals of the cathode structure with other metals, such as Al^{3+} or Ti^{4+}.[181, 182] These species are not involved in electrochemistry and therefore stabilize the chemical environment around dopant sites, suppressing phase transformations at the expense of some reversible capacity of the base cathode material, which lowers the overall energy density of the cell.

Another approach to surface modification is synthesizing cathode particles with a variable composition between the core and surface. Early attempts at this approach were referred to as core-shell particles, with an abrupt step from the core composition to the surface composition. This often resulted in cracking and separation of the structure due to mismatch of lattice parameters during cycling,[183, 184] and so full concentration gradient materials such as those seen in Figure 15a were developed by Sun and Amine *et al.*[185] In this case, cathode particles with nominal composition $LiNi_{0.6}Mn_{0.2}Co_{0.2}O_2$ had a Ni-rich core (72 at.%) which gradually reduced to the outer surface (61 at.%), with the Mn proportion increasing from 11 at.% to 24 at.% and Co remaining nearly constant (from 17 – 15 at.%). The Ni-rich core provided high capacity while the higher Mn content of the exterior stabilized the surface compared to homogenous NMC622.[185]

In terms of strictly surface treatments, atomic layer deposition (ALD), sol-gel synthesis, and wet-coating are common techniques used to coat the cathode with uniform layers of a

Table 6. Electrolyte additives for Ni-rich NMC CEI

Additive	Structure	Remarks
Glutaric Anhydride (GA)	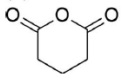	High CE, suppresses gas generation, high impedance on formation[177]
Citraconic Anhydride (CA)	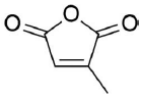	Good CE, rapid voltage decay[177]
prop-1-ene-1,3 sultone (PES)		Rock salt suppression, high impedance on formation, low impedance growth, shorter cycle life[177, 179]
vinylene carbonate (VC)		Rock salt suppression, high impedance growth with cycling[179]
pyridine boron trifluoride (PBF)	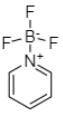	Low impedance on formation, high impedance with cycling[137, 179]
tris(trimethylsilyl)borate (TMSB)		Thin CEI; dissolves LiF[186]
ethylene glycol bis (propionitrile) ether (EGBE)	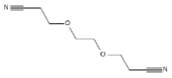	Suppresses metal dissolution[187]

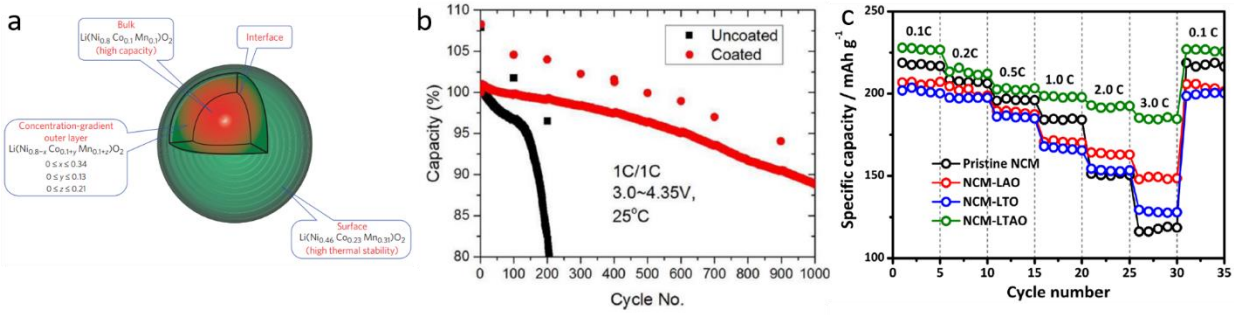

Figure 15. Schematic of a) full concentration gradient Ni-rich NMC reproduced with permission from Ref.,[188] b) improved cycling stability of NMC622 with Al_2O_3 coating reproduced with permission from Ref.[179], and c) rate capability of NMC811 with $LiAlO_2$ ("NCM-LAO"), $LiTi_2O_4$ ("NCM-LTO"), and combination $Li_xAlO_2/Li_xTi_2O_4$ coating ("NCM-LTAO") reproduced with permission from Ref.[189]

preformed CEI. NMC622 has been coated with species such as Al_2O_3,[177, 179, 190] Co_3O_4,[191] SiO_2,[47] and TiO_2[167, 182] to prevent the cathode surface from contacting the electrolyte, often at the expense of Li^+ diffusivity at the interface, which can reduce rate capability. Thin coatings will be examined further in Section 5.3. Several recent reports have selected Li^+ conductors such as $LiAlO_2$[189, 190] and $LiTi_2O_4$[189] to improve Ni-rich NMC performance at high rates and upper cutoff voltages, as seen in the rate capability plot in Figure 15c. These solid electrolyte coatings suggest a pathway to stable solid-state batteries with Ni-rich NMC, although so far reports have been limited to model systems,[192] so a Ni-rich NMC coated with Lipon will be examined in Section 5.4. Furthermore, these pretreatment methods often focus more on performance rather than underlying chemistry, such as whether cathode surface termination groups influence electrolyte decomposition and CEI formation. While some computational studies have suggested that -OH and -F surface termination groups can somewhat passivate Ni-rich NMC,[193] experimental work remains limited and will be explored in the scope of this thesis (Section 3), as will the role of inactive cell components in the following section.

2.6 Inactive Battery Components and their Influence on Interfaces

The remaining components to discuss are often referred to as "inactive" because they are not designed to participate in chemistry or electrochemistry in a cell, although their significant surface area in contact with active components make them worthy of examination. These can be considered in two categories: cell components (the separator, current collectors, and cell casing) and composite electrode components (conductive carbon additives and binders).[194]

2.6.1 Cell Components

As mentioned in Section 2.3, the separator is designed to wet easily with the electrolyte to allow for facile Li^+ transport between electrodes while preventing their physical contact. Once a cell is fully constructed, the electrolyte-soaked separator is in contact with both electrodes as well as the cell casing. Therefore, the separator material must be chemically and electrochemically stable toward other components such that no adverse reactions occur at any interface between materials. The material is typically a microporous polymer membrane, but non-woven fabric mats or an inorganic composite are sometimes used for their high porosity and thermal stability.[195] High porosity allows for greater absorption of electrolyte, and thus minimize losses in electrolyte conductivity due to inactive separator volume. The ionic resistance of the separator can be reduced by limiting its thickness (typically 20 – 30 μm), but too thin of a separator with high porosity can reduce its mechanical strength and increase the likelihood of a short circuit.[195, 196] By comparison, alkaline batteries can incorporate separators an order of magnitude thicker because their chemistry has a lower risk for shorting (i.e. no dendrites) which allows for great membrane porosity.[196] Several commercial separators and relevant physical properties are listed in Table 7. The selectivity of the separator for chemical species is relevant to the chemistry of the SEI and CEI, as soluble species evolved at the surface of either electrode may pass through the separator to react with the surface. In Section 2.4, metal species dissolved at the cathode surface can interfere with the SEI and intercalate into a graphite anode, reducing available Li^+ sites and thus capacity, so there is motivation for the design of separators which impede certain ionic species. Fang *et al.* also observed crosstalk between electrodes with CEI formation from species originally formed at the anode.[197] Interestingly, they observed a decrease in the amount of CEI species when they increased the number of separators from 1 to 3, meaning electrode spacing and/or separator thickness and overall available electrolyte volume plays a role in modulating interphase formation.

Table 7. Selected physical properties of common separators: a) microporous polymer membrane, b) non-woven fabric mat, and c) an inorganic composite. Values collected from product brochures and Ref.[195]

Membrane Property	Separator Brand		
	Celgard	**Dreamweaver**	**Separion**
Product Name	Celgard 2325	Gold 20	S240-P25
Type	Microporous Polymer	Non-woven mat	Inorganic Composite
Composition	Polypropylene-Polyethylene-Polypropylene	Aromatic Polyamide	Al_2O_3/SiO_2
Thickness (μm)	25	22	25±3
Porosity (%)	41	37	>40
Melt Integrity (°C)	134	500	210
Tensile Strength, MD (kgf/cm^2)	1900	800	>3 N/cm [a]

[a] Values reported with different precision and units between companies

As mentioned in Section 1.1, good electrical contact between the current collectors and electrode active materials is necessary for reliable battery operation with low impedance.[194] This contact may be interrupted if the aluminum or copper current collectors form a resistive passivation layer or corrode in contact with the electrolyte. While corrosion (or dissolution) of Al has been observed in several different electrolytes with lithium salts, it has been reported that electrolytes based on $LiPF_6$ and $LiBF_4$ significantly suppress reactions with Al foils.[198, 199] There is some disagreement in literature about the mechanism by which the Al current collector reacts with the electrolyte – either by corrosion or dissolution[200, 201] – but Chen *et al.* recently reported a coupled electrochemical-chemical reaction by oxidation of solvent molecules on Al above 3.9 V providing protons, rather than trace water in $LiPF_6$-based electrolytes.[18]

Copper foil is typically used as the negative electrode current collector. While pitting of Cu has been observed in electrolytes above 3.6 V *vs.* Li/Li$^+$,[202] in practical cells the anode is limited to >0 – 1.5 V *vs.* Li/Li$^+$ depending on the material, so Cu is a reliable anode current collector.[202, 203] The stainless steel cell casing or polymer pouch is the final cell component which contacts the electrolyte as well as the anode and cathode current collectors. Although the cell casing is not essential for operation, its primary function is to hermetically seal the battery components from the atmosphere while providing a robust form factor to fit in the desired application.

2.6.2 Conductive Additives

Many active materials have an intrinsically low electronic conductivity, or poor electrical connection between particles, and require conductive carbon as part of a composite electrode. Various carbon nanostructures (*e.g.* nanotubes,[204] nanofibers,[81] and graphene[205]) have been explored, but the most commonly used form is carbon black for its high specific surface area. The role of conductive carbon in electrolyte decomposition and CEI formation in Ni-rich systems remains a point of contention in the literature. In one camp, carbon additives are seen as potential catalysts for electrolyte decomposition due to their large surface area of 65 m^2/g as compared to 0.35 m^2/g NMC622 resulting in comparable total surface areas in a composite electrode with 91.5 wt% active material, 4.4 wt% carbon, and 4.1 wt% binder (85.6 x 10^{-3} and 9.59 x 10^{-3} m^2 carbon

black and NMC622, respectively).[13, 53, 206, 207] Manthiram *et al.* used time-of-flight secondary-ion mass spectrometry (ToF-SIMS) to observe the formation of a CEI layer on conductive carbon particles upon contacting a $LiPF_6$/EC-based electrolyte.[208] Interestingly, they proposed a mechanism (seen in Figure 16a) for CEI evolution on Ni-rich NMC cathode particles by mutual exchange of interphase species between the cathode material and carbon. A similar environment was suggested by Stevenson *et al.*[206] and Novak *et al.*[53] for carbon additives in $Li_3V_2(PO_4)_3$ and Li-rich NMC systems, respectively. Winter *et al.* also demonstrated the relevance of the surface chemistry of carbon additives through thermal treatment to produce more "noble" carbon surfaces which demonstrated less oxidative electrolyte decomposition in LMNO cells.[207]

Contrary to those reports, Gasteiger's group found that carbon additives did not contribute to electrolyte oxidation below 5 V *vs.* Li/Li^+ by using ^{13}C labeled conductive carbon to find that CO_2 and CO were generated from the decomposition of the carbonate electrolyte, not carbon additives.[209] A follow-up study purported that electrolyte oxidation was induced by oxygen release from the Ni-rich cathode upon charging, rather than strictly electrochemical oxidation.[13] This supports the argument that electrolyte decomposition in these Ni-rich systems is primarily due to chemical oxidation at the active material CEI, rather than electrochemical oxidation of conductive carbon. The complexity of either case can be isolated by studying carbon-free electrodes to gather information on the active material alone through methods such as PVD, which would also reduce overlapping carbon signals in XPS (to be discussed in Sections 4.1 and 5.1).[210]

2.6.3 Binders

Besides the active material and conductive carbon, composite electrodes also contain a polymeric binder matrix to cohesively bond particles together and adhere them to the current collector. This binder is typically 2 – 10 wt.% of the composite to accomplish its structural role without impeding electrochemistry. This balance is necessary because the most common binder, poly(vinylidene fluoride) (PVDF), has poor electronic and ionic conductivity but provides good electrochemical stability.

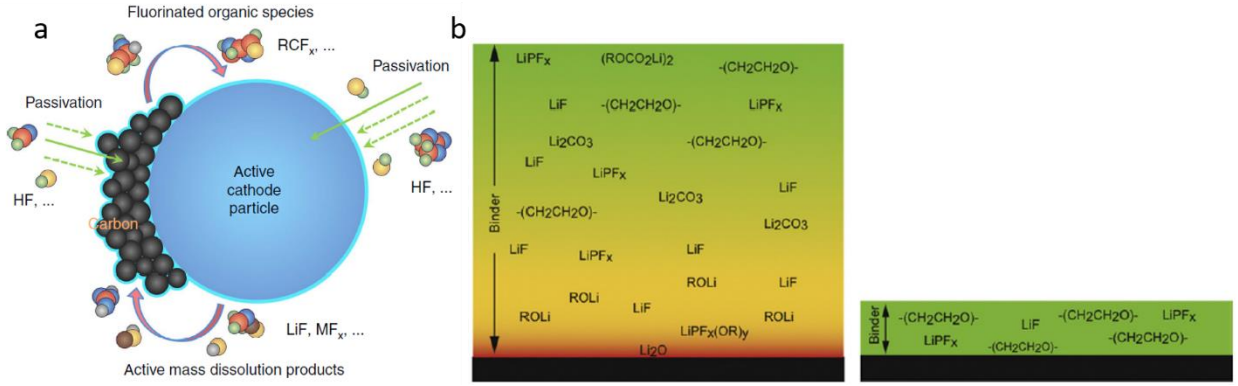

Figure 16. a) reported decomposition mechanism on conductive carbon and CEI of Ni-rich NMC, reproduced with permission from Ref.[208] and b) schematic of SEI (left) and CEI (right) species detected with synchrotron-based XPS, reproduced with permission from Ref.[211]

Unfortunately, PVDF is expensive to produce, difficult to recycle, and requires environmentally harmful volatile organic compounds such as N-methyl-2-pyrrolidone (NMP) for processing.[212] Water-soluble alternatives have been of interest lately to balance manufacturing costs and environmental concerns with increasing lithium-ion battery production. Among them, carboxymethyl cellulose (CMC) and alginate are of interest as they originate from natural sources (cellulose and brown algae, respectively). These also benefit from higher tensile strength and elasticity than PVDF,[213] which are important properties for preventing cracking in alloying electrodes such as Si that swell and contract significantly during cycling.[214] Poly(acrylic acid) (PAA) is a common water-soluble synthetic binder which provides similar mechanical properties to CMC but has a tunable molecular weight (which can improve solubility) during synthesis as opposed to naturally-sourced polymers.[131, 215] PAA is sometimes neutralized to form sodium or lithium polyacrylate (NaPAA, LiPAA) as binders with the dual purpose of improved ionic conductivity and as an initial passivation layer on graphite[216] and LNMO,[217] for example.

While the binders discussed above have been examined for several anodes and cathodes, there is an absence of literature dedicated to the role of binders in Ni-rich cathode materials despite its potential role in chemistry at high voltages.[214] In particular, there is a lack of understanding with regards to the morphology and coverage of binder at these highly reactive surfaces and what role the binder might play in electrolyte decomposition. This is likely due to ambiguities which arise when using surface sensitive techniques such as XPS on composite electrodes. Multiple sources of carbon and fluorine signals – from the conductive carbon, binder, and electrolyte degradation products – are difficult to deconvolute. Studying binder and carbon-free electrodes have enabled more targeted studies of active materials[197, 218] and will be discussed further in the next section. Groups such as Edström *et al.* have used XPS with varying energy sources to provide a depth profile of the CEI and SEI.[219] As seen in Figure 16b, their model shows that the vinylidene fluoride trifluoroethylene copolymer binder used in their study was detected throughout both interphase layers which were comprised of LiF, semicarbonates, and polymeric species.[211] While the SEI was found to be thicker than the CEI in their study, the binder was detected throughout both surface layers.

The implications of binder in the CEI is not well understood, nor is the composition, formation, and passivation mechanism of the CEI for high voltage operation of NMC622. As discussed above, the crystal structure of cathode materials and their compatibility with electrolytes define the constraints of battery operation (e.g. voltage window). The interfacial stability in not well understood for high voltage operation, nor is the influence of the binder at the interface, how the initial surface chemistry effects CEI composition and cell performance, or whether a solid electrolyte with proven high voltage stability can enable full utilization of this material. These knowledge gaps define the scope of this thesis, which will be further defined in the next section.

3. THE SCOPE OF THIS THESIS

As discussed in Section 2.1, Ni-rich NMCs such as NMC622 provide an enticing balance of high energy density, ionic conductivity, and better environmental responsibility than current cathode materials. The challenges preventing these materials from full utilization can be traced back to the CEI and high voltages (≥ 4.5 V *vs.* Li/Li^+). Specifically, the knowledge gaps surrounding electrolyte decomposition at high voltages (chemical *vs.* electrochemical), the role of the active material in CEI formation (compared to carbon black and binders), and how best to control this interface provide the motivation to investigate this material in depth by asking the following questions: how does the presence of binders at the interface influence electrolyte decomposition and CEI formation? Why do some metal oxide coatings prevent electrolyte decomposition and capacity fading better than others? And how might replacing the typical liquid carbonate electrolyte with a solid electrolyte stable at high voltages influence the performance of NMC622?

In order to isolate these effects and reduce the complexity of surface analysis, the design and synthesis of a binder and carbon-free thin film cathode will be discussed in Section 5 (**Paper I**). Physical vapor deposition and x-ray diffraction are essential techniques for synthesizing and characterizing this model system and will be detailed in the next section. That thin film procedure provides a platform for studying the role of surface coverage by the binder and its interactions with the CEI, as highlighted in Section 2.6. The influence of binder chemistry and morphology on the CEI of thin film NMC622 cathodes will be investigated in Section 6 (**Paper II)**. X-ray photoelectron spectroscopy is an essential technique for studying interfacial chemistry and will be detailed in Section 4.1. It was noted by several research groups discussed in Sections 2.4 and 2.5 that the passivation of electrode surfaces may be influenced by the initial chemical environment (*i.e.* surface termination groups). In Section 7 (**Paper III**), the surface chemistry of NMC622 will be controlled using thin metal oxide coatings to study the formation of the CEI from different initial chemical environments. Finally, the behavior of NMC622 in an all solid-state battery configuration with Lipon and Li metal will be investigated in Section 8 (**Paper IV**) for insight into the solid-solid CEI and the potential for Ni-rich NMC materials in solid-state applications. The experimental techniques noted above – PVD, XRD, XPS – and electrochemical measurements are critical to these studies, so a discussion of them follows in Section 4.

4. EXPERIMENTAL METHODS

4.1 Core/Primary Techniques

4.1.1 Physical Vapor Deposition by Magnetron Sputtering

Magnetron sputtering, a form of PVD, was employed frequently in this thesis. A schematic of RF magnetron sputtering can be seen in Figure 17a, where an ion (typically Ar^+, chosen for its high mass to improve sputter yield) is accelerated into a target material to sputter atoms from the surface. These atoms deposit on the substrate surface as a thin film (a few nm to tens of μm), ideally with a similar stoichiometry to the target material.[220] The deposition rate is dependent on the sputter yield: the number of sputtered atoms ejected *vs.* the number of incident sputtering atoms, which approaches unity around ion energies of 100 eV, depending on the target material. This means that the sputtering rate varies as a function of energy transfer from Ar^+ to each element (Li, Mn, Ni, etc.). The chamber is pumped down to a low base pressure ($<10^{-6}$ torr) to minimize background gases and contaminants (i.e. H_2O, CO_2) before introducing the sputter gas through an isobaric value at <40 mtorr such that a plasma can be maintained without sputtered atoms colliding with gaseous species before depositing on the substrate (mean free path ~10 cm).[221] In direct current (DC) sputtering, a potential is applied between the target (negative terminal) and the chamber (positive terminal) such that accelerated electrons collide with gas molecules (ionizing collisions) to form a plasma of positive ions. A magnetron source is used here to confine secondary electrons close to the target surface with magnets, increasing their residence time, thus increasing the number of ionization events which increases plasma density and deposition rates. DC sources can be used to sputter metals, but do not work for insulating target materials because no current may pass through, causing a charge buildup at the surface. Radio frequency (RF) sputtering is used for dielectric materials because an alternating current (at 13.56 MHz, designated for RF sources by the FCC) alternates the polarization of the target surface to prevent charge buildup.[220]

In this thesis, RF sputtering is used for ceramics and polymers and DC sputtering is used for metal targets. In either case, a quartz crystal microbalance placed within the plasma measures the deposition thickness, *t*, based on the deviation from is base mechanical oscillation frequency (~6 MHz) according to the equation:

$$\mathbf{t} = \frac{\mathbf{N}*\boldsymbol{\rho}_\mathbf{q}}{\boldsymbol{\rho}_\mathbf{f}*\mathbf{f}^2}(\mathbf{f}_\mathbf{q} - \mathbf{f}) \quad \textbf{(3)}$$

Where N is the frequency constant for the quartz crystal, ρ_q is the density of quartz, ρ_f is the density of the film, f is the resonant frequency of uncoated quartz, and f_q is the resonant frequency of the loaded crystal.[222]

Reactive sputtering is employed for metal oxide films in Section 5.3 and Lipon in Section 5.4. The sputtering gas, in this case, is an O_2/Ar blend or N_2 such that sputtered species (metals or Li_3PO_4) react with their respective gas at the sample surface. This provides more control over the stoichiometry of materials which are sensitive to minor changes in composition, such as Lipon.[97]

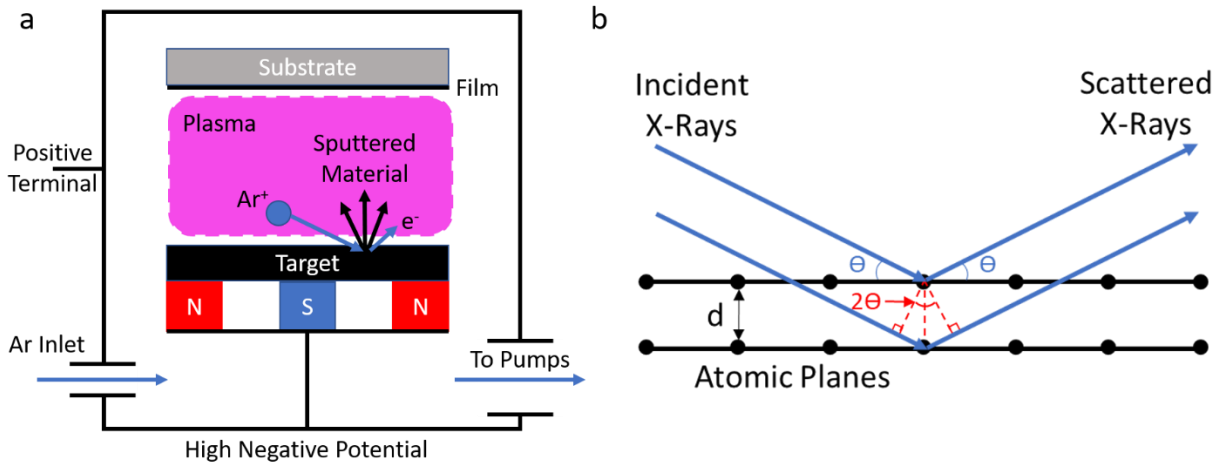

Figure 17. Schematic of a) RF magnetron sputtering system and b) principle of XRD for a layered crystal structure

4.1.2 X-ray Diffraction

Structural characterization of thin film electrodes and synthesized target materials was carried out by XRD. Figure 17b depicts the basic principle of XRD, where parallel x-rays of some wavelength, λ, are incident at an angle, Θ, to a crystal with atomic planes spaced a distance, d, apart. These x-rays are scattered in all directions, but in some of these directions, their path lengths allow them to be completely in phase, thus positively reinforcing one another. Such constructively interfering scattered x-rays are defined as diffracted beams. Two scattered x-rays will be completely in phase if their path difference is a whole number, *n*, of wavelengths – called the order of diffraction – according to the relation:[223]

$$\mathbf{n\lambda = 2dsin\theta} \quad (4)$$

This is known as Bragg's Law, and it states the essential condition necessary for diffraction to occur. For a given x-ray wavelength and crystal spacing, several angles of incidence (Θ_1, Θ_2,…) may allow for diffraction (at n = 1, 2,…). At these angles, x-rays may be detected above the background signal of other scattered beams due to constructive interference, and so Bragg's Law may be used to determine the spacing and relative angles between crystal planes in a material to describe its crystal structure.[223]

4.1.3 X-ray Photoelectron Spectroscopy

A useful technique for surface studies is XPS, which uses X-rays (*e.g.* 1253.6 eV for Mg Kα) to generate photoelectrons from core electron shells to provide quantitative chemical information of the top few nm of material. The top of Figure 18a demonstrates the XPS emission process for a model atom with orbitals 1s, 2s, and 2p, where an incident photon excites a core shell electron as a photoelectron of characteristic energy for each atom. The emitted electron has kinetic energy, *KE*, according to the relation:

$$\boldsymbol{KE = h\nu - BE - \phi_s} \quad (5)$$

Where *hν* is the energy of the photon, *BE* is the binding energy of the electron's atomic orbital, and ϕ_s is the spectrometer work function.[224] Variation in binding energy due to differences in the chemical potential and polarizability of a compound is referred to as a chemical shift and may be

used to identify the chemical state of a compound. Photoelectron emission may be followed by relaxation of an outer shell electron, shown in the bottom of Figure 18a, which falls into the vacancy left by the photoelectron and causes the release of an Auger electron which carries off excess energy. The Auger electron kinetic energy equals the difference between the initial singly charged ion and the final ion with two electron vacancies, and so it is characteristic of the element, allowing for another means of chemical identification.[224]

XPS has limited depth resolution because although incident photons may excite photoelectrons several microns into the sample, there is a higher probability of photoelectrons interacting with matter (due to their larger cross-section than photons) and so only photoelectrons from the top few nm may escape without energy loss. Electrons which experience inelastic collisions before detection contribute to the background reading. Photoelectrons are detected by an electron spectrometer according to their kinetic energy with intensity in number of counts plotted against kinetic energy or binding energy across some range. An example of a typical plot across a broad range – referred to as a survey spectrum – can be seen in Figure 18b. Most elements have a major photoelectron binding energy peak below 1100 eV, so a survey scan from 1100 – 0 eV (relative to the Fermi level corresponding to zero binding energy) is useful to determine all detectable elements before following up with narrow scans of small energy step sizes at low pass energy for higher resolution.[224]

Analysis of these spectra can require peak deconvolution due to multiple elements and compounds, multiple oxidation states of a species, and charging of samples. A common first step is calibration of a spectrum to a standard of known position – such as adventitious carbon at 284.8 eV – to account for incremental charging. While there are databases of standards available for identifying peak positions (*e.g.* National Institute of Standards and Technology), it is beneficial to collect spectra on one's own instrument with standards of known compositions.[225] Further complexity may arise due to overlapping contributions of conductive carbons and binders in composite electrodes, so thin films solely comprised of active materials are useful for quantitative investigations of surface species and materials behavior.

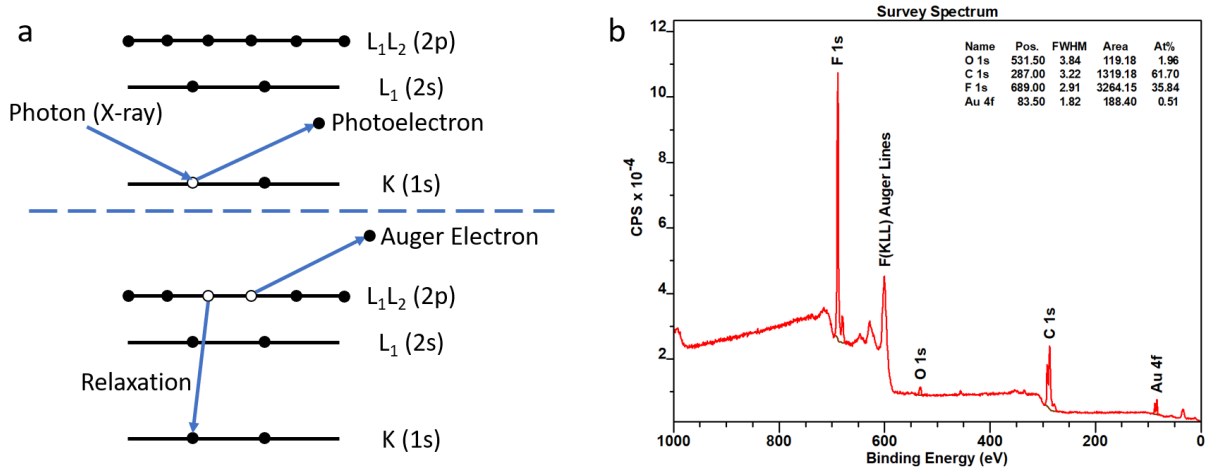

Figure 18. XPS a) photoelectron emission (top) and Auger electron emission (bottom) with b) typical survey scan profile of PVDF-coated Au with Mg Kα source showing photoelectron lines F1s, O1s, C1s, and Au4f and F(KLL) Auger lines.

4.1.4 Electrochemistry

Electrochemical cells with liquid electrolytes were assembled in an Ar-filled glove box, whereas solid-state cells were deposited by sputtering and thermal evaporation of Li in a series of vacuum chambers (NMC>Lipon>Li, detailed in Section 5.4). Liquid cells were either in coin or Swagelok cell configurations seen in Figure 19a and b, respectively. Coin cells allowed for rapid assembly and performance testing whereas Swagelok cells enabled cell disassembly for nondestructive post-mortem characterization of electrodes. In each case, Li metal was both the counter and the reference electrode, which allow for fast electron transfer kinetics and an abundant supply of lithium so that the working electrode, NMC622, can be examined with minimal electrochemical influence by the counter electrode.

Several examples of galvanostatic cycling were provided in Sections 2.1 and 2.2, where a constant current is applied to a cell until it reaches an upper cutoff voltage (UCV) or lower cutoff voltage (LCV), at which point the direction of current flow is reversed to study the intercalation reaction during charge and discharge. The applied current density is often referred to as C-rate in commercial cells, which is defined as a proportion of the capacity of the working electrode per unit time (*e.g.* 1C = all the specific capacity of the working electrode is extracted in one hour). This may also be expressed as the amount of Li^+ extracted or inserted over that unit time. The ratio between charge capacity to the UCV and discharge capacity to the LCV is referred to as coulombic efficiency and is a measure of how efficiently a system can reversibly cycle ions. Potentiostatic holds may be included at the UCV or LCV to extract Li^+ which is kinetically hindered. In these regions, the voltage of a cell is held at the desired potential until the measured current approaches equilibrium. [194]

Electrochemical Impedance Spectroscopy (EIS) – also known as AC Impedance Spectroscopy – is used to probe electrochemical processes of a system in different time domains. The AC (sinusoidal) potential, *E(t)*, is applied with a small excitation signal ($|E_0|$~10 mV) such that the cell response is pseudo-linear, resulting in a current response, *I(t)*, at the same frequency but phase shifted, ϕ. Because a battery does not behave like an ideal resistor, an analogous description of the ability of a system to resist the flow of current, called impedance, can be expressed as:

$$Z(t) = \frac{E(t)}{I(t)} = \frac{E_0 \sin(\omega t)}{I_0 \sin(\omega t + \phi)} = Z_0 \frac{sin(\omega t)}{sin(\omega t + \phi)} \quad (6)$$

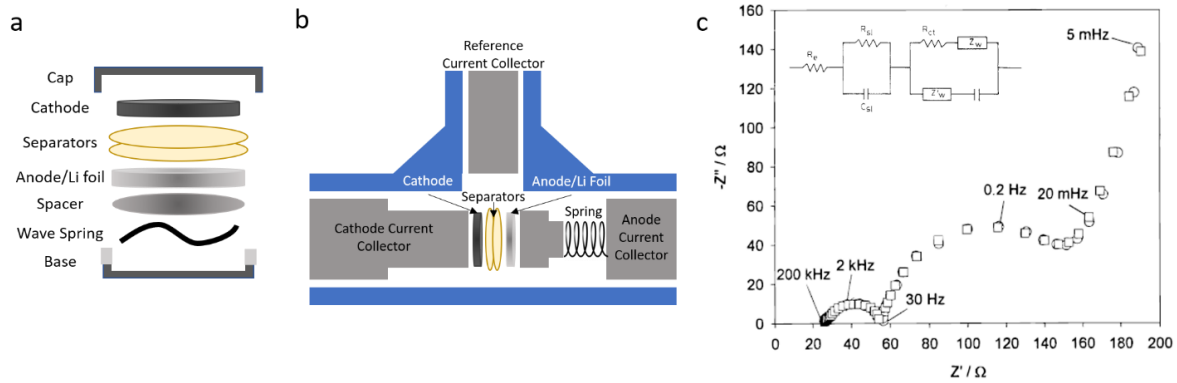

Figure 19. Schematic of a) coin cell battery and b) Swagelok cell, and c) EIS curve with inset equivalent circuit reproduced with permission from Ref.[226]

Where the frequency, *f*, is expressed as radial frequency, $\omega = 2\pi f$, such that impedance can be expressed as a complex vector:

$$\boldsymbol{Z(\omega) = Z_0 e^{i\theta} = Z' + Z''} \quad (7)$$

By Euler's Relationship, with the real term, *Z'*, corresponding to ohmic resistance (potential and current in phase), and imaginary, *Z"*, accounting for capacitive effects (phase shifted). Because electrode reactions have both resistive and capacitive reactions (charge transfer and double layer formation, respectively), the impedance can be modeled with an equivalent electrical circuit. A typical EIS spectrum for LCO is shown as a Nyquist plot in Figure 19c with the equivalent circuit inset. In this case, a modified Randles circuit can account for double layer capacitance at the interface (represented as a constant phase element, CPE, due to the porous nature of electrodes rather than flat plates), the bulk electrolyte resistance (R_s), the resistance associated with the surface, called charge transfer resistance (R_{ct}), and diffusion resistance, called Warburg impedance (W_t).[227] Notably, EIS was used to rationalize the impedance measurements of LCO by introducing a surface layer component as the first report of the CEI[159] (included here as CPE_{CEI} and R_{CEI}).

4.2 Materials Synthesis and Supplemental Characterization

Cathode target materials for PVD were prepared by a solid-state synthesis route of metal carbonate precursors and cold pressing (described further in Section 5.1).[210] Binder solutions were spin coated and spray coated onto thin film samples, as seen in Section 5.2.

In some studies, supplemental characterization by optical microscopy provided bulk morphological insight while SEM/EDS provided higher resolution morphology and elemental characterization to supplement XPS of the surface. Transmission electron microscopy (TEM) provided local structural information with selected area electron diffraction to compliment XRD. Atomic force microscopy (AFM) provided surface roughness and stiffness information of films. Fourier transform infrared spectroscopy and Raman spectroscopy provided additional insight into bulk chemical states by studying vibrational modes. Inductively coupled plasma – optical emission spectroscopy provided bulk elemental compositions when determining film compositions. Each technique is discussed as they appear in the studies of Section 5.

Several classes of techniques which were not used in this thesis but are frequently applied for battery analysis are nuclear magnetic resonance (NMR) and secondary ion mass spectrometry (SIMS), and neutron-based techniques. NMR is particularly useful for monitoring changes in chemical environments, as the high natural abundances of ^{7}Li, ^{1}H, ^{19}F, and ^{31}P allow for rich datasets of changes while cycling.[228] SIMS allows indirect measurement of the species in the SEI through gravimetric and charge ratio analysis by sputtering the surface.

Several exotic and specialized techniques have proven useful in understanding the SEI. The cross-section of Li^+ is too small for significant electron or x-ray collisions necessary for other techniques, so neutron-based techniques fill a niche in the lithium-ion battery field. Neutron reflectometry is often employed for interfacial studies to determine the thickness of the SEI as well as the distribution of chemical species within the layer.[229] This specific analysis is possible due to the different scattering length density of each element (and thus, each species). Small angle neutron scattering (SANS) can provide complementary information on the size and morphology of the SEI nanostructure by measuring the intensity of neutrons at a given scattering vector.[228] Developing *operando* techniques has been a point of interest lately in pursuit of nondestructive diagnostic methods for battery cells and packs.[230]

5. SYNTHESIS OF NI-RICH THIN-FILM CATHODE AS MODEL SYSTEM FOR LITHIUM ION BATTERIES

This article was published in the journal *American Chemical Society Applied Energy Materials* and addresses the synthesis of thin films of NMC622 used in this thesis. My contribution was planning and executing all experiments with G. M. V. with the exceptions of Transmission Electron Microscopy (TEM) and Rutherford Backscatter Spectroscopy (RBS). I participated in the collection of TEM data while X. S. and R. R. U. collected the data, which I then analyzed. Y. W. collected and analyzed RBS data with my input for experimental conditions and results. All authors assisted with data interpretation and editing the manuscript. Supplemental figures have been added to the main text for clarity.

Nathan D. Phillip,[1,2] Rose E. Ruther,[5] Xiahan Sang,[3] Yongqiang Wang,[4] Raymond R. Unocic,[3] Andrew Westover,[2] Claus Daniel,[1,5] Gabriel M. Veith[2*]*

[1] The Bredesen Center for Interdisciplinary Research and Graduate Education, University of Tennessee, Knoxville, TN, 37996, USA

[2]Chemical Sciences Division, Oak Ridge National Laboratory, Oak Ridge, TN 37831, USA

[3]Center for Nanophase Materials Sciences, Oak Ridge National Laboratory, Oak Ridge, TN 37831, USA

[4] Ion Beam Materials Laboratory, Los Alamos National Laboratory, New Mexico 87545, USA

[5] Energy and Environmental Sciences Directorate, Oak Ridge National Laboratory, Oak Ridge, TN 37831, USA

5.1 Abstract

We demonstrate a process to prepare model electrodes of the Ni-rich layered compound $LiNi_{0.6}Mn_{0.2}Co_{0.2}O_2$. These thin film cathodes are compared with the composite materials to demonstrate the system is a viable platform for isolating interfacial phenomena between the electrolyte and active material without the influence of binders and conductive additives. The appropriate choice of heterolayers was found to influence the preferential orientation of the (101) and (104) planes relative to the (003) plane of the layered $R\bar{3}m$ crystal structure, enhancing Li^+ diffusion and improving electrochemical performance. The addition of a Co interlayer between the Pt current collecting layer and alumina substrate increased the (101) and (104) texturing of the 500 nm Ni-rich film and allowed cells to deliver greater than 50% of their theoretical capacity. This work provides an architecture for isolating complex mechanisms of active materials which suffer from surface reconstruction and degradation in electrochemical cells.

5.2 Introduction

Despite the adoption of lithium ion batteries for large scale energy storage in automotive and electric grid applications, they are yet to reach their full potential due to limited storage capacity, energy density, and lifetime.[15, 231, 232] The layered rock salt ($R\bar{3}m$ crystal structure) class of cathode materials is commonly investigated in different stoichiometries of $LiNi_xMn_yCo_zO_2$, where x + y + z = 1 (NMCxyz). These materials are of commercial interest due to their demonstrated stable capacity up to ~160 mAh/g_{NMC} when cycled to an upper cutoff voltage of 4.3 V *vs.* Li/Li^+ for $LiNi_{1/3}Mn_{1/3}Co_{1/3}O_2$,[232, 233] with capacity up to ~200 mAh/g_{NMC} possible for the Ni-rich variants, such as NMC622 and NMC811, but higher upper cutoff voltages must be applied to access that capacity.[39, 234] In this regime, electrolyte stability and surface reactivity are critical considerations due to active material and electrolyte degradation which can be detrimental to cell performance and lifetime.[13, 27, 39, 235, 236] These degradation products, along with surface phase transitions from layered to spinel and rock salt-type structures,[237, 238] comprise the cathode electrolyte interface (CEI), which increases cell impedance.[239] Understanding this interface is essential to stabilize these materials for commercial implementation.

The CEI on Ni-rich NMC can be considered as the complex layer of decomposition products from electrolyte degradation deposited on the cathode active material in contact with the electrolyte. While common electrolyte solvents such as ethylene carbonate (EC) and ethyl methyl carbonate (EMC) have a high intrinsic stability against oxidation, in practical cells with electrolyte salts such as $LiPF_6$ these solvent molecules have a smaller stability window of 1.3-4.3 V *vs.* Li/Li^+.[15] It has been suggested that the solvent molecules coordinate with anions such as PF_6^- from the electrolyte salt to form complexes which can then donate an electron to the cathode surface and possibly spur nucleophilic attack by the anion.[162, 163] In contrast to those claims, dissociative adsorption of EC has recently been reported to be more energetically favorable.[240] While these mechanisms are not agreed upon in literature, it is thought that the CEI on Ni-rich NMC can suppress this electrolyte degradation at higher voltages. X-ray photoelectron spectroscopy studies have detected species such as LiF, Li_2CO_3, RCO_3, and $LiPF_xO_y$ in this passivation layer,[33] but this interface is perhaps disrupted due to structural evolution of Ni-rich materials at high voltages. Over-delithiation of the cathode causes progressive structural rearrangement from the layered structure to spinel (LiM_2O_4, then M_3O_4) and finally MO-type rock salts.[12] This transition is accompanied by the loss of lattice oxygen, providing opportunities for chemical oxidation of the electrolyte, which has been detected by Gasteiger *et al.* using on-line electrochemical mass spectrometry (OEMS).[209]

The complex surface environment of the cathode material is further convoluted by the presence of conductive and binding agents typically found in a composite electrode which make it difficult to study the origin and dynamics of the CEI. The so-called "inactive" components have been investigated for their contributions to electrochemical performance and side reactions with the electrolyte. La Mantia *et al.* found a significant electrolyte oxidation during the first few cycles of electrodes made of carbon black when charged beyond 4.6 V *vs.* Li/Li^+, [241] which is a region of interest for accessing maximum capacity of Ni-rich materials such as NMC622.[242] One of the challenges in determining which factors influence electrolyte decomposition is deconvoluting contributions from the active material and conductive carbon. For example, Demeaux *et al.* investigated carbon black/PVDF electrodes in an EC/dimethyl carbonate (DMC) 1 M $LiPF_6$ electrolyte and found significant CEI formation on cycling and during storage at open circuit voltage (OCV).[243] This suggests not only electronic but chemical contributions of the carbon black and binder electrodes to the CEI, perhaps catalyzing additional solvent decomposition reactions in

composite electrodes. Membreno *et. al* studied the CEI on α-$Li_3V_2(PO_4)_3$ and found that conductive carbon formed a surface layer both spontaneously in electrolyte and electrochemically, comprised of ethers, esters, alkoxides, carboxylates, and carbonates as well as inorganic species from salt decomposition (LiF, $Li_xPO_yF_z$, and Li_xPF_y). They attributed the majority of the SEI formation to the surface of the carbon due to its nanoscale size providing a significantly higher total surface area relative to that of the micron-sized active material particles. [206] This ratio has been measured by the Brunauer-Emmett-Teller method (BET) to find that 89% of the cathode surface area was comprised of conductive carbon (C65) in an electrode containing NMC622, C65, and PVDF in a weight ratio of 91.5/4.4/4.1.[13] These contributions to electrolyte decomposition can obscure reactions between the active material and electrolyte, and so it would be prudent to develop a simplified system for studying the complex interactions between the active material and electrolyte.

Thin films (<2 μm) of electrochemically active materials offer a path to isolate the surface reactivity and degradation mechanisms between the electrolyte and cathode material from the influence of conductive additives and binders. Much of the pioneering work on thin film layered cathode materials was accomplished by Bates and Dudney for applications in solid state batteries.[232, 234, 244-246] $LiCoO_2$ proved to be of particular interest given the tunable preferred orientation, or texturing, of thin films which provided performance rivaling or exceeding that of the active material in composite electrode geometries.[246] This system has been applied recently to probe the CEI composition at high voltages.[218] Other high energy cathodes such as $LiMn_{1.5}Ni_{0.5}O_4$[247] and $LiNi_{1/3}Mn_{1/3}Co_{1/3}O_2$[248, 249] have been isolated in thin film electrodes for fundamental studies of interfacial phenomena such as structural rearrangement, electrolyte decomposition, and CEI formation. Single crystal NMC622 has been used for studying facet-dependence of reactions,[250] but to our knowledge, no one has successfully produced Ni-rich NMC622 thin film electrodes despite their utility in studying interfacial reactions between the active material and electrolyte.

Here we describe a synthesis method for thin film NMC622 electrodes by means of radio frequency (RF) magnetron sputtering. Structural characterization reveals a preferential ordering of crystalline grains in favor of Li^+ diffusion which is dependent on the choice of heterolayers used for the substrate. The morphology, structure, composition, and electrochemical performance of the thin films are also compared to typical NMC622 composite electrodes to demonstrate their utility as a model interface of the isolated active material with a well-defined surface. This approach enables investigations of the interfacial reactivity between active materials, electrolytes, and coatings without contributions from conductive additives and binders.

5.3 Methods

Synthesis. Current collectors were prepared by DC magnetron sputtering of Co, Pt, Au, or Cr targets (Kurt J. Lesker) on the entire surfaces of Al_2O_3 substrates (99.6% Al_2O_3 disk, 1 cm x 3.8 mm, 480 nm average surface roughness from Valley Design), depending on the experiment. Thin film electrodes were deposited on Al_2O_3, Si, or Pt foil substrates by RF magnetron sputtering of ceramic targets following a pre-sputter step of at least 30 minutes to clean the surface of any residual contimants. Targets were prepared in house by solid state synthesis from carbonate precursors– Li_2CO_3, $MnCO_3$ (Sigma Aldrich), $NiCO_3$, and $CoCO_3$ (Alfa Aesar) – in a stoichiometric mixture of the transition metals for NMC 622 with 60% excess Li. The precursors were milled in isopropyl alcohol with yttria-stabilized zirconia pellets for at least 24 hours before subsequent pre-calcination at 450°C for 4 hours in air. The resultant powder was cold pressed into

a 2" pellet under 5000 psi for 1 minute before annealing at 750°C for 12 hours in air with a heating rate of 5 °C/min. Targets were bonded to a copper substrate. Before deposition, the chamber was evacuated to a base pressure of $<2x10^{-6}$ torr. Each RF deposition was performed at a bias of 90 W in an ultra-pure Ar gas flow rate of 55.0 sccm with a pre-sputter step for 30 minutes to clean the target surface. The deposition rates were calculated using a quartz crystal microbalance to typically be ~3 nm/min for films ranging in thickness from 0.5 – 1.5 μm. Sputtered films were annealed under high purity air flow (~0.1 LPM) for 1 hour at 700°C and stored in an Ar filled glove box.

Characterization. X-ray diffractometry (XRD) was conducted on a PANalytical Empyrean diffractometer at a standard operating mode of 45 kV and 40 mA with a Cu $K\alpha_1$ monochromated radiation source (λ = 1.5406 Å) with a PIXcel3D detector. The Θ:2Θ scan range and step size were 10° – 90° and 0.02626°, respectively. Raman spectra were collected with a confocal Raman microscope (WITec Alpha 300) with a solid state 532 nm laser source, 20x objective lens, 600 grooves/mm grating, and a laser spot size of ~1 μm. Raman maps were collected over a 50 μm by 50 μm area and scanned with 1 μm by 1 μm steps. The pole figures were measured using an X-ray diffractometer (Panalytical X'Pert MRD Pro) with Cu-$K\alpha_1$ radiation to find the orientation of the (104) crystal plane of the films with $2\theta = 44°$. Inductively Coupled Plasma Optical Emission Spectroscopy (ICP-OES) measurements were carried out on a Thermo Scientific iCAP 7400 ICP-OES Duo. For analysis the NMC films were dissolved in Aqua Regia overnight and then diluted with pure water (18 MΩ). The dilute solution was then run through the ICP along with standards. TraceCert ICP standards were obtained from Sigma-Aldrich and diluted from the initial 1000 ppm to 50, 20, 10, 5, 4, 2, and 1 ppm solutions for calibration using the same concentration of aqua regia in water as the samples. A scanning electron microscope equipped with an energy-dispersive X-ray spectrometer (SEM/EDS, Hitachi TM3030 Plus with Quantax 70) provided surface morphology and composition information of thin films and composite electrodes from 5-minute scans. Crystal structure visualization was accomplished with VESTA.[46, 251] Multilayer film samples were prepared using focused ion beam (FIB, Hitachi NB5000) extraction with a C protective layer against Ga beam damage for scanning/transmission electron microscopy (S/TEM). High resolution S/TEM images and selected area electron diffraction (SAED) patterns were acquired using a probe corrected FEI Titan operated at 300kV.

Rutherford Backscattering Spectroscopy was carried out with a 3.045 MeV ^{4}He+ analyzing beam which was generated using an NEC 3 MV Pelletron tandem accelerator at the Ion Beam Materials Laboratory at Los Alamos National Laboratory. PIPS particle detectors were used for measurements in two configurations: the first at a scattering angle of 167° (Cornell geometry) and the second at 90° (IBM geometry) from the beam direction. The sample normal was tilted 13° from the incident beam, and the accumulated charge was 5 μC for each of the films with a beam current of 5 nA.

Electrochemical Measurements. Both thin film and composite electrodes were cycled in 2032 coin half cells *vs.* Li metal for two formation cycles at C/20 with ten subsequent cycles at C/10 (C = 200 mAh/g NMC622) at 2.5 – 4.2 V *vs.* Li/Li$^+$. The electrolyte in all cases was 1.2 M $LiPF_6$ dissolved in EC and EMC in a 3:7 weight ratio (Tomiyama). Composite electrodes (8 mg/cm^2) were cast from a slurry of NMC622 (Umicore), carbon black (Denka), and PVDF (Solvay 5130) (90:5:5 wt% in NMP) and dried at 100°C under vacuum (<10 mtorr) overnight. Coin cells were assembled in an Ar-filled glove box at Oak Ridge National Laboratory: one case, one spring, one stainless steel spacer (Hohsen), Li foil (Alfa Aesar), two separators (Dreamweaver) soaked with electrolyte, followed by the cathode which was in direct contact with the cap via the bare Pt-coated Al_2O_3 side of the thin film substrate or Al foil of the composite electrode. Electrochemical

impedance spectroscopy (EIS) steps were included after formation cycling and every ten cycles using a BioLogic MPG-2 Battery Tester when cells were at open circuit voltage (~3.3 V) over 10 mHz to 20 kHz with 6 mV applied signal. All cells were built with at least 2 replicates.

5.4 Results & Discussion

In order to develop carbon and binder-free thin film NMC622 electrodes, different substrates were prepared by RF magnetron sputtering. The alumina substrates were coated with different combinations of current collecting and adhesion layers for this investigation: Pt, Au, Cr, and Co. The best performing electrodes were prepared by DC sputtering 20 nm of Co on both sides of the alumina wafer followed by 500 nm of Pt on top of the Co layer (Figure 20a). 500 nm of NMC622 is then deposited on top of the Pt layer on one side. The films are conformal and show the same pattern of surface roughness as the base substrate after annealing (Figure 20b).

NMC622 films deposited on stainless steel and Pt:Cr:Al_2O_3 failed rapidly when cycled in half coin half cells, due to poor adhesion and delamination. Discharge capacities <50% of theoretical were accessible for the first C/20 cycle for 500 nm NMC622 films deposited on Pt-coated Si (Pt:Si), Pt foil, 1.5 µm Pt-coated alumina (Pt:Al_2O_3), and Au:Co:Al_2O_3, but only electrodes using Pt on Co-coated alumina (Pt:Co:Al_2O_3) retained their capacity past the first cycle. When using a substrate with a 200 nm Co interlayer, the capacity was stable, but redox activity was found to occur at 3.9 V, corresponding to a $LiCoO_2$ phase, so a thinner (20 nm) Co layer was used for all experiments and is discussed later.

The resultant film is contrasted against the more complex geometry of a typical composite electrode, comprising of a matrix of PVDF binder and carbon black coating the secondary particles of active material (Figure 20c). Figure 20d shows the top view of an NMC622 composite electrode. Primary particles, which are ~50 nm in diameter, make up the spheroidal secondary particles, which are ~10 µm in diameter, on average. Noticeable cracking can be observed in individual secondary particles comprised of primary particles for the pristine slurry cast electrode (inset image of Figure 20d). The black regions between these secondary particles are binder and carbon black agglomerates. These observations prompt a number of questions about the different cathode interfacial environments: to what degree do the binder and carbon coat the active material and does binder fill the cracks within secondary particles? What is the local electrolyte concentration in the cracks relative to the bulk? How do these variables influence transport across the cathode/electrolyte interface? Thin film electrodes such as these can isolate these questions by reducing the number of interfaces under investigation to only that of the electrolyte and the active material as a fully dense planar surface.

A range of sputter targets were synthesized for deposition of films at a variety of working plasma pressures to better understand the effects of deposition conditions on thin film stoichiometry (Figure 21). ICP analysis compared the stoichiometric ratio of Li to the sum of transition metals in the films as deposited and after annealing at either 700°C or 800°C for 1 hour. The relative Li content of all the films decreased after annealing, which was expected due to Li sublimation. This was mitigated by varying the target stoichiometry from slightly Li deficient ("Li0.8NMC622" signifies $Li_{0.8}Ni_{0.6}Mn_{0.2}Co_{0.2}O_2$ target composition) to 20% and 60% Li excess (e.g. Li1.2NMC622 and Li1.6NMC622 of Figure 21) such that the final film stoichiometry approaches the desired NMC622 composition. This was accomplished for films deposited from the plasma of 60% Li excess targets operated at 7 and 20 mtorr and annealed at 700°C. The overall Li:(NMC) ratio decreased slightly upon annealing at higher temperatures (800°C), but the Ni:Mn:Co ratios were not found to deviate from the target composition. This suggests that the Li

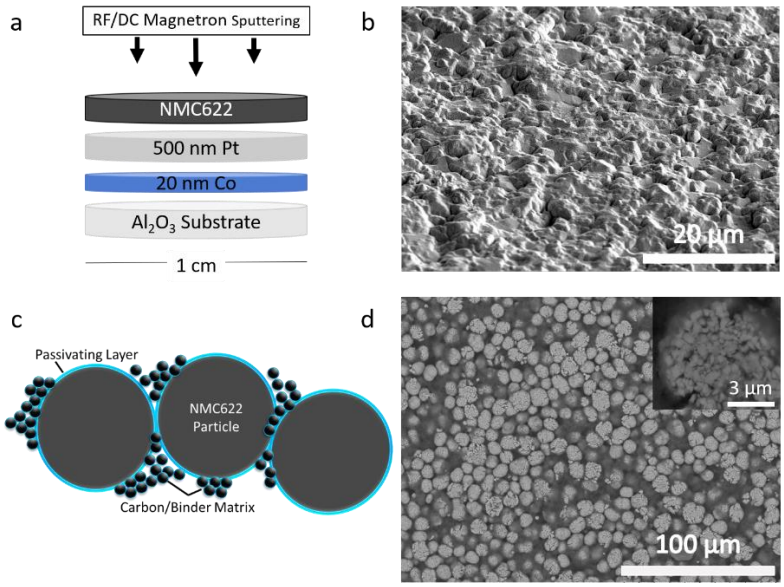

Figure 20. Schematic of a) thin film NMC electrode prepared by magnetron sputtering with b) SEM surface view of thin film and c) traditional coating morphology schematic for d) SEM of composite NMC electrode with inset image of secondary particle

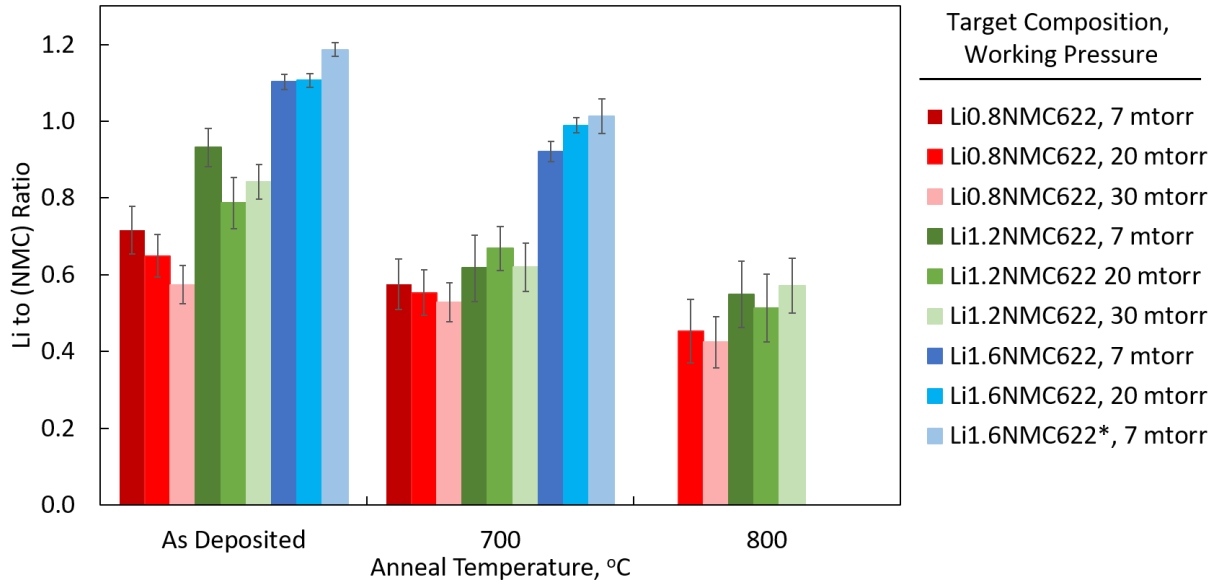

Figure 21. Li:(NMC) stoichiometric ratio of annealed and unannealed films deposited from various target stoichiometries and working plasma pressures. All error bars are two sigma.

content of the target and annealing temperature have the most dramatic influence on final film stoichiometry. The relative transition metal ratios are slightly varied for target Li1.6NMC622* ($Li_{1.6}Ni_{0.58}Mn_{0.21}Co_{0.21}O_2$) and are discussed later with the ICP of an individual film.

XRD was employed to compare the crystal structure of the NMC thin films on the Pt:Al_2O_3 and Pt:Co:Al_2O_3 substrates to investigate the influence of the Co addition. Comparing the films to the reference composite material finds a good agreement with the hexagonal layered structure ($R\bar{3}m$ space group) of the desired material. The lattice parameters *a* and *c* are 2.850 and 14.360 Å, respectively, which is also in good agreement with reported values (Figure 22).[252] Interestingly, the addition of a 20 nm Co layer between the Pt current collecting layer and the Al_2O_3 substrate increases the ratio of the (104) and (101) planes relative to the (003) plane. The thin film electrodes with this 20 nm Co layer have a (003):(104) peak ratio of ~1:4 (Table 8). This preferential orientation is also beneficial to electrochemical performance, as evidenced by the improved capacity of films on Pt:Co:Al_2O_3 compared to films on Pt:Al_2O_3 (discussed later). A likely cause of this improved performance is that Li^+ diffusion occurs through a vacancy hopping mechanism within the lithium plane and is therefore two-dimensional. Facile ion transport occurs along the (104) and (101) planes but is hindered along the (003) orientation, as depicted in the schematic in Figure 22. This result is similar to previous findings for $LiCoO_2$ thin films. Varying the substrate composition, film thickness, and substrate temperature influenced the dynamic between volume strain energy and surface energy, and therefore changed the texturing of $LiCoO_2$ films from the (104) and (101) planes to (003).[246, 253] The (104):(003) ratio increase was also observed in films with a thicker interlayer of Co (200 nm), but observations of the additional Co migrating through the Pt layer during annealing encouraged the choice of a thinner (20 nm) Co layer for all experiments to avoid changing the active material stoichiometry. SEM with EDS confirmed that the Co migration through the Pt layer is prevented with the 20 nm Co interlayer while retaining its utility for induced texturing in the NMC layer (Figure 23 and 24, respectively).

An X-ray pole figure measurement was used to examine the crystallographic texture of the NMC grains (Figure 25). Films on both Pt:Al_2O_3 and Pt:Co:Al_2O_3 substrates demonstrate a preferred orientation, based on the maximum intensity of the measurement centered on the (104) plane at $2\Theta = 44^o$ (Figures 4a and 4b, respectively). The film on Pt:Co:Al_2O_3 has a noticeably higher degree of texturing compared to the film on Pt:Al_2O_3, as evidenced by the greater maximum intensity of the pole figure. These observations indicate that more of the NMC (104) planes rise normal to the surface of the substrate with a Co interlayer than for films on substrates without the heterolayer.

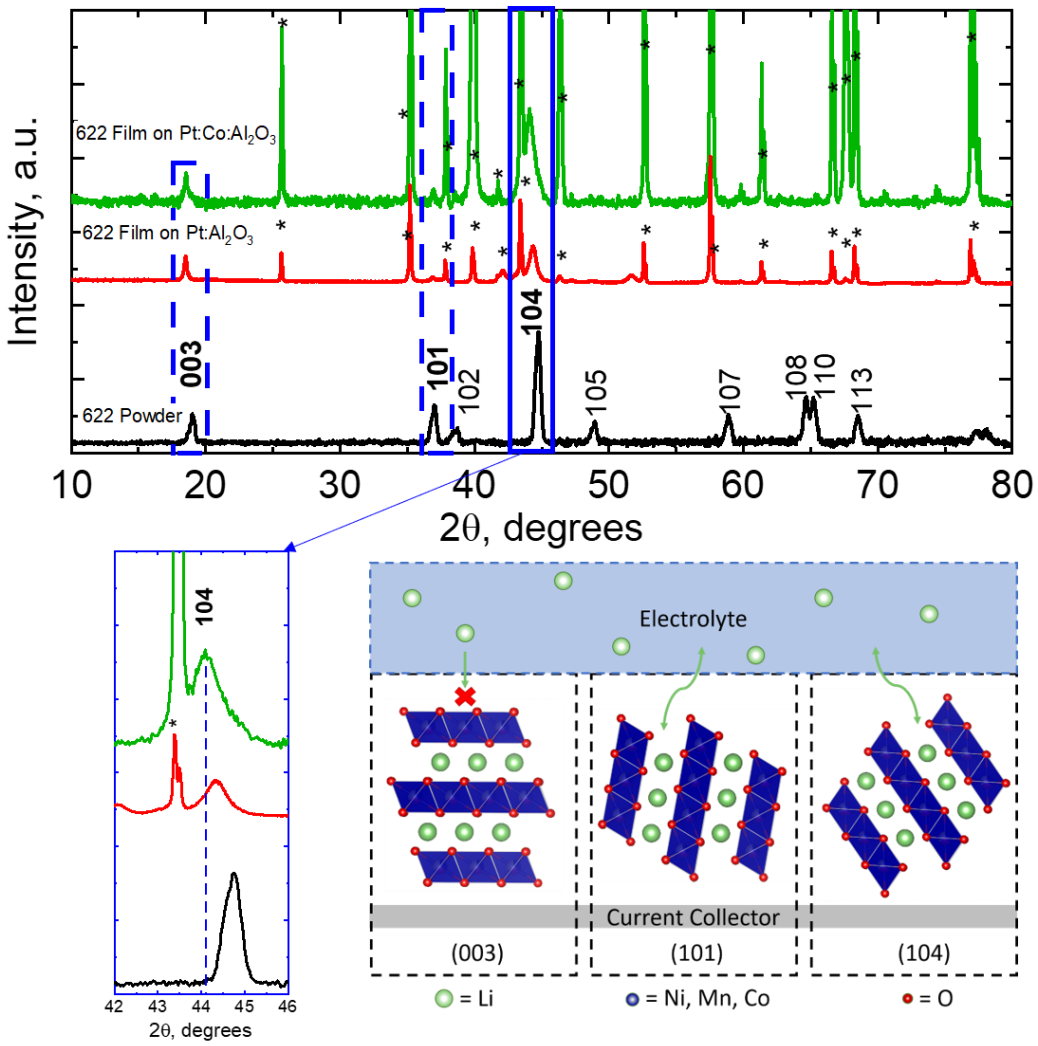

Figure 22. XRD highlighting ordering of the (104) and (101) planes relative to the (003) plane for NMC622 powder and thin films on different substrates with the (104) region expanded on the right (* = substrate peaks).

Table 8. Relative integrated intensities of the primary diffraction lines of NMC622 powder and films on different substrates

Sample	(003)	(101)	(104)
Film on Pt:Co:Al_2O_3	1	0.48	4.08
Film on Pt:Al_2O_3	1	0.16	1.47

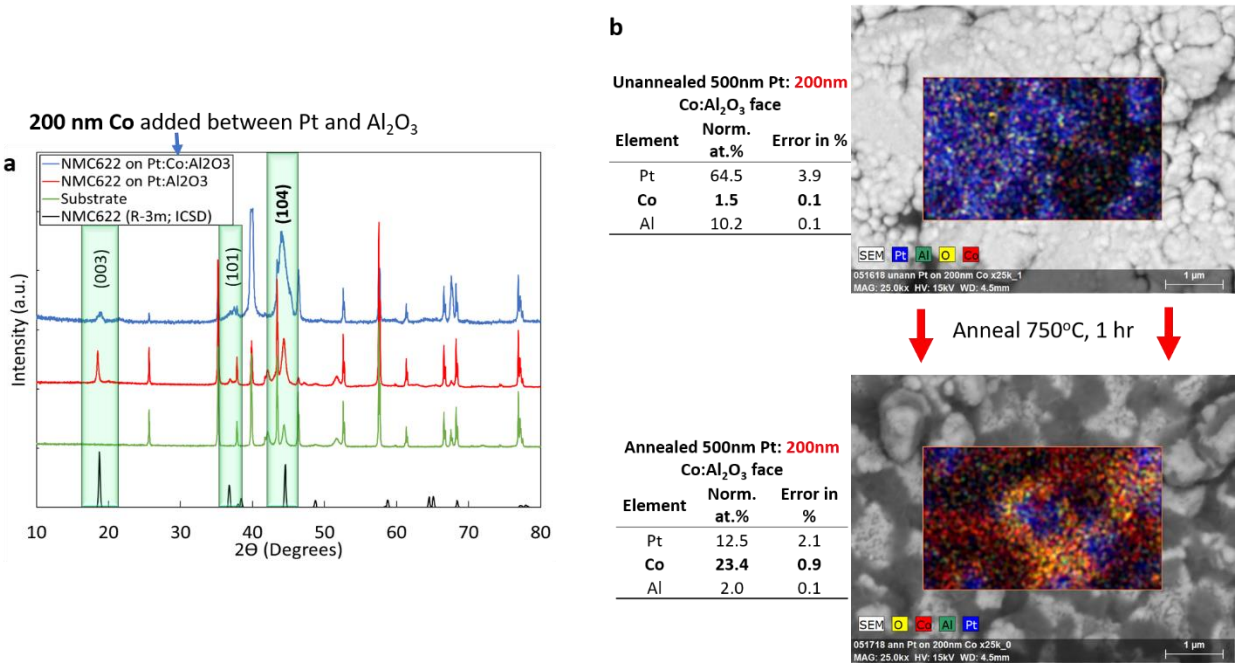

Figure 23. a) XRD of NMC622 films on substrate with 200 nm Co layer reveals significant (104) preferential ordering over film on Pt-coated substrate, but b) EDS reveals significant Co migration on annealing substrates with a thick (200 nm) Co layer

Annealed 500nm Pt: 20nm Co:Al2O3 face x25k

Element	[norm. at.%]	Error in %
Platinum	65.6	4.0
Cobalt	2.1	0.1
Aluminum	8.8	0.1
Oxygen	23.5	0.7

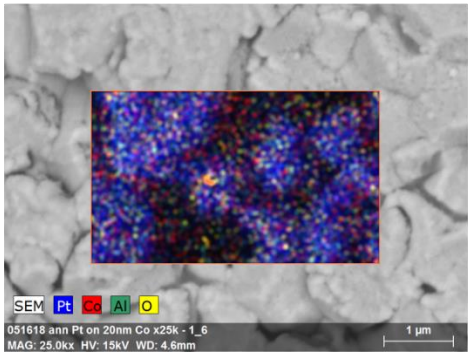

Figure 24. 20 nm Co interlayer of substrate does not penetrate surface and thus does not influence stoichiometry of the active material. Co detected in annealed sample due to EDS beam penetration depth

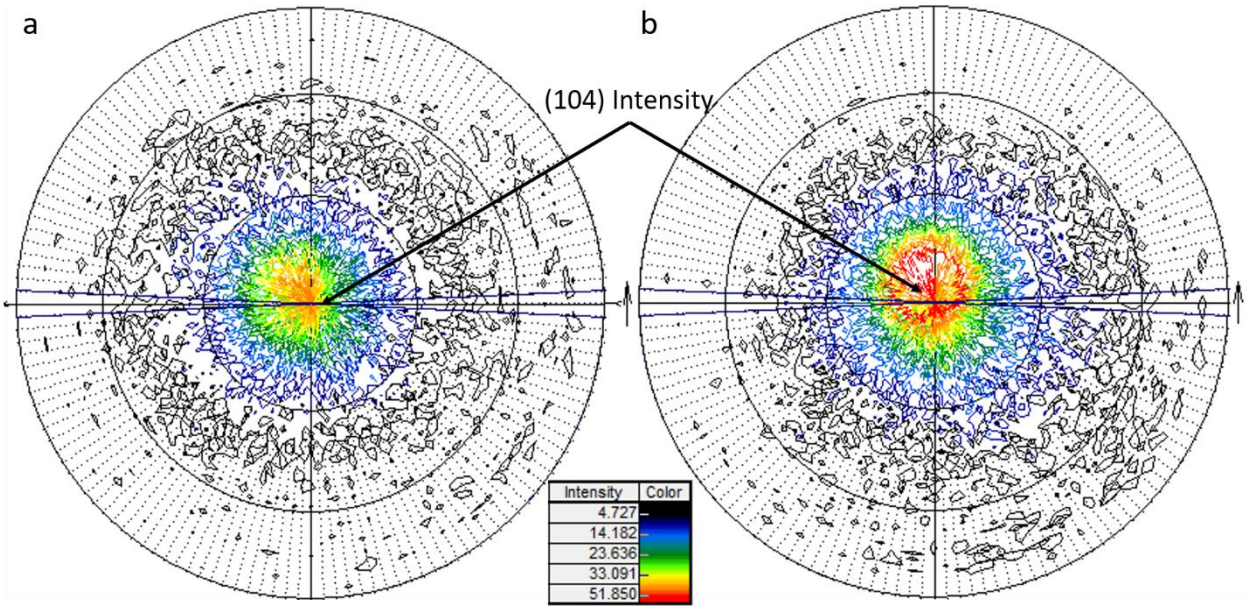

Figure 25. Intensity of (104) orientation in pole figures of NMC622 films on a) Pt:Al_2O_3 and b) Pt:Co:Al_2O_3

Given the interesting preferential orientation of the (104) and (101) to (003) planes in the thin film electrodes with the Co interlayer, the local morphology and surface structure is investigated with TEM. FIB milling is a particularly useful method for extracting thin samples and observing the discrete layers of the films (Figure 26). Small voids are present in the NMC622 films, which are commonly formed between columnar grains from crystallization during annealing of oxide films (Figure 26a, 26b).[254, 255] Some voids might cause isolation of portions of the active material, which could be a contributing factor for the difference between the practical and theoretical capacity of the films. Bright regions are apparent in the NMC layer and are caused by the stacking of lattice planes in similar orientations causing higher image contrast in the cross section. The region highlighted in red corresponds to the selected area electron diffraction (SAED) pattern of the NMC film on Pt:Al_2O_3 inset in Figure 26a. The high intensity arcs visible in the SAED data suggest texturing along a preferred orientation. The (104) and (101)/(012) reflections are identified based on d-spacing measurements from the diffraction patterns. The intensities of these reflections vary with the addition of a Co interlayer in the substrate, and the (110) reflection becomes visible in Figure 26b, suggesting variation in local orientation of the films.

The interface between the NMC622 films and Pt layer of the substrate is further inspected in Figures 5c and 5d. The film on Pt:Al_2O_3 have a largely polycrystalline contact layer with distinguishable crystallites (Figure 26c). This is in direct contrast to the film with a Co interlayer in the substrate, which demonstrates longer range ordering from the Pt interface (Figure 26d). The crystal growth induced at this interface provides the seed layer for the overall texturing observed in these films.

To further examine what is occurring at the Co interlayer, Rutherford Backscattering Spectrometry is used to investigate inter-diffusion of substrate layers (Figure 27a). Polished alumina was coated with 50 nm Co and 164 nm Pt using DC magnetron sputtering and studied in its pristine state as well as after standard annealing conditions for the thin film electrodes for 1 or 18 hours at 750^{o}C. The substrate retained discrete layers in the as-deposited sample but after

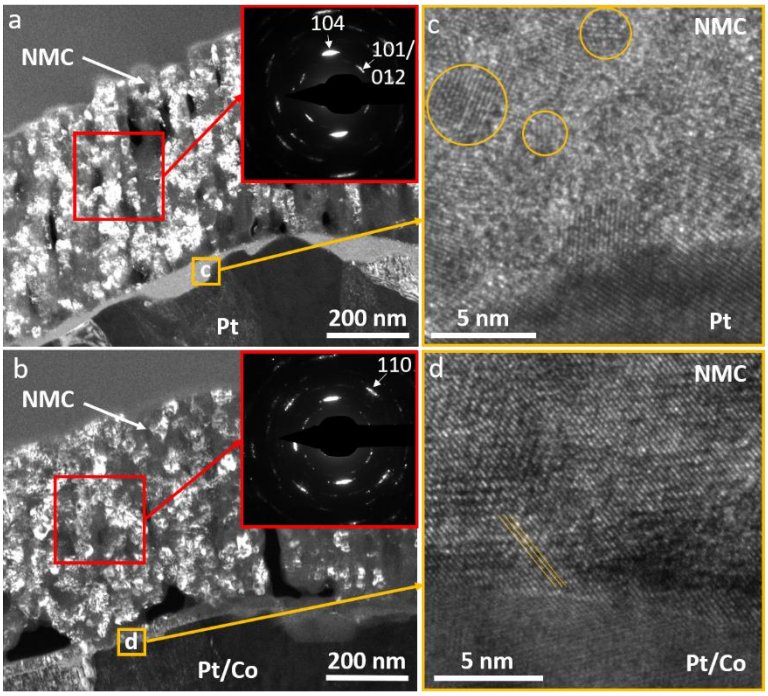

Figure 26. HAADF STEM images of NMC622 films on a) Pt:Al_2O_3 and b) Pt:Co:Al_2O_3 with inset SAED patterns. HRTEM images of the NMC/Pt interface with crystal orientations highlighted for c) Pt:Al_2O_3 and d) Pt:Co:Al_2O_3

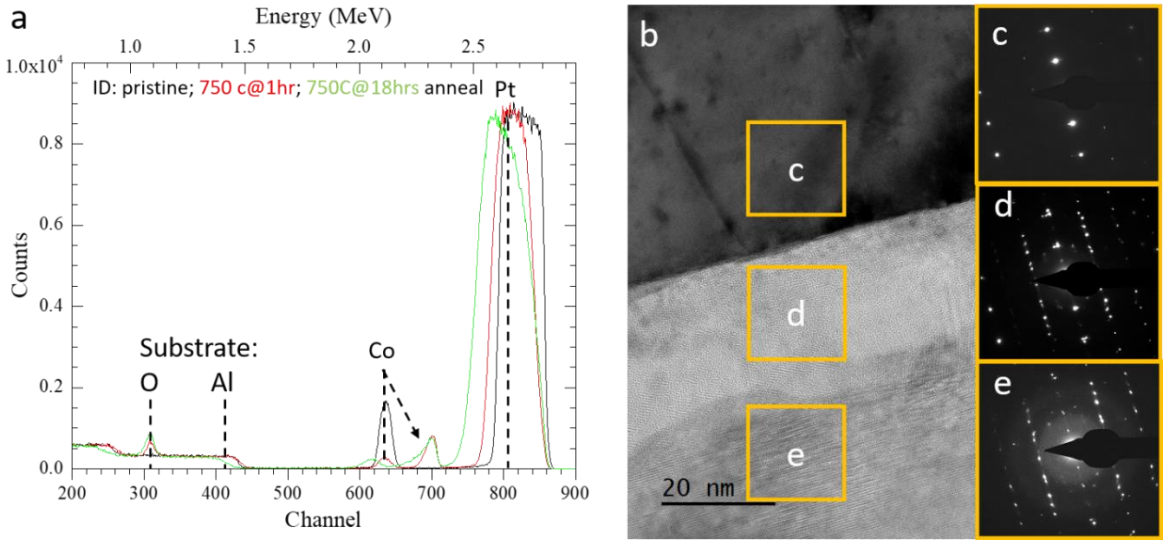

Figure 27. a) Rutherford Backscattering Spectroscopy plot of the Pt:Co:Al_2O_3 substrate before and after annealing with corresponding b) TEM image of substrate with SAED patterns of c) Pt, d) Co, and e) Al_2O_3 layers

annealing had a small amount of migration at the Pt/Co interface, as evidenced by the appearance of a peak around 2.3 MeV. The minimal Pt/Co migration aligns well with the small amount of Co detected in the plan-view EDS data of the substrate (Figure 24). This effect was slightly more pronounced for the longer annealing condition than the standard 1-hour hold. In both cases, another peak appears in the O/Al substrate region (1.1 MeV), suggesting an influence on the Pt phase due to O and Co diffusion. Indeed, XRD of these two substrates finds that the addition of the Co interlayer results in a significant increase of the (111) and (002) peaks of the Pt_4 $Fd\bar{3}m$ space group (Figure 28). The influence of the Co interlayer on local ordering is observed in the SAED patterns of the Pt, Co, and Al_2O_3 contact region (Figure 27c-e). A preferential orientation is observed in each of the patterns, suggesting the addition of a Co interlayer translates ordering into the Pt layer from the Al_2O_3.

The texturing feature is a global phenomenon in these films, so to investigate localized phase differences we use Raman microscopy to map the near-surface region. Prominent features around 601 and 505 cm^{-1} correspond to the A_{1g} and E_g vibrational modes caused by O-M-O bending and M-O stretching (M = Ni, Mn, Co), respectively (Figure 30a).[256] A decreased prominence of the E_g peak relative to the A_{1g} peak is noticeable for the thin film on Pt:Co:Al_2O_3 relative to the film on Pt:Al_2O_3 and the composite.[257] This could be attributed to changes in the local structure around the M-O layers such as interlayer spacing or structural disorder. Additionally, both the A_{1g} and E_g scattering bands of the thin films are red shifted relative to the composite material (from 601 cm^{-1} to 596 and 583 cm^{-1} for A_{1g} of thin films on Pt:Al_2O_3 and Pt:Co:Al_2O_3, respectively). This shift is attributed to the formation of nano-crystalline structures.[248, 258] A principal component analysis was used to identify any additional phases present in the films using WITec Project Plus software. Films deposited on both substrates – with and without a Co interlayer – were found to be homogeneous. None of the principal components beyond the first component had physical meaning beyond instrument noise (Figure 29).

Various stoichiometries of the NMC material may satisfy similar layered crystal structures, so we use ICP-OES to verify the elemental composition of the thin films and composite materials. After the annealing step, the films on Pt:Al_2O_3 have a Li:Ni:Mn:Co ratio that matches the NMC622 stoichiometry within a standard deviation (2σ) of 5.7% (Figure 30b). EDS is used as a complementary tool to verify the transition metal composition of thin films on Pt:Co:Al_2O_3 and the composite materials (Figure 30c), as the narrow cross section of Li for scattering electrons precludes an accurate measurement. The composition of the film matches the composite material as well as the ICP data except for the Co signal, which is 18% higher than the Co signal of the composite material measured by EDS. This is to be expected given the penetration depth of the instrument into the Co layer, as evidenced by the detection of the Al_2O_3 substrate with EDS in Figure 24.

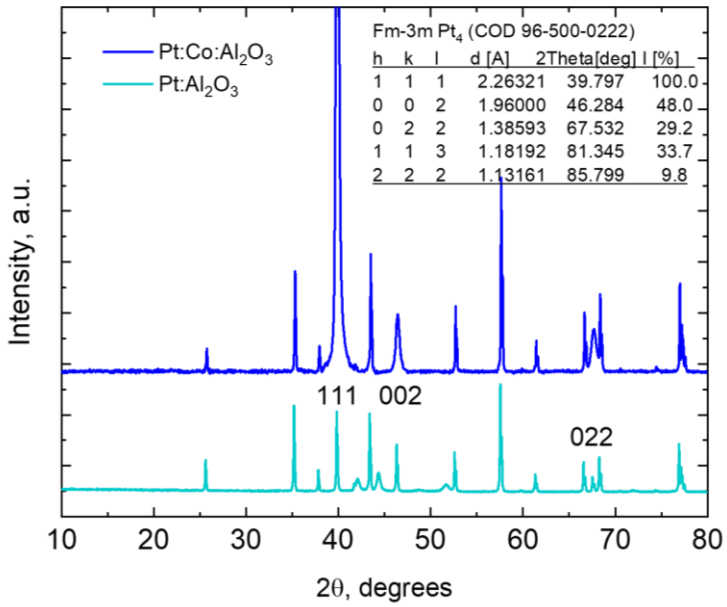

Figure 28. XRD of Pt:Co:Al_2O_3 and Pt:Al_2O_3 substrates and reference data

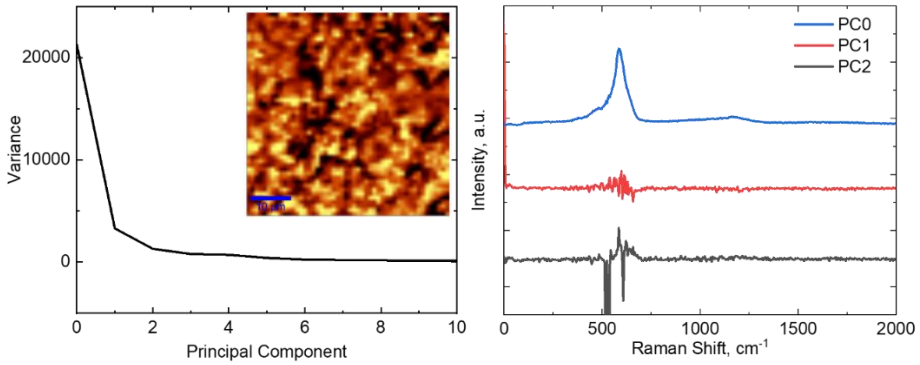

Figure 29. Raman Principal Component Analysis of thin film NMC622 for first three components

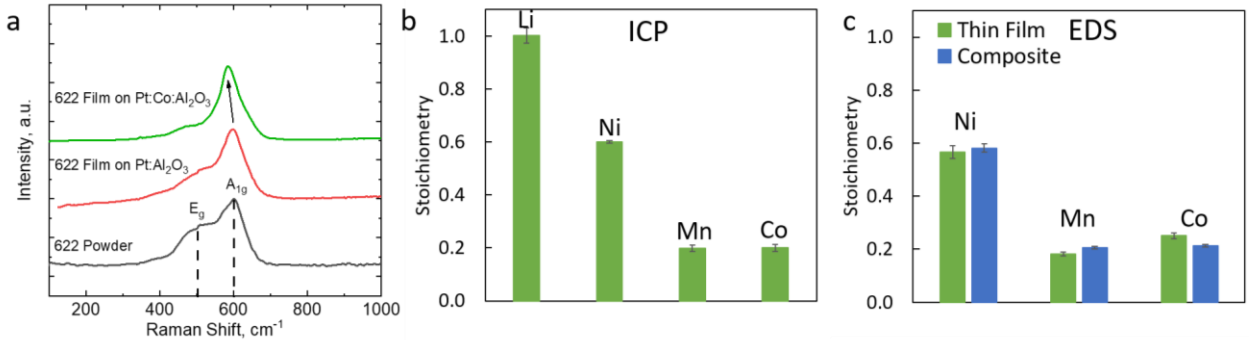

Figure 30. a) Raman spectra of thin film and composite electrodes, b) film stoichiometry measured by ICP-OES, and c) EDS comparison of film and composite stoichiometry. All error bars are two sigma.

Cycling data for the thin films and composite material are shown in Figures 7a-c for a voltage window of 2.5 – 4.2 V *vs.* Li/Li^+. A typical cycle at 10 mA/g (C/20) demonstrates poorly defined voltage plateaus for films on a thin (200 nm) layer of Pt (shown in blue in Figure 31a, magnified by 10 for clarity). A somewhat improved specific discharge capacity of 78 mAh/g can be achieved with films on a thicker (1500 nm) layer of Pt, but the discharge plateau remains sloping and unresolved (Figure 31a). This capacity improvement due to additional Pt was limited, however, as thin films deposited on Pt foil did not demonstrate further improved capacity. The addition of a Co interlayer enables the NMC622 films to match the voltage plateaus of the composite material and greatly improves the specific discharge capacity to 118 mAh/g. Redox peaks are more apparent in the differential capacity plot, with both the composite cell and thin film on $Pt:Co:Al_2O_3$ having a primary peak at around 3.7 V, corresponding to the $Ni^{2+/3+}$ oxidation step (Figure 31b). A secondary peak around 3.75 V can be observed for the composite cell which has been assigned to the $Ni^{3+/4+}$ oxidation step.[250, 259] Polarization is noticeable between the charge and discharge redox peaks for the thin films on $Pt:Al_2O_3$ and to a lesser degree for films on $Pt:Co:Al_2O_3$.

The electrochemical impedance for the NMC622 films and composite electrode were studied with EIS (Figure 31c). Nyquist plots of the films and composite material at open circuit voltage (~3.3 V) are shown after formation cycles and after 10 cycles at C/10. A semicircle in the high frequency region represents charge transfer resistance (R_{ct}) and double layer capacitance (C_{dl}) while the low frequency straight line corresponds to the Warburg impedance (Z_w) due to Li^+ diffusion in the bulk cathode material. The low R_{ct} value of about 4 Ω*cm^2 and 69 Ω*cm^2 for the composite electrode before and after cycling indicates that bulk Li^+ diffusion dominates impedance in that system. The thin films of NMC622 had much larger R_{ct} contributions of 167 Ω*cm^2 and 218 Ω*cm^2 for films on $Pt:Al_2O_3$ and $Pt:Co:Al_2O_3$, respectively. After cycling, these initial values increased to 532 Ω*cm^2 and 269 Ω*cm^2, which is comparable to $LiCoO_2$ films cycled with liquid carbonate electrolytes.[260] With charge transfer resistance more than tripling for the films on $Pt:Al_2O_3$, it is clear that the electrochemical kinetics are hindered over time when compared to the modest increase of films with the Co substrate heterolayer. This is likely due to the range of crystal orientations normal to the substrate surface: with a greater number of (104) planes favoring Li^+ diffusion compared to Li^+ blocking (003) planes, as observed in the diffraction data. The difference in crystallite sizes and orientations observed in the HRTEM data may also contribute to this difference in impedance rise. In the case of films on $Pt:Al_2O_3$, smaller crystallites in several different orientations are observed in Figure 26d which may cause more tortuous pathways for Li^+ diffusion than the larger crystallites of films on $Pt:Co:Al_2O_3$ (Figure 26c). The films on $Pt:Co:Al_2O_3$ have a good charge capacity of 142 mAh/g which is ~70% that of the composite. This limit is likely due to the partial texturing of the thin films, indicated by the presence of (003) peaks in the XRD data for NMC on $Pt:Co:Al_2O_3$ – which are unfavorable to Li^+ diffusion in thin films – rather than consisting entirely of more favorable planes such as (104) and (101). Further optimization may be possible through adjustments to deposition conditions, substrate composition, or annealing environments.

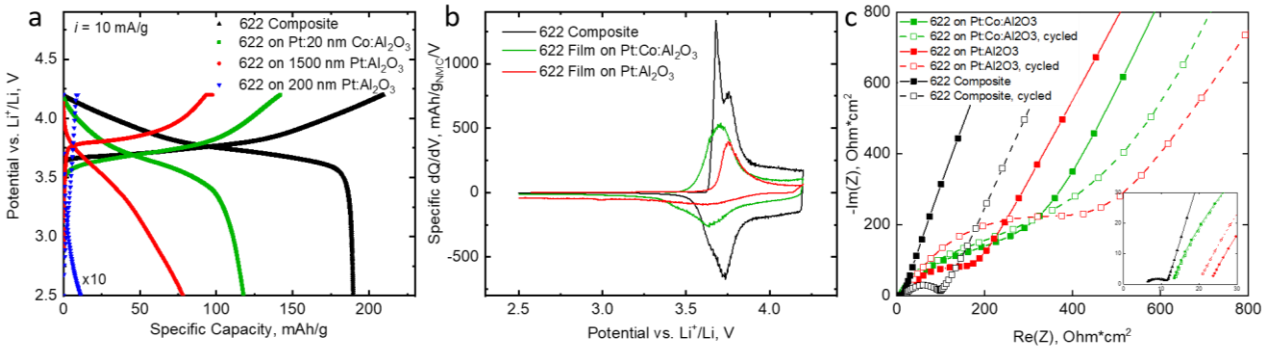

Figure 31. a) Typical electrochemical cycling at C/20 and b) differential capacity of thin film and composite material. c) Nyquist plot of impedance of thin films and composite material after formation cycles (solid lines) and after cycling (dashed lines)

5.5 Conclusions

We have synthesized thin film $LiNi_{0.6}Mn_{0.2}Co0._2O_2$ electrodes by means of magnetron sputter deposition on various substrates and contrasted them against a standard composite electrode of the same active material. Structural characterization revealed that the films were of the desired layered phase from bulk and localized perspectives, with thin film crystalline orientation influenced by the addition of a Co substrate interlayer in favor of lattice planes with facile Li^+ diffusion. This tunable orientation offers opportunities to study the surface chemistry of different lattice planes of the active material. The desired stoichiometry was also observed for both classes of samples. Electrochemical performance of these thin film electrodes was comparable to that of the composite electrode with well aligned redox peaks observed for films on $Pt:Co:Al_2O_3$. These complementary characterization methods demonstrate that the synthesized films are a valid model for studying the active material of the composite electrode as they are isolated from influences by conductive carbon, binder, and variable electrolyte environments present in composite electrodes with complex interfacial geometries.

Acknowledgements. This research at the Oak Ridge National Laboratory, managed by UT Battelle, LLC, for the U.S. Department of Energy (DOE) under contract DE-AC05-00OR22725, was sponsored by the Office of Energy Efficiency and Renewable Energy (EERE) Vehicle Technologies Office (VTO) (Deputy Director: David Howell) Applied Battery Research subprogram (Program Manager: Peter Faguy) (N.D.P., R.E.R., C.D., and G.M.V.). Funding for A.S.W. was provided by ARPA-E Award No. DE-AR0000775. The authors are grateful for FIB sample preparation by Dorothy Coffey of the ORNL Center for Nanophase Materials Science (CNMS), which is a DOE Office of Science User Facility. Thin film XRD and S/TEM studies (X.S. and R.R.U.) were conducted at the CNMS. RBS experiments were performed at the Center for Integrated Nanotechnologies, an Office of Science User Facility operated for the U.S. DOE Office of Science. Los Alamos National Laboratory, an affirmative action equal opportunity employer, is operated by Los Alamos National Security, LLC, for the National Nuclear Security Administration of the U.S. DOE under Contract DE-AC52-06NA25396 (Y.W.).

6. INFLUENCE OF BINDER COVERAGE ON INTERFACIAL CHEMISTRY OF THIN FILM $LINI_{0.6}MN_{0.2}CO_{0.2}O_2$ CATHODES

This manuscript has been submitted to the *Journal of the Electrochemical Society* and investigates how polymeric binder composition and coverage on the surface of NMC622 influences performance and CEI formation at high voltages. My contribution as the primary author was executing all experiments planned with G. M. V. as well as data analysis and writing the manuscripts. All authors assisted with data interpretation and editing the manuscript. Supplemental figures have been added to the main text for clarity.

Nathan D. Phillip,[1,2] Claus Daniel,[1,3] Gabriel M. Veith[2*]*

[1] The Bredesen Center for Interdisciplinary Research and Graduate Education, University of Tennessee, Knoxville, TN, 37996, USA

[2]Chemical Sciences Division, Oak Ridge National Laboratory, Oak Ridge, TN 37831, USA

[3]Energy and Environmental Sciences Directorate, Oak Ridge National Laboratory, Oak Ridge, TN 37831, USA

6.1 Abstract

In this work, we explore the influence of binder coverage and chemistry on the interfacial properties of the Ni-rich cathode $LiNi_{0.6}Mn_{0.2}Co_{0.2}O_2$. We find that the formation of the cathode/electrolyte interphase (CEI) composition varies significantly for cathodes coated with either poly(vinylene fluoride) (PVDF), carboxymethyl cellulose (CMC), or lithium polyacrylate (LiPAA) after cycling to high upper cutoff voltages (4.5 V *vs.* Li/Li). We found that the PVDF-coated samples had a thinner CEI and twice the relative concentration of LiF and Li_2CO_3 to $Li_xPO_yF_z$ species in the CEI compared to the uncoated sample. This correlated with significantly lower interfacial impedance and improved capacity retention between cycles of the PVDF-coated samples compared to the other binder compositions and the uncoated sample. CMC-coated samples performed worst, with a CEI comprised of greater amounts of $Li_xPO_yF_z$. This suggests that the choice of binder can impact the surface chemistry and performance of high voltage cathodes and supports an avenue for interest in multifunctional binders for stabilizing the CEI.

6.2 Introduction

Composite lithium-ion battery electrodes are comprised of an electrochemically active material, conductive additives, and a binding agent which are primarily responsible for Li^+ storage, providing continuous electronic conductivity, and mechanical cohesion and adhesion, respectively. Binder and conductive carbon are commonly referred to as inactive components, but in promising cathodes such as Ni-rich $LiNi_xMn_yCo_zO_2$ (where $x + y + z = 1$ and $x > 0.5$) these components can be more involved. At high upper cutoff voltages (> 4.4 V *vs.* Li/Li^+), $LiNi_{0.6}Mn_{0.2}Co_{0.2}O_2$ (NMC622) undergoes surface structural rearrangement from layered $R\bar{3}m$ to spinel-like and rock salt phases (Fm3m).[50] This structural rearrangement has been correlated with the onset of oxygen evolution as atomic oxygen or singlet oxygen[261] which induces chemical oxidation of the electrolyte prior to electrochemical oxidation.[209] The reaction mechanism proposed by

Gasteiger *et al.*[262] for this decomposition involves ethylene carbonate (EC) oxidation into vinylene carbonate (VC) and H_2O_2 at the interface followed by electrooxidation of H_2O_2 above 3.8 V *vs.* Li/Li^+ to form H_2, O_2, and H_2O. These species are known to initiate additional electrolyte decomposition reactions such as the formation of HF with fluorinated salts like $LiPF_6$.[262] Oxidation of EC may be followed by a ring opening reaction, producing CO_2 and oligomers at the surface.[162] Electrolyte decomposition products deposit on the surface of the cathode in a layer referred to as the cathode/electrolyte interphase (CEI). This surface layer is typically comprised of lithium fluorophosphates ($Li_xPO_yF_x$) and LiF from salt decomposition[263] and lithium carbonates, polycarbonates (Li_2CO_3, $ROCO_2Li$), and lithium alkoxides (ROLi) from solvent decomposition.[162, 167, 170]

The CEI is often referred to as a passivation layer against continuous electrolyte decomposition, but continuous transition metal dissolution[264] and gas evolution from the cathode at high voltages[265] suggest that this layer does not fully stabilize the interface. Indeed, little is known about the factors which influence CEI formation when compared to the solid electrolyte interphase (SEI) at the anode. Recent work on novel binders has provided a promising route toward forming a stable CEI for high voltage operations of Ni-rich NMC materials. Song et al. reported a fluorinated polyimide binder which covalently bound to the surface of Ni-rich NMC via its carboxylic acid group to form a highly stable chemical network which reduced capacity fade at high voltage operation.[266] Manthiram *et al.* proposed lithium polyacrylate (LiPAA) could form an artificial CEI on the surface of high voltage spinel $LiNi_{0.5}Mn_{1.5}O_4$ (LNMO).[217] Dou *et al.* demonstrated the improved rate capability of NMC333 electrodes with carboxymethyl cellulose over PVDF when cycled between 2.5 – 4.6 V *vs.* Li/Li^+.[267] Despite this evidence of promising CEI stabilization options, common binders such as poly(vinylidene fluoride) (PVDF), CMC, and LiPAA have not been thoroughly investigated for their influence on CEI formation of Ni-rich NMC cathode materials. Additionally, the morphology of these binders is rarely considered in composite electrodes, which raises the question whether the extent of coverage might influence the formation of the CEI.

In this study, we examined the effects of binder morphology and composition on the formation of the CEI on Ni-rich NMC622. Thin planar films comprised solely of active material were used to model potential binder coverage environments in composite electrodes by spin and spray coating. PVDF is selected as a reference case to typical composite systems, CMC represents a common water-processed binder, and LiPAA is chosen as a potential multifunctional binder (*i.e.* Li source for CEI formation). These systems are compared to the baseline uncoated case to discern trends in surface composition and electrochemical performance.

6.3 Methods

Synthesis. Thin films of $LiNi_{0.6}Mn_{0.2}Co_{0.2}O_2$ were prepared by radio frequency magnetron sputtering of home-built targets, further detailed in our previous work.[210] Deposition conditions in this study were a base chamber pressure $<2 \times 10^{-6}$ Torr with 55.0 sccm high purity Ar gas (Airgas) flow rate providing 6.0 mTorr deposition pressure at 90 W forward power. Following deposition of 500 nm NMC622 on 1 cm diameter Al_2O_3 substrates coated with Co and Pt, thin films were annealed at 700°C for 1 hour under high purity air flow (~0.2 LPM, Airgas) with a ramp rate of 5 °C/min then stored in an Ar-filled glove box.

Binder solutions were prepared by roller milling (U.S. Stoneware) powders with solvents for 24 hours. 0.1 wt% PVDF (5130, Solvay) was dissolved in N-methyl pyrrolidinone (NMP) and 1.0 wt% CMC-Na (Acros Organics, 90 K MW) was dissolved in ultrapure (18 MΩ) deionized

water. LiPAA was produced by dissolving polyacrylic acid (PAA, Sigma Aldrich, 450 K MW) in water to ~10 wt% then titrating the binder solution with LiOH until a neutral pH was reached.[268] The binder solution used here was diluted to 0.2 wt% LiPAA in water.

Binder coatings were spin-coated on a Cee Model 100CB by dropping 20 µL binder solution onto the center of the sample disk which was spun at 3000 RPM for 30 seconds such that excess binder solution was spun off into the catch cup. Spray coating were done with a Talon Gravity Feed Airbrush Set in a single pass across the sample at a 2" fixed standoff distance. Spin and spray-coated films were dried in air at 80 °C then placed in a vacuum oven at 100 °C overnight to remove residual water. Samples were weighed on a microbalance before and after deposition, but the mass change was not significantly above the error margin of the balance so alternative methods of characterization were employed.

Characterization. Surface morphology and composition data were collected with a Scanning Electron Microscope equipped with an Energy-Dispersive X-ray Spectrometer (SEM/EDS, Hitachi TM3030 Plus with Quantax 70). X-ray Photoelectron Spectroscopy (XPS) was conducted on a PHI 3056 XPS spectrometer operated at 350 W and 15 kV with an Mg Kα (1253.6 eV) source. Pristine samples were transferred in air and cycled films were transferred under vacuum for measurement in a cryo-pumped vacuum chamber at 10^{-9} Torr or less (10^{-11} Torr base pressure). Survey scans were collected at 93.9 eV pass energy with 0.5 eV energy steps while high-resolution scans were acquired at 23.5 eV pass energy and 0.05 eV energy steps with 20−60 repeated scans of all spectra to improve the signal-to-noise ratio. Spectra were shifted relative to the adventitious carbon peak (284.8 eV) to correct for charging. Raw data was fit to component peaks based on pure binder powders and Li salts collected in the same instrument to provide standard references for relative peak area, position, and full width at half maximum (FWHM). Quantification of species by atomic concentration, X_A, was calculated in CasaXPS based on the corrected area:

$$X_A = \frac{A}{RSF * T * \lambda}$$

Where A is the raw area intensity, RSF is the relative sensitivity factor of the element based on Scofield cross sections, T is the transmission factor for the instrument, and λ is the inelastic mean free path of an electron at the given binding energy.

Electrochemical Measurements. Electrochemical cells were assembled in an Ar-filled glove box in Swagelok cells vs. Li metal (1 cm diameter), in duplicate. Two 1.3 cm diameter separators (Dreamweaver Gold 40) were soaked in 300 µL 1.2 M $LiPF_6$ in ethylene carbonate (EC) and ethyl methyl carbonate (EMC) in a 3:7 wt. ratio (Tomiyama). Cells rested at open circuit voltage for 2 hours before cycling for two formation cycles between 3.0 – 4.5 V vs. Li/Li^+ in a constant current, constant voltage protocol (CCCV). Constant current steps of 10 mA/g (~C/20, where theoretical capacity, C = 200 mAh/g) were held until the upper cutoff voltage (UCV) followed by a constant potential hold at UCV until measured current dropped below 5 mA/g (C/40) then cells were discharged at 10 mA/g constant current to the lower cutoff voltage. Electrochemical Impedance Spectroscopy tests were conducted after the 2 formation cycles on a BioLogic MPG-2 Battery Tester when cells were at open circuit voltage over 10 mHz to 20 kHz with 6 mV applied signal. Cycled electrodes were extracted in an Ar-filled glove box, rinsed in 1 mL dimethyl carbonate (DMC) for 30 seconds before drying and transferring to the XPS chamber under vacuum.

6.4 Results & Discussion

The active material of a composite electrode is difficult to study with surface sensitive techniques such as XPS due to the presence of conductive carbon and binders. These additional components support good electronic contact and mechanical robustness of the electrode but attenuate the signal of the active material when examined in XPS, as demonstrated for the Ni2p signal collected from the composite NMC622 electrode in Figure 32 (bottom) with 90 wt.% NMC622, 5 wt.% PVDF, and 5 wt.% carbon black. In this example one can see we isolated the active material by preparing planar thin film (0.5 μm) electrodes by magnetron sputtering.[210] These films provide a controlled environment for experimenting on the cathode material and enable detection of interfacial signals which are attenuated by inactive components in composite electrodes, as evidenced by the clear Ni2p signal of the pristine film in Figure 32. Consequently, the cathode/electrolyte interface of NMC622 can be studied, with attenuation of the surface signal caused by the formation of a layer of electrolyte degradation products. This difference is schematically illustrated in Figure 32 and provides a platform for studying the effects of artificial surface layers.

The morphology of a composite electrode can vary depending on the mixing method, slurry composition, and quality of slurry coating.[194] Hypothetical morphologies are schematically depicted in Figure 33 beginning with minimal surface coverage (Figure 33a), where binder and conductive carbon fills voids between active material particles to form a cohesive network while leaving a majority of the active material surface exposed to the electrolyte, as has been proposed for PVDF-based electrodes.[269] A heterogeneous layer of binder and carbon may form instead (Figure 33b), where the active material particles are coated sporadically with regions of substantial binder agglomerates alternating with bare or thin regions of binder coverage. A third case is shown in Figure 33c, where uniform coverage of binder across the surface of the active material effectively encapsulates particles in a thin layer of polymer.

These different binder coverage environments can be modeled by controlling the coating of binders on a well-defined thin film surface. The minimal surface coverage situation (Figure 1a) is represented with an uncoated thin film of NMC622 and serves as our baseline. Sporadic globular coverage (Figure 33b) is studied by spray coating binders on the surface of thin films, while uniform thin coverage (Figure 33c) is accomplished by spin coating binder solutions. Conductive carbon is omitted so that the influence of binder coverage on the cathode/electrolyte interface may be studied in isolation.

The baseline coverage case – an uncoated thin film of NMC622 – was probed with *ex situ* XPS before and after 2 cycles between 3.0 – 4.5 V *vs.* Li/Li^+ in half cells at 10 mA/g. Overall, a CEI comprised of semicarbonates, oligomeric species, and inorganic components formed during the first few cycles which may be discontinuous or else thin due to the observation of lattice oxygen in the O1s core spectra. The C1s spectra for the pristine and cycled samples can be seen in Figure 34a as green and blue traces, respectively. The F1s and P2p signals of the pristine material had no peaks above the baseline signal so they are excluded from the figure. A substantial increase in the relative contribution of C-O and O-C-O bonds can be seen after cycling (at ~286.2 eV and ~287.1 eV, respectively). There is also a modest increase in the CO_3 signal (~288.5 eV) from 2 at.% to 6 at.% after cycling, suggesting that more oligomeric and polymeric species form on the surface relative to semicarbonates or Li_2CO_3 in the first two cycles. A similar trend was observed on binder-free and carbon-free $LiCoO_2$ cathodes cycled to 4.6 V *vs.* Li/Li^+,[218] indicating the growth of a CEI layer during the first few cycles in high voltage environments. This is reflected in the O1s spectra shown in Figure 34b, where initially the largest component around 529.5 eV, attributed to

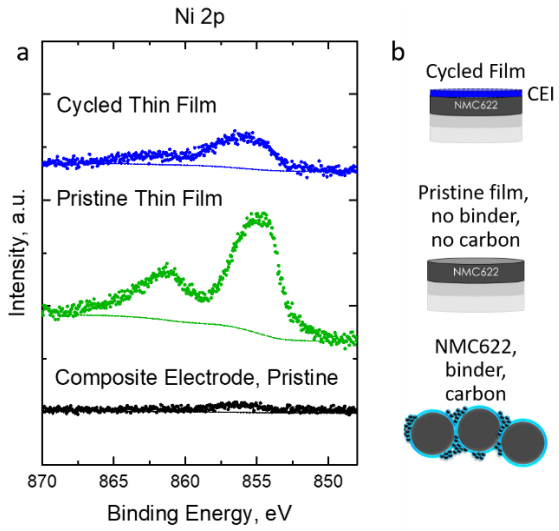

Figure 32. a) Ni2p XPS spectra for pristine (middle) and cycled thin films (top) and pristine composite NMC622 (bottom) with b) schematic of electrode configurations

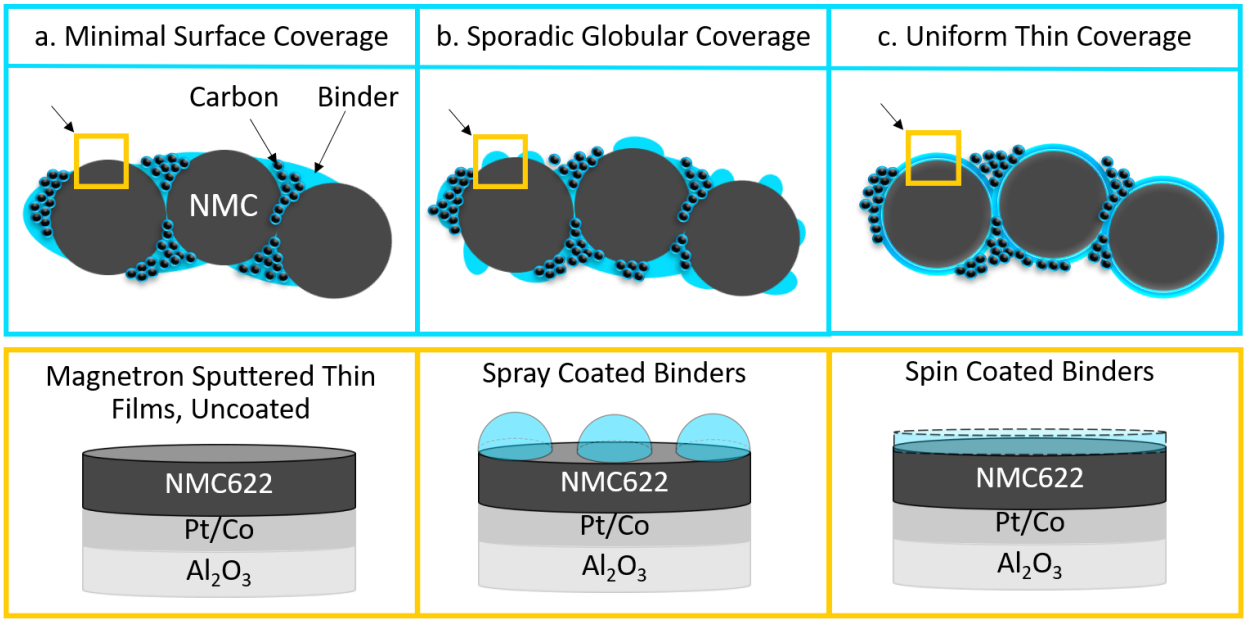

Figure 33. Potential binder morphology in composite electrodes and thin film analogs for a) minimal surface coverage, b) sporadic globular coverage, and c) uniform thin coverage

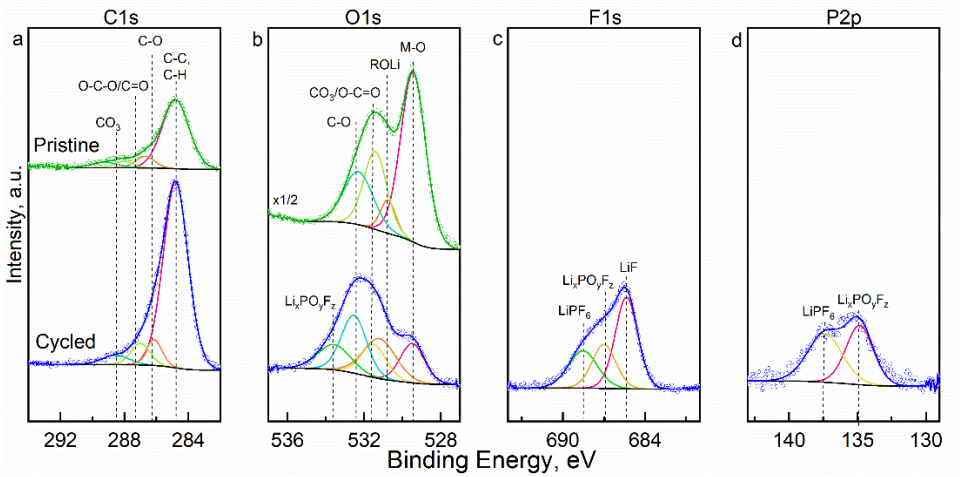

Figure 34. Pristine and cycled NMC622 thin films extracted for XPS of a) C1s, b) O1s, c) F1s, d) P2p, and e) Ni2p spectra after 2 formation cycles between 3.0 – 4.5 V vs. Li/Li$^+$ with the intensity of the pristine O1s signal multiplied as labeled for clarity

lattice oxygen bound to transition metals (M-O), diminishes from 52 at.% to 18 at.% of the O1s signal after cycling. It is important to note that while the intensity of this peak is substantially lower for the cycled film, the fact that it is still visible suggests that either the CEI is discontinuous on these films or that it is sufficiently thin for photoelectrons emitted from the lattice can escape the surface layer and reach the detector. The thickness of the surface layer, in this case, would be ~2 nm, based on the inelastic mean free path of an electron through a polymeric surface layer.[270, 271] The O1s spectra shows a greater increase of the oligomer/C-O contribution (532.1 eV) than the carbonate peak (531.1 eV), which was similarly seen in the C1s spectra. An additional peak in the cycled O1s spectrum was assigned to lithium fluorophosphates ($Li_xPO_yF_z$) and was confirmed in the F1s and P2p spectra seen in Figure 34c and Figure 34d at 687.3 eV and 134.8 eV, respectively. A signal contribution by LiF was detected at 685.6 eV, likely from the decomposition of the electrolyte salt, $LiPF_6$, with trace amounts of water in the electrolyte.[272] Partially decomposed or residual $LiPF_6$ not removed by rinsing the electrodes was detected at ~688.5 eV. The position of Li salts observed here match well with the reference spectra for pure Li salts (Li_2CO_3, $LiPF_6$, LiF) collected on this instrument.

NMC films were coated with binder solutions by spin coating or spray coating before drying overnight under vacuum at 100^{o}C. The morphology of a PVDF spin coating can be seen in Figures 35a. The thin coating provides poor contrast relative to the background, so EDS maps were collected. Binder signals for C and F can be seen in Figure 35b and 35d, respectively. These signals have relatively low intensity compared to the bulk element signals due to the thin surface layer (<5 nm) compared to the penetration depth of EDS (several µm). The Pt-coated Al_2O_3 substrate signals are visible in the O, Al, and Pt spectra (Figure 35c, 35e, and 35f) and have some variation in intensity, likely due to the top layer of 500 nm NMC622. The elements of the bulk NMC622 film can be seen in the Mn, Co, and Ni spectra (Figure 35g and 35i) and are uniformly dispersed. This morphology is a good representation of the full thin coating of binder on NMC particles in composite electrodes, which would likely have some nonuniformities due to variation in particle size and shape.[210]

XPS was used to characterize the surface chemistry of the pristine binder coated films. The spectra for these samples can be seen in Figure 36 which were fit using reference XPS spectra of pure binder powders collected on our instrument (Figure 37). The structures of the three binders selected for this study are included in Figure 36a as a reference for the bonds expected in the XPS data. The C1s spectra of the pristine binder-coated samples are compared to the uncoated sample in Figure 36b with the regions corresponding to characteristic bonds of each binder marked. The PVDF-coated sample has primary contributions at ~285.5 eV and ~290 eV, corresponding to the CF_2 and CH_2 bonds of the binder, respectively. There is a minor amount of adventitious carbon at ~284.8 eV used for charge correction in all the samples as well as C-O, C=O, and CO_3-type species which will be discussed later. The C1s profiles of LiPAA-coated samples are seen in green in Figure 36b, with a strong COO^- at ~288 eV corresponding to the carboxylic acid group of the binder. The CMC-coated samples are plotted in purple in Figure 36b and have a characteristic peak for C-O-C and C-O-H bonds at ~286.6 eV. The relative area of the ether bond signal of the spin-coated CMC films is more intense than that of the spray-coated sample, corresponding to a greater amount of CMC in the XPS sampling volume. This is expected for a continuous thin coating versus a sporadic coating of similar overall thickness and the same trend is observed for the C-F bonds of the PVDF-coated films and the carboxylic acid bonds of the LiPAA-coated films.

These trends are similarly observed in the O1s spectra of Figure 36c, where the peak for lattice oxygen bonded to a transition metal is denoted as M-O and appears at ~529.5 eV. The spray-coated spectrum has a 22% lower M-O peak area than the spin-coated sample, meaning that more of the NMC622 film is obscured from detection by overall thicker coverage of spray-coated LiPAA than spin-coated LiPAA. The O1s spectra for CMC and PVDF samples follow the same trend as the C1s spectra, with a substantially lower intensity of the M-O signal in the spin-coated samples compared to the spray-coated samples in each case (28% and 51% lower, respectively). Although the M-O signal is significantly attenuated in these spin-coated samples, it is still visible. Based on the inelastic mean free path of a Ni2p photoelectron in a uniform polymeric coating,[270, 271] the thickness of the spin-coated films are approximately 1.8 nm.

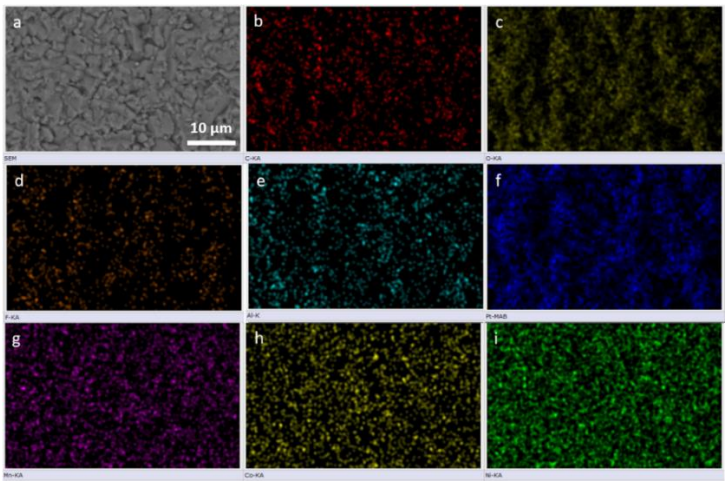

Figure 35. 0.1 wt% PVDF spin coating on NMC622 thin film a) SEM top down image and EDS maps corresponding to b) C, c) O, d) F, e) Al, f) Pt, g) Mn, h) Co, and i) Ni

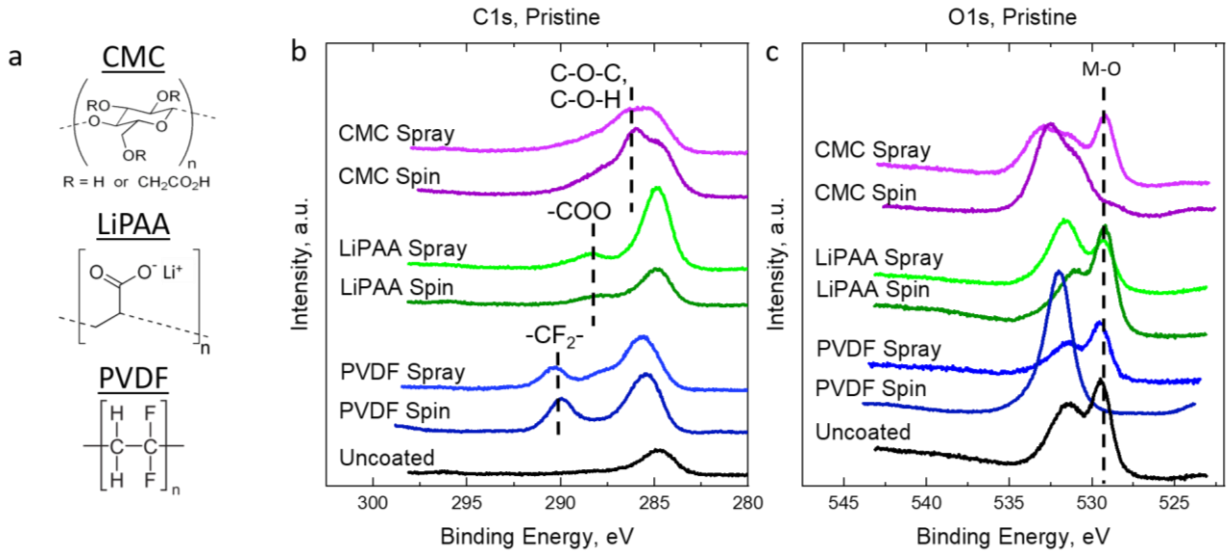

Figure 36. a) Chemical structure of binders used in this study and XPS of pristine coated samples b) C1s and c) O1s spectra

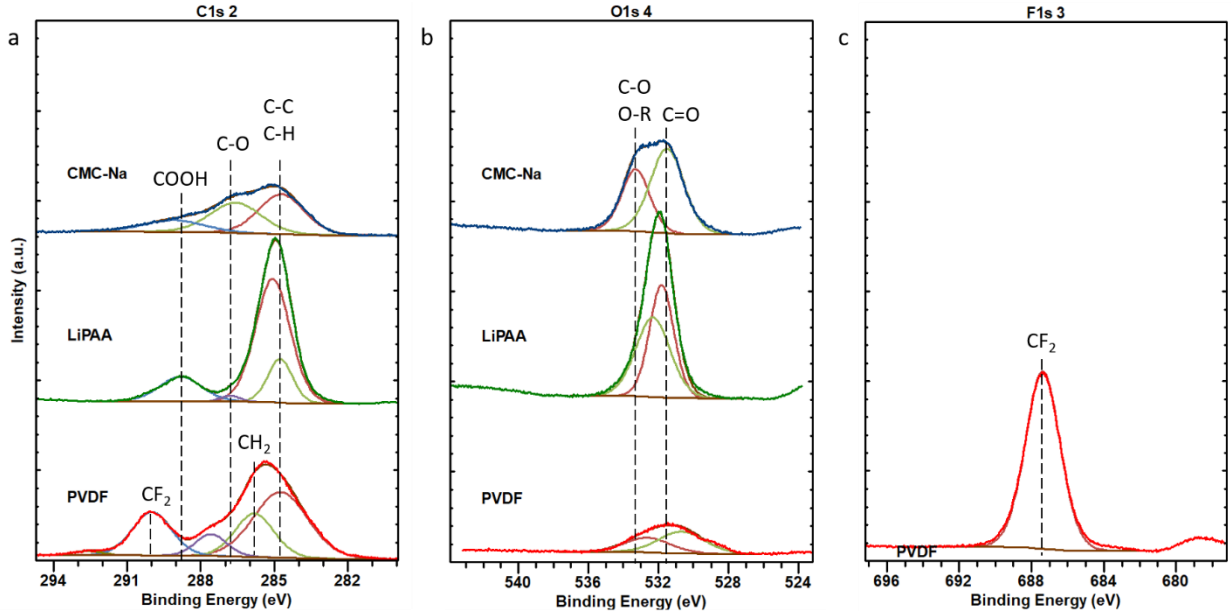

Figure 37. XPS spectra of stock binder powders for a) C1s, b) O1s, and c) F1s

NMC materials are known to form a surface layer of Li_2CO_3 when processed in water for 15 minutes or more via the formation of LiOH and Li_2O by reaction with water which are rapidly converted to Li_2CO_3 upon exposure to CO_2.[273, 274] We investigated whether the short-term (~1 min) exposure of our NMC thin films to water had a pronounced effect on interfacial chemistry. Deionized (18 MΩ) water was spin-coated onto a pristine NMC622 thin film with the same procedure as binder solutions and studied with XPS after drying overnight under vacuum at 100°C. The relative contribution of carbonate bonds in the C1s and O1s signals are nearly identical for the pristine and water processed samples. There is a 10% increase intensity of the C-C, C-H peak for the water processed sample, which may be attributed to additional carbon contamination of the surface. These minor differences and the clear Ni2p signal demonstrates that any surface layer formed by water content must be less than the ~10 nm calculated by others using magnetic susceptibility measurements of NMC cathode powders mixed in water for 15 minutes or more.[274] There is also no change in the shape of the Ni2p spectra which would be expected if the surface Ni were reduced or the formation of NiOOH.[275]

Uncoated and binder coated NMC622 thin films were cycled between 3.0 – 4.5 V *vs.* Li/Li^+ for two cycles at 10 mA/g (~C/20) to study the influence of binder coverage on CEI formation and initial cathode performance. The first cycle voltage profiles for each sample are included as a function of specific capacity in Figure 38a, with filled and hollow symbols corresponding to spin-coated and spray-coated samples, respectively. Specific capacity, coulombic efficiency, and capacity retention between cycles were determined from Figure 38. The first cycle charge capacity of the spin-coated PVDF and LiPAA samples were 208 and 191 mAh/g, which were closest to the theoretical capacity of NMC622 in this study (~200 mAh/g at 4.5 V *vs.* Li/Li^+). The baseline uncoated sample charged to 177 mAh/g which was close to that of the spray-coated PVDF and LiPAA samples (165 and 164 mAh/g, respectively). The CMC spin and spray-coated samples had the worst first cycle charge capacity overall (112 and 100 mAh/g, respectively), but all binder coated samples followed the same trend of spin-coated samples higher first cycle charge and discharge capacities. This is somewhat counterintuitive because one would expect insulating polymers to inhibit Li^+ diffusion into the cathode. This might be explained by the low rates studied here, where cells were cycled at a constant current of 10 mA/g (C/20) until reaching the upper cutoff voltage at which point the voltage was held until the measured charge current decreased below 5 mA/g (~C/40). A contributing factor to capacity loss is likely due to surface structural rearrangement and oxygen evolution from the cathode which occurs when cycling NMC622 to 4.5 V *vs.* Li/Li^+.[13, 265]

The capacity retention between cycles is 27% larger for the spin-coated PVDF sample than the uncoated material. This is emphasized in Figure 38b, where the green traces corresponding to PVDF-coated samples have retained more of their initial capacity than the baseline and other binder coatings. The PVDF spin-coated sample has retained the distinct sloping plateaus characteristic to Ni^{2+}/Ni^{4+} redox in NMC whereas most other samples have suppressed plateaus, likely due to polarization of the cell or loss of electrochemical capacity from the surface layer. This may be caused by the build-up of a highly resistive surface reconstruction layer and a layer of electrolyte decomposition products, as observed by others for Ni-rich NMC materials cycled to high voltages.[167, 276] We examine whether this is the case by AC impedance spectroscopy in Figure 38c. These Nyquist plots are fit to an equivalent circuit model corresponding to the processes occurring in series in this cell: bulk electrolyte resistance to Li^+ conduction in solution, R_e, desolvation of Li^+ at the interface – referred to here as charge transfer resistance, R_{ct} and Q_{dl}, Li diffusion through the CEI, R_{CEI} and Q_{CEI}, and a constant phase element for Li diffusion into the

thin film, Q_b[92, 226, 277] Charge transfer resistance is sometimes attributed to a convolution of effects at the interface (i.e. intercalation, diffusion through SEI, desolvation), but work by Xu et al demonstrated the serial nature of charge transfer resistance as desolvation of Li^+ followed by diffusion through the interface,[92, 278] and so we employ discrete elements for these in our equivalent circuit (Table 9).

The bulk electrolyte and charge transfer resistances are relatively small and comparable between samples (12 – 54 Ohm*cm^2), but the medium frequency semicircle corresponding to R_{CEI} varies significantly between samples depending on coating morphology and chemistry. The cycled PVDF spin-coated and spray-coated samples had R_{CEI} of 399 Ohm*cm^2 and 285 Ohm*cm^2, respectively, lower than the 1650 Ohm*cm^2 of the baseline. At 910 Ohm*cm^2, the LiPAA spin-coated had a slightly lower R_{CEI} than the baseline, whereas the LiPAA spray-coated sample had a higher value of 1762 Ohm*cm^2. Both CMC samples had higher R_{CEI} than the baseline, at 1864 Ohm*cm^2 and 1745 Ohm*cm^2 for the spin and spray-coated samples, respectively. These values match the general trend of the specific capacity and capacity retention data, with lower R_{CEI} corresponding to a higher specific capacity. This contrasts previous work where LiPAA was used as an artificial CEI in composite electrodes of LNMO, providing lower interfacial resistance compared to PVDF.[217] This is likely due to the difference in surface chemistry of NMC622 (*e.g.* oxygen evolution from the surface at high upper cutoff voltages), which will be discussed in the next section.

XPS was employed to determine whether the differences in interfacial impedance could be related to the morphology or compositions of the binders and CEI between samples. No F1s or P2p component spectra are shown for pristine uncoated or pristine CMC or LiPAA-coated samples because there were no distinguishable peaks in those regions. Components of all spectra were deconvoluted using reference spectra of the pure binders and common Li salts, collected on our instrument. Due to the presence of similar binding energies between the binders and decomposed species (e.g. ether bonds in CMC and oligomeric C-O from EC decomposition) absolute identification of the quantity of certain species is ambiguous and will be compared qualitatively. Components which do not have significant overlap with signals observed in the pure binder samples will be compared quantitatively (*i.e.* Li_2CO_3, $Li_xPO_yF_z$, and LiF signals in the C1s, P2p, and F1s spectra, respectively).

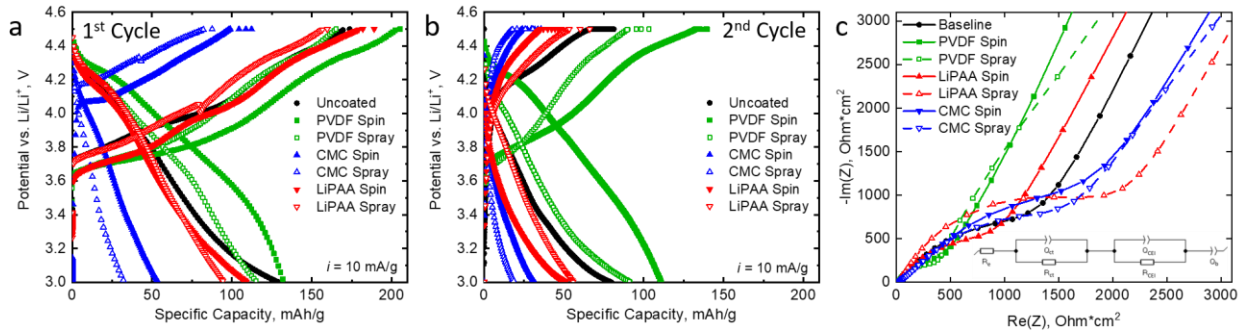

Figure 38. Cycling data for a) the first cycle specific capacity, b) the second cycle specific capacity, and c) AC impedance of electrodes after cycle 2 of each binder coating morphology and composition

Table 9. Specific capacity and coulombic efficiency of the first two cycles of uncoated and binder coated samples

Sample	Cycle 1, mAh/g			Cycle 2, mAh/g			Capacity Retention, %	
	Charge	Discharge	C.E., %	Charge	Discharge	C.E., %	Charge	Discharge
Uncoated	177	129	73	81.2	79.7	98	46	62
PVDF Spin	208	132	63	141	111	79	68	84
PVDF Spray	165	116	70	104	92.0	88	63	79
CMC Spin	112	53.1	47	37.0	30.9	84	33	58
CMC Spray	99.5	32.6	33	33.0	18.9	57	33	58
LiPAA Spin	191	110	58	49.1	51.1	104	26	46
LiPAA Spray	164	94.7	58	68.7	56.1	82	42	59

The P2p and F1s data for the three binder compositions and two coating techniques are compared to the uncoated material before and after cycling in Figure 39. The F1s spectra of Figure 39a show that pristine PVDF-coated samples have a primary peak at ~687.5 eV corresponding to the CF_2 bonds of the binder which was fit to the FWHM of the pure binder spectrum. There was also a minor peak at ~685.1 eV for the spin-coated PVDF which may be due to trace LiF. No signals were detected above the background for the F1s and P2p regions of the other pristine samples, so they are excluded from Figure 39. The F1s spectra of cycled PVDF-coated samples exhibit two component peaks corresponding to salt decomposition products: LiF and $Li_xPO_yF_z$ at ~687 eV, which aligns with what was observed in the O1s spectra. An additional minor contribution around ~689.2 eV corresponds to residual $LiPF_6$ on the sample surface. Samples were rinsed in DMC before analysis, so residual salt may have been loosely bound in the CEI or as a precipitate on the surface. The CF_2 signal of the binder was still visible in the cycled samples with a relative intensity of 63 at.% in the F1s spectra of the cycled spray-coated sample compared to 37 at.% for the spin-coated sample. The difference in signal attenuation suggests that the larger binder agglomerates on the spray-coated samples were less obscured by the CEI than the spin-coated PVDF samples. This means that the PVDF either coexists within the CEI layer (for the spray coated sample) or has a thin coating of decomposition products deposited on top of the binder layer (for either the spin or spray-coated samples).

The cycled spin-coated PVDF sample had noticeably more LiF when compared to the other cycled samples in Figure 39. Decomposition of salt species can be confirmed by considering the P2p spectra of cycled samples in Figure 39b. For both PVDF-coated samples and the uncoated sample, $Li_xPO_yF_z$ is detected at ~134.8 eV and residual $LiPF_6$ can be seen at ~137.4 eV. The same species are observed of the PVDF sample analysis can be observed in the LiPAA F1s spectra of Figure 39c except for the CF_2 bond due to the difference in binder chemistry. In this case, the cycled uncoated sample has a higher LiF:$Li_xPO_yF_z$ ratio of 2.0 when compared to the cycled LiPAA-coated samples with 1.6 and 1.5 for spin and spray-coating, respectively. The P2p spectra of Figure 39d show a ratio of $Li_xPO_yF_z$ to $LiPF_6$ which was slightly larger between the LiPAA-coated samples (1.4) than the uncoated sample (0.96).

The cycled CMC-coated samples had a different overall F1s peak ratios than the uncoated sample and the other binder samples. The CMC F1s spectra seen in Figure 39e demonstrates similar concentrations of LiF and $Li_xPO_yF_z$, whereas the baseline sample had predominantly LiF.

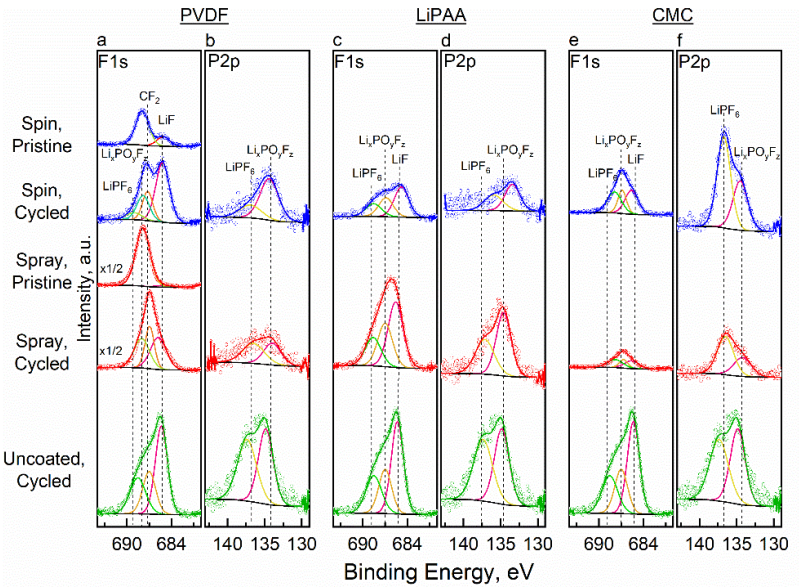

Figure 39. *Ex situ* XPS component spectra before and after cycling NMC622 films coated with PVDF (a,b), LiPAA (c,d), and CMC (e,f) for F1s and P2p with the intensity of some spectra multiplied as labeled for clarity

Additionally, the CMC-coated samples have the opposite trend of other samples for the P2p data in Figure 39f, with a $Li_xPO_yF_z$ to $LiPF_6$ ratio of 0.67 and 0.59 for the spin and spray-coated samples, respectively. The comparable amounts of LiF and $Li_xPO_yF_z$ at the surface of CMC demonstrates a different CEI chemistry compared to the other samples which correlates with the poorer cycling performance discussed earlier. To summarize the F1s and P2p XPS data, salt decomposition products were observed in the spectra of all cycled samples. The PVDF-coated samples had a greater ratio of LiF:$Li_xPO_yF_z$ than all other samples, and the cycled LiPAA and CMC-coated samples all had similar ratios of LiF:$Li_xPO_yF_z$ which were lower than the baseline (cycled uncoated) sample. Figure 40 shows the core level spectra of C1s and O1s for the three binder compositions and two coating techniques compared to the uncoated material before and after cycling. Similar bonds are detected in the C1s spectra of both the spin and spray-coated PVDF samples shown in Figure 40a. There is a appearance of -CO_3 species (~288.5 eV) after cycling for the PVDF-coated and uncoated samples indicate the presence of Li_2CO_3 or semicarbonates formed by EC oxidation.[279]

The characteristic CF_2 bond of PVDF was detected at ~290 eV in the pristine samples and was depressed in the cycled samples in good agreement with the F1s spectra of Figure 39a. O-C-O/C=O and C-O bonds were detected at ~287.1 eV and ~286.2 eV, respectively. These likely correspond to oligomers and lithium alkoxide species (ROLi), which can form from EC oxidation followed by a ring-opening polymerization reaction.[279, 280] Compounds appear in a narrow range in the O1s spectra seen in Figure 40b, with the lowest energy peak at ~529.5 eV attributed to lattice oxygen (M-O), and ROLi species assigned to ~531.0 eV. CO_3 and O-C=O groups were observed at ~531.9 eV, and oligomer (C-O) species were assigned to ~533 eV. The highest energy component appears at ~534 eV and corresponds to $Li_xPO_yF_z$ species. Cycled PVDF-coated samples had more intense M-O signals of 45 at.% and 32 at.% for spin and spray-coated PVDF, respectively, compared to the 18.5 at.% of the uncoated sample, indicating a thinner CEI or more

exposed active material surfaces. The $Li_xPO_yF_z$ contribution in the O1s spectra of the uncoated sample was larger than both the spin and spray-coated PVDF-coated sample, as was the case in the F1s spectra of Figure 39a. Such fluorinated species necessarily originate from the decomposition of the electrolyte salt, $LiPF_6$:[263]

$$LiPF_6\ (sol.) \leftrightarrow PF_5\ (sol.) + LiF\ (s) \quad (1)$$

$$PF_5\ (sol.) + H_2O\ (l) \rightarrow POF_3\ (sol.) + HF\ (sol.) \quad (2)$$

There are similar C1s moieties detected for the uncoated sample and the LiPAA-coated samples in Figure 40c. There C-C/C-H intensity is greater for the LiPAA-coated samples, which can be attributed to the bonds of the binder. This is reflected in the O1s spectra of Figure 40d, in which the greater contribution around 532 eV in the LiPAA-coated samples aligns with the primary component of the O1s spectra for the pure binder (Figure 37). The CMC-coated samples had larger contributions of C-O and O-C-O/C=O components than the baseline, as seen in Figure 40e. There was a substantial decrease in the relative concentration of M-O for the CMC-coated samples compared to the uncoated sample's O1s spectra in Figure 40f. This could be attributed to the formation of a thicker CEI, given that the M-O signal was visible in the coated samples before cycling.

After cycling, a metal oxide (M-O) signal is visible in the XPS O1s spectrum for each sample and can be seen in Figure 8a. This signifies either a discontinuous CEI or a thin enough surface layer for electrons to escape the NMC surface and reach the detector. The intensity of these signals matches the attenuation of Ni2p spectra in Figure 41. Such a thin CEI is in line with previous reports of the CEI.[167, 281] The M-O signal for the uncoated sample is 18% of the overall O1s signal, which is substantially lower than the spin and spray-coated PVDF samples at 45% and 32%, respectively. This suggests a thinner overall coating on the PVDF-coated samples because the combined signal effects of the PVDF coating and CEI on those samples suppresses the M-O signal less than the CEI alone on the uncoated sample. In contrast, the relative amount of M-O detected from the LiPAA-coated samples is close to that of the baseline. The CMC-coated samples had low relative M-O signals, indicating a thicker or more attenuating surface layer. These trends match the impedance trends observed in Figure 5c, suggesting that lower interfacial resistance and higher capacity retention between cycles might be due to a thinner overall surface layer.

Figure 42b shows the relative atomic percent of different bonds detected at the surface of each cycled cathode thin film by XPS. Quantification of at.% is based on the area of each component peak fit to the raw data and weighted according to the relative sensitivity factor of each element based on Scofield cross sections, the transmission factor of the instrument, and the inelastic mean free path of an electron at the given binding energy. The active material and electrolyte salt contributions were excluded for clarity in comparing decomposed species present in the CEI. Bonds with significant overlap with binder contributions were also excluded to reduce ambiguity in discussing common bonds shared between CEI components and the binders (e.g. $-COO^-$ of ROLi and LiPAA). This method of comparison necessarily omits potential CEI species which overlap with binder binding energies (e.g. ROLi, oligomeric C-O, carboxylates) and does not account for any species formed below thick regions of binder which attenuate signals of surface species. The remaining components – Li_2CO_3/polycarbonates, $Li_xPO_yF_z$, and LiF – do not have significant overlap with signals observed in the pure binder samples for their respective spectra: C1s, P2p, and F1s.

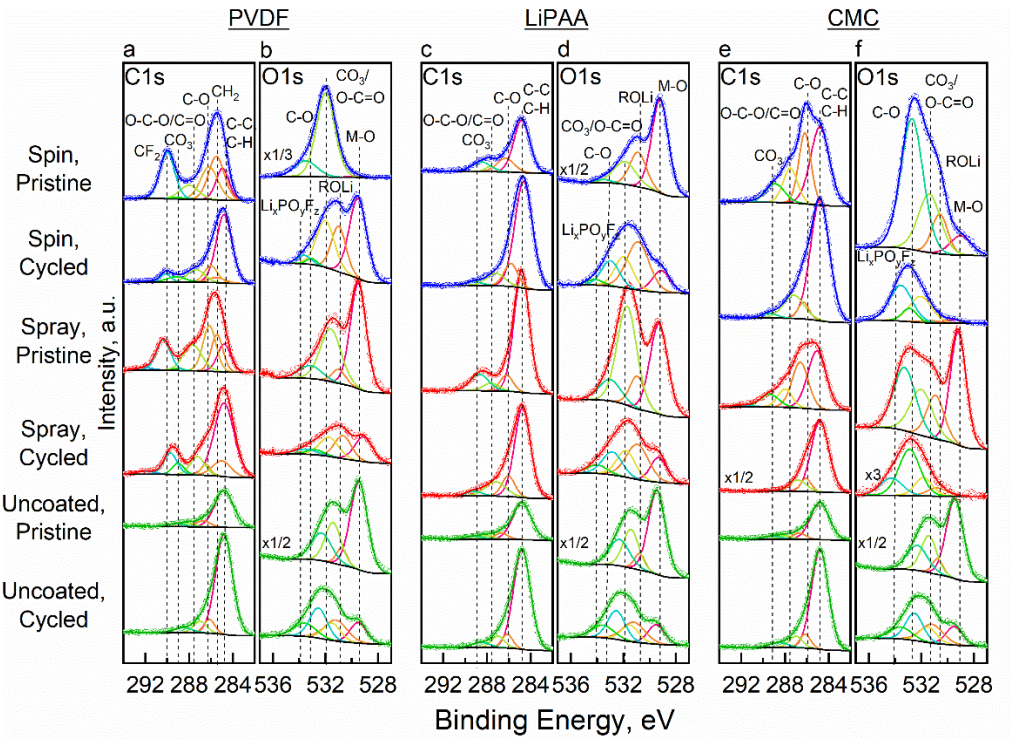

Figure 40. *Ex situ* XPS component spectra before and after cycling NMC622 films coated with PVDF (a,b), LiPAA (c,d), and CMC (e,f) for C1s and O1s with the intensity of some spectra multiplied as labeled for clarity

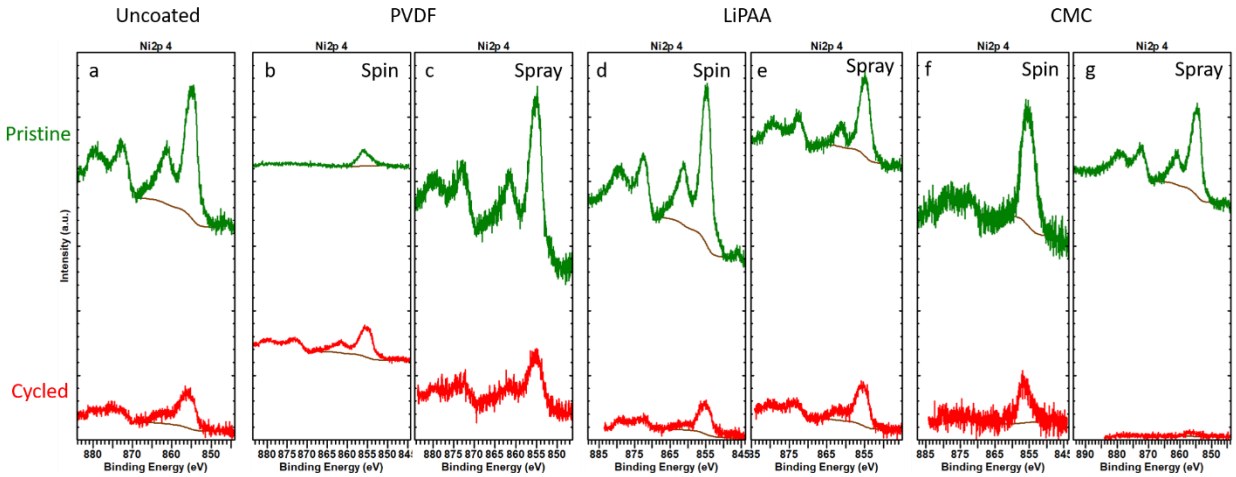

Figure 41. Ni2p spectra of pristine and cycled uncoated (a), PVDF-coated (b, c), LiPAA-coated (d, e), and CMC-coated (f, g) thin film electrodes

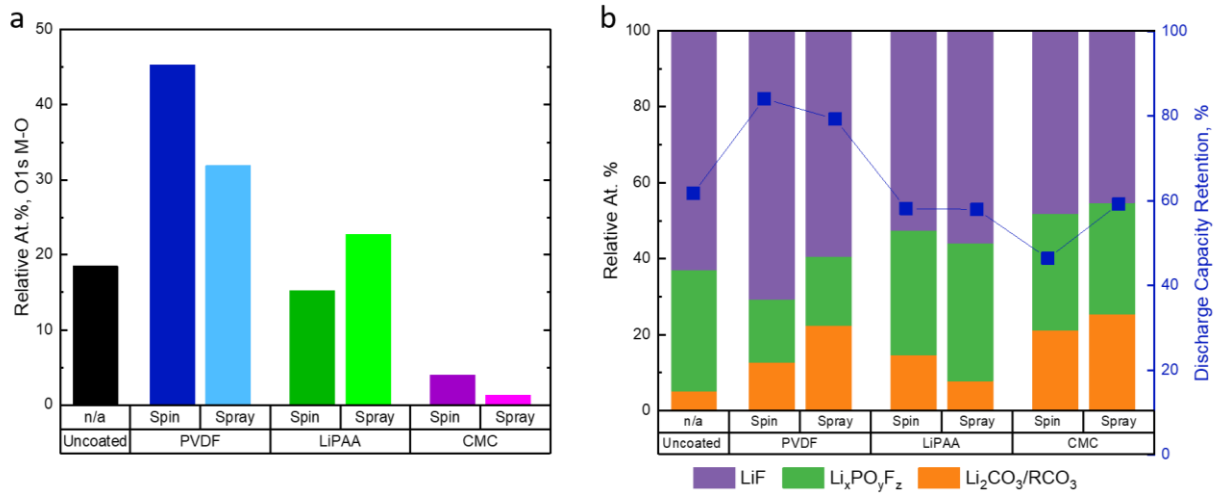

Figure 42. Relative composition of surface species measured after cycling by *ex situ* XPS for a) M-O, and b) Li_2CO_3 and polycarbonates (orange), $Li_xPO_yF_z$ (green), and LiF (purple) with discharge capacity retention overlaid

These species are normalized in Figure 42b to compare their relative proportion in the CEI. The majority of this three species ratio of the CEI on each sample is comprised of LiF, except for the CMC samples which have 48 at.% and 45 at.% LiF for the spin and spray-coated samples, respectively. There is a larger proportion of Li_2CO_3/RCO_3 observed on the binder coated samples compared to the uncoated film, which might be attributed to processing conditions for the aqueous binders (LiPAA and CMC), but the increase for the PVDF samples as well suggests a mechanistic role of the binders.

There is slightly more $Li_xPO_yF_z$ observed on the spray-coated samples compared to the spin-coated samples in each case, although the PVDF-coated samples show the least relative amount of $Li_xPO_yF_z$ overall. The PVDF samples also exhibit the largest relative LiF signals after the uncoated sample, which might contribute to their higher capacity retention when considered alongside the M-O data in Figure 42a.

The role of LiF in passivating interfaces is not well understood,[282] although a thin layer of predominantly LiF has been observed as an effective passivation layer for NMC333[271] as well as high voltage operation of LMNO.[283] In this case, the CEI formed on PVDF-coated samples may differ from the LiPAA and CMC-coated samples due to a difference in water content at the interface. While these samples were dried in a vacuum oven, residual water may have been trapped at the surface by the aqueous binders (LiPAA and CMC). This water could be hydrolyzed by the strong Lewis acid PF_5 according to Equation 1 and 2 to form POF_3. Residual Li_2O at the surface of the cathodes could then react to form lithium fluorophosphates:[284, 285]

$$POF_3\ (sol.) + Li_2O\ (s) \rightarrow LiF\ (s) + Li_xPO_yF_z\ (s) \quad (3)$$

The increased proportion of $Li_xPO_yF_z$ observed on the LiPAA and CMC-coated samples as well as the increased thickness of the CEI can be explained by the additional water content at the surface. This highlights the importance of minimizing water content at the surface for high voltage cathode materials. The improved performance and surface chemistry of the PVDF-coated

NMC622 over the LiPAA-coated samples somewhat contradicts the observation of previous work on LiPAA-coated LNMO composite electrodes which had reduced charge transfer resistance and similar capacity at low rates compared to PVDF-coated samples.[217] This difference in observations of performance might be attributed to different mechanisms of CEI formation in LNMO compared to Ni-rich NMC. The crystal structure of LNMO is known to remain stable when cycling to voltages up to ~5 V *vs.* Li/Li^+, at which electrochemical oxidation of the electrolyte becomes the primary source for CEI components. Ni-rich NMC systems, on the other hand, undergo structural rearrangement of the cathode and release oxygen from the lattice, causing chemical oxidation of the electrolyte.

6.5 Conclusions

In this study, we examined the effects of binder morphology and composition on the formation of the CEI on Ni-rich NMC622 thin film electrodes. Spin and spray coating of PVDF, LiPAA, and CMC allowed for experimental control of the planar interface such that the surface chemistry of cycled films could be probed with XPS. The PVDF-coated samples had the thinnest CEI which were comprised of greater relative concentrations of LiF and Li_2CO_3 than $Li_xPO_yF_z$ when compared to the other samples.

CMC had the thickest CEI and a more even composition of the three species of interest, whereas LiPAA had a similar CEI thickness to the uncoated sample with similar surface chemistry. These trends aligned with capacity retention between formation cycles and the substantially lower interfacial impedance of PVDF-coated samples. All binder coated samples had more Li_2CO_3 on the surface than the uncoated sample, which might be attributed to processing conditions. This work demonstrates that the presence of binder on the interface of cathode active materials directly influences the chemistry of CEI formation which impacts the performance of the cell. The presence of residual water trapped at the interface by binders changes the composition and thickness of CEI, so a good binder should provide adequate adhesion between active material particles and conductive carbon while minimizing water introduced to the interface. As such, close attention to processing conditions and binder selection is imperative for the application of high voltage cathode materials such as Ni-rich NMC.

Acknowledgements. This research at the Oak Ridge National Laboratory, managed by UT Battelle, LLC, for the U.S. Department of Energy (DOE) under contract DE-AC05-00OR22725, was sponsored by the Office of Energy Efficiency and Renewable Energy (EERE) Vehicle Technologies Office (VTO) (Deputy Director: David Howell) Applied Battery Research subprogram (Program Manager: Peter Faguy) (N.D.P., C.D., and G.M.V.). N.D.P. also thanks Beth Armstrong for constructive feedback on the structure of this report, Robert Sacci for assistance on FTIR, and Katie Browning for assistance on spin coating and insightful discussions.

7. CONTROLLING THE ISOELECTRIC POINT OF NI-RICH NMC CATHODE INTERFACES

This manuscript is in its final review stages with coauthors to be submitted to *American Chemical Society Advanced Materials and Interfaces*. The study investigates the role of initial surface chemistry on high voltage cycling of NMC622 by modifying the surface charge with thin metal oxide coatings of varying isoelectric points. My contribution as the primary author was executing all experiments planned with G. M. V. as well as data analysis and writing the manuscripts. K. B. and B. L. A. assisted with initial zeta potential experiments and subsequent data analysis. All authors assisted with data interpretation and editing the manuscript. Supplemental figures have been added to the main text for clarity.

Nathan D. Phillip,[1,2] Beth L. Armstrong,[3] Claus Daniel,[1,4] Gabriel M. Veith[2*]*

[1] The Bredesen Center for Interdisciplinary Research and Graduate Education, University of Tennessee, Knoxville, TN, 37996, USA

[2]Chemical Sciences Division, Oak Ridge National Laboratory, Oak Ridge, TN 37831, USA

[3]Materials Science and Technology Division, Oak Ridge National Laboratory, Oak Ridge, TN 37831, USA

[4]Energy and Environmental Sciences Directorate, Oak Ridge National Laboratory, Oak Ridge, TN 37831, USA

7.1 Abstract

Metal oxide coatings have been reported to be an effective approach for stabilizing cathode interfaces, but the associated chemistry is unclear. In this work, thin films of TiO_2, ZnO, and Cr_2O_3 were used to modify the surface charge of thin films of $LiNi_{0.6}Mn_{0.2}Co_{0.2}O_2$ and study its role on the cathode/electrolyte interphase composition and impedance under high voltage cycling (4.5 V *vs.* Li/Li^+). Cathodes with more acidic surfaces (negatively charged) provided higher initial specific capacity and capacity retention with cycling. More basic surfaces (positively charged) had higher initial impedance and greater impedance growth with cycling. These differences appeared to depend on the degree of $LiPF_6$ salt decomposition at the interface, which was related to surface charge, with more neutral surfaces having a $LiF:Li_xPO_yF_z$ ratio close to unity but basic surfaces had substantially more LiF. This chemistry was more significant than the thickness as the more acidic surfaces formed a thicker CEI than the basic surface. These results suggest that the surface charge of cathodes directly influence electrolyte degradation, ion transport, and thus cell lifetime.

7.2 Introduction

Inorganic coatings of metal oxides are a common mitigation strategy for stabilizing lithium ion battery cathode interfaces which degrade during operation at high voltages (≥ 4.5 V *vs.* Li/Li^+). Thin layers (up to tens of nm) of Al_2O_3,[190, 286, 287] TiO_2,[167, 182, 288] Cr_2O_3[289, 290] and ZnO[291, 292] have been coated on the surface of the cathode active materials before electrode preparation. These deposition methods include atomic layer deposition,[287] sol-gel synthesis,[190] hydrolyzation,[288] and

physical vapor deposition[293] and the coatings are reported to reduce charge transfer impedance rise during cycling and extend cell cycle life by suppressing electrolyte decomposition.[238, 292, 294, 295] The cause of this stabilization is often attributed to scavenging HF, suppressing transition metal dissolution, and preventing contact between the electrolyte and the active material surface. [238, 288, 292, 295] The mechanisms involved remain a subject of ongoing study, although synergies between surface coatings and electrolyte decomposition have been observed, such as Al_2O_3 reacting with $LiPF_6$ salt to form a passivating layer of AlF_3 at the interface and the beneficial additive $LiPO_2F_2$ in the electrolyte.[296]

The relationship between these metal oxide coatings to electrolyte decomposition is not well understood for cathode materials such as Ni-rich NMC ($LiNi_xMn_yCo_zO_2$, where $x + y + z = 1$ and $x > 0.5$) cycled to high upper cutoff voltages (e.g. 4.5 V *vs.* Li^+/Li) for additional capacity. Electrolyte decomposition coupled with structural rearrangement (i.e. layered $R\bar{3}m$ to rock salt) prevents commercial operation of these materials at high voltages, so understanding how coatings might stabilize the cathode electrolyte interphase (CEI) would inform cell designs for increased energy density of these promising materials. A rough 25-35 nm layer of anatase TiO_2 was shown to improve the rate capability of NMC622 cycled to 4.5 V *vs.* Li/Li^+ and was attributed to reduced impedance growth due to suppression of interfacial reactions and reduced cation mixing in the bulk structure of the pristine material.[288] Surface doping of Ti^{4+} in NMC622 with a nano-sized coating of TiO_2 was also found to reduce film impedance over additional cycles to 4.4 V *vs.* Li/Li^+.[167, 182] Cr_2O_3 has been deposited on NMC111 to improve rate capability at 3C and structural integrity at high temperatures[289] and suppress Mn^{2+} dissolution from spinel $LiMn_2O_4$.[290] Similarly, metal dissolution from $LiNi_{0.8}Co_{0.15}Al_{0.05}O_2$ was reduced when coated with sputtered films of ZnO with a thickness of 20 nm was preferred to limit impedance rise due to the coating.[292]

Studying interfacial phenomena related to the cathode active material in composite electrodes is challenging due to potential interactions between the metal oxide coatings and the binder, conductive carbon, and slurry solvent. To reduce the complexity of the system of interest (the electrolyte | metal oxide | cathode interface), thin film electrodes solely comprised of the cathode active material can be used as a model environment. The fully dense film removes the need for binders, conductive carbon, and slurry processing as well as enables planar geometry for simplified electrochemical impedance analysis and direct control of the interfacial environment.[247] Depositing a thin layer of metal oxide atop a thin film cathode provides a well-defined environment for studying interactions between the cathode, metal oxide, and the electrolyte and was therefore the process applied in this work.

The surfaces of metal oxides are terminated by hydroxyl groups and the adsorption of species in air may lead to additional surface groups such as CO_3^{2-} from adsorbed CO_2.[297] This surface termination is the origin of charge at the surface of metal oxides and governs the charge transfer reaction of the electric double layer.[298]

The intrinsic surface charge varies between metal oxides and can be described by their zero point of surface charge, or isoelectric point (IEP).[298, 299] Increased hydroxylation of NMC cathode surfaces is expected to increase the reaction energy barrier for ethylene carbonate (EC) decomposition based on modeling studies.[193] The ring opening decomposition reaction of EC was found to be impeded by NMC surfaces with more M-OH groups compared to the M-F and O-H surface models,[193] so different amounts of surface -OH groups might explain the influence of metal oxide coatings on the CEI. This also might offer insight as to how the initial surface chemistry on the interface of pristine NMC622 influences to cycling stability.[300] Paulsen *et. al* observed the initial surface chemistry of NMC can be characterized by "soluble base content" (SBC) or the

amount of LiOH and Li_2CO_3 formed on the surface during reaction with water.[300] They found an optimum range for Ni-rich NMC materials at 80 – 120 µmol/g SBC, indicating that having a complex initial surface chemistry is more beneficial to cycling than neat NMC.[300] By selecting coatings with different IEP values, the initial surface chemistry can be modified (*i.e.* acidity of terminating -OH). In this study, the relationship of surface charge to the formation of species in the CEI was investigated by controlling the NMC622 interface with thin metal oxide films.

7.3 Methods

Synthesis. Thin films of $LiNi_{0.6}Mn_{0.2}Co_{0.2}O_2$ (NMC622) were prepared by radio frequency magnetron sputtering of home-built NMC622 targets, detailed in our previous work.[301] Deposition conditions in this study included a base chamber pressure <2 x 10^{-6} Torr with 55.0 sccm high purity Ar gas (99.9995%, Airgas) flow rate providing 6.0 mTorr deposition pressure at 90 W forward power. Following deposition of 1 µm NMC622 on 1 cm diameter Al_2O_3 substrates coated with Co and Pt, thin films were annealed at 700ºC for 1 hour under high purity air flow (~0.2 LPM, Airgas) with a ramp rate of 5 ºC/min then stored in an Ar-filled glove box. Metal oxide films (3 nm) were deposited on sintered NMC622 films by direct current sputtering of Ti, Cr, or Zn metal (99.95 – 99.99% purity, Kurt J. Lesker) under 15 sccm Ar and 5 sccm O_2 at 20 mTorr and 30 W.

Characterization. Zeta potential of films were collected on a Brookhaven Zeta Potential Analyzer using Phase Analysis Light Scattering (ZetaPALS) with a Surface Zeta Potential probe attachment. The negative and positive probe particle solutions had pH values of 6.67 and 4.13, respectively. Reference standards were pellets of TiO_2 (Johnsen Matthey), Cr_2O_3 (Alfa Products, 98%), and ZnO (Alfa Aesar, Puratronic, 99.9995%) sintered at 1250ºC and direct current sputtered films (~200 nm) of amorphous TiO_2, Cr_2O_3, and ZnO on 1 cm Al_2O_3 wafers. The isoelectric point of each compound was measured by dispersing metal oxide powders in 1 mM KNO_3 and titrating with HNO_3 and NH_4OH for an array of solutions with a pH range of ~2 – 10. The reported zeta potential data of each solution are an average of 100 measurements at 25.0 ºC.

X-ray Photoelectron Spectroscopy (XPS) was conducted on a PHI 3056 XPS spectrometer operated at 350 W and 15 kV with an Mg Kα (1253.6 eV) source. Pristine samples were transferred in air and cycled films were transferred under vacuum for measurement in a cryo-pumped vacuum chamber at 10^{-9} Torr or less (10^{-11} Torr base pressure). Survey scans were collected at 93.9 eV pass energy with 0.5 eV energy steps while high-resolution scans were acquired at 23.5 eV pass energy and 0.05 eV energy steps with 20−60 repeated scans of all spectra to improve the signal-to-noise ratio. Spectra were shifted relative to the adventitious carbon peak (284.8 eV) to correct for charging. Raw data was fit to component peaks based on Li salts collected in the same instrument to provide standard references for relative peak area, position, and full width at half maximum (FWHM).

Electrochemical Measurements. Electrochemical cells were assembled in an Ar-filled glove box in Swagelok cells vs. Li metal (1 cm diameter). Two 1.3 cm diameter separators (Dreamweaver Gold 40) were soaked in 300 µL 1.2 M $LiPF_6$ in ethylene carbonate (EC) and ethyl methyl carbonate (EMC) in a 3:7 wt. ratio (Tomiyama). Cells rested at open circuit voltage for 2 hours before cycling for two formation cycles between 3.0 – 4.5 V vs. Li/Li^+ in a constant current, constant voltage protocol (CC/CV). Constant current steps of 10 mA/g (~C/20, where theoretical capacity, C = 200 mAh/g) were held until the upper cutoff voltage (UCV) followed by a constant potential hold at UCV until measured current dropped below 5 mA/g (C/40) then cells were discharged at 10 mA/g constant current to the lower cutoff voltage. This was followed by 10 CC/CV cycles at 40 mA/g (~C/5) with the same cutoff limitations. Electrochemical impedance

spectroscopy tests were conducted before and after the 2 formation cycles and after the 10 C/5 cycles on a BioLogic MPG-2 Battery Tester when cells were at open circuit voltage over 10 mHz to 20 kHz with 6 mV applied signal. Cycled electrodes were extracted in an Ar-filled glove box, rinsed in 1 mL dimethyl carbonate (DMC, Aldrich, 99.95%) for 30 seconds before drying under vacuum and transferring to the XPS chamber under vacuum.

7.4 Results & Discussion

Three metal oxides were selected to modify the surface charge of NMC622. Cr_2O_3 was chosen to induce a more acidic surface, based on the low IEP reported for the powder and Cr_2O_3-coated particles around pH of 2.[290] ZnO served as a basic surface modification due to its higher IEP of 9.0-10.3, depending on synthesis conditions.[299] TiO_2 was selected as a coating which would not modify the surface charge significantly due to its similar IEP to NMC622 (4.7-6.2).[299] Al_2O_3 was not selected for this study due to the wide range of IEP values reported (5.0-9.25) depending on phases and synthesis conditions.[299]

These surface environments were established by depositing a thin layer of metal oxides onto NMC622 thin film cathodes by DC magnetron sputtering of Ti, Cr, or Zn in a reactive atmosphere (3:1 Ar:O_2). A quartz crystal microbalance measured the deposition rate such that 3 nm of TiO_2, Cr_2O_3, and ZnO could be deposited on the surface of different NMC622 samples. These coatings were examined with XPS as shown in Figure 43 to determine the oxidation state of the metals to infer the metal oxide composition on the surface. Ti2p spectra are shown in Figure 43a, where two sharp peaks were observed at 458.2 eV and 464.0 eV, corresponding to the orbital splitting of $Ti2p^{3/2}$ and $Ti2p^{1/2}$, respectively. The peak positions and separation of 5.8 eV corresponds to an oxidation state of Ti^{4+}, confirming a surface coating of TiO_2.[224] The Cr2p spectra shows a similar orbital splitting in Figure 43b, with characteristic satellite lines appearing as shoulders to the primary peaks at 576.5 eV and 586.1 eV which match the peak positions of Cr^{3+} in Cr_2O_3.[224, 302] The Zn2p spectra appear at a higher binding energy as seen in Figure 43c. Two sharp peaks at 1022.3 eV and 1045.4 eV indicate Zn^{2+} for the ZnO coating.[224] Ni2p signals were still visible from the underlying cathode for each of these samples and are included in Figure 44. This indicates the metal oxide coatings were sufficiently thin (~3 nm) to not block photoelectrons emitted from the bulk cathode material.

To characterize how the chemical environment at the interface varied between metal oxide coatings, the zeta potential was calculated using a surface probe attachment. These data are included in Table 10 along with measured IEP values for crystalline samples of the respective oxides. Crystalline powders of each of the metal oxides studied here were titrated over a pH range of ~2 – 10. The IEP values in Table 10 were determined by measuring the zeta potential of the solution at each pH and interpolating the pH value where there was zero surface charge, as shown for each compound in Figure 45. The isoelectric point of a compound can vary substantially between different crystal structures and preparation methods,[299, 303] so the surface charges of sintered pellets of the same crystalline powders used for IEP measurements were compared to ~200 nm of films sputtered on polycrystalline Al_2O_3 wafers at the same pH to determine whether they had comparable values. These were found to be in good agreement (±3.9 mV) with the exception of ZnO where the surface charge of the pellet was twice the magnitude of the film (see Table 10). This could be due to the crystalline nature of the pellet compared to the amorphous sputtered thin film or the concentration of surface -OH. Thin film zeta potential measurements are dependent upon the competing effects of electrophoresis and electroosmosis of the solution at the

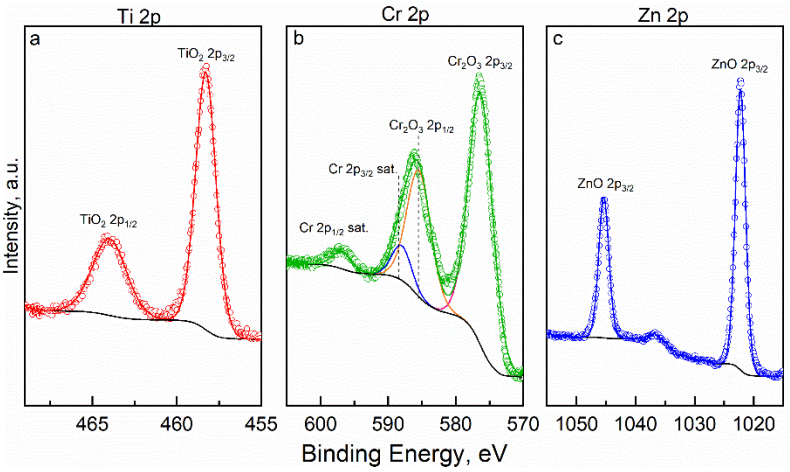

Figure 43. XPS spectra of pristine M-O coatings of a) Ti 2p, b) Cr 2p, and c) Zn 2p on NMC622

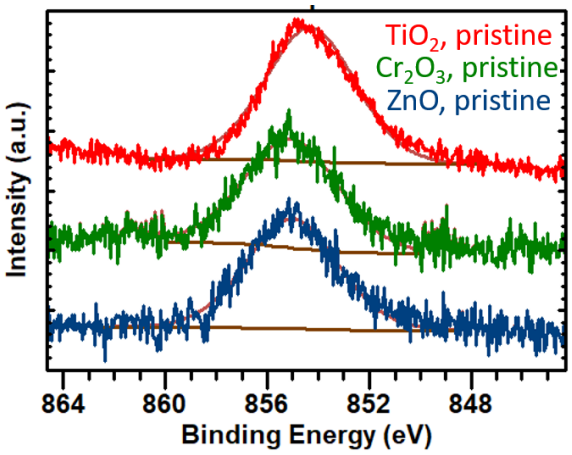

Figure 44. Ni2p spectra of pristine metal oxide coated NMC622

Table 10. Surface charge for sputtered films on NMC622, Al_2O_3, pellets of pristine metal oxide powders and measured IEP of metal oxide powders used in this study

Oxide	Sample	Surface Zeta, mV	Powder IEP
Cr_2O_3	3 nm on 1 µm NMC	-21.4	2.6
	200 nm on Al_2O_3	-11.0	
	Pellet	-7.1	
TiO_2	3 nm on 1 µm NMC	-13.7	3.4
	230 nm on Al_2O_3	-28.7	
	Pellet	-28.7	
NMC	1 µm	-9.2	3.5
ZnO	3 nm on 1 µm NMC	9.8	6.5
	200 nm on Al_2O_3	10.3	
	Pellet	23.1	

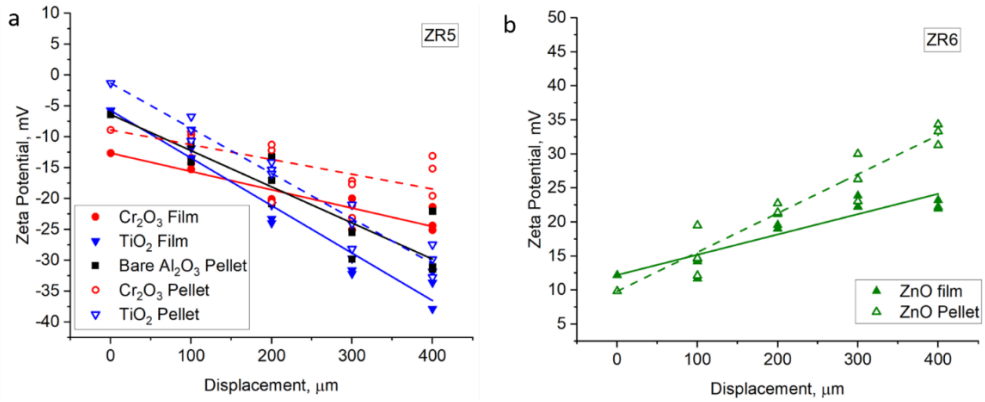

Figure 45. Surface zeta potential measurements in a) Brookhaven ZR5 and b) Brookhaven ZR6 probe particle solutions

surface and the tracer particles in the bulk solution. The zeta potential of the thin film surface (ζ_S) was calculated as the difference between the charge measured in the bulk solution (ζ_B, due to electrophoresis only) compared to that of the film/solution interface (ζ_W, due to electroosmosis and electrophoresis). These values are determined by zeta potential measurements at increasing displacements from the surface (see Figure 46), where[304] $\zeta_S = \zeta_B - \zeta_W$.

For an accurate measurement it is important to select a probing solution which matches the sign of the surface charge at the solution pH. For metal oxides with an IEP less than the pH of the probe solution the negatively charged probe particle solution (Brookhaven Zeta Potential Reference, ZR5) was selected, and for oxides with an IEP greater than the pH of the probe solution the positively charged probe particle solution (Brookhaven Zeta Potential Reference, ZR6) was selected. When a surface is immersed in a solution at a pH lower than the material's IEP, the surface will usually be positively charged so a probing solution with positively charged probe particles must be selected so that the magnitude of electrostatic repulsion in the slipping plane (zeta potential) can be measured. This way it can be estimated if a surface is acidic or basic as well as the magnitude of the surface charge at that pH.

An array of metal oxide coatings was selected to generate different chemical environments at the cathode surface. The TiO_2-coated samples served as the baseline model in this study as a metal oxide coating with a similar surface zeta potential to that of uncoated NMC, which was expected due the nearly identical IEP values of 3.4 and 3.5 for the powders measured here, seen in Table 10. The Cr_2O_3-coated NMC films had a surface charge 7.7 mV less than the TiO_2-coated samples whereas the ZnO-coated samples were 23.5 mV greater. The negatively charged surfaces originate dissociation of surface sites or adsorption of protons whereas more positive values originate from basic groups such as hydroxyl groups known to terminate metal oxide surfaces.[298] The magnitude of zeta potential is based on the sum of the reactions of those surface groups at a given pH. As such, the Cr_2O_3-coated samples had more acidic sites or fewer basic groups than the TiO_2-coated films and the ZnO-coated films had more basic groups. These varied surface environments might impact the behavior of Li^+ solvation complexes at the interface and thus cell degradation, which will be discussed presently.

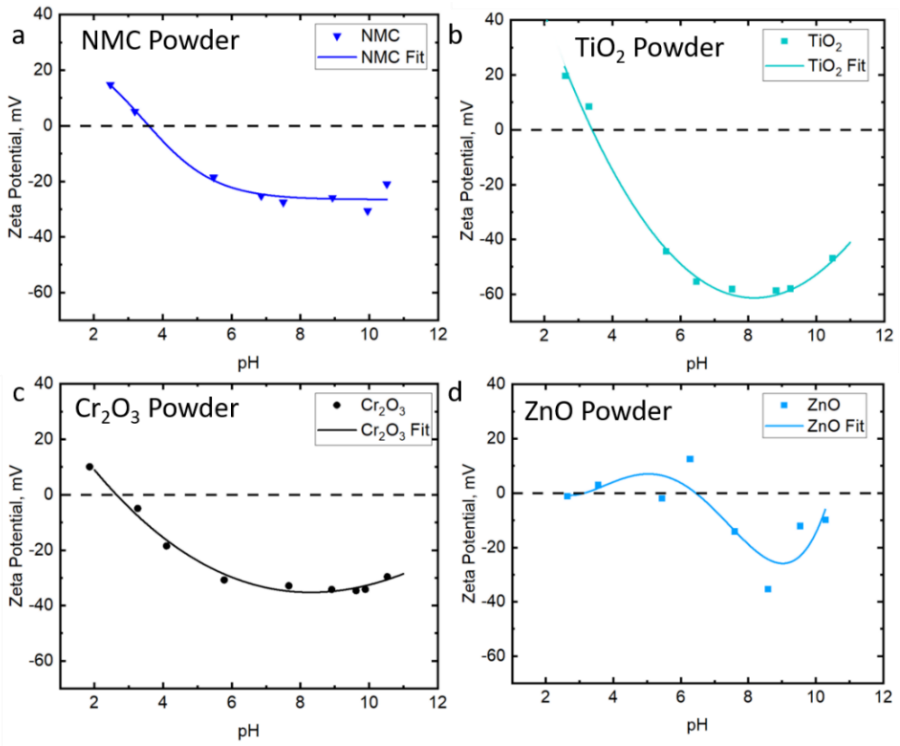

Figure 46. Isoelectric point measurements through titration of solutions of a) NMC622, b) TiO_2, c) Cr_2O_3, and d) ZnO powders at immediately after titration and after 24 hours in suspension

Cells were first cycled twice between 4.5 – 3.0 V *vs.* Li/Li^+ at 10 mA/g (~C/20) with the first cycle specific capacity shown in Figure 48a. The overall structure of the voltage profile was similar between samples, with a plateau at 3.8 V corresponding to Ni^{2+}/Ni^{4+} redox and a secondary plateau at higher voltage (~4.4 V), possibly due to phase change induced by cycling Ni-rich NMCs to high voltages.[50, 209] The TiO_2-coated samples have a suppressed 3.8 V plateau and an extended plateau at 4.4 V compared to the other two samples, which may indicate partial oxidation of Co^{3+} to Co^{4+} because Mn^{4+} is expected to remain electrochemically inactive.[50] The ZnO coated sample reached a slightly higher specific capacity of 170 mAh/g, but only the Cr_2O_3-coated sample achieved the theoretical specific capacity at 200 mAh/g. Each of the three cathode types had similar first cycle discharge capacities, with the Cr_2O_3-coated sample discharging 94 mAh/g and the TiO_2 and ZnO-coated samples providing 87 and 84 mAh/g, respectively. Based on the position of the primary plateau for the Cr_2O_3-coated sample being at the expected Ni redox center, the additional capacity was likely due to additional utilization of the bulk Li inventory rather than parasitic reactions.

All metal oxide coated cells thin films studied here exhibited substantial capacity loss at a higher charge and discharge rate of 40 mA/g (~C/5). These data are included in Figure 48b, where the Cr_2O_3-coated cells again exhibited the highest initial specific charge capacity at 32 mAh/g. The ZnO-coated sample had the highest coulombic efficiency at 95% on the 10th cycle while the TiO_2-coated sample had the lowest at 81%. The voltage profiles had a similar shape between each sample (Figure 47). The massive loss in specific capacity (80+%) at higher charge and discharge rates was likely due to the irreversible structural change which is known to occur at the surface of NMC622 when cycled to high upper cutoff voltages and amplified in this thin film configuration.[50] The 4.5 V *vs.* Li/Li^+ cutoff voltage was chosen here to accentuate material degradation to study interfacial effects. The inset of Figure 48c shows the impedance data for the pristine samples, with similar R_{el} (12-29 Ohm*cm^2). Interfacial impedance (R_{ct} and R_{CEI}) was considered as one element for the pristine samples and may originate from charge transfer resistance between the solvated Li^+ and metal oxide coatings at the electrode surface.

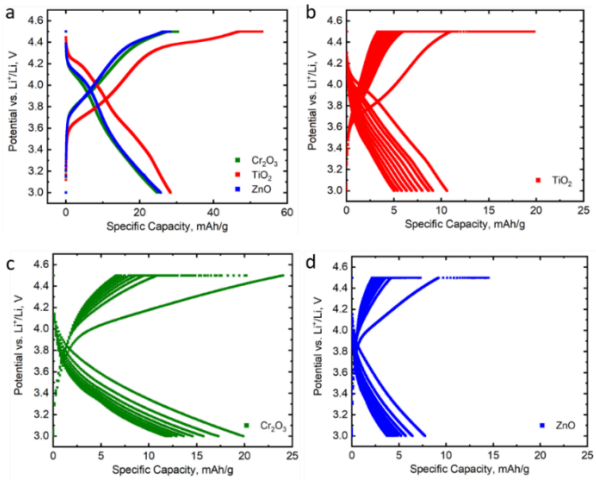

Figure 47. Voltage profiles of a) second cycle at 10 mA/g (C/20) and 10 cycles at 40 mA/g for b) TiO_2:NMC, c) Cr_2O_3:NMC, and d) ZnO:NMC

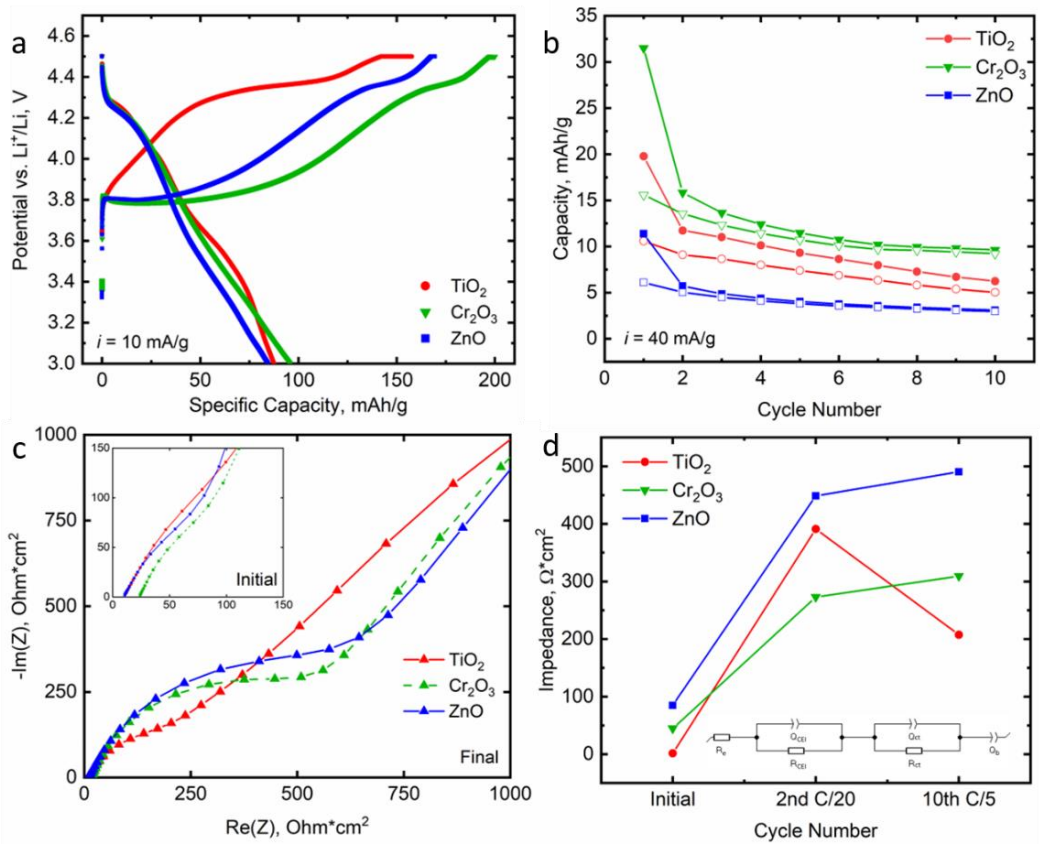

Figure 48. Electrochemical cycling of metal oxide coated NMC622 vs. Li metal at constant current/constant voltage (CC/CV) for a) the first cycle at 10 mA/g (~C/20), b) the specific capacity during 40 mA/g (~C/5) cycles with solid and hollow symbols for charge and discharge capacity, respectively, c) impedance measurements before cycling (inset) and after formation cycles and 40 mA/g cycles, and d) growth of CEI impedance with cycling

After cycling, impedance components were more distinguishable than the sloping profile of the initial impedance and so were fit according to the equivalent circuit model in the inset of Figure 48d corresponding to processes occurring in series in this cell. Resistance by the bulk electrolyte to Li^+ conduction in solution was represented by R_e, with desolvation of Li^+ at the interface and diffusion through the CEI in the high frequency regime (R_{CEI} and Q_{CEI}), charge transfer impedance and double layer capacitance at the NMC surface (R_{ct} and Q_{dl}), and a constant phase element for Li diffusion in the thin film (Q_b).[226]

ZnO-coated samples experienced the greatest impedance rise, from 85 Ohm*cm^2 in the pristine sample to 490 Ohm*cm^2 after cycling. Cr_2O_3 and TiO_2-coated cathodes had lower R_{CEI} values at 309 Ohm*cm^2 and 207 Ohm*cm^2, respectively. The same trend was observed in the impedance data after formation cycles. The evolution of R_{CEI} is plotted in Figure 49d. While Cr_2O_3 and ZnO-coated samples follow the trend of continuous impedance growth with cycling, R_{CEI} for TiO_2-coated samples decreased between formation cycles and the end of cycling at C/5, which has been observed previously for NMC622 cycled to 4.4 V vs. Li/Li^+ and may indicate a suppression of oxidative decomposition of the electrolyte.[182]

The electrodes were extracted from Swagelok cells after 2 cycles at 10 mA/g and 10 cycles at 40 mA/g then transferred under vacuum to the XPS chamber for surface analysis. Thin film electrodes enable a facilitated view of interfacial species in XPS due to the lack of binder and conductive carbon signals. The data for each of the metal oxide-coated samples is included in Figure 49 for both the pristine and cycled electrodes and was deconvoluted into component peaks based on pristine electrodes and Li salts previously observed on our instrument.

NMC622 films without metal oxide coatings are also included at the top in black as a reference. The C1s spectra in Figure 49a highlights four primary peak components which were observed on all samples: aliphatic carbon and C-H bonds at 284.8 eV, C-O at 286.2 eV, O-C-O/C=O at 287.2 eV, and CO_3/O-C=O bonds at 288.9 eV. Each of the pristine metal oxide coated electrodes had a greater at.% of CO_3 type bonds relative to the cycled samples, with the pristine TiO_2 sample (shown in red) having the most at 37 at.% of its C1s signal. This larger proportion of CO_3 was reproducible in the all TiO_2 samples and may be due to carbonate formation from TiO_2 exposed to CO_2 which has been observed previously in photocatalysis studies.[305]

Each electrode experienced an increase in the C-C/C-H and O-C-O peak contributions after cycling, suggesting the formation of polymerized species at the interface due to solvent decomposition. The ZnO-coated samples (shown in blue) had an additional minor C1s contribution by the edge of the Zn(LMM) Auger line, which accounts for the asymmetric peak shape and broad component at ~290.1 eV. The cycled uncoated NMC622 had an increase in the relative at.% of the CO_3 peak, which differed from all of the metal oxide coated samples and suggests the metal oxide coatings suppressed the formation or deposition of carbonate species.

The O1s spectra in Figure 49b supported the observations of the C1s spectra as well as suggested differences in the CEI thickness between samples. In each of the pristine samples, a peak at ~529.8 eV originates from metal oxide bonds which were convoluted between the TiO_2, Cr_2O_3, and ZnO coatings and the NMC622 lattice contributions. This signal was reduced in intensity after cycling, indicating the formation of a CEI layer atop the M-O coatings. The Cr_2O_3-coated sample had the greatest M-O signal reduction at 87%, followed by the TiO_2-coated and ZnO-coated samples at 70%. This indicates that the CEI was thickest for the most acidic surface. The chemistry of the CEI was complex, with LiOR bonds observed at 530.8 eV, CO_3/O-C=O species at 531.5 eV, C-O bonds at 532.5 eV, and $Li_xPO_yF_z$ species at 533.7 eV.

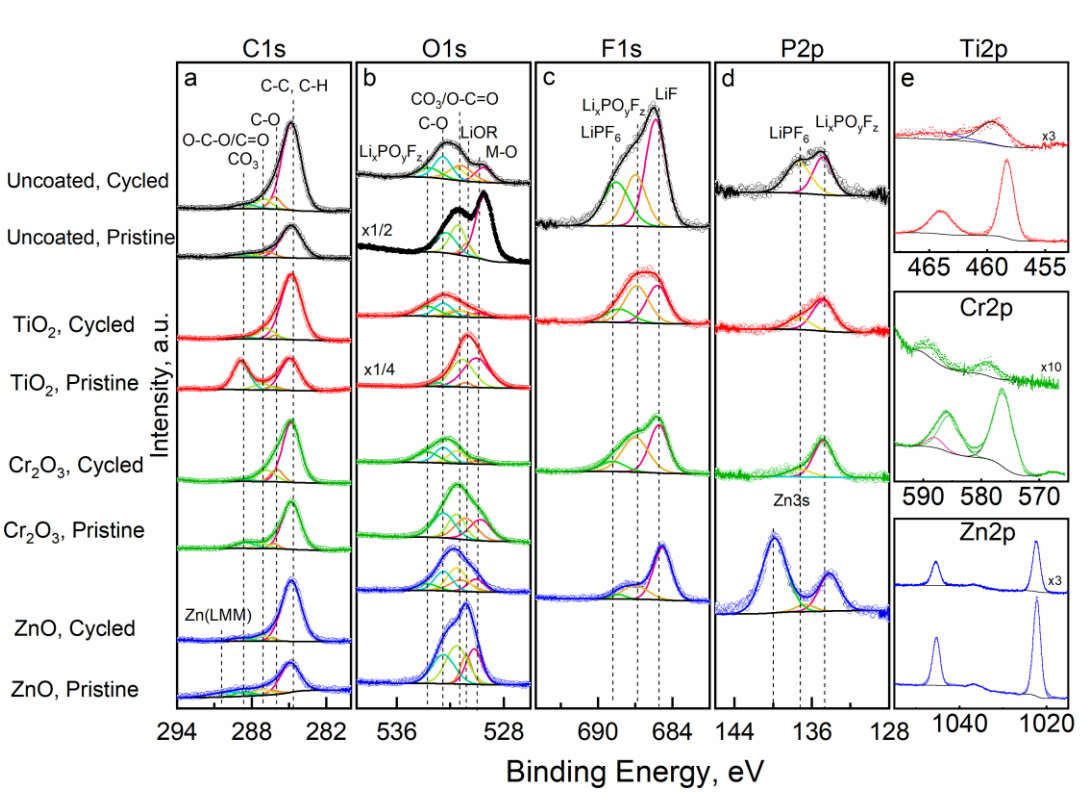

Figure 49. XPS spectra of pristine and cycled metal oxide-coated NMC622 electrodes of a) C1s, b) O1s, c) F1s, d) P2p, and e) Ti2p, Cr2p, and Zn2p with certain spectra multiplied as indicated for clarity and uncoated NMC622 data included in black from Ref.[306]

Only the cycled samples are included in the F1s and P2p spectra of Figure 49c and 4d because the pristine materials had no peaks above the background noise. The species observed in the F1s spectra for each sample necessarily originate from the only fluorinated component of the system: $LiPF_6$, of which residual amounts can be observed at 688.3 eV despite the electrodes being gently rinsed in DMC after extraction. The other contributions in the F1s spectra of each sample were LiF at ~685.1 eV and $Li_xPO_yF_z$ at ~686.9 eV. Cr-F and Ti-F bonds may also contribute at ~685 eV and will be discussed below. The ratio of these species varies between compounds, with a LiF:$Li_xPO_yF_z$ ratio of 1.97, 0.93, 1.09, and 2.72 for the uncoated, TiO_2, Cr_2O_3, and ZnO-coated cathodes, respectively. This difference in surface chemistry supported by the P2p spectra, where the relative amount of $Li_xPO_yF_z$ was similar in each case. This suggests that the amount of LiF detected at the surface was the primary difference in decomposed salt species at the surface. The more basic surface of the ZnO-coated electrode had almost three times more LiF:$Li_xPO_yF_z$ compared to the more acidic samples, suggesting that the more basic surface charge increases LiF formation. The more acidic surfaces may also suppress LiF formation by favoring CrF_3, TiF_4, or $TiOF_2$ formation, as their LiF:$Li_xPO_yF_z$ was about half that of the uncoated NMC and the Cr_2O_3 and TiO_2 samples had a shift in their respective spectra which will be discussed presently.

The metal oxide signals observed in the O1s spectra can be further investigated in the Ti2p, Cr2p, and Zn2p spectra of Figure 49e. In each case the metal oxide signal was attenuated after cycling, indicating the formation of a CEI layer atop the coating. Interestingly, the degree of attenuation is different between samples, with the Cr2p signal almost completely obstructed after cycling, followed by the Ti2p signal. The Zn2p signal retained a higher signal relative to the other metals. This suggests the thinnest CEI on ZnO followed by TiO_2 and Cr_2O_3 with the thickest layer.

This trend of increasing CEI thickness aligns with the surface becoming more acidic. There was also a shift of the $Cr2p^{3/2}$ peak to a higher binding energy (from 576.3 to 578.7 eV), indicating either a transition from Cr^{3+} to Cr^{6+} or bonding with a more electronegative species (i.e. F).[307] The $Ti2p^{3/2}$ peak had a more modest shift from 458.2 to 459.4, which may also indicate the formation of TiF_4 or $TiOF_2$.[308] This reaction of surface metal oxides with electrolyte salt species has previously been observed for Al_2O_3.[296] Interestingly, there was no shift of the Zn2p peaks, indicating that the basic ZnO surface layer does not react to form fluorinated species or further oxidize as was the case for the more acidic surfaces of the TiO_2 and Cr_2O_3-coated samples.

A trend emerges when considering the XPS data alongside the impedance measurements: the cathode with a more basic surface created by the ZnO coating had higher impedance in all cases while having significantly more LiF and a thinner CEI relative to the more acidic samples. This suggests a more compact inorganic CEI induced by the basic surface, either due to increased salt decomposition or reduced solvent decomposition. Additionally, the metal oxide films of the more acidic surfaces reacted with the electrolyte to form fluorinated species or perhaps further oxidize, in the case of Cr_2O_3. This difference in CEI composition correlates with the greater impedance rise and the poorer cycling performance of the more basic ZnO surface and aligns with previous work finding that a thin, fluorinated CEI was preferable for high voltage cycling of NMC622.[306] This trend of relative acidity validates theoretical calculations of C-H bond dissociation of EC on different organic surfaces by Shao-Horn *et al.*[309] This decomposition mechanism was shown to be more energetically favorable than electrophilic or nucleophilic attack and indicated that metal fluorides which have a lower affinity for hydrogen would be preferable for minimizing EC decomposition. There has also been evidence in recent literature that some coatings (e.g. Al_2O_3) outperforming other NMC622 coatings is due to a synergistic reaction of the coating with salt anions to form metal oxyfluorides.[287] $Li_2PO_2F_2$ may also form, and has recently

been identified as an effective electrolyte additive for capacity retention by forming a thin uniform CEI which passivates the cathode against continuous electrolyte decomposition at high voltages,[310, 311] perhaps by forming Li_3PO_4 at the surface.[312] This supports the results described above because there was an increase in the $Li_xPO_yF_z$ signal for the metal oxide coatings which reacted with $LiPF_6$ to form metal fluoride or metal oxyfluoride in the CEI. A study of NMC622 pellets coated with Al_2O_3, TiO_2, or Nb_2O_5 also observed the formation of metal oxyfluoride species. [313] In that work, oxides which formed thicker layers of metal oxyfluorides had greater EC dehydrogenation and lower capacity retention than thinner layers of metal oxyfluorides.[313] This suggests there may be an optimal CEI composition which is rich with metal fluorides or oxyfluorides while remaining sufficiently thin to minimize interfacial impedance.

7.5 Conclusions

Metal oxide films of varying IEPs were deposited on NMC622 thin films to control the initial surface chemical environment and study its effects on CEI formation and evolution. The metal oxidation states determined by XPS confirmed the presence of ZnO, Cr_2O_3, and TiO_2 formed by DC sputtering of metal targets in an O_2/Ar environment. Zeta potential measurements of the coated cathodes found that the samples had increasing acidity in the order: ZnO < TiO_2 < Cr_2O_3 which correlated to differences in cycling performance and CEI composition. The most acidic sample (Cr_2O_3 coating) had the highest initial specific capacity and best capacity retention. The less acidic TiO_2-coated sample had the lowest interfacial impedance after cycling, whereas the most basic sample (ZnO) had the highest impedance at all periods measured. The ZnO-coated sample also had a thinner CEI with a greater LiF concentration than the other samples, indicating that a more basic surface correlates with increased electrolyte salt decomposition but less solvent decomposition and higher impedance overall. The metal oxides of the more acidic samples were oxidized with cycling, possibly forming CrF_3 and TiF_4 or $TiOF_2$, respectively. The efficacy of Al_2O_3 coatings has also been attributed to the formation of AlF_3, suggesting that surface oxide layers which react with the electrolyte salt to form a highly fluorinated passivation layer are desirable. This suggests that the IEP of metal oxide coatings directly impacts electrolyte decomposition in high voltage operation of Ni-rich NMC, with more acidic surfaces preferred for better cycle life and increased cell capacity.

Acknowledgements. This research at the Oak Ridge National Laboratory, managed by UT Battelle, LLC, for the U.S. Department of Energy (DOE) under contract DE-AC05-00OR22725, was sponsored by the Office of Energy Efficiency and Renewable Energy (EERE) Vehicle Technologies Office (VTO) (Deputy Director: David Howell) Applied Battery Research subprogram (Program Manager: Peter Faguy) (N.D.P., C.D., and G.M.V.). A portion (IEP) was sponsored by the Office of Energy Efficiency and Renewable Energy (EERE) Vehicle Technologies Office (VTO) (Deputy Director: David Howell) Silicon Deep Dive subprogram (BLA). N.D.P. thanks Alex Rogers and Katie Burdette for assistance in zeta potential analysis.

8. STRUCTURAL DEGRADATION OF HIGH VOLTAGE NMC IN SOLID STATE BATTERY

This manuscript is in its final review stages with coauthors to be submitted to *American Chemical Society Energy Letters*. This work answers the question of whether Ni-rich NMC cathodes are viable for high voltage solid state batteries. My contribution as the primary author was executing all experiments planned with G. M. V. as well as data analysis and writing the manuscripts. A. S. W. evaporated Li for most of the solid state cells. All authors assisted with data interpretation and editing the manuscript. Supplemental figures have been added to the main text for clarity.

Nathan D. Phillip,[1,2] Andrew S. Westover,[2] Claus Daniel,[1,3] Gabriel M. Veith[2*]*

[1] The Bredesen Center for Interdisciplinary Research and Graduate Education, University of Tennessee, Knoxville, TN, 37996, USA

[2]Chemical Sciences Division, Oak Ridge National Laboratory, Oak Ridge, TN 37831, USA

[3]Energy and Environmental Sciences Directorate, Oak Ridge National Laboratory, Oak Ridge, TN 37831, USA

8.1 Abstract

High voltage Ni-rich $LiNi_xMn_yCo_zO_2$ is an enticing cathode for high energy density solid state batteries. NMC622/Lipon/Li batteries were found to suffer from degradation at high voltage, which was not prevented by a stable solid electrolyte, Lipon. When cycled to 4.5 V *vs.* Li/Li^+ and compared to conventional liquid cells, thin films of NMC622 structurally degraded after the first charge cycle for both configurations and continuously at the cathode/electrolyte interface in cells with liquid carbonate electrolyte. The interfacial resistance of the solid state cells was stable with cycling, suggesting minimal degradation of the NMC622/Lipon interface. This stable cathode/electrolyte interface did not prevent capacity loss as both the solid and liquid cells had similarly low specific discharge capacities during cycling, with the specific charge capacity of solid state cells decreasing from 203 mAh/g to 78 mAh/g after 100 cycles. This indicates that accessing additional Li inventory with high voltage operation of Ni-rich NMC is not enabled by a stable cathode/electrolyte interface alone.

8.2 Introduction

Solid state lithium ion batteries offer the opportunity for higher volumetric energy density and reduced flammability compared to liquid organic electrolyte-based batteries.[98] Ni-rich $LiNi_xMn_yCo_zO_2$ (NMC, where $x + y + z = 1$ and $x > 0.5$) cathodes are considered the next step to achieve higher energy density batteries but it remains an open question whether they are viable for high voltage ($\geq$4.5 V vs. Li/Li^+) solid state batteries. While cycling to such high upper cutoff voltages allows for high energy density (>200 mAh/g) in Ni-rich NMC batteries, it also induces electrolyte decomposition in conventional carbonate electrolytes, possibly due to oxygen evolution from the lattice during structural rearrangement. [13, 276] Solid state electrolytes which are

intrinsically stable in this voltage regime might offer a means to stabilize the system to take full advantage of the material.

Several studies have focused on slurry casting composite electrodes mixed with solid electrolytes such as β-Li_3PS_4, $Li_{6.4}La_3Zr_{1.4}Ta_{0.6}O_{12}$, $Li_{1.5}Al_{0.5}Ti_{1.5}(PO_4)_3$, and $Li_{1.5}Al_{0.5}Ge_{1.5}(PO_4)_3$.[101, 314-317] These works have highlighted the challenges of NMC622 and NMC811 solid state batteries including the formation of an unstable cathode/electrolyte interphase (CEI) layer against β-Li_3PS_4 which caused large first cycle capacity losses (~30%) and a continuous rise in cell impedance.[314] A study of NMC622 slurry cast on an $Li_{6.4}La_3Zr_{1.4}Ta_{0.6}O_{12}$ solid electrolyte pellet with Li_3BO_3 as a sintering agent reported large first cycle capacity losses of 34 – 45% and continuously low coulombic efficiency (55 – 70%) when cycled to 4.2 V vs. Li/Li^+.[317] They attributed these capacity losses to microcrack formation at the interfaces. [317] Others found that a phosphate electrolyte – $Li_{1.5}Al_{0.5}Ti_{1.5}(PO_4)_3$ – had no detrimental side reactions due to higher oxidative stability of the electrolyte, although substantial capacity loss was still observed.[316] The cause of these capacity losses may be due to structural rearrangement at the surface of Ni-rich NMCs, which is exacerbated at higher states of charge (≥4.5 V vs. Li/Li^+ for NMC622).

Previous studies of Ni-rich solid state batteries used composite cathodes comprised of binders and conductive carbon with dual electrolytes to stabilize the interfaces.[101, 315, 316] The complex nature of these composite cathodes make it difficult to isolate materials challenges and interfacial reactions, and can exacerbate the challenges of mechanical damage and contact loss between the active material and solid electrolyte.[317, 318]

These characteristics make it challenging to study the intrinsic behavior of cathode materials, but thin film batteries provide a means to study materials and effects at electrode/electrolyte interfaces with well-defined boundary conditions.[244] Previous work demonstrated NMC622 thin films which were stable up to 4.2 V vs. Li/Li^+.[301] Magnetron sputtering of fully dense, planar electrodes with a solid electrolyte such as lithium phosphorous oxynitride (Lipon) is proven to be stable when operating in high voltage windows such as 3.5 – 5.1 V in a $LiNi_{0.5}Mn_{1.5}O_4$ battery, [100] which allows for isolating cathode properties at high voltages without interference of electrolyte decomposition.

In this work, the first Ni-rich NMC thin film battery with a Lipon electrolyte and Li anode was compared to a conventional liquid cell with thin film electrodes cycled to 4.5 V. The simplified geometry allowed for isolated study of the cathode material which was not stabilized by the solid electrolyte and suffers from structural degradation with the same loss in capacity as the liquid cell. This indicated intrinsic limitations of the NMC622 structure at high states of delithiation which were not remedied by a stable cathode/electrolyte interface.

8.3 Methods

Synthesis. Thin films of $LiNi_{0.6}Mn_{0.2}Co_{0.2}O_2$ (NMC622) were prepared by radio frequency magnetron sputtering of home-built NMC622 targets, detailed in our previous work.[210] Deposition conditions in this study included a base chamber pressure <2 x 10^{-6} Torr with 55.0 sccm high purity Ar gas (Airgas) flow rate providing 6.0 mTorr deposition pressure at 90 W forward power. Following deposition of 1.5 µm NMC622 on a 1 cm^2 area of polished Al_2O_3 substrates coated with 10 nm Co and 250 nm Pt, thin films were annealed at 700ºC for 1 h our under high purity air flow (~0.2 LPM, Airgas) with a ramp rate of 5 ºC/min then stored in an Ar-filled glove box. Lipon films were deposited by RF sputtering of a Li_3PO_4 target (99.95% pure, Kurt J. Lesker) under 20 sccm N_2 at 20 mTorr and 90 W for 1.7 µm. A 3 µm layer of Li metal was deposited on the Lipon layer

using a custom built evaporation chamber. All film thicknesses were estimated using a quartz crystal microbalance to measure deposition rates.

Characterization. X-ray diffraction was conducted on a Scintag XDS 2000 at a standard operating mode of 45 kV and 32 mA with a Cu $K\alpha_1$ monochromated radiation source (λ = 1.5406 Å) across a Θ:2Θ scan range of 10º – 80º. Cycled cells were extracted in an Ar-filled glove box and covered with Kapton tape to prevent air exposure.

Electrochemical Measurements. Solid state cells were sealed in stainless steel vessels in an Ar-filled glove box. Electrochemical cells with liquid electrolyte were assembled in an Ar-filled glove box in coin cells with one wave spring, one stainless steel spacer, and one 1.5 µm NMC622 thin film vs. Li metal (1 cm diameter). Two 1.3 cm diameter separators (Dreamweaver Gold 40) were placed between electrodes and soaked in 300 µL 1.2 M $LiPF_6$ in ethylene carbonate (EC) and ethyl methyl carbonate (EMC) in a 3:7 wt. ratio (Tomiyama). Cells rested at open circuit voltage for 2 hours before being cycled from 2.5 – 4.5 V *vs.* Li/Li^+ in a constant current, constant voltage protocol (CC/CV). The first cycle charge and discharge rates were 3 µA (5 mA/g) whereas subsequent cycles were charged and discharged at 10 µA (16.$\overline{6}$ mA/g). The upper cutoff voltage (4.5 V) was held until the measured current dropped below 1 µA. All cells were tested at least in duplicate.

Electrochemical Impedance Spectroscopy tests were conducted with a potentiostat/galvanostat with frequency response analyzer (BioLogic). Cells were at open circuit voltage after charging to 4.5 V *vs.* Li/Li^+ with a 6 mV applied signal over 10 mHz to 1 MHz for solid state cells and 10 mHz to 20 kHz for cells with liquid electrolyte with an average of 3 measurements per frequency. Impedance measurements were collected before and after the first cycle (± 3 µA) then after every other cycle at ± 10 µA.

8.4 Results & Discussion

Additional Li^+ inventory can be accessed by cycling intercalation cathodes to higher upper cutoff voltages (*i.e.* ≥4.5 V *vs.* Li/Li^+), but this high voltage operation often induces structural degradation and electrolyte decomposition.[50, 209] In the case of Ni-rich NMC, surface structural rearrangement caused by high delithiation may release reactive oxygen species which contribute to electrolyte oxidation and the buildup of degradation products at the cathode surface in carbonate electrolytes.[13, 209, 276] This surface layer can impede Li^+ diffusion into the cathode and phase change can reduce the number of available Li sites for reintercalation, lowering the effective capacity of the cell at high upper cutoff voltages. Lipon is stable at these high voltages[319] and so offers the potential to stabilize the CEI for long term operation.

Figure 50a shows the specific capacity of a NMC622 half cell with liquid electrolyte (1.2 M $LiPF_6$ in EC:EMC 3:7 wt.) cycled to 4.5 V *vs.* Li/Li^+ at a current density of ± 5 mA/g for the first cycle and ± 17 mA/g for the second cycle in a constant current/constant voltage protocol (CC/CV). The first charge specific capacity reached 274 mAh/g which exceeded the theoretical specific capacity of 200 mAh/g; the first cycle discharge was closer to the expected value at 193 mAh/g. This difference between theoretical and measured capacity as well as the irreversible capacity loss between the first charge and discharge suggest undesirable side reactions and structural degradation may be involved. The sloping plateau around 3.6 V is expected for the Ni^{2+}/Ni^{4+} redox couple, but the plateau at ~4.4 V might correspond to side reactions induced by structural rearrangement of the cathode releasing reactive oxygen species.[209] This latter plateau appeared to a lesser extent on the first discharge curve at ~4.3 V, seen in the differential capacity plot in Figure 50c. This suggests the reaction was partially reversible and

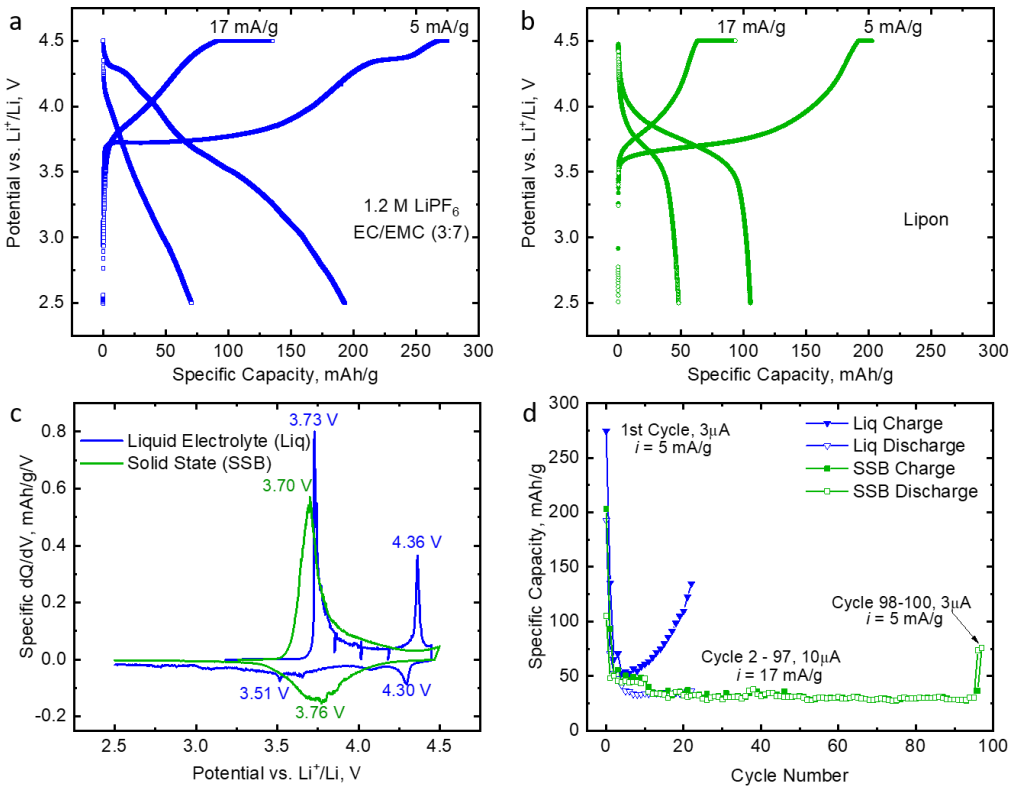

Figure 50. Specific capacity of a) liquid carbonate electrolyte cell and b) solid state cell with a constant current/constant voltage cycling protocol at ±5 mA/g (~C/40) and ±17 mA/g (~C/12) current densities for the first and second cycles, respectively with c) differential capacity for the liquid and solid cells at 5 mA/g and d) extended cycling at 17 mA/g until cycle 98 where the current density was returned to 5 mA/g. All cells were cycled in duplicate.

indicated a phase change and may be due to partial oxygen redox at high states of charge.[50] This plateau was not observed on the first cycle at 17 mA/g nor on subsequent cycles, which means that this oxygen activity induced an irreversible change in the cathode material which might explain the observed capacity loss and will be discussed below with the XRD data.

The oxygen redox plateau was not present for the solid state cells. The first and second cycles of a solid state NMC622/Lipon/Li cell are shown in Figure 50b at the same current densities, voltage window, and CC/CV protocol as the liquid electrolyte cell. The voltage profile in this case was in better agreement with literature, having a first cycle specific capacity of 203 mAh/g (81.3 μAh/(cm^2 *μm)) and one sloping Ni^{2+}/Ni^{4+} redox plateau at ~3.6 V. A 48% capacity drop between the first charge and discharge cycle indicated irreversible structural changes occurred during the first charge cycle which will be investigated with XRD below. This loss of available lithium sites for reintercalation into the NMC622 cathode was similar to the 30% capacity loss after the first charge cycle in the liquid cell. The $Ni^{2+/4+}$ redox plateau can be seen in Figure 50c as a single sharp peak for the solid state cell at 3.7 V on the charge cycle and 3.8 V on discharge. The shape of the solid state cell voltage profile was preserved at the higher current rate of 17 mA/g, however the suppressed Ni redox plateau lead to a low second cycle specific charge capacity of 93 mAh/g.

Interestingly, the specific discharge capacity of the liquid cell and solid cell were almost identical during the extended cycling experiment shown in Figure 50d at 34 and 35 mAh/g at 17 mA/g, respectively, on cycle 10. This indicated that the capacity loss mechanism was the same in both cells and therefore independent of electrolyte composition and was an intrinsic limitation of the NMC622 cathode itself. The steep capacity loss of 54% between charge cycles of the solid state cell stabilized to an average coulombic efficiency of 97% after cycle 2. While the specific charge capacity of the solid state cell was 30.6 mAh/g at the 97th cycle, the coulombic efficiency improved to 99.2%. This minimal capacity loss during extended cycling means that following the initial structural degradation, little electrolyte decomposition took place, which was expected for Lipon at high voltages.[100] Some of this capacity was rate limited, as the specific charge capacity in the 98th cycle increased to 76.0 mAh/g (30.4 μAh/(cm^2 *μm)) at 3 μA. This was due to the relatively thick layer of Lipon (1.7 μm) impeding Li^+ transport. The cycling data of the solid state cells indicated that the majority of the capacity was lost in the first cycle but stabilized due to no electrolyte decomposition.

Conversely, the specific charge capacity of the liquid electrolyte cell first decreased before increasing steeply due to continuous electrolyte consumption. The specific charge capacity rose starting at cycle 9 while the discharge capacity remained around 33 mAh/g. This low coulombic efficiency of the liquid cell indicated an irreversible reaction occurred during the charge cycle which increased until the liquid cell was unable to reach 4.5 V at the same charge rate (after cycle 22, as seen in Figure 51). This suggested an unstable CEI which continuously consumed the liquid electrolyte until cell failure and will be discussed with AC impedance data below (see Figure 52).

The evolution of the liquid electrolyte cells and solid state cells was investigated using AC impedance spectroscopy. Figure 53a shows EIS data of a liquid cell from the uncycled state through the last cycle before cell failure. Following bulk electrolyte resistance (R_e) at the highest frequency, a depressed semicircle in the high frequency regime is assigned to the CEI impedance (R_{CEI}) and capacitance (Q_{CEI}), charge transfer resistance (R_{ct}), double layer capacitance (Q_{dl}) and a low frequency linear component corresponds to a finite diffusion constant phase element (Q_b) as shown in the equivalent circuit model of Figure 53a.

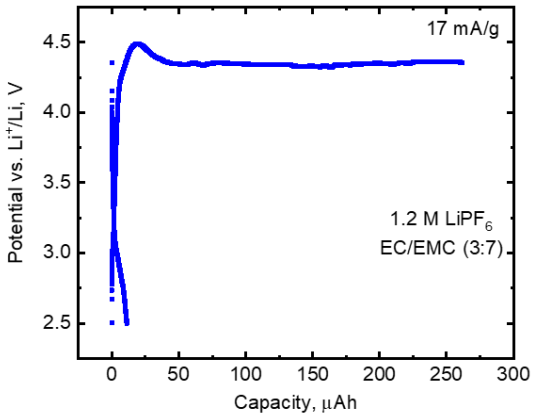

Figure 51. Charge and discharge profile of liquid cell cycle 23 at ± 17 mA/g

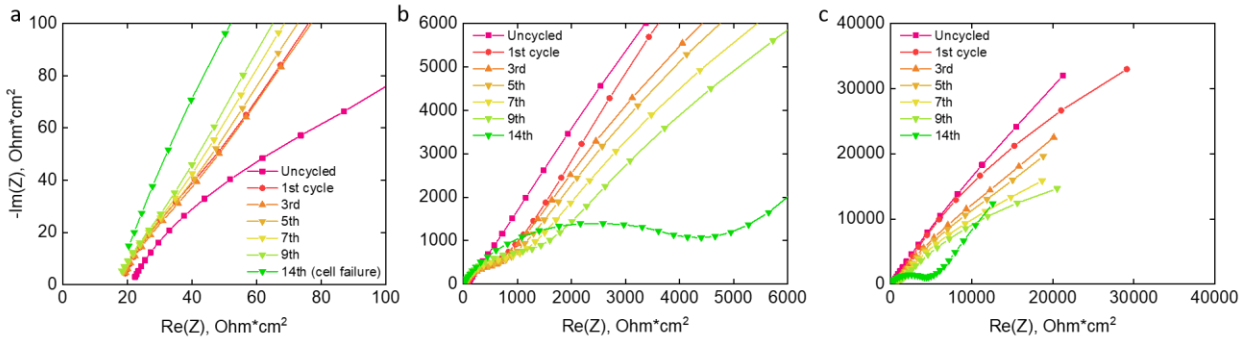

Figure 52. AC impedance data of liquid electrolyte cell for a) high frequency, b) medium frequency, and c) low frequency from uncycled through cell failure during cycle 14

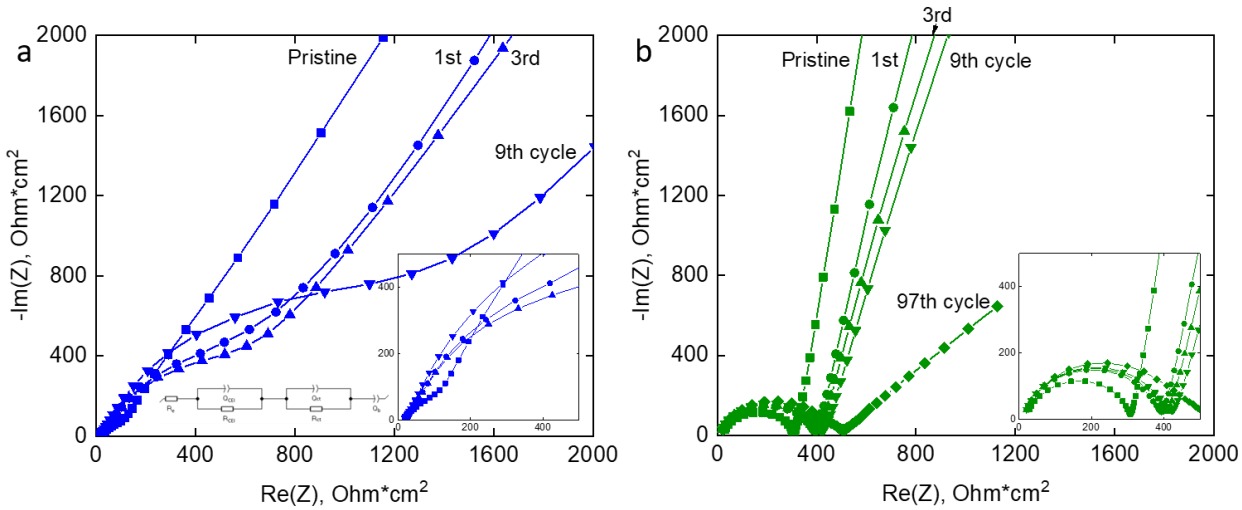

Figure 53. AC impedance of uncycled and cycled a) liquid carbonate electrolyte cell and b) solid state cell with insets showing the high frequency regimes for each sample and the equivalent circuit model used

While some examples in literature separately quantify R_{ct} and R_{CEI}, in practice these effects are challenging to quantitatively decouple and so are reported as a single value of interfacial impedance here. The interfacial impedance of the liquid cell increased from 251 Ohm*cm^2 to 1037 Ohm*cm^2 after the first cycle at 5 mA/g and gradually increased to 2019 Ohm*cm^2 after 8 cycles at 17 mA/g. This 9th cycle correlates to the increasing first cycle specific charge capacity seen in Figure 50c. This value continued to grow with this increasing capacity until it reached ~5000 Ohm*cm^2 right before cell failure (Figure 52). This continuous buildup of charge transfer resistance coupled with the increasing charge capacity with low discharge capacity observed in Figure 50d suggests continual growth of the CEI layer with cycling in the liquid electrolyte. This CEI is comprised of inorganic species from salt decomposition (e.g. $Li_xPO_yF_z$, LiF) and organic species from solvent decomposition (e.g. polycarbonates, alkyl carbonates), as detected by XPS previously.[306]

By contrast, the impedance data for a solid state cell remained relatively stable over the same cycles as the liquid cell, as shown in Figure 53b. The interfacial resistance in the case of the solid state cell is a convolution of the resistance of the solid electrolyte and the electrolyte/electrode interfaces, with typical values for Lipon being 100 – 500 Ohm*cm^2 in $LiCoO_2$ cells.[244] In this case, a high frequency semicircle corresponded to Lipon and the Lipon/NMC622 interfacial resistance and capacitance. This semicircle was more well defined than the liquid cell – reaching the x-axis before transitioning into an ~80^o diffusion tail – which is characteristic of a charge transfer limited process.[320] The growth of the total resistance was much less severe than the liquid cell, increasing modestly from 307 Ohm*cm^2 for the pristine cell to 476 Ohm*cm^2 at cycle 97. A magnified view of the high frequency semicircle is shown in the inset of Figure 53b and additional impedance data for cycles 10 – 97 are included in Figure 54. These results, coupled with the increasing coulombic efficiency with cycling, suggest that the NMC622/Lipon interface is more stable during high voltages cycling than the liquid electrolyte after structural failure.

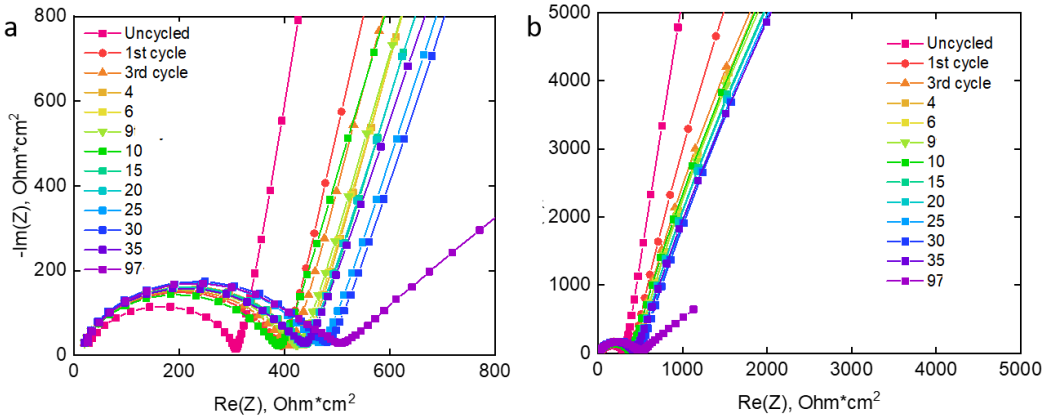

Figure 54. AC impedance data of solid state battery for a) high frequency and b) medium frequency and low frequency region from uncycled through cycle 97 when cell was removed for XRD

The crystal structure of the NMC622 solid state films decayed dramatically after cycling, as seen in the XRD spectra of Figure 55. The pristine 1.5 μm NMC622 film (in black) had distinct diffraction peaks for the Pt and Co-coated Al_2O_3 substrates, the spectrum of which is included in Figure 56. Due to the limited amount of cathode material and limited instrument resolution, only the (003), (101), and (104) reflections were visible for the $R\bar{3}m$ NMC structure for the pristine sample. After cycling, the cells were extracted in an Ar-filled glove box and covered with Kapton tape to prevent air exposure. The Kapton tape introduced a background signal which is highlighted in Figure 55 and can be seen in the XRD spectrum of a bare substrate coated with Kapton tape in Figure 56. The (003) peak intensity is reduced after cycling for both the liquid and solid cells, although it is difficult to distinguish unambiguously due to the background signal from the Kapton. The (101) and (104) peaks are almost completely lost for the liquid cells whereas the solid cells retained their diffraction peaks after cycling. This is particularly interesting when considering the (104) plane, as it was found to be key to enabling good performance of thin films of NMC622 due to preferred orientation of the (104) plane allowing for facile Li diffusion into the bulk compared to the (003) plane which inhibits intercalation.[301] The degradation of these favored (104) grains explains the massive capacity loss observed in these films due to reordering into an amorphous or disordered rock salt phase, as suggested in literature.[321] The greater capacity loss in the liquid cells compared to solid cells was caused by the exacerbated loss of (104) grains. A conventional interpretation in literature is that this structural degradation is solely caused by Ni^{2+} ions migrating from octahedral 3a sites of the $R\bar{3}m$ structure into Li^+ octahedral 3b sites at high states of delithiation due to similar ionic radii (0.69 and 0.76 Å, respectively).[27] These data support previous works' observations capacity loss due to structural rearrangement, but suggests an additional cause beyond the conventional cation migration mechanism for this degradation, and that is related to the oxygen redox catalyzed by the carbonate electrolyte observed here.

When considering the XRD data, electrochemistry data, and evidence in literature for oxygen evolution from Ni-rich NMC interfaces,[265] there is evidently an irreversible mechanism for Ni-rich NMC structural degradation tied to electrolyte composition which was not previously identified in literature. The proposed mechanism is that EC bonds with cathode surface oxygen atoms of NMC622 as part of its dissociation reaction. This reaction was found to have lower activation energy for edge on planes of NMC333 and $LiCoO_2$ with EC[193] such as the preferential orientation of the (104) planes of the thin films studied here. This orientation lowers the activation energy for this reaction because lattice oxygen atoms are exposed at the surface rather than predominantly transition metals or Li as would be the case for (003) planes lying parallel to the substrate.[193] Oxygen vacancies then in the crystal structure during EC decomposition which has can form disordered rock salt and amorphous structures.[27] The EC-driven oxygen vacancy formation explains why the (104) plane degradation is worse in the liquid electrolyte than the solid electrolyte and why the irreversible oxygen redox plateau is observed only for liquid cells.

The degraded crystal structure is responsible for the massive capacity loss on the first cycle for both the solid and liquid cells. This accounts for the similar specific discharge capacities observed in both configurations, as available Li storage sites were lost from the host NMC structure in both cases. This also highlights the inherent limitation of NMC622 cycled to a high upper cutoff voltage in solid state cells and indicates that the system is not viable for high energy density solid state cells. Additionally, the use of a stable high voltage solid electrolyte did not significantly improve capacity retention, which is contrary to a prevailing hypothesis in literature that stabilizing the CEI in liquid carbonate cells will enable good performance of Ni-rich NMC at high voltage. The solid state cells did have less apparent structural degradation than the liquid cells, based on

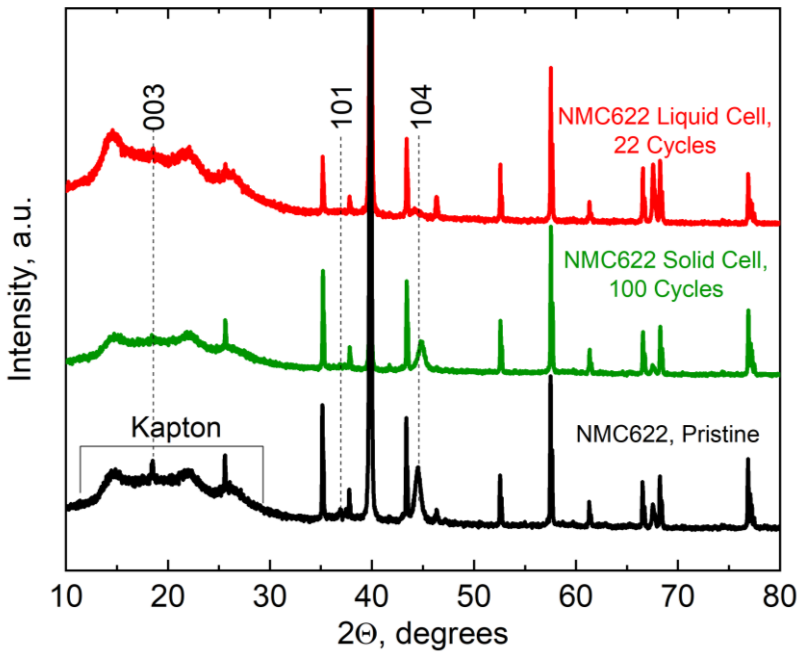

Figure 55. XRD of pristine 1.5 µm solid state NMC622 electrode and after 96 cycles at 10 mA/g. The cycled cell had a 1.7 µm layer of Lipon, 3 µm of Li, and Kapton tape on top of the NMC622. The pristine data was normalized to the Al_2O_3 substrate peak at 57.6º for comparison.

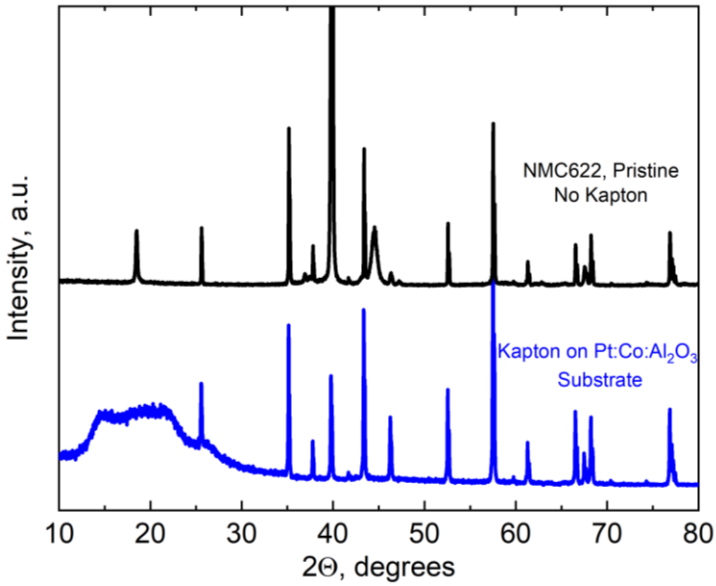

Figure 56. XRD of pristine 1.5 µm solid state NMC622 electrode without Kapton covering and Pt:Co:Al2O3 substrate with Kapton covering.

XRD data. When considered alongside the cycling data, this correlates with the oxygen redox plateau present only during the first cycle of the liquid cells. The presence of the high voltage electrolyte effectively inhibited this behavior to produce a voltage profile which more closely aligns with literature on composite NMC622 electrodes. This also helps explain the disagreement in literature with regards to whether reactive oxygen species are present at the NMC surface during high voltage cycling. For example, Gasteiger's group hypothesized that singlet oxygen species evolve from the NMC lattice at high states of charge when the structure decomposes, driving electrolyte decomposition through chemical oxidation of ethylene carbonate.[13] While the results of this work cannot ascribe the oxygen redox to singlet oxygen formation, they do support the oxygen activity driven by high voltage operation. The partially reversible oxygen redox which is only observed on the first cycle might be explained by consumption of those active oxygen species by reaction with the electrolyte, contributing to the observed impedance rise and lower capacity due to CEI growth and structural degradation, respectively.

8.5 Conclusions

Despite the interest in developing high voltage Ni-rich NMC solid state cells with high energy density, intrinsic limitations of the cathode were observed in this study. Both the solid state cells and conventional liquid carbonate electrolyte cells exhibited severe capacity loss after the first charge cycle to 4.5 V *vs.* Li/Li^+ due to structural failure. The liquid cell continuously consumed electrolyte until cell failure while the solid state cell remained stable, but they had nearly identical discharge capacities throughout those cycles. The thin film system used here resolves the ambiguity of studying composite electrodes and demonstrates that the initial capacity loss of NMC622 is decoupled from the cathode electrolyte interface, as both the continuously reacting interface in the liquid cell and the stable interface in the solid cell had the same discharge capacities. This bulk structural degradation was not prevented by a stable CEI from a high voltage electrolyte (Lipon), so high voltage operation of Ni-rich NMC cathodes might only be achieved by modifying the bulk structure.

Acknowledgements. This research at the Oak Ridge National Laboratory, managed by UT Battelle, LLC, for the U.S. Department of Energy (DOE) under contract DE-AC05-00OR22725, was sponsored by the Office of Energy Efficiency and Renewable Energy (EERE) Vehicle Technologies Office (VTO) (Deputy Director: David Howell) Applied Battery Research subprogram (Program Manager: Peter Faguy) (N.D.P., C.D., and G.M.V.). Funding for A.S.W. was provided by ARPA-E Award No. DE-AR0000775.

9. CONCLUSIONS

Ever-increasing demand for improvements in battery performance has spurred the search for novel materials and pushing known materials to their limits. Cathode materials in lithium ion batteries are often considered a bottleneck for increasing energy density so promising classes of materials like Ni-rich NMC have been an intense focus of the research community.[322] Stabilizing the interface of this material at high voltage remains a challenge due to a limited understanding of the cathode/electrolyte interface (CEI).[13] In this work, fundamental questions of the CEI were addressed such as: how does the presence of binders at the interface influence electrolyte decomposition and CEI formation? Why do some metal oxide coatings prevent electrolyte decomposition and capacity fading better than others? And how might replacing the typical liquid carbonate electrolyte with a solid electrolyte stable at high voltages prevent the degradation of NMC622?

To isolate these questions, thin films of NMC622 were developed here and used as a tool to model different interfacial environments because surface phenomena are challenging to study in composite electrodes due to attenuation of XPS signals in Figure 57, for example. By modifying the surface with binders and metal oxides of varying acidity, it was determined that a CEI rich with simple metal fluorides (LiF) is desirable for improved capacity retention (Figure 58a). This is supported by literature data for composite NMC622 cells which found that LiF-rich interfaces generated by a highly concentrated electrolyte (10 M LiFSI in EC/DMC) had improved cyclability and was attributed to the dense, fluorine-rich interface preventing solvent decomposition.[323] A thin uniform coating with a fluorinated binder (*i.e.* PVDF) proved to have the thinnest layer of surface decomposition products (~2 nm) and highest capacity retention (20% greater than the baseline). This is relatable to the limited literature on the subject, such as comparable work of composite $LiNi_{0.5}Mn_{1.5}O_4$ (LNMO) spinel electrodes prepared with PVDF or LiPAA.[217] In that study and the one discussed in Chapter 6, uniform binder coverage was found to improve electrochemical performance compared to sparse binder coverage. This suggests that uniform binder coatings might suppress oxidative electrolyte decomposition which will be discussed below for NMC622. A notable difference though is the PVDF-LNMO electrodes were outperformed by the LiPAA-LNMO electrodes in their study,[217] which is the opposite trend of the study discussed in Chapter 6. This is likely due to the different degradation mechanism of NMC622 compared to LNMO: the crystal structure of NMC622 is shown here and in previous works[12, 209] to rearrange to disordered rock salt above ~4.4 V (discussed below) whereas LNMO is proven to be stable up to 5.1 V, but both cathode materials suffer from CEI buildup due to electrolyte decomposition which was suppressed by thin binder coatings.[100]

This work also validated a physical model by Battaglia *et al.*[324] which posited active material particles and conductive carbon additives in composite electrodes compete to form chemically bound or physically adsorbed layers of polymers on their surfaces from the limited amount of binder content in the composite. They developed this hypothesis as a possible reason for the significant variation in composite electrode performance dependent on slight adjustment of the conductive carbon and binder in composites (5 – 10 wt.%).[324]

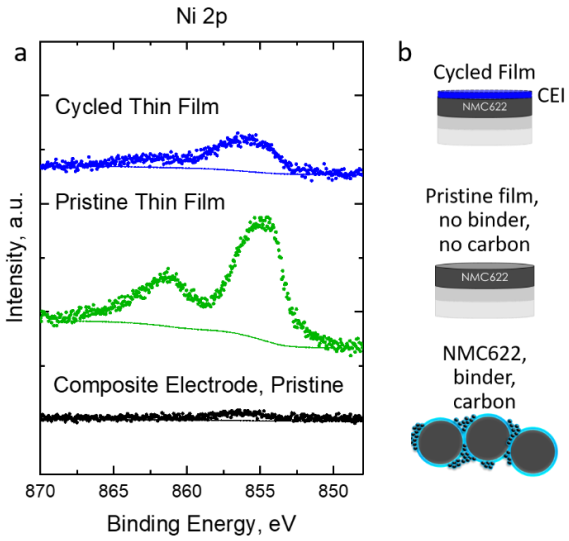

Figure 57. a) XPS signal is less attenuated for solid thin films compared to composite electrodes, (b) schematically depicted

This work supports the hypothesis that an optimal electrode has minimal "free binder" – that is, binder agglomerates which are not bound to the cathode surface in a thin (1 – 5 nm) layer. For each of the binder compositions studied here, the initial specific charge capacity was improved for the thin binder coating compared to the binder agglomerate case. This composite electrode optimization parameter was examined further here by studying the surface chemistry of each case to find that thin binder coatings – particularly for PVDF, as seen in Figure 58a – improved cell performance by suppressing ethylene carbonate (EC) decomposition to form a LiF-rich CEI from $LiPF_6$ salt decomposition. This mechanism may be due to fluorine groups raising the activation energy for EC decomposition by a C-O bond breaking (ring opening reaction) on cathode surfaces, as depicted in transition state 2 (TS2) of Figure 59 for $Li_{0.5}CoO_2$.[325] Modeling work of this reaction validates this hypothesis, because NMC surfaces modified with fluorine groups raised the energy barrier from 17 meV for the uncoated material to 490 meV.[193] This might also explain why CMC and LiPAA coatings were not as effective at suppressing electrolyte decomposition as PVDF, because -OH terminating groups raised the activation energy only modestly to 150 meV.[193] Therefore the CMC and LiPAA coatings presented less of an energetic barrier to EC decomposition than the PVDF coatings, as evidenced by the increased CEI thickness which was richer in organic products of solvent decomposition. These conclusions indicate that composite cathode binder composition and coverage can influence the CEI and processing conditions should be designed for uniform coverage of binder on active material particles.

While inorganic coatings such as SiO_2,[47] TiO_2,[182, 313] Al_2O_3,[287, 313, 326, 327] Nb_2O_5,[313] and $LiCoPO_4$[328] on NMC622 have recently been shown to improve electrochemical performance, limited fundamental work has been done on why certain coatings improve performance more than others. This topic was explored here through different surface acidities generated by metal oxide coatings and their subsequent reactions with the electrolyte forming different CEI compositions.

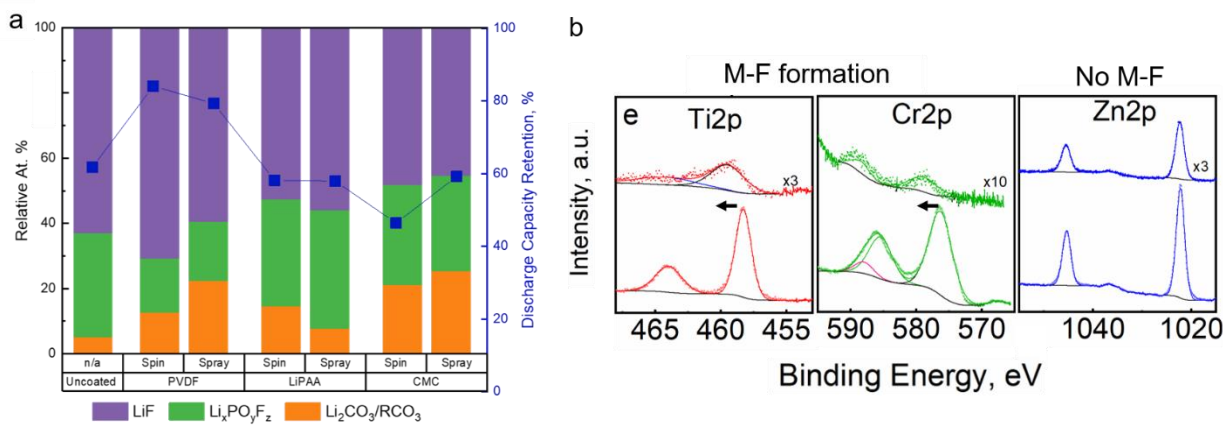

Figure 58. CEI compositions measured by XPS where a) PVDF-coated cathodes had LiF-rich surfaces and b) acidic metal oxide surfaces formed metal fluoride species after cycling but basic ZnO did not. XPS and specific capacity trends were verified in duplicate samples.

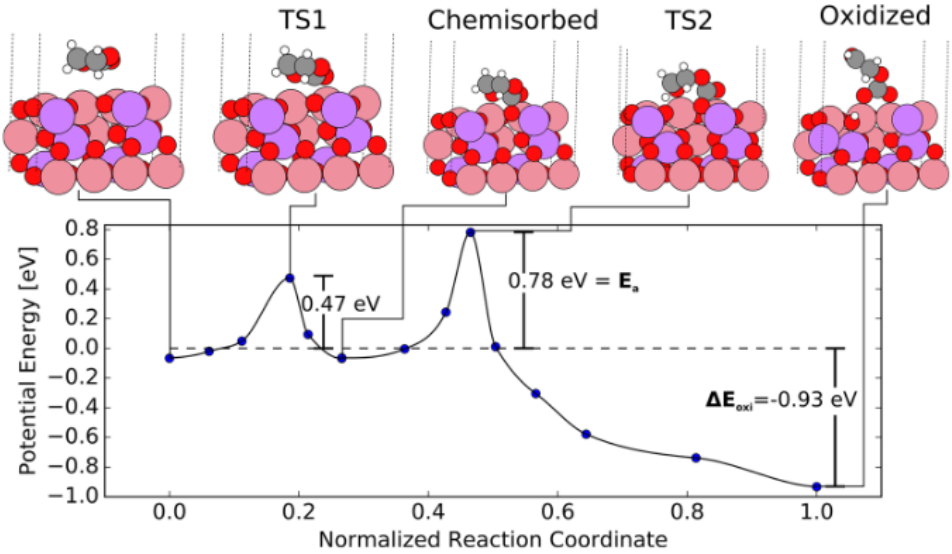

Figure 59. Schematic of EC oxidation on $Li_{0.5}CoO_2$ with potential energy diagram with EC chemisorbing by nucleophilic attack to form a $C_{EC} - O_{surface}$ bond before transferring H in the transition state 2 (TS2) ring opening reaction which forms an oxygen vacancy in the surface. Reproduced with permission from Ref.[325]

The more acidic surfaces generated by the TiO_2 and Cr_2O_3 coatings reacted with the electrolyte salt to form metal-fluoride surfaces, as seen in Figure 58b, whereas the more basic ZnO surface did not. This finding based on relative acidity validates the trends calculated in recent work by Shao-Horn *et al*.[309] studying the energetics of C-H bond dissociation of EC (occurring before the C-O cleavage of ring opening in Figure 59) on different inorganic surfaces. This decomposition mechanism was shown to be more energetically favorable than electrophilic attack and was proposed to be a route for minimizing electrolyte decomposition.[240] Their calculations suggested that metal fluorides which have a lower affinity for hydrogen (and thus higher C-H bond breaking activation energy for the TS2 step of Figure 59) would be preferable for minimizing EC decomposition. The surface acidity study of Chapter 7 corroborates this theory because the metal oxide surfaces which reacted to form metal fluorides suppressed continual EC decomposition more than the basic ZnO surface, as seen in Figure 58b. This relates back to the binder work where the LiF-rich CEI also prevented continual electrolyte decomposition. There has also been evidence in recent literature that a reason for Al_2O_3 outperforming other NMC622 coatings might be a synergistic reaction with $PF6^-$ to form metal oxyfluorides and $Li_2PO_2F_2$.[287] $Li_2PO_2F_2$ has recently been shown to be a beneficial electrolyte additive for capacity retention at high voltages by forming a thin uniform CEI which passivates the cathode against continuous electrolyte decomposition,[310, 311] possibly by forming Li_3PO_4 at the surface.[312] This supports the conclusions from Chapter 7 because there was an increase in the $Li_xPO_yF_z$ signal measured by XPS for the metal oxide coatings which reacted with $LiPF_6$ to form metal fluoride or metal oxyfluoride in the CEI. Another XPS study of NMC622 pellets coated with Al_2O_3, TiO_2, or Nb_2O_5 observed the formation of metal oxyfluoride species and found that oxides with thicker layers of metal oxyfluorides had less capacity retention and greater EC dehydrogenation than those with thinner layers.[313] This suggests there may be an optimal CEI configuration which is rich with metal fluorides or oxyfluorides but sufficiently thin to minimize interfacial impedance.

Additionally, the relative acidity was due to the metal oxide coatings have different pK_a values, where the surfaces with higher Brønsted acidity correlated with worse capacity retention. This may explain the exacerbated interfacial degradation observed in the study by supplying protons (from increased EC C-H dissociation) to drive the formation of HF from the dissociated $LiPF_6$ salt, which has been suggested for degradation of Co-OH groups on $LiCoO_2$ by others.[329] This is contrary to the common assumption in literature that the only source of protons for HF formation is residual water in the electrolyte ($PF_5^- + H_2O \rightarrow 2\ HF + POF_3$).

These metal fluoride rich interfaces improved specific capacity and capacity retention by reducing interfacial impedance rise relative to untreated interfaces. As discussed above, metal fluoride rich interfaces have lower affinity for EC dissociation and so suppress continuous CEI buildup from EC decomposition products and prevent $LiPF_6$ decomposition into HF by minimizing protons available at the interface. PVDF-coated cathodes had almost an order of magnitude lower interfacial impedance after cycling than uncoated NMC and all other polymer coatings, as seen in Figure 60a. Similarly, the most acidic surface generated by Cr_2O_3 had lower initial impedance and less impedance rise during cycling compared to the more basic ZnO surface, seen in Figure 60b. While both metal oxide coatings reduced interfacial impedance relative to the uncoated baseline after cycling – as typically seen for extended cycling of metal oxide coatings in literature[182] – the more acidic surface exhibited less impedance rise with cycling due to the formation of M-F species which suppressed EC decomposition and subsequent CEI buildup from decomposition precipitates. In contrast, interfacial impedance rise was almost completely prevented in solid state cells seen in the EIS data of Figure 60z. In the case of the solid state cells, the dominant component

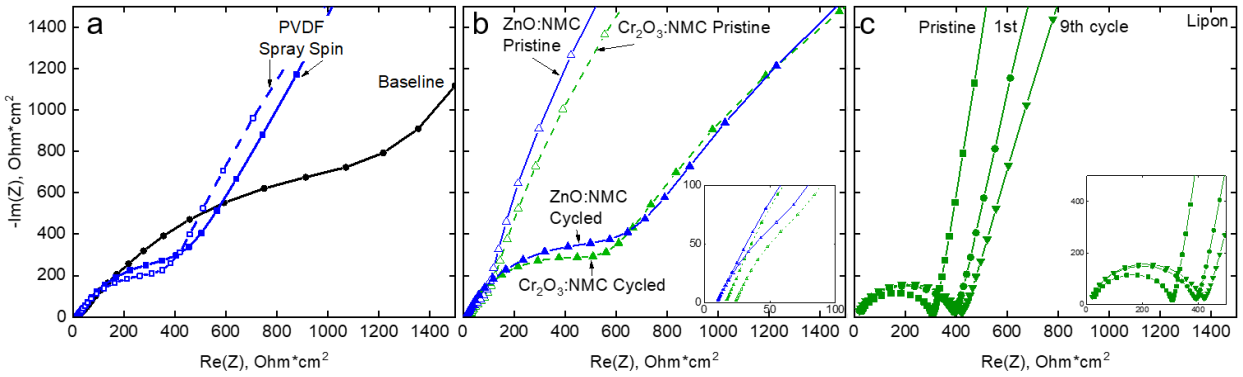

Figure 60. Interfaces with simple metal fluorides demonstrated a) lower interfacial resistance for PVDF-coated samples and b) acidic surfaces whereas c) a stable high voltage electrolyte had the lowest interfacial impedance and minimal growth with cycling. Trends were confirmed with replicate cells.

of impedance was due to the 1.7 µm Lipon electrolyte which remained stable due to minimal degradation unlike the continuous CEI buildup of the liquid cells. This indicates that interfacial degradation can be suppressed by binder and metal oxide coatings which drive the formation of metal fluoride rich interfaces, but a stable high voltage electrolyte avoids the problem altogether. There has been evidence in literature that cathode particles coated with thin solid electrolytes with bulk liquid electrolytes can improve capacity retention,[330] so a thin Lipon coating on cathode particles in a liquid electrolyte may offer a pathway toward stabilizing high voltage operation of NMC622 in full cells.

The role of the solid state electrolyte in stabilizing high voltage NMC622 is twofold. First, the intrinsic electrochemical stability of Lipon removes the challenge of continuous CEI growth and associated interfacial impedance rise seen above in Figure 60. The second effect becomes apparent when considering the first cycle charge and discharge profiles from each study in Figure 61. The oxygen redox plateau detected at 4.3 – 4.4 V *vs.* Li/Li^+ for the uncoated NMC film in Figure 61a was ~42 mAh/g of the capacity is suppressed by the binder coatings of Figure 61b to ~17 mAh/g and less so by the metal oxide coatings in Figure 61c (25 – 26 mAh/g). This suggests that modification of the interface between the cathode and liquid electrolyte can govern this additional redox plateau. This is further evidenced by the fact that the plateau disappears completely for the solid state electrolyte, which also has more stable redox behavior for the Ni^{2+}/Ni^{3+} redox couple at ~3.6 V, as seen in Figure 61d.

From these data it is clear that the presence of liquid carbonate electrolyte is a driving force for NMC622 decomposition at high voltages. The additional oxygen redox activity was not observed in the solid state cells, which also experienced less structural degradation as seen in Figure 62 where the diffraction peaks of the NMC layered structure were almost lost for the liquid cells whereas the solid state cells retained their diffraction peaks after cycling. This is especially true for the (104) plane, which was found to be the key enabling orientation for the thin film synthesis study of Chapter 5: good electrochemical performance was only achieved in thin films which had a texturing effect favoring the (104) orientation because the Li planes of the crystal structure are nearly orthogonal to the substrate in that case, which allows for facile diffusion into

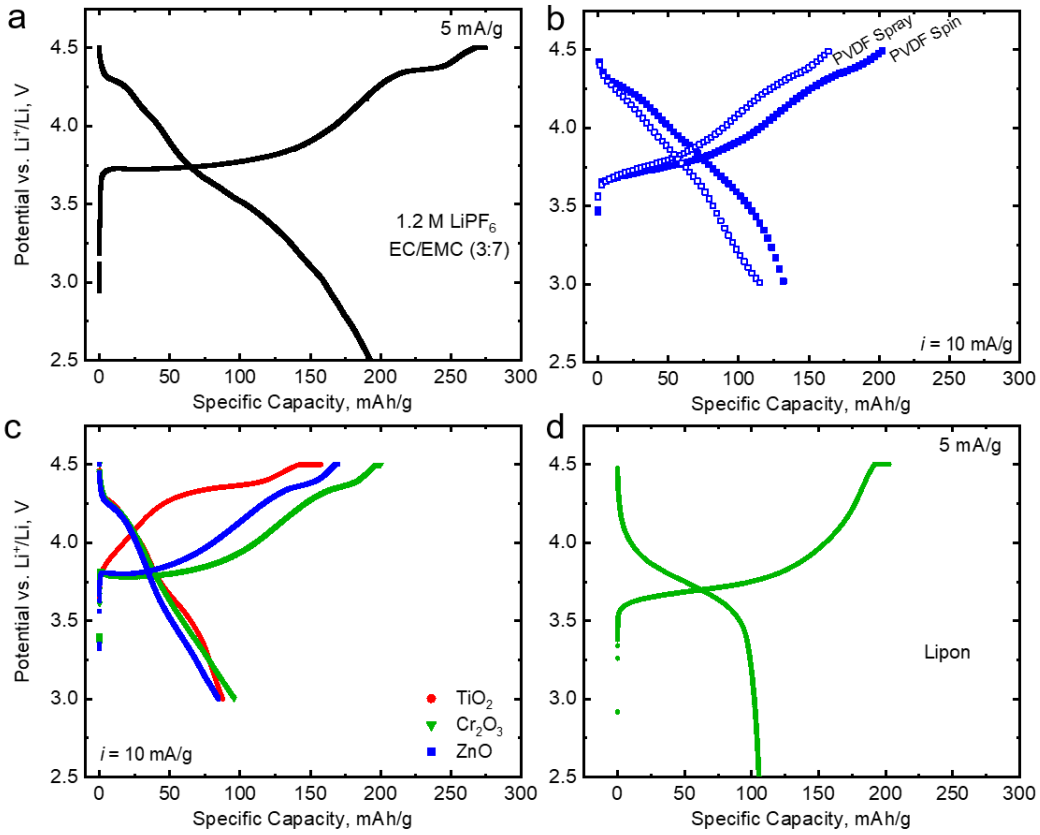

Figure 61. An oxygen redox plateau was detected at ~4.4 V vs. Li/Li$^+$ for a) uncoated NMC622 films cycled at 5 mA/g (C/40), which was suppressed in b) binder-coated samples cycled at 10 mA/g (C/20), and c) metal oxide coatings had an oxygen redox plateau of similar magnitude whereas d) solid state batteries with a Lipon electrolyte had no 4.4 V plateau. All data was reproduced in duplicate.

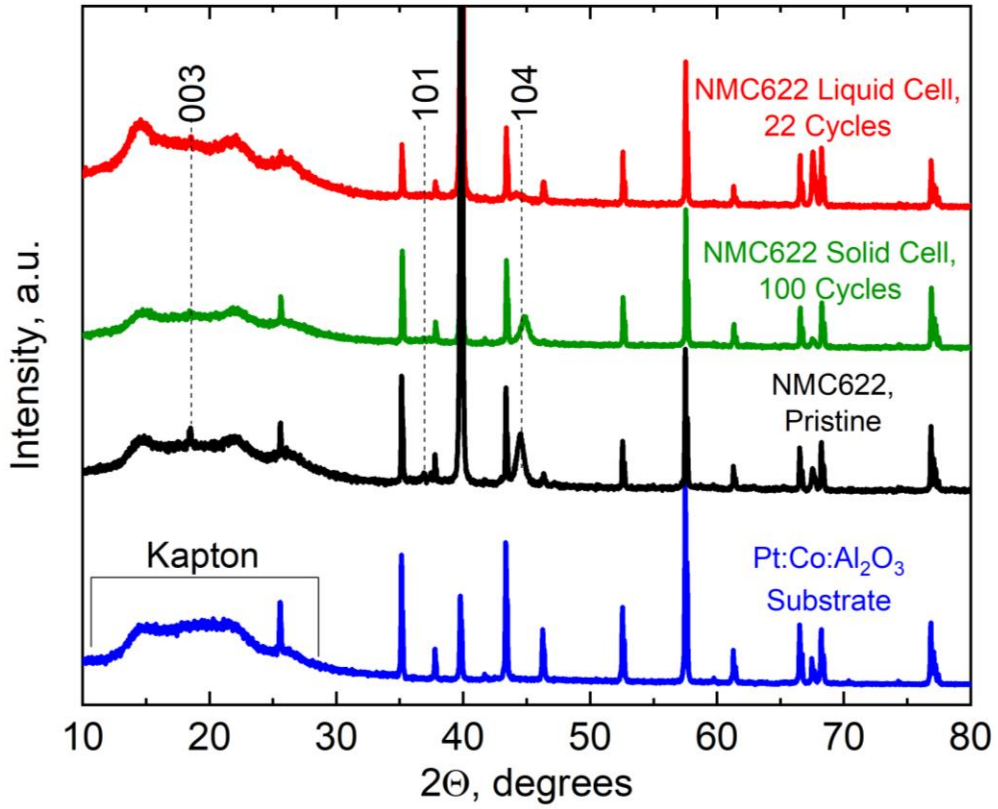

Figure 62. XRD of pristine and cycled NMC622 cathodes extracted from liquid carbonate electrolyte or solid state cells. All samples were coated with Kapton tape to prevent reaction with atmosphere during data acquisition.

the lattice compared to the Li intercalation inhibited by (003) texturing. This phenomenon explains the massive capacity loss associated with the observed structural degradation because the favorable (104)-oriented grains reorder into an amorphous or disordered rock salt phase when cycling to high voltages, which has been suggested in literature.[321]

The greater capacity loss of the liquid cells compared to the solid state cells was caused by the exacerbated loss of these (104) grains, seen in the XRD data. This capacity loss is particularly apparent in the thin films studied here because of their reliance on (104) planes for Li diffusion. The conventional interpretation in literature is that this structural degradation is caused at high voltages due to Ni^{2+} ions migrating from octahedral 3a sites of the $R\bar{3}m$ structure into Li^{+} octahedral 3b sites at high states of delithiation due to their similar ionic radii (0.69 and 0.76 Å, respectively).[27] These data support previous works' observations of structural degradation related to capacity loss, but suggests an additional cause beyond the conventional cation migration mechanism for this degradation, and that is related to the oxygen redox catalyzed by the electrolyte observed here.

When considering this result with the electrochemistry data and evidence in literature for oxygen evolution from Ni-rich NMC interfaces,[265] there is evidently an irreversible mechanism for Ni-rich NMC structural degradation tied to electrolyte composition which was not previously identified in literature. The proposed mechanism is that EC bonds with cathode surface oxygen atoms of NMC622 as part of its dissociation reaction. This reaction has been modeled to have lower activation energy for edge on planes of NMC333 and $LiCoO_2$ with EC[193] such as the textured (104) planes of the NMC622 thin films used here. This reaction is enabled in this orientation because oxygen atoms are exposed at the surface rather than predominantly transition metals or Li as would be the case for (003) planes.[193] This causes oxygen vacancy formation in the crystal structure which has been shown to form disordered rock salt and amorphous structures.[27] This also explains why the structural degradation is worse for thin films in liquid electrolyte compared to solid electrolyte and why the irreversible oxygen redox plateau is observed only for liquid cells.

The associated capacity loss is not entirely resolved by the choice of a stable electrolyte which does not remove oxygen from the cathode, as the Lipon-coated samples also exhibit structural decomposition to a lesser extent. Due to the lack of EC to drive decomposition of the (104) planes which favor Li diffusion, the extended cycling stability of the solid state cell is improved over liquid cells. Additionally, the presence of thin polymer binders on the surface suppressed that oxygen redox in liquid cells by minimizing contact between EC and the (104) cathode surface (Figure 58). In order to address this challenge of structural and interfacial degradation and push the boundaries of this class of materials, the interface must be stabilized with an electrolyte which does not drive this oxygen redox. This must be done while simultaneously stabilizing the bulk structure of the Ni-rich NMC (*e.g.* by dopants with other transition metals) such that it does not degrade into an amorphous or rock salt state. This solution may be accomplished by controlling processing conditions such as a slurry formulation which is more acidic to minimize hydroxyl formation on the NMC surface, through a dry processing step to fully coat cathode particles in polymeric binders to minimize contact between the cathode surface and liquid electrolyte, and by preventing the structural degradation of the crystal structure through modification of the bulk composition in order to operate Ni-rich NMC at high upper cutoff voltages.

REFERENCES

1. Davis, S.C. and S.E. Williams, *Transportation Energy Data Book*. 36.1 ed. 2018: Oak Ridge National Laboratory.
2. *Energy Flow Charts: Charting the Complex Relationships among Energy, Water, and Carbon*. 2017; Available from: https://flowcharts.llnl.gov/.
3. *US Energy Facts Explained*. May 16, 2018; Available from: https://www.eia.gov/energyexplained/?page=us_energy_home.
4. *USDRIVE Partnership Plan*. US Department of Energy Office of Energy Efficiency & Renewable Energy.
5. *USDRIVE Electrochemical Energy Storage Technical Team Roadmap*. US Department of Energy Office of Energy Efficiency & Renewable Energy.
6. Schmuch, R., R. Wagner, G. Hörpel, T. Placke, and M. Winter, *Performance and cost of materials for lithium-based rechargeable automotive batteries.* Nature Energy, 2018. **3**: p. 267-278.
7. Helbig, C., A.M. Bradshaw, L. Wietschel, A. Thorenz, and A. Tuma, *Supply risks associated with lithium-ion battery materials.* Journal of Cleaner Production, 2018. **172**: p. 274-286.
8. Frankel, T. and P. Whoriskey. *The Cobalt Pipeline: Tracing the path from deadly hand-dug mines in Congo to consumers' phones and laptops*. 2016 September 30, 2016; Available from: https://www.washingtonpost.com/graphics/business/batteries/congo-cobalt-mining-for-lithium-ion-battery/.
9. USGS, *Mineral commodity summaries 2019.* 2019. **U.S. Geological Survey**: p. 50-51.
10. Li, W., B. Song, and A. Manthiram, *High-voltage positive electrode materials for lithium-ion batteries.* Chem. Soc. Rev., 2017. **46**: p. 3006-3059.
11. Xu, J., F. Lin, M.M. Doeff, and W. Tong, *A review of Ni-based layered oxides for rechargeable Li-ion batteries.* Journal of Materials Chemistry A, 2017. **5**: p. 874-901.
12. Tian, C., F. Lin, and M.M. Doeff, *Electrochemical Characteristics of Layered Transition Metal Oxide Cathode Materials for Lithium Ion Batteries: Surface, Bulk Behavior, and Thermal Properties.* Acc. Chem. Res., 2018. **51**: p. 89-96.
13. Jung, R., M. Metzger, F. Maglia, C. Stinner, and H.A. Gasteiger, *Chemical versus Electrochemical Electrolyte Oxidation on NMC111, NMC622, NMC811, LNMO, and Conductive Carbon.* J Phys Chem Lett, 2017. **8**: p. 4820-4825.
14. Mizushima, K., P. Jones, P. Wiseman, and J.B. Goodenough, *LixCoO2 (0< x<-1): A new cathode material for batteries of high energy density.* Mater. Res. Bull., 1980. **15**: p. 783-789.
15. Xu, K., *Electrolytes and Interphases in Li-Ion Batteries and Beyond.* Chem. Rev., 2014. **114**: p. 11503-11618.
16. Peled, E., *The electrochemical behavior of alkali and alkaline earth metals in nonaqueous battery systems—the solid electrolyte interphase model.* J. Electrochem. Soc., 1979. **126**: p. 2047-2051.
17. Edström, K., T. Gustafsson, and J.O. Thomas, *The cathode–electrolyte interface in the Li-ion battery.* Electrochim. Acta, 2004. **50**: p. 397-403.
18. Ma, T., G.-L. Xu, Y. Li, L. Wang, X. He, J. Zheng, J. Liu, M.H. Engelhard, P. Zapol, and L.A. Curtiss, *Revisiting the corrosion of the aluminum current collector in lithium-ion batteries.* The journal of physical chemistry letters, 2017. **8**: p. 1072-1077.
19. Delmas, C., C. Fouassier, and P. Hagenmuller, *Structural Classification and Properties of the Layered Oxides.* Physics B+C. **99**: p. 81-85.
20. Radin, M.D., S. Hy, M. Sina, C. Fang, H. Liu, J. Vinckeviciute, M. Zhang, M.S. Whittingham, Y.S. Meng, and A. Van der Ven, *Narrowing the Gap between Theoretical and Practical Capacities in Li-Ion Layered Oxide Cathode Materials.* Advanced Energy Materials, 2017. **7**.
21. Julien, C., A. Mauger, A. Vijh, and K. Zaghib, *Principles of Intercalation*, in *Lithium Batteries: Science and Technology*. 2016, Springer International Publishing: Cham. p. 69-91.
22. Julien, C., A. Mauger, A. Vijh, and K. Zaghib, *Cathode Materials with Two-Dimensional Structure*, in *Lithium Batteries: Science and Technology*. 2016, Springer International Publishing: Cham. p. 119-162.
23. Reimers, J.N. and J. Dahn, *Electrochemical and in situ X-ray diffraction studies of lithium intercalation in Li x CoO2.* J. Electrochem. Soc., 1992. **139**: p. 2091-2097.
24. Ohzuku, T. and A. Ueda, *Solid-state redox reactions of LiCoO2 (R3m) for 4 volt secondary lithium cells.* J. Electrochem. Soc., 1994. **141**: p. 2972-2977.
25. Cho, J., C.S. Kim, and S.I. Yoo, *Improvement of structural stability of LiCoO2 cathode during electrochemical cycling by sol-gel coating of SnO2.* Electrochem. Solid-State Lett., 2000. **3**: p. 362-365.
26. Wang, H., Y.I. Jang, B. Huang, D.R. Sadoway, and Y.M. Chiang, *TEM study of electrochemical cycling-induced damage and disorder in LiCoO2 cathodes for rechargeable lithium batteries.* J. Electrochem. Soc., 1999. **146**: p. 473-480.

27. Liu, W., P. Oh, X. Liu, M.J. Lee, W. Cho, S. Chae, Y. Kim, and J. Cho, *Nickel-rich layered lithium transition-metal oxide for high-energy lithium-ion batteries.* Angew. Chem. Int. Ed. Engl., 2015. **54**: p. 4440-57.
28. Arai, H., S. Okada, Y. Sakurai, and J.-i. Yamaki, *Reversibility of LiNiO2 cathode.* Solid State Ionics, 1997. **95**: p. 275-282.
29. Ohzuku, T., A. Ueda, and M. Nagayama, *Electrochemistry and Structural Chemistry of LiNi02 (R3m) for 4 Volt Secondary Lithium Cells.* J. Electrochem. Soc., 1993. **140**: p. 1862-1870.
30. Yoshio, M., H. Noguchi, J.-I. Itoh, M. Okada, and T. Mouri, *Preparation and properties of $LiCo_yMn_xNi_{1-x-y}O_2$ as a cathode for lithium ion batteries.* 2000. **90**: p. 176-181.
31. Liu, Z., A. Yu, and J.Y. Lee, *Synthesis and characterization of LiNi Co Mn O as the cathode 1yxyyx y 2 materials of secondary lithium batteries.* J. Power Sources, 1999. **81-82**: p. 416-419.
32. Noh, H.-J., S. Youn, C.S. Yoon, and Y.-K. Sun, *Comparison of the structural and electrochemical properties of layered Li[NixCoyMnz]O2 (x = 1/3, 0.5, 0.6, 0.7, 0.8 and 0.85) cathode material for lithium-ion batteries.* J. Power Sources, 2013. **233**: p. 121-130.
33. Kasnatscheew, J., M. Evertz, B. Streipert, R. Wagner, R. Klopsch, B. Vortmann, H. Hahn, S. Nowak, M. Amereller, A.C. Gentschev, P. Lamp, and M. Winter, *The truth about the 1st cycle Coulombic efficiency of LiNi1/3Co1/3Mn1/3O2 (NCM) cathodes.* Phys. Chem. Chem. Phys., 2016. **18**: p. 3956-65.
34. Kannan, A.M., L. Rabenberg, and A. Manthiram, *High capacity surface-modified LiCoO2 cathodes for lithium-ion batteries.* Electrochem. Solid-State Lett., 2003. **6**: p. A16-A18.
35. Qiao, R., J. Liu, K. Kourtakis, M.G. Roelofs, D.L. Peterson, J.P. Duff, D.T. Deibler, L.A. Wray, and W. Yang, *Transition-metal redox evolution in LiNi0. 5Mn0. 3Co0. 2O2 electrodes at high potentials.* J. Power Sources, 2017. **360**: p. 294-300.
36. Qiao, R., L.A. Wray, J.-H. Kim, N.P.W. Pieczonka, S.J. Harris, and W. Yang, *Direct Experimental Probe of the Ni(II)/Ni(III)/Ni(IV) Redox Evolution in LiNi0.5Mn1.5O4 Electrodes.* The Journal of Physical Chemistry C, 2015. **119**: p. 27228-27233.
37. Wakihara, M. and O. Yamamoto, *Lithium ion batteries: fundamentals and performance*. 2008: John Wiley & Sons.
38. Li, D., Y. Sasaki, M. Kageyama, K. Kobayakawa, and Y. Sato, *Structure, morphology and electrochemical properties of LiNi0.5Mn0.5−xCoxO2 prepared by solid state reaction.* J. Power Sources, 2005. **148**: p. 85-89.
39. Li, J., L.E. Downie, L. Ma, W. Qiu, and J.R. Dahn, *Study of the Failure Mechanisms of LiNi0.8Mn0.1Co0.1O2 Cathode Material for Lithium Ion Batteries.* J. Electrochem. Soc., 2015. **162**: p. A1401-A1408.
40. Kim, M.-H., H.-S. Shin, D. Shin, and Y.-K. Sun, *Synthesis and electrochemical properties of Li [Ni0. 8Co0. 1Mn0. 1] O2 and Li [Ni0. 8Co0. 2] O2 via co-precipitation.* J. Power Sources, 2006. **159**: p. 1328-1333.
41. Woo, S.-U., C. Yoon, K. Amine, I. Belharouak, and Y.-K. Sun, *Significant improvement of electrochemical performance of AlF3-coated Li [Ni0. 8Co0. 1Mn0. 1] O2 cathode materials.* J. Electrochem. Soc., 2007. **154**: p. A1005-A1009.
42. Lu, C.-H. and L. Wei-Cheng, *Reaction mechanism and kinetics analysis of lithium nickel oxide during solid-state reaction.* J. Mater. Chem., 2000. **10**: p. 1403-1407.
43. Kanno, R., H. Kubo, and Y. Kawamoto, *Phase Relationship and Lithium Deintercalation in Lithium Nickel Oxides.* J. Solid State Chem., 1994. **110**: p. 216-225.
44. Zheng, X., X. Li, Z. Huang, B. Zhang, Z. Wang, H. Guo, and Z. Yang, *Enhanced electrochemical performance of Lini0. 6co0. 2mn0. 2o2 cathode materials by ultrasonic-assisted co-precipitation method.* J. Alloys Compd., 2015. **644**: p. 607-614.
45. Julien, C., A. Mauger, K. Zaghib, and H. Groult, *Comparative issues of cathode materials for Li-ion batteries.* Inorganics, 2014. **2**: p. 132-154.
46. Momma, K. and F. Izumi, *VESTA 3 for three-dimensional visualization of crystal, volumetric, and morphology data.* J. Appl. Crystallogr., 2011: p. 1272-1276.
47. Cho, W., S.-M. Kim, J.H. Song, T. Yim, S.-G. Woo, K.-W. Lee, J.-S. Kim, and Y.-J. Kim, *Improved electrochemical and thermal properties of nickel rich LiNi 0.6 Co 0.2 Mn 0.2 O 2 cathode materials by SiO 2 coating.* J. Power Sources, 2015. **282**: p. 45-50.
48. Jain, A., G. Hautier, S.P. Ong, S. Dacek, and G. Ceder, *Relating voltage and thermal safety in Li-ion battery cathodes: a high-throughput computational study.* Phys. Chem. Chem. Phys., 2015. **17**: p. 5942-53.

49. Ma, J., P. Hu, G. Cui, and L. Chen, *Surface and Interface Issues in Spinel LiNi0.5Mn1.5O4: Insights into a Potential Cathode Material for High Energy Density Lithium Ion Batteries.* Chem. Mater., 2016. **28**: p. 3578-3606.
50. Tian, C., D. Nordlund, H.L. Xin, Y. Xu, Y. Liu, D. Sokaras, F. Lin, and M.M. Doeff, *Depth-Dependent Redox Behavior of $LiNi_{0.6}Mn_{0.2}Co_{0.2}O_2$.* J. Electrochem. Soc., 2018. **165**: p. A696-A704.
51. Erickson, E.M., H. Sclar, F. Schipper, J. Liu, R. Tian, C. Ghanty, L. Burstein, N. Leifer, J. Grinblat, M. Talianker, J.-Y. Shin, J.K. Lampert, B. Markovsky, A.I. Frenkel, and D. Aurbach, *High-Temperature Treatment of Li-Rich Cathode Materials with Ammonia: Improved Capacity and Mean Voltage Stability during Cycling.* Advanced Energy Materials, 2017. **7**.
52. Cho, D.H., C.H. Jo, W. Cho, Y.J. Kim, H. Yashiro, Y.K. Sun, and S.T. Myung, *Effect of Residual Lithium Compounds on Layer Ni-Rich Li[Ni0.7Mn0.3]O2.* J. Electrochem. Soc., 2014. **161**: p. A920-A926.
53. Guéguen, A., D. Streich, M. He, M. Mendez, F.F. Chesneau, P. Novák, and E.J. Berg, *Decomposition of LiPF6in High Energy Lithium-Ion Batteries Studied with Online Electrochemical Mass Spectrometry.* J. Electrochem. Soc., 2016. **163**: p. A1095-A1100.
54. Thackeray, M., *Structural considerations of layered and spinel lithiated oxides for lithium ion batteries.* J. Electrochem. Soc., 1995. **142**: p. 2558-2563.
55. Thackeray, M.M., *Manganese oxides for lithium batteries.* Prog. Solid State Chem., 1997. **25**: p. 1-71.
56. Santhanam, R. and B. Rambabu, *Research progress in high voltage spinel LiNi0. 5Mn1. 5O4 material.* J. Power Sources, 2010. **195**: p. 5442-5451.
57. Tarascon, J., E. Wang, F. Shokoohi, W. McKinnon, and S. Colson, *The spinel phase of LiMn2 O 4 as a cathode in secondary lithium cells.* J. Electrochem. Soc., 1991. **138**: p. 2859-2864.
58. Zhong, Q., A. Bonakdarpour, M. Zhang, Y. Gao, and J. Dahn, *Synthesis and Electrochemistry of LiNi x Mn2− x O 4.* J. Electrochem. Soc., 1997. **144**: p. 205-213.
59. Kim, J.-H., S.-T. Myung, C. Yoon, S. Kang, and Y.-K. Sun, *Comparative Study of LiNi0. 5Mn1. 5O4-δ and LiNi0. 5Mn1. 5O4 Cathodes Having Two Crystallographic Structures: Fd 3 m and P 4332.* Chem. Mater., 2004. **16**: p. 906-914.
60. Padhi, A.K., K.S. Nanjundaswamy, and J.B. Goodenough, *Phospho-olivines as positive-electrode materials for rechargeable lithium batteries.* J. Electrochem. Soc., 1997. **144**: p. 1188-1194.
61. Xu, Y. and J. Mao, *Enhanced electrochemical performance of LiFePO4 cathode with carbon-TiO2 hybrid coating.* Journal of Materials Science, 2016. **51**: p. 10026-10034.
62. Mukai, K. and T. Uyama, *Toward Positive Electrode Materials with High-Energy Density: Electrochemical and Structural Studies on LiCo x Mn2–x O4 with 0≤x≤ 1.* ACS Omega, 2017. **2**: p. 5142-5149.
63. Janssen, Y., D. Santhanagopalan, D. Qian, M. Chi, X. Wang, C. Hoffmann, Y.S. Meng, and P.G. Khalifah, *Reciprocal salt flux growth of LiFePO4 single crystals with controlled defect concentrations.* Chem. Mater., 2013. **25**: p. 4574-4584.
64. Satyavani, T., A.S. Kumar, and P.S. Rao, *Methods of synthesis and performance improvement of lithium iron phosphate for high rate Li-ion batteries: a review.* Engineering Science and Technology, an International Journal, 2016. **19**: p. 178-188.
65. Yazami, R. and P. Touzain, *A reversible graphite-lithium negative electrode for electrochemical generators.* J. Power Sources, 1983. **9**: p. 365-371.
66. Winter, M., J.O. Besenhard, M.E. Spahr, and P. Novak, *Insertion electrode materials for rechargeable lithium batteries.* Adv. Mater., 1998. **10**: p. 725-763.
67. Dahn, J., *Phase diagram of Li x C 6.* Physical Review B, 1991. **44**: p. 9170.
68. Ohzuku, T., Y. Iwakoshi, and K. Sawai, *Formation of lithium-graphite intercalation compounds in nonaqueous electrolytes and their application as a negative electrode for a lithium ion (shuttlecock) cell.* J. Electrochem. Soc., 1993. **140**: p. 2490-2498.
69. Fong, R., U. Von Sacken, and J.R. Dahn, *Studies of lithium intercalation into carbons using nonaqueous electrochemical cells.* J. Electrochem. Soc., 1990. **137**: p. 2009-2013.
70. Deschanvres, A., B. Raveau, and Z. Sekkal, *Mise en evidence et etude cristallographique d'une nouvelle solution solide de type spinelle Li1+ xTi2− xO4 0⩽x⩽0, 333.* Mater. Res. Bull., 1971. **6**: p. 699-704.
71. Ferg, E., R. Gummow, A. De Kock, and M. Thackeray, *Spinel anodes for lithium-ion batteries.* J. Electrochem. Soc., 1994. **141**: p. L147-L150.
72. Zhao, B., R. Ran, M. Liu, and Z. Shao, *A comprehensive review of Li4Ti5O12-based electrodes for lithium-ion batteries: the latest advancements and future perspectives.* Materials Science and Engineering: R: Reports, 2015. **98**: p. 1-71.

73. Chen, C., J. Vaughey, A.N. Jansen, D. Dees, A. Kahaian, T. Goacher, and M. Thackeray, *Studies of Mg-Substituted Li4− xMg x Ti5O12 Spinel Electrodes (0≤ x≤ 1) for Lithium Batteries.* J. Electrochem. Soc., 2001. **148**: p. A102-A104.
74. Ohzuku, T., A. Ueda, and N. Yamamoto, *Zero-strain insertion material of Li [Li1/3Ti5/3] O 4 for rechargeable lithium cells.* J. Electrochem. Soc., 1995. **142**: p. 1431-1435.
75. Zhang, W.-J., *A review of the electrochemical performance of alloy anodes for lithium-ion batteries.* J. Power Sources, 2011. **196**: p. 13-24.
76. Jung, H., M. Park, Y.-G. Yoon, G.-B. Kim, and S.-K. Joo, *Amorphous silicon anode for lithium-ion rechargeable batteries.* J. Power Sources, 2003. **115**: p. 346-351.
77. Huggins, R.A., *Lithium alloy negative electrodes.* J. Power Sources, 1999. **81**: p. 13-19.
78. Zhang, W.-J., *Lithium insertion/extraction mechanism in alloy anodes for lithium-ion batteries.* J. Power Sources, 2011. **196**: p. 877-885.
79. Ryu, J.H., J.W. Kim, Y.-E. Sung, and S.M. Oh, *Failure modes of silicon powder negative electrode in lithium secondary batteries.* Electrochem. Solid-State Lett., 2004. **7**: p. A306-A309.
80. Feng, K., M. Li, W. Liu, A.G. Kashkooli, X. Xiao, M. Cai, and Z. Chen, *Silicon-Based Anodes for Lithium-Ion Batteries: From Fundamentals to Practical Applications.* Small, 2018. **14**: p. 1702737.
81. Liang, B., Y. Liu, and Y. Xu, *Silicon-based materials as high capacity anodes for next generation lithium ion batteries.* J. Power Sources, 2014. **267**: p. 469-490.
82. Shi, F., Z. Song, P.N. Ross, G.A. Somorjai, R.O. Ritchie, and K. Komvopoulos, *Failure mechanisms of single-crystal silicon electrodes in lithium-ion batteries.* Nature communications, 2016. **7**: p. 11886.
83. Winter, M., B. Barnett, and K. Xu, *Before Li Ion Batteries.* Chem. Rev., 2018.
84. Xu, K., *Nonaqueous liquid electrolytes for lithium-based rechargeable batteries.* Chem. Rev., 2004. **104**: p. 4303-4418.
85. Hughes, M., N. Hampson, and S. Karunathilaka, *A review of cells based on lithium negative electrodes (anodes).* J. Power Sources, 1984. **12**: p. 83-144.
86. Monroe, C. and J. Newman, *The impact of elastic deformation on deposition kinetics at lithium/polymer interfaces.* J. Electrochem. Soc., 2005. **152**: p. A396-A404.
87. Kalnaus, S., A.S. Sabau, W.E. Tenhaeff, N.J. Dudney, and C. Daniel, *Design of composite polymer electrolytes for Li ion batteries based on mechanical stability criteria.* J. Power Sources, 2012. **201**: p. 280-287.
88. Ren, Y., Y. Shen, Y. Lin, and C.-W. Nan, *Direct observation of lithium dendrites inside garnet-type lithium-ion solid electrolyte.* Electrochem. Commun., 2015. **57**: p. 27-30.
89. Younesi, R., G.M. Veith, P. Johansson, K. Edström, and T. Vegge, *Lithium salts for advanced lithium batteries: Li–metal, Li–O 2, and Li–S.* Energy & Environmental Science, 2015. **8**: p. 1905-1922.
90. Harris, W.S., *Electrochemical studies in cyclic esters.* 1958.
91. Lewis, G.N. and F.G. Keyes, *THE POTENTIAL OF THE LITHIUM ELECTRODE.* J. Am. Chem. Soc., 1913. **35**: p. 340-344.
92. Xu, K., *"Charge-transfer" process at graphite/electrolyte interface and the solvation sheath structure of Li+ in nonaqueous electrolytes.* J. Electrochem. Soc., 2007. **154**: p. A162-A167.
93. Xu, K., Y. Lam, S.S. Zhang, T.R. Jow, and T.B. Curtis, *Solvation sheath of Li+ in nonaqueous electrolytes and its implication of graphite/electrolyte interface chemistry.* The Journal of Physical Chemistry C, 2007. **111**: p. 7411-7421.
94. Bard, A.J., L.R. Faulkner, J. Leddy, and C.G. Zoski, *Electrochemical methods: fundamentals and applications*. Vol. 2. 1980: wiley New York.
95. Reddy, T.B., *Linden's handbook of batteries*. Vol. 4. 2011: Mcgraw-hill New York.
96. Bachman, J.C., S. Muy, A. Grimaud, H.-H. Chang, N. Pour, S.F. Lux, O. Paschos, F. Maglia, S. Lupart, and P. Lamp, *Inorganic solid-state electrolytes for lithium batteries: mechanisms and properties governing ion conduction.* Chem. Rev., 2015. **116**: p. 140-162.
97. Lacivita, V., A.S. Westover, A. Kercher, N.D. Phillip, G. Yang, G. Veith, G. Ceder, and N.J. Dudney, *Resolving the amorphous structure of lithium phosphorus oxynitride (Lipon).* J. Am. Chem. Soc., 2018. **140**: p. 11029-11038.
98. Manthiram, A., X. Yu, and S. Wang, *Lithium battery chemistries enabled by solid-state electrolytes.* Nature Reviews Materials, 2017. **2**: p. 16103.
99. Buschmann, H., J. Dölle, S. Berendts, A. Kuhn, P. Bottke, M. Wilkening, P. Heitjans, A. Senyshyn, H. Ehrenberg, and A. Lotnyk, *Structure and dynamics of the fast lithium ion conductor "Li 7 La 3 Zr 2 O 12".* PCCP, 2011. **13**: p. 19378-19392.

100. Li, J., C. Ma, M. Chi, C. Liang, and N.J. Dudney, *Solid Electrolyte: the Key for High-Voltage Lithium Batteries.* Advanced Energy Materials, 2015. **5**.
101. Ates, T., M. Keller, J. Kulisch, T. Adermann, and S. Passerini, *Development of an all-solid-state lithium battery by slurry-coating procedures using a sulfidic electrolyte.* Energy Storage Materials, 2019. **17**: p. 204-210.
102. Fox, D.M., J.W. Gilman, A.B. Morgan, J.R. Shields, P.H. Maupin, R.E. Lyon, H.C. De Long, and P.C. Trulove, *Flammability and thermal analysis characterization of imidazolium-based ionic liquids.* Industrial & Engineering Chemistry Research, 2008. **47**: p. 6327-6332.
103. Lewandowski, A. and A. Świderska-Mocek, *Ionic liquids as electrolytes for Li-ion batteries—an overview of electrochemical studies.* J. Power Sources, 2009. **194**: p. 601-609.
104. Srour, H., L. Chancelier, E. Bolimowska, T. Gutel, S. Mailley, H. Rouault, and C.C. Santini, *Ionic liquid-based electrolytes for lithium-ion batteries: review of performances of various electrode systems.* J. Appl. Electrochem., 2016. **46**: p. 149-155.
105. Nair, J.R., F. Colò, A. Kazzazi, M. Moreno, D. Bresser, R. Lin, F. Bella, G. Meligrana, S. Fantini, and E. Simonetti, *Room temperature ionic liquid (RTIL)-based electrolyte cocktails for safe, high working potential Li-based polymer batteries.* J. Power Sources, 2019. **412**: p. 398-407.
106. Xu, K. and C.A. Angell, *Sulfone-based electrolytes for lithium-ion batteries.* J. Electrochem. Soc., 2002. **149**: p. A920-A926.
107. Lee, S.-Y., K. Ueno, and C.A. Angell, *Lithium salt solutions in mixed sulfone and sulfone-carbonate solvents: a walden plot analysis of the maximally conductive compositions.* The Journal of Physical Chemistry C, 2012. **116**: p. 23915-23920.
108. Ren, X., S. Chen, H. Lee, D. Mei, M.H. Engelhard, S.D. Burton, W. Zhao, J. Zheng, Q. Li, and M.S. Ding, *Localized high-concentration sulfone electrolytes for high-efficiency lithium-metal batteries.* Chem, 2018. **4**: p. 1877-1892.
109. Shin, J.H. and E.J. Cairns, *Characterization of N-methyl-N-butylpyrrolidinium bis (trifluoromethanesulfonyl) imide-LiTFSI-tetra (ethylene glycol) dimethyl ether mixtures as a Li metal cell electrolyte.* J. Electrochem. Soc., 2008. **155**: p. A368-A373.
110. Wang, J., Y. Yamada, K. Sodeyama, C.H. Chiang, Y. Tateyama, and A. Yamada, *Superconcentrated electrolytes for a high-voltage lithium-ion battery.* Nature communications, 2016. **7**: p. 12032.
111. Suo, L., O. Borodin, T. Gao, M. Olguin, J. Ho, X. Fan, C. Luo, C. Wang, and K. Xu, *"Water-in-salt" electrolyte enables high-voltage aqueous lithium-ion chemistries.* Science, 2015. **350**: p. 938-943.
112. Jackson, G. and G. Blomgren, *Lithium Anode Properties in a Nonaqueous Cell.* J. Electrochem. Soc., 1969. **116**: p. 1483-1487.
113. Scarr, R.F., *Kinetics of the Solid Lithium Electrode in Propylene Carbonate.* J. Electrochem. Soc., 1970. **117**: p. 295-299.
114. Yu, X. and A. Manthiram, *Electrode–electrolyte interfaces in lithium-based batteries.* Energy & Environmental Science, 2018. **11**: p. 527-543.
115. Aurbach, D., M. Daroux, P. Faguy, and E. Yeager, *Identification of surface films formed on lithium in propylene carbonate solutions.* J. Electrochem. Soc., 1987. **134**: p. 1611-1620.
116. Peled, E., D. Golodnitsky, and G. Ardel, *Advanced model for solid electrolyte interphase electrodes in liquid and polymer electrolytes.* J. Electrochem. Soc., 1997. **144**: p. L208-L210.
117. Dedryvère, R., S. Leroy, H. Martinez, F. Blanchard, D. Lemordant, and D. Gonbeau, *XPS valence characterization of lithium salts as a tool to study electrode/electrolyte interfaces of Li-ion batteries.* The Journal of Physical Chemistry B, 2006. **110**: p. 12986-12992.
118. Goodenough, J.B. and Y. Kim, *Challenges for rechargeable Li batteries.* Chem. Mater., 2009. **22**: p. 587-603.
119. Chou, S.L., Y. Pan, J.Z. Wang, H.K. Liu, and S.X. Dou, *Small things make a big difference: binder effects on the performance of Li and Na batteries.* Phys. Chem. Chem. Phys., 2014. **16**: p. 20347-59.
120. An, S.J., J. Li, C. Daniel, D. Mohanty, S. Nagpure, and D.L. Wood, *The state of understanding of the lithium-ion-battery graphite solid electrolyte interphase (SEI) and its relationship to formation cycling.* Carbon, 2016. **105**: p. 52-76.
121. Philippe, B., R.m. Dedryvère, J. Allouche, F. Lindgren, M. Gorgoi, H.k. Rensmo, D. Gonbeau, and K. Edström, *Nanosilicon electrodes for lithium-ion batteries: interfacial mechanisms studied by hard and soft X-ray photoelectron spectroscopy.* Chem. Mater., 2012. **24**: p. 1107-1115.
122. Lee, Y.M., J.Y. Lee, H.-T. Shim, J.K. Lee, and J.-K. Park, *SEI layer formation on amorphous Si thin electrode during precycling.* J. Electrochem. Soc., 2007. **154**: p. A515-A519.

123. Saint, J., M. Morcrette, D. Larcher, L. Laffont, S. Beattie, J.P. Pérès, D. Talaga, M. Couzi, and J.M. Tarascon, *Towards a fundamental understanding of the improved electrochemical performance of silicon–carbon composites.* Adv. Funct. Mater., 2007. **17**: p. 1765-1774.
124. Nie, M., D.P. Abraham, Y. Chen, A. Bose, and B.L. Lucht, *Silicon solid electrolyte interphase (SEI) of lithium ion battery characterized by microscopy and spectroscopy.* The Journal of Physical Chemistry C, 2013. **117**: p. 13403-13412.
125. Zhang, X., R. Kostecki, T.J. Richardson, J.K. Pugh, and P.N. Ross, *Electrochemical and infrared studies of the reduction of organic carbonates.* J. Electrochem. Soc., 2001. **148**: p. A1341-A1345.
126. Aurbach, D., Y. Gofer, M. Ben-Zion, and P. Aped, *The behaviour of lithium electrodes in propylene and ethylene carbonate: Te major factors that influence Li cycling efficiency.* J. Electroanal. Chem., 1992. **339**: p. 451-471.
127. Philippe, B., R.m. Dedryvère, M. Gorgoi, H.k. Rensmo, D. Gonbeau, and K. Edström, *Improved performances of nanosilicon electrodes using the salt LiFSI: a photoelectron spectroscopy study.* J. Am. Chem. Soc., 2013. **135**: p. 9829-9842.
128. Hubaud, A.A., Z. Yang, D.J. Schroeder, F. Dogan, L. Trahey, and J.T. Vaughey, *Interfacial study of the role of SiO2 on Si anodes using electrochemical quartz crystal microbalance.* J. Power Sources, 2015. **282**: p. 639-644.
129. Graetz, J., C. Ahn, R. Yazami, and B. Fultz, *Highly reversible lithium storage in nanostructured silicon.* Electrochem. Solid-State Lett., 2003. **6**: p. A194-A197.
130. Chan, C.K., H. Peng, G. Liu, K. McIlwrath, X.F. Zhang, R.A. Huggins, and Y. Cui, *High-performance lithium battery anodes using silicon nanowires.* Nature nanotechnology, 2008. **3**: p. 31.
131. Magasinski, A., B. Zdyrko, I. Kovalenko, B. Hertzberg, R. Burtovyy, C.F. Huebner, T.F. Fuller, I. Luzinov, and G. Yushin, *Toward efficient binders for Li-ion battery Si-based anodes: polyacrylic acid.* ACS applied materials & interfaces, 2010. **2**: p. 3004-3010.
132. Obrovac, M. and V. Chevrier, *Alloy negative electrodes for Li-ion batteries.* Chem. Rev., 2014. **114**: p. 11444-11502.
133. Komaba, S., K. Shimomura, N. Yabuuchi, T. Ozeki, H. Yui, and K. Konno, *Study on polymer binders for high-capacity SiO negative electrode of Li-ion batteries.* The Journal of Physical Chemistry C, 2011. **115**: p. 13487-13495.
134. Besenhard, J., M. Wagner, M. Winter, A. Jannakoudakis, P. Jannakoudakis, and E. Theodoridou, *Inorganic film-forming electrolyte additives improving the cycling behaviour of metallic lithium electrodes and the self-discharge of carbon—Lithium electrodes.* J. Power Sources, 1993. **44**: p. 413-420.
135. Haregewoin, A.M., A.S. Wotango, and B.-J. Hwang, *Electrolyte additives for lithium ion battery electrodes: progress and perspectives.* Energy Environ. Sci., 2016. **9**: p. 1955-1988.
136. Xia, J., R. Petibon, A. Xiao, W.M. Lamanna, and J.R. Dahn, *The effectiveness of electrolyte additives in fluorinated electrolytes for high voltage Li[Ni 0.4 Mn 0.4 Co 0.2]O 2 /graphite pouch Li-ion cells.* J. Power Sources, 2016. **330**: p. 175-185.
137. Xia, J., L. Ma, K.J. Nelson, M. Nie, Z. Lu, and J.R. Dahn, *A Study of Li-Ion Cells Operated to 4.5 V and at 55°C.* J. Electrochem. Soc., 2016. **163**: p. A2399-A2406.
138. Downie, L.E., S.R. Hyatt, and J.R. Dahn, *The Impact of Electrolyte Composition on Parasitic Reactions in Lithium Ion Cells Charged to 4.7 V Determined Using Isothermal Microcalorimetry.* J. Electrochem. Soc., 2015. **163**: p. A35-A42.
139. Tornheim, A., R. Sahore, M. He, J.R. Croy, and Z. Zhang, *Preformed Anodes for High-Voltage Lithium-Ion Battery Performance: Fluorinated Electrolytes, Crosstalk, and the Origins of Impedance Rise.* J. Electrochem. Soc., 2018. **165**: p. A3360-A3368.
140. Mogi, R., M. Inaba, S.-K. Jeong, Y. Iriyama, T. Abe, and Z. Ogumi, *Effects of some organic additives on lithium deposition in propylene carbonate.* J. Electrochem. Soc., 2002. **149**: p. A1578-A1583.
141. Aurbach, D., K. Gamolsky, B. Markovsky, Y. Gofer, M. Schmidt, and U. Heider, *On the use of vinylene carbonate (VC) as an additive to electrolyte solutions for Li-ion batteries.* Electrochim. Acta, 2002. **47**: p. 1423-1439.
142. Chen, L., K. Wang, X. Xie, and J. Xie, *Enhancing electrochemical performance of silicon film anode by vinylene carbonate electrolyte additive.* Electrochem. Solid-State Lett., 2006. **9**: p. A512-A515.
143. Zhang, X.Q., X.B. Cheng, X. Chen, C. Yan, and Q. Zhang, *Fluoroethylene carbonate additives to render uniform Li deposits in lithium metal batteries.* Adv. Funct. Mater., 2017. **27**: p. 1605989.
144. McMillan, R., H. Slegr, Z. Shu, and W. Wang, *Fluoroethylene carbonate electrolyte and its use in lithium ion batteries with graphite anodes.* J. Power Sources, 1999. **81**: p. 20-26.

145. Choi, N.-S., K.H. Yew, K.Y. Lee, M. Sung, H. Kim, and S.-S. Kim, *Effect of fluoroethylene carbonate additive on interfacial properties of silicon thin-film electrode.* J. Power Sources, 2006. **161**: p. 1254-1259.
146. Aurbach, D., Y. Ein-Eli, O. Chusid, Y. Carmeli, M. Babai, and H. Yamin, *The Correlation Between the Surface Chemistry and the Performance of Li-Carbon Intercalation Anodes for Rechargeable 'Rocking-Chair'Type Batteries.* J. Electrochem. Soc., 1994. **141**: p. 603-611.
147. Strehle, B., S. Solchenbach, M. Metzger, K.U. Schwenke, and H.A. Gasteiger, *The Effect of CO2 on Alkyl Carbonate Trans-Esterification during Formation of Graphite Electrodes in Li-Ion Batteries.* J. Electrochem. Soc., 2017. **164**: p. A2513-A2526.
148. Han, G.-B., J.-N. Lee, D.J. Lee, H. Lee, J. Song, H. Lee, M.-H. Ryou, J.-K. Park, and Y.M. Lee, *Enhanced cycling performance of lithium metal secondary batteries with succinic anhydride as an electrolyte additive.* Electrochim. Acta, 2014. **115**: p. 525-530.
149. Lee, H., S. Choi, S. Choi, H.-J. Kim, Y. Choi, S. Yoon, and J.-J. Cho, *SEI layer-forming additives for LiNi0. 5Mn1. 5O4/graphite 5 V Li-ion batteries.* Electrochem. Commun., 2007. **9**: p. 801-806.
150. Han, G.-B., M.-H. Ryou, K.Y. Cho, Y.M. Lee, and J.-K. Park, *Effect of succinic anhydride as an electrolyte additive on electrochemical characteristics of silicon thin-film electrode.* J. Power Sources, 2010. **195**: p. 3709-3714.
151. Sinha, N.N., J. Burns, and J. Dahn, *Comparative study of tris (trimethylsilyl) phosphate and tris (trimethylsilyl) phosphite as electrolyte additives for Li-ion cells.* J. Electrochem. Soc., 2014. **161**: p. A1084-A1089.
152. Ding, F., W. Xu, X. Chen, J. Zhang, M.H. Engelhard, Y. Zhang, B.R. Johnson, J.V. Crum, T.A. Blake, and X. Liu, *Effects of carbonate solvents and lithium salts on morphology and coulombic efficiency of lithium electrode.* J. Electrochem. Soc., 2013. **160**: p. A1894-A1901.
153. Pieczonka, N.P., L. Yang, M.P. Balogh, B.R. Powell, K. Chemelewski, A. Manthiram, S.A. Krachkovskiy, G.R. Goward, M. Liu, and J.-H. Kim, *Impact of lithium bis (oxalate) borate electrolyte additive on the performance of high-voltage spinel/graphite Li-ion batteries.* The Journal of Physical Chemistry C, 2013. **117**: p. 22603-22612.
154. Choi, N.-S., K.H. Yew, H. Kim, S.-S. Kim, and W.-U. Choi, *Surface layer formed on silicon thin-film electrode in lithium bis (oxalato) borate-based electrolyte.* J. Power Sources, 2007. **172**: p. 404-409.
155. Etacheri, V., O. Haik, Y. Goffer, G.A. Roberts, I.C. Stefan, R. Fasching, and D. Aurbach, *Effect of fluoroethylene carbonate (FEC) on the performance and surface chemistry of Si-nanowire Li-ion battery anodes.* Langmuir, 2011. **28**: p. 965-976.
156. Xu, C., F. Lindgren, B. Philippe, M. Gorgoi, F. Björefors, K. Edström, and T.r. Gustafsson, *Improved performance of the silicon anode for Li-ion batteries: understanding the surface modification mechanism of fluoroethylene carbonate as an effective electrolyte additive.* Chem. Mater., 2015. **27**: p. 2591-2599.
157. Nakai, H., T. Kubota, A. Kita, and A. Kawashima, *Investigation of the solid electrolyte interphase formed by fluoroethylene carbonate on Si electrodes.* J. Electrochem. Soc., 2011. **158**: p. A798-A801.
158. Jung, R., M. Metzger, D. Haering, S. Solchenbach, C. Marino, N. Tsiouvaras, C. Stinner, and H.A. Gasteiger, *Consumption of fluoroethylene carbonate (FEC) on Si-C composite electrodes for Li-ion batteries.* J. Electrochem. Soc., 2016. **163**: p. A1705-A1716.
159. Thomas, M., P. Bruce, and J. Goodenough, *AC Impedance Analysis of Polycrystalline Insertion Electrodes: Application to Li1− x CoO2.* J. Electrochem. Soc., 1985. **132**: p. 1521-1528.
160. Matsumoto, K., R. Kuzuo, K. Takeya, and A. Yamanaka, *Effects ofCO in air on Li deintercalation from LiNi Co Al O21yxyyx y 2.* J. Power Sources, 1999. **81-82**: p. 558-561.
161. Mijung, N., Y. Lee, and J. Cho, *Water Adsorption and Storage Characteristics of Optimized LiCoO2 and LiNi1/3Co1/3Mn1/3O2 Composite Cathode Material for Li-Ion Cells.* J. Electrochem. Soc., 2006. **153**: p. A935-A940.
162. Xing, L., W. Li, C. Wang, F. Gu, M. Xu, C. Tan, and J. Yi, *Theoretical Investigations on Oxidative Stability of Solvents and Oxidative Decomposition Mechanism of Ethylene Carbonate for Lithium Ion Battery Use.* J. Phys. Chem. B, 2009. **113**: p. 16596–16602.
163. Borodin, O., W. Behl, and T.R. Jow, *Oxidative Stability and Initial Decomposition Reactions of Carbonate, Sulfone, and Alkyl Phosphate-Based Electrolytes.* The Journal of Physical Chemistry C, 2013. **117**: p. 8661-8682.
164. Jung, S.-K., H. Gwon, J. Hong, K.-Y. Park, D.-H. Seo, H. Kim, J. Hyun, W. Yang, and K. Kang, *Understanding the Degradation Mechanisms of LiNi0.5Co0.2Mn0.3O2 Cathode Material in Lithium Ion Batteries.* Advanced Energy Materials, 2014. **4**.

165. Sathiya, M., A.M. Abakumov, D. Foix, G. Rousse, K. Ramesha, M. Saubanere, M.L. Doublet, H. Vezin, C.P. Laisa, A.S. Prakash, D. Gonbeau, G. VanTendeloo, and J.M. Tarascon, *Origin of voltage decay in high-capacity layered oxide electrodes.* Nat Mater, 2015. **14**: p. 230-8.
166. Zeng, X., G.L. Xu, Y. Li, X. Luo, F. Maglia, C. Bauer, S.F. Lux, O. Paschos, S.J. Kim, P. Lamp, J. Lu, K. Amine, and Z. Chen, *Kinetic Study of Parasitic Reactions in Lithium-Ion Batteries: A Case Study on LiNi(0.6)Mn(0.2)Co(0.2)O2.* ACS Appl Mater Interfaces, 2016. **8**: p. 3446-51.
167. Gao, H., J. Cai, G.-L. Xu, L. Li, Y. Ren, X. Meng, K. Amine, and Z. Chen, *Surface Modification for Suppressing Interfacial Parasitic Reactions of Nickel-rich Lithium-Ion Cathode.* Chem. Mater., 2019.
168. Imhof, R. and P. Novák, *Oxidative Electrolyte Solvent Degradation in Lithium-Ion Batteries An In Situ Differential Electrochemical Mass Spectrometry Investigation.* J. Electrochem. Soc., 1999. **146**: p. 1702-1706.
169. Kasnatscheew, J., M. Evertz, B. Streipert, R. Wagner, S. Nowak, I. Cekic Laskovic, and M. Winter, *Changing Established Belief on Capacity Fade Mechanisms: Thorough Investigation of LiNi1/3Co1/3Mn1/3O2 (NCM111) under High Voltage Conditions.* The Journal of Physical Chemistry C, 2017. **121**: p. 1521-1529.
170. Niehoff, P. and M. Winter, *Composition and growth behavior of the surface and electrolyte decomposition layer of/on a commercial lithium ion battery LixNi1/3Mn1/3Co1/3O2 cathode determined by sputter depth profile X-ray photoelectron spectroscopy.* Langmuir, 2013. **29**: p. 15813-21.
171. Wohlfahrt-Mehrens, M., C. Vogler, and J. Garche, *Aging mechanisms of lithium cathode materials.* J. Power Sources, 2004. **127**: p. 58-64.
172. Hunter, J.C., *Preparation of a new crystal form of manganese dioxide: λ-MnO2.* J. Solid State Chem., 1981. **39**: p. 142-147.
173. Gallus, D.R., R. Schmitz, R. Wagner, B. Hoffmann, S. Nowak, I. Cekic-Laskovic, R.W. Schmitz, and M. Winter, *The influence of different conducting salts on the metal dissolution and capacity fading of NCM cathode material.* Electrochim. Acta, 2014. **134**: p. 393-398.
174. Lin, F., I.M. Markus, D. Nordlund, T.C. Weng, M.D. Asta, H.L. Xin, and M.M. Doeff, *Surface reconstruction and chemical evolution of stoichiometric layered cathode materials for lithium-ion batteries.* Nat Commun, 2014. **5**: p. 3529.
175. Shin, H., J. Park, A.M. Sastry, and W. Lu, *Degradation of the solid electrolyte interphase induced by the deposition of manganese ions.* J. Power Sources, 2015. **284**: p. 416-427.
176. Kasnatscheew, J., M. Evertz, B. Streipert, R. Wagner, S. Nowak, I.C. Laskovic, and M. Winter, *Improving cycle life of layered lithium transition metal oxide (LiMO2) based positive electrodes for Li ion batteries by smart selection of the electrochemical charge conditions.* J. Power Sources, 2017. **359**: p. 458-467.
177. Hall, D.S., J. Li, K. Lin, N. Stakheiko, J. Baltazar, and J. Dahn, *A Tale of Two Additives: Effects of Glutaric and Citraconic Anhydrides on Lithium-Ion Cell Performance.* J. Electrochem. Soc., 2019. **166**: p. A793-A801.
178. Li, J., H. Liu, J. Xia, A.R. Cameron, M. Nie, G.A. Botton, and J. Dahn, *The impact of electrolyte additives and upper cut-off voltage on the formation of a rocksalt surface layer in LiNi0. 8Mn0. 1Co0. 1O2 electrodes.* J. Electrochem. Soc., 2017. **164**: p. A655-A665.
179. Arumugam, R.S., L. Ma, J. Li, X. Xia, J. Paulsen, and J. Dahn, *Special synergy between electrolyte additives and positive electrode surface coating to enhance the performance of Li [Ni0. 6Mn0. 2Co0. 2] O2/graphite cells.* J. Electrochem. Soc., 2016. **163**: p. A2531-A2538.
180. Zhao, W., J. Zheng, L. Zou, H. Jia, B. Liu, H. Wang, M.H. Engelhard, C. Wang, W. Xu, Y. Yang, and J.-G. Zhang, *High Voltage Operation of Ni-Rich NMC Cathodes Enabled by Stable Electrode/Electrolyte Interphases.* Advanced Energy Materials, 2018. **8**.
181. Yu, H., S. Qian, L. Yan, P. Li, X. Lin, M. Luo, N. Long, M. Shui, and J. Shu, *Morphological, electrochemical and in-situ XRD study of LiNi0. 6Co0. 2Mn0. 1Al0. 1O2 as high potential cathode material for rechargeable lithium-ion batteries.* J. Alloys Compd., 2016. **667**: p. 58-64.
182. Gao, H., X. Zeng, Y. Hu, V. Tileli, L. Li, Y. Ren, X. Meng, F. Maglia, P. Lamp, S.-J. Kim, K. Amine, and Z. Chen, *Modifying the Surface of a High-Voltage Lithium-Ion Cathode.* ACS Applied Energy Materials, 2018. **1**: p. 2254-2260.
183. Sun, Y.-K., S.-T. Myung, B.-C. Park, and K. Amine, *Synthesis of Spherical Nano-to Microscale Core− Shell Particles Li [(Ni0. 8Co0. 1Mn0. 1) 1-x (Ni0. 5Mn0. 5) x] O2 and Their Applications to Lithium Batteries.* Chem. Mater., 2006. **18**: p. 5159-5163.

184. Hou, P., H. Zhang, Z. Zi, L. Zhang, and X. Xu, *Core–shell and concentration-gradient cathodes prepared via co-precipitation reaction for advanced lithium-ion batteries.* Journal of Materials Chemistry A, 2017. **5**: p. 4254-4279.
185. Li, Y., R. Xu, Y. Ren, J. Lu, H. Wu, L. Wang, D.J. Miller, Y.-K. Sun, K. Amine, and Z. Chen, *Synthesis of full concentration gradient cathode studied by high energy X-ray diffraction.* Nano Energy, 2016. **19**: p. 522-531.
186. Zuo, X., C. Fan, J. Liu, X. Xiao, J. Wu, and J. Nan, *Effect of tris (trimethylsilyl) borate on the high voltage capacity retention of LiNi0. 5Co0. 2Mn0. 3O2/graphite cells.* J. Power Sources, 2013. **229**: p. 308-312.
187. Hong, P., M. Xu, D. Chen, X. Chen, L. Xing, Q. Huang, and W. Li, *Enhancing Electrochemical Performance of High Voltage (4.5 V) Graphite/LiNi0.5Co0.2Mn0.3O2 Cell by Tailoring Cathode Interface.* J. Electrochem. Soc., 2016. **164**: p. A137-A144.
188. Sun, Y.K., S.T. Myung, B.C. Park, J. Prakash, I. Belharouak, and K. Amine, *High-energy cathode material for long-life and safe lithium batteries.* Nat Mater, 2009. **8**: p. 320-4.
189. Li, L., M. Xu, Q. Yao, Z. Chen, L. Song, Z. Zhang, C. Gao, P. Wang, Z. Yu, and Y. Lai, *Alleviating Surface Degradation of Nickel-Rich Layered Oxide Cathode Material by Encapsulating with Nanoscale Li-Ions/Electrons Superionic Conductors Hybrid Membrane for Advanced Li-Ion Batteries.* ACS Appl Mater Interfaces, 2016. **8**: p. 30879-30889.
190. Liu, W., X. Li, D. Xiong, Y. Hao, J. Li, H. Kou, B. Yan, D. Li, S. Lu, and A. Koo, *Significantly improving cycling performance of cathodes in lithium ion batteries: the effect of Al_2O_3 and $LiAlO_2$ coatings on $LiNi_{0.6}Co_{0.2}Mn_{0.2}O_2$.* Nano Energy, 2018. **44**: p. 111-120.
191. Tao, F., X.-x. Yan, J.-J. Liu, H.-L. Zhang, and L. Chen, *Effects of PVP-assisted Co3O4 coating on the electrochemical and storage properties of LiNi0. 6Co0. 2Mn0. 2O2 at high cut-off voltage.* Electrochim. Acta, 2016. **210**: p. 548-556.
192. Strauss, F., T. Bartsch, L. de Biasi, A.-Y. Kim, J.r. Janek, P. Hartmann, and T. Brezesinski, *Impact of cathode material particle size on the capacity of bulk-type all-solid-state batteries.* ACS Energy Letters, 2018. **3**: p. 992-996.
193. Xu, S., G. Luo, R. Jacobs, S. Fang, M.K. Mahanthappa, R.J. Hamers, and D. Morgan, *Ab Initio Modeling of Electrolyte Molecule Ethylene Carbonate Decomposition Reaction on $Li(Ni,Mn,Co)O_2$ Cathode Surface.* ACS Appl Mater Interfaces, 2017. **9**: p. 20545-20553.
194. Daniel, C. and J.O. Besenhard, *Handbook of battery materials*. 2012: John Wiley & Sons.
195. Zhang, S.S., *A review on the separators of liquid electrolyte Li-ion batteries.* J. Power Sources, 2007. **164**: p. 351-364.
196. Huang, X., *Separator technologies for lithium-ion batteries.* J. Solid State Electrochem., 2011. **15**: p. 649-662.
197. Fang, S., D. Jackson, M.L. Dreibelbis, T.F. Kuech, and R.J. Hamers, *Anode-originated SEI migration contributes to formation of cathode-electrolyte interphase layer.* J. Power Sources, 2018. **373**: p. 184-192.
198. Zhang, X. and T. Devine, *Factors that influence formation of AlF3 passive film on aluminum in Li-ion battery electrolytes with LiPF6.* J. Electrochem. Soc., 2006. **153**: p. B375-B383.
199. Zhang, S.S., K. Xu, and T.R. Jow, *Study of LiBF4 as an electrolyte salt for a Li-ion battery.* J. Electrochem. Soc., 2002. **149**: p. A586-A590.
200. Zampardi, G., R. Trocoli, W. Schuhmann, and F. La Mantia, *Revealing the electronic character of the positive electrode/electrolyte interface in lithium-ion batteries.* PCCP, 2017. **19**: p. 28381-28387.
201. Krämer, E., T. Schedlbauer, B. Hoffmann, L. Terborg, S. Nowak, H.J. Gores, S. Passerini, and M. Winter, *Mechanism of anodic dissolution of the aluminum current collector in 1 M LiTFSI EC: DEC 3: 7 in rechargeable lithium batteries.* J. Electrochem. Soc., 2013. **160**: p. A356-A360.
202. Kawakita, J. and K. Kobayashi, *Anodic polarization behavior of copper in propylene carbonate.* J. Power Sources, 2001. **101**: p. 47-52.
203. Braithwaite, J.W., A. Gonzales, G. Nagasubramanian, S.J. Lucero, D.E. Peebles, J.A. Ohlhausen, and W.R. Cieslak, *Corrosion of lithium-ion battery current collectors.* J. Electrochem. Soc., 1999. **146**: p. 448-456.
204. Lee, J.H., C.S. Yoon, J.-Y. Hwang, S.-J. Kim, F. Maglia, P. Lamp, S.-T. Myung, and Y.-K. Sun, *High-energy-density lithium-ion battery using a carbon-nanotube–Si composite anode and a compositionally graded Li[Ni0.85Co0.05Mn0.10]O2 cathode.* Energy & Environmental Science, 2016. **9**: p. 2152-2158.
205. Jiang, W., H. Wang, Z. Xu, N. Li, C. Chen, C. Li, J. Li, H. Lv, L. Kuang, and X. Tian, *A review on manifold synthetic and reprocessing methods of 3D porous graphene-based architecture for Li-ion anode.* Chem. Eng. J., 2018. **335**: p. 954-969.

206. Membreño, N., K. Park, J.B. Goodenough, and K.J. Stevenson, *Electrode/Electrolyte Interface of Composite α-Li3V2(PO4)3 Cathodes in a Nonaqueous Electrolyte for Lithium Ion Batteries and the Role of the Carbon Additive.* Chem. Mater., 2015. **27**: p. 3332-3340.
207. Qi, X., B. Blizanac, A. DuPasquier, A. Lal, P. Niehoff, T. Placke, M. Oljaca, J. Li, and M. Winter, *Influence of Thermal Treated Carbon Black Conductive Additive on the Performance of High Voltage Spinel Cr-Doped LiNi0.5Mn1.5O4 Composite Cathode Electrode.* J. Electrochem. Soc., 2014. **162**: p. A339-A343.
208. Li, W., A. Dolocan, P. Oh, H. Celio, S. Park, J. Cho, and A. Manthiram, *Dynamic behaviour of interphases and its implication on high-energy-density cathode materials in lithium-ion batteries.* Nat Commun, 2017. **8**: p. 14589.
209. Jung, R., M. Metzger, F. Maglia, C. Stinner, and H.A. Gasteiger, *Oxygen Release and Its Effect on the Cycling Stability of $LiNi_xMn_yCo_zO_2$ (NMC) Cathode Materials for Li-Ion Batteries.* J. Electrochem. Soc., 2017. **164**: p. A1361-A1377.
210. Phillip, N.D., R.E. Ruther, X. Sang, Y. Wang, R.R. Unocic, A.S. Westover, C. Daniel, and G.M. Veith, *Synthesis of Ni-rich Thin Film Cathode as Model System for Lithium Ion Batteries.* ACS Applied Energy Materials, 2019.
211. Malmgren, S., K. Ciosek, M. Hahlin, T. Gustafsson, M. Gorgoi, H. Rensmo, and K. Edström, *Comparing anode and cathode electrode/electrolyte interface composition and morphology using soft and hard X-ray photoelectron spectroscopy.* Electrochim. Acta, 2013. **97**: p. 23-32.
212. Lux, S., F. Schappacher, A. Balducci, S. Passerini, and M. Winter, *Low cost, environmentally benign binders for lithium-ion batteries.* J. Electrochem. Soc., 2010. **157**: p. A320-A325.
213. Li, J., R. Lewis, and J. Dahn, *Sodium carboxymethyl cellulose a potential binder for Si negative electrodes for Li-ion batteries.* Electrochem. Solid-State Lett., 2007. **10**: p. A17-A20.
214. Chen, H., M. Ling, L. Hencz, H.Y. Ling, G. Li, Z. Lin, G. Liu, and S. Zhang, *Exploring chemical, mechanical, and electrical functionalities of binders for advanced energy-storage devices.* Chem. Rev., 2018. **118**: p. 8936-8982.
215. Cao, P.-F., M. Naguib, Z. Du, E. Stacy, B. Li, T. Hong, K. Xing, D.N. Voylov, J. Li, and D.L. Wood III, *Effect of Binder Architecture on the Performance of Silicon/Graphite Composite Anodes for Lithium Ion Batteries.* ACS applied materials & interfaces, 2018. **10**: p. 3470-3478.
216. Komaba, S., K. Okushi, T. Ozeki, H. Yui, Y. Katayama, T. Miura, T. Saito, and H. Groult, *Polyacrylate modifier for graphite anode of lithium-ion batteries.* Electrochem. Solid-State Lett., 2009. **12**: p. A107-A110.
217. Pieczonka, N.P.W., V. Borgel, B. Ziv, N. Leifer, V. Dargel, D. Aurbach, J.H. Kim, Z.Y. Liu, X.S. Huang, S.A. Krachkovskiy, G.R. Goward, I. Halalay, B.R. Powell, and A. Manthiram, *Lithium Polyacrylate (LiPAA) as an Advanced Binder and a Passivating Agent for High-Voltage Li-Ion Batteries.* Advanced Energy Materials, 2015. **5**.
218. Gauthier, M., P. Karayaylali, L. Giordano, S. Feng, S.F. Lux, F. Maglia, P. Lamp, and Y. Shao-Horn, *Probing Surface Chemistry Changes Using $LiCoO_2$-only Electrodes in Li-Ion Batteries.* J. Electrochem. Soc., 2018. **165**: p. A1377-A1387.
219. Philippe, B., M. Hahlin, K. Edstro m, T. Gustafsson, H. Siegbahn, and H. Rensmo, *Photoelectron Spectroscopy for Lithium Battery Interface Studies.* J. Electrochem. Soc., 2015. **163**: p. A178-A191.
220. Seshan, K. and D. Schepis, *Handbook of thin film deposition*. 2018: William Andrew.
221. Swann, S., *Magnetron sputtering.* Physics in technology, 1988. **19**: p. 67.
222. O'sullivan, C. and G. Guilbault, *Commercial quartz crystal microbalances–theory and applications.* Biosens. Bioelectron., 1999. **14**: p. 663-670.
223. Cullity, B.D., *Elements of X-ray Diffraction.* 2001.
224. Moulder, J.F., *Handbook of X-ray photoelectron spectroscopy.* Physical electronics, 1995: p. 230-232.
225. Biesinger, M.C., B.P. Payne, L.W.M. Lau, A. Gerson, and R.S.C. Smart, *X-ray photoelectron spectroscopic chemical state quantification of mixed nickel metal, oxide and hydroxide systems.* Surf. Interface Anal., 2009. **41**: p. 324-332.
226. Levi, M., G. Salitra, B. Markovsky, H. Teller, D. Aurbach, U. Heider, and L. Heider, *Solid-State Electrochemical Kinetics of Li-Ion Intercalation into $Li_{1-x}CoO_2$: Simultaneous Application of Electroanalytical Techniques SSCV, PITT, and EIS.* J. Electrochem. Soc., 1999. **146**: p. 1279-1289.
227. Barsoukov, E. and J.R. Macdonald, *Impedance spectroscopy: theory, experiment, and applications*. 2018: John Wiley & Sons.

228. Tripathi, A.M., W.-N. Su, and B.J. Hwang, *In situ analytical techniques for battery interface analysis.* Chem. Soc. Rev., 2018. **47**: p. 736-851.
229. Fears, T.M., M. Doucet, J.F. Browning, J.K. Baldwin, J.G. Winiarz, H. Kaiser, H. Taub, R.L. Sacci, and G.M. Veith, *Evaluating the solid electrolyte interphase formed on silicon electrodes: a comparison of ex situ X-ray photoelectron spectroscopy and in situ neutron reflectometry.* Phys. Chem. Chem. Phys., 2016. **18**: p. 13927-40.
230. Grey, C.P. and J.M. Tarascon, *Sustainability and in situ monitoring in battery development.* Nat Mater, 2016. **16**: p. 45-56.
231. Li, J., Z. Du, R.E. Ruther, S.J. An, L.A. David, K. Hays, M. Wood, N.D. Phillip, Y. Sheng, C. Mao, S. Kalnaus, C. Daniel, and D.L. Wood, *Toward Low-Cost, High-Energy Density, and High-Power Density Lithium-Ion Batteries.* JOM, 2017. **69**: p. 1484-1496.
232. Hausbrand, R., G. Cherkashinin, H. Ehrenberg, M. Gröting, K. Albe, C. Hess, and W. Jaegermann, *Fundamental degradation mechanisms of layered oxide Li-ion battery cathode materials: Methodology, insights and novel approaches.* Materials Science and Engineering: B, 2015. **192**: p. 3-25.
233. Belharouak, I., Y.K. Sun, J. Liu, and K. Amine, *Li(Ni1/3Co1/3Mn1/3)O2 as a suitable cathode for high power applications.* J. Power Sources, 2003. **123**: p. 247-252.
234. Schipper, F., E.M. Erickson, C. Erk, J.-Y. Shin, F.F. Chesneau, and D. Aurbach, *Review—Recent Advances and Remaining Challenges for Lithium Ion Battery Cathodes.* J. Electrochem. Soc., 2016. **164**: p. A6220-A6228.
235. Cherkashinin, G., M. Motzko, N. Schulz, T. Späth, and W. Jaegermann, *Electron Spectroscopy Study of Li[Ni,Co,Mn]O2/Electrolyte Interface: Electronic Structure, Interface Composition, and Device Implications.* Chem. Mater., 2015. **27**: p. 2875-2887.
236. Aurbach, D., O. Srur-Lavi, C. Ghanty, M. Dixit, O. Haik, M. Talianker, Y. Grinblat, N. Leifer, R. Lavi, D.T. Major, G. Goobes, E. Zinigrad, E.M. Erickson, M. Kosa, B. Markovsky, J. Lampert, A. Volkov, J.Y. Shin, and A. Garsuch, *Studies of Aluminum-Doped LiNi0.5Co0.2Mn0.3O2: Electrochemical Behavior, Aging, Structural Transformations, and Thermal Characteristics.* J. Electrochem. Soc., 2015. **162**: p. A1014-A1027.
237. Oh, G., M. Hirayama, O. Kwon, K. Suzuki, and R. Kanno, *Bulk-Type All Solid-State Batteries with 5 V Class LiNi0.5Mn1.5O4 Cathode and Li10GeP2S12 Solid Electrolyte.* Chem. Mater., 2016. **28**: p. 2634-2640.
238. Mohanty, D., K. Dahlberg, D.M. King, L.A. David, A.S. Sefat, D.L. Wood, C. Daniel, S. Dhar, V. Mahajan, M. Lee, and F. Albano, *Modification of Ni-Rich FCG NMC and NCA Cathodes by Atomic Layer Deposition: Preventing Surface Phase Transitions for High-Voltage Lithium-Ion Batteries.* Sci Rep, 2016. **6**: p. 26532.
239. Nelson, K.J., G.L. d'Eon, A.T.B. Wright, L. Ma, J. Xia, and J.R. Dahn, *Studies of the Effect of High Voltage on the Impedance and Cycling Performance of Li[Ni0.4Mn0.4Co0.2]O2/Graphite Lithium-Ion Pouch Cells.* J. Electrochem. Soc., 2015. **162**: p. A1046-A1054.
240. Giordano, L., P. Karayaylali, Y. Yu, Y. Katayama, F. Maglia, S. Lux, and Y. Shao-Horn, *Chemical Reactivity Descriptor for the Oxide-Electrolyte Interface in Li-Ion Batteries.* J Phys Chem Lett, 2017. **8**: p. 3881-3887.
241. La Mantia, F., R.A. Huggins, and Y. Cui, *Oxidation processes on conducting carbon additives for lithium-ion batteries.* J. Appl. Electrochem., 2012. **43**: p. 1-7.
242. Manthiram, A., J.C. Knight, S.-T. Myung, S.-M. Oh, and Y.-K. Sun, *Nickel-Rich and Lithium-Rich Layered Oxide Cathodes: Progress and Perspectives.* Advanced Energy Materials, 2016. **6**.
243. Demeaux, J., M. Caillon-Caravanier, H. Galiano, D. Lemordant, and B. Claude-Montigny, *LiNi0.4Mn1.6O4/Electrolyte and Carbon Black/Electrolyte High Voltage Interfaces: To Evidence the Chemical and Electronic Contributions of the Solvent on the Cathode-Electrolyte Interface Formation.* J. Electrochem. Soc., 2012. **159**: p. A1880-A1890.
244. Dudney, N.J., *Solid-state thin-film rechargeable batteries.* Materials Science and Engineering: B, 2005. **116**: p. 245-249.
245. Bates, J.B., N.J. Dudney, G.R. Gruzalski, R.A. Zuhr, A. Choudhury, and C.F. Luck, *Fabrication and Characterization of Amorphous Lithium Electrolyte Thin Films and Rechargeable Thin-Film Batteries.* J. Power Sources, 1993. **43-44**: p. 103-110.
246. Bates, J.B., N.J. Dudney, B.J. Neudecker, F.X. Hart, H.P. Jun, and S.A. Hackney, *Preferred Orientation of Polycrystalline $LiCoO_2$.* J. Electrochem. Soc., 2000. **1**: p. 59-70.

247. Baggetto, L., R.R. Unocic, N.J. Dudney, and G.M. Veith, *Fabrication and characterization of Li–Mn–Ni–O sputtered thin film high voltage cathodes for Li-ion batteries.* J. Power Sources, 2012. **211**: p. 108-118.
248. Tan, G., F. Wu, J. Lu, R. Chen, L. Li, and K. Amine, *Controllable crystalline preferred orientation in Li-Co-Ni-Mn oxide cathode thin films for all-solid-state lithium batteries.* Nanoscale, 2014. **6**: p. 10611-22.
249. Strafela, M., H. Leiste, K. Seemann, H.J. Seifert, and S. Ulrich, *Influence of substrate surface roughness on microstructural and electrical properties of Lithium-rich Li-Ni-Mn-Co-O thin film cathodes.* Vacuum, 2016. **131**: p. 240-245.
250. Li, H., J. Li, X. Ma, and J.R. Dahn, *Synthesis of Single Crystal LiNi0.6Mn0.2Co0.2O2 with Enhanced Electrochemical Performance for Lithium Ion Batteries.* J. Electrochem. Soc., 2018. **165**: p. A1038-A1045.
251. Yin, S.-C., Y.-H. Rho, I. Swainson, and L.F. Nazar, *X-ray/neutron diffraction and electrochemical studies of lithium de/re-intercalation in Li(1-x) Co(1/3) Ni(1/3) Mn(1/3) O2 (x = 0 - 1).* Chem. Mater., 2006: p. 1901-19010.
252. Zheng, J., G. Teng, C. Xin, Z. Zhuo, J. Liu, Q. Li, Z. Hu, M. Xu, S. Yan, W. Yang, and F. Pan, *Role of Superexchange Interaction on Tuning of Ni/Li Disordering in Layered Li(NixMnyCoz)O2.* J Phys Chem Lett, 2017. **8**: p. 5537-5542.
253. Bouwman, P.J., B.A. Boukamp, H.J.M. Bouwmeester, and P.H.L. Notten, *Structure-related intercalation behaviour of LiCoO2 films.* Solid State Ionics, 2022. **152-153**: p. 181-188.
254. Dirks, A.G. and H.J. Leamy, *Columnar Microstructure in Vapor-Deposited Thin Films.* Thin Solid Films, 1977. **47**: p. 219-223.
255. Kim, H.S., Y. Oh, K.H. Kang, J.H. Kim, J. Kim, and C.S. Yoon, *Characterization of Sputter-Deposited LiCoO2 Thin Film Grown on NASICON-type Electrolyte for Application in All-Solid-State Rechargeable Lithium Battery.* ACS Appl Mater Interfaces, 2017. **9**: p. 16063-16070.
256. Zhang, X., A. Mauger, Q. Lu, H. Groult, L. Perrigaud, F. Gendron, and C.M. Julien, *Synthesis and characterization of LiNi1/3Mn1/3Co1/3O2 by wet-chemical method.* Electrochim. Acta, 2010. **55**: p. 6440-6449.
257. Fernandez-Garcia, M., A. Martinez-Arias, J.C. Hanson, and J.A. Radriguez, *Nanostructured Oxides in Chemistry: Characterization and Properties.* Chem. Rev., 2004. **104**: p. 4063-4104.
258. Pan, H. and Y. Yang, *Effects of radio-frequency sputtering powers on the microstructures and electrochemical properties of LiCoO2 thin film electrodes.* J. Power Sources, 2009. **189**: p. 633-637.
259. Ruan, Y., X. Song, Y. Fu, C. Song, and V. Battaglia, *Structural evolution and capacity degradation mechanism of LiNi0.6Mn0.2Co0.2O2 cathode materials.* J. Power Sources, 2018. **400**: p. 539-548.
260. Xia, H., L. Lu, and G. Ceder, *Li diffusion in LiCoO2 thin films prepared by pulsed laser deposition.* J. Power Sources, 2006. **159**: p. 1422-1427.
261. Wandt, J., A.T.S. Freiberg, A. Ogrodnik, and H.A. Gasteiger, *Singlet oxygen evolution from layered transition metal oxide cathode materials and its implications for lithium-ion batteries.* Mater. Today, 2018. **21**: p. 825-833.
262. Freiberg, A.T., M.K. Roos, J. Wandt, R. de Vivie-Riedle, and H.A. Gasteiger, *Singlet Oxygen Reactivity with Carbonate Solvents Used for Li-Ion Battery Electrolytes.* The Journal of Physical Chemistry A, 2018. **122**: p. 8828-8839.
263. Kraft, V., M. Grützke, W. Weber, J. Menzel, S. Wiemers-Meyer, M. Winter, and S. Nowak, *Two-dimensional ion chromatography for the separation of ionic organophosphates generated in thermally decomposed lithium hexafluorophosphate-based lithium ion battery electrolytes.* J. Chromatogr. A, 2015. **1409**: p. 201-209.
264. Jung, R., F. Linsenmann, R. Thomas, J. Wandt, S. Solchenbach, F. Maglia, C. Stinner, M. Tromp, and H.A. Gasteiger, *Nickel, Manganese, and Cobalt Dissolution from Ni-Rich NMC and Their Effects on NMC622-Graphite Cells.* J. Electrochem. Soc., 2019. **166**: p. A378-A389.
265. Jung, R., P. Strobl, F. Maglia, C. Stinner, and H.A. Gasteiger, *Temperature Dependence of Oxygen Release from $LiNi_{0.6}Mn_{0.2}Co_{0.2}O_2$ (NMC622) Cathode Materials for Li-Ion Batteries.* J. Electrochem. Soc., 2018. **165**: p. A2869-A2879.
266. Pham, H.Q., J. Lee, H.M. Jung, and S.-W. Song, *Non-flammable LiNi0. 8Co0. 1Mn0. 1O2 cathode via functional binder; stabilizing 4.4 V interface and performance for safer and high-energy lithium rechargeable batteries.* Electrochim. Acta, 2019.
267. Xu, J., S.-L. Chou, Q.-f. Gu, H.-K. Liu, and S.-X. Dou, *The effect of different binders on electrochemical properties of $LiNi_{1/3}Mn_{1/3}Co_{1/3}O_2$ cathode material in lithium ion batteries.* J. Power Sources, 2013. **225**: p. 172-178.

268. Hays, K.A., R.E. Ruther, A.J. Kukay, P. Cao, T. Saito, D.L. Wood III, and J. Li, *What makes lithium substituted polyacrylic acid a better binder than polyacrylic acid for silicon-graphite composite anodes?* J. Power Sources, 2018. **384**: p. 136-144.
269. Liu, G., H. Zheng, A. Simens, A. Minor, X. Song, and V. Battaglia, *Optimization of acetylene black conductive additive and PVDF composition for high-power rechargeable lithium-ion cells.* J. Electrochem. Soc., 2007. **154**: p. A1129-A1134.
270. Seah, M.P. and W. Dench, *Quantitative electron spectroscopy of surfaces: A standard data base for electron inelastic mean free paths in solids.* Surf. Interface Anal., 1979. **1**: p. 2-11.
271. Qian, Y., P. Niehoff, M. Börner, M. Grützke, X. Mönnighoff, P. Behrends, S. Nowak, M. Winter, and F.M. Schappacher, *Influence of electrolyte additives on the cathode electrolyte interphase (CEI) formation on $LiNi_{1/3}Mn_{1/3}Co_{1/3}O_2$ in half cells with Li metal counter electrode.* J. Power Sources, 2016. **329**: p. 31-40.
272. Campion, C.L., W. Li, and B.L. Lucht, *Thermal decomposition of $LiPF_6$-based electrolytes for lithium-ion batteries.* J. Electrochem. Soc., 2005. **152**: p. A2327-A2334.
273. Çetinel, F.A. and W. Bauer, *Processing of water-based $LiNi_{1/3}Mn_{1/3}Co_{1/3}O_2$ pastes for manufacturing lithium ion battery cathodes.* Bull. Mater. Sci., 2014. **37**: p. 1685-1690.
274. Zhang, X., W. Jiang, X. Zhu, A. Mauger, and C. Julien, *Aging of $LiNi_{1/3}Mn_{1/3}Co_{1/3}O_2$ cathode material upon exposure to H2O.* J. Power Sources, 2011. **196**: p. 5102-5108.
275. Villa, A., G.M. Veith, D. Ferri, A. Weidenkaff, K.A. Perry, S. Campisi, and L. Prati, *NiO as a peculiar support for metal nanoparticles in polyols oxidation.* Catalysis Science & Technology, 2013. **3**: p. 394-399.
276. Tian, C., Y. Xu, D. Nordlund, F. Lin, J. Liu, Z. Sun, Y. Liu, and M. Doeff, *Charge Heterogeneity and Surface Chemistry in Polycrystalline Cathode Materials.* Joule, 2018. **2**: p. 464-477.
277. Levi, M. and D. Aurbach, *Simultaneous measurements and modeling of the electrochemical impedance and the cyclic voltammetric characteristics of graphite electrodes doped with lithium.* The Journal of Physical Chemistry B, 1997. **101**: p. 4630-4640.
278. Xu, K., A. von Cresce, and U. Lee, *Differentiating contributions to "ion transfer" barrier from interphasial resistance and Li+ desolvation at electrolyte/graphite interface.* Langmuir, 2010. **26**: p. 11538-43.
279. Joho, F. and P. Novák, *SNIFTIRS investigation of the oxidative decomposition of organic-carbonate-based electrolytes for lithium-ion cells.* Electrochim. Acta, 2000. **45**: p. 3589-3599.
280. Matsushita, T., K. Dokko, and K. Kanamura, *In situ FT-IR measurement for electrochemical oxidation of electrolyte with ethylene carbonate and diethyl carbonate on cathode active material used in rechargeable lithium batteries.* J. Power Sources, 2005. **146**: p. 360-364.
281. Browning, J.F., L. Baggetto, K.L. Jungjohann, Y. Wang, W.E. Tenhaeff, J.K. Keum, D.L. Wood, 3rd, and G.M. Veith, *In situ determination of the liquid/solid interface thickness and composition for the Li ion cathode LiMn(1.5)Ni(0.5)O4.* ACS Appl Mater Interfaces, 2014. **6**: p. 18569-76.
282. Wang, C., Y.S. Meng, and K. Xu, *Perspective—Fluorinating Interphases.* J. Electrochem. Soc., 2019. **166**: p. A5184-A5186.
283. Alvarado, J., M.A. Schroeder, M. Zhang, O. Borodin, E. Gobrogge, M. Olguin, M.S. Ding, M. Gobet, S. Greenbaum, and Y.S. Meng, *A carbonate-free, sulfone-based electrolyte for high-voltage Li-ion batteries.* Mater. Today, 2018. **21**: p. 341-353.
284. Jo, C.-H., D.-H. Cho, H.-J. Noh, H. Yashiro, Y.-K. Sun, and S.T. Myung, *An effective method to reduce residual lithium compounds on Ni-rich Li [Ni 0.6 Co 0.2 Mn 0.2] O 2 active material using a phosphoric acid derived Li 3 PO 4 nanolayer.* Nano Research, 2015. **8**: p. 1464-1479.
285. Terborg, L., S. Nowak, S. Passerini, M. Winter, U. Karst, P.R. Haddad, and P.N. Nesterenko, *Ion chromatographic determination of hydrolysis products of hexafluorophosphate salts in aqueous solution.* Anal. Chim. Acta, 2012. **714**: p. 121-126.
286. Han, B., B. Key, S.H. Lapidus, J.C. Garcia, H. Iddir, J.T. Vaughey, and F. Dogan, *From Coating to Dopant: How the Transition Metal Composition Affects Alumina Coatings on Ni-Rich Cathodes.* ACS Appl Mater Interfaces, 2017. **9**: p. 41291-41302.
287. Hall, D.S., R. Gauthier, A. Eldesoky, V.S. Murray, and J. Dahn, *New Chemical Insights into the Beneficial Role of Al_2O_3 Cathode Coatings in Lithium-ion Cells.* ACS applied materials & interfaces, 2019. **11**: p. 14095-14100.
288. Chen, Y., Y. Zhang, B. Chen, Z. Wang, and C. Lu, *An approach to application for $LiNi_{0.6}Co_{0.2}Mn_{0.2}O_2$ cathode material at high cutoff voltage by TiO_2 coating.* J. Power Sources, 2014. **256**: p. 20-27.
289. Cheng, C., H. Yi, and F. Chen, *Effect of Cr_2O_3 coating on $LiNi_{1/3}Co_{1/3}Mn_{1/3}O_2$ as cathode for lithium-ion batteries.* J. Electron. Mater., 2014. **43**: p. 3681-3687.

290. Şahan, H., H. Göktepe, Ş. Patat, and A. Ülgen, *Effect of the Cr_2O_3 coating on electrochemical properties of spinel $LiMn_2O_4$ as a cathode material for lithium battery applications.* Solid State Ionics, 2010. **181**: p. 1437-1444.
291. Chang, W., J.-W. Choi, J.-C. Im, and J.K. Lee, *Effects of ZnO coating on electrochemical performance and thermal stability of $LiCoO_2$ as cathode material for lithium-ion batteries.* J. Power Sources, 2010. **195**: p. 320-326.
292. Lai, Y.-Q., M. Xu, Z.-A. Zhang, C.-H. Gao, P. Wang, and Z.-Y. Yu, *Optimized structure stability and electrochemical performance of $LiNi_{0.8}Co_{0.15}Al_{0.05}O_2$ by sputtering nanoscale ZnO film.* J. Power Sources, 2016. **309**: p. 20-26.
293. Baggetto, L., N.J. Dudney, and G.M. Veith, *Surface chemistry of metal oxide coated lithium manganese nickel oxide thin film cathodes studied by XPS.* Electrochim. Acta, 2013. **90**: p. 135-147.
294. Myung, S.-T., K. Amine, and Y.-K. Sun, *Surface modification of cathode materials from nano-to microscale for rechargeable lithium-ion batteries.* J. Mater. Chem., 2010. **20**: p. 7074-7095.
295. Li, X., J. Liu, X. Meng, Y. Tang, M.N. Banis, J. Yang, Y. Hu, R. Li, M. Cai, and X. Sun, *Significant impact on cathode performance of lithium-ion batteries by precisely controlled metal oxide nanocoatings via atomic layer deposition.* J. Power Sources, 2014. **247**: p. 57-69.
296. Myung, S.-T., K. Izumi, S. Komaba, Y.-K. Sun, H. Yashiro, and N. Kumagai, *Role of alumina coating on Li− Ni− Co− Mn− O particles as positive electrode material for lithium-ion batteries.* Chem. Mater., 2005. **17**: p. 3695-3704.
297. Moses, A.W., H.G.G. Flores, J.-G. Kim, and M.A. Langell, *Surface properties of $LiCoO_2$, $LiNiO_2$ and $LiNi_{1-x}Co_xO_2$.* Appl. Surf. Sci., 2007. **253**: p. 4782-4791.
298. Parks, G.A. and P.D. Bruyn, *The zero point of charge of oxides1.* The Journal of Physical Chemistry, 1962. **66**: p. 967-973.
299. Parks, G.A., *The Isoelectric Points of Solid Oxides, Solid Hydroxides, and Aqueous Hydroxo Complex Systems.* Chem. Rev., 1964. **65**: p. 177-198.
300. Paulsen, J. and J. Kim, *High nickel cathode material having low soluble base content*. 2017, Google Patents.
301. Phillip, N.D., R.E. Ruther, X. Sang, Y. Wang, R.R. Unocic, A.S. Westover, C. Daniel, and G.M. Veith, *Synthesis of Ni-Rich Thin-Film Cathode as Model System for Lithium Ion Batteries.* ACS Applied Energy Materials, 2019. **2**: p. 1405-1412.
302. Grohmann, I., E. Kemnitz, A. Lippitz, and W. Unger, *Curve fitting of Cr 2p photoelectron spectra of Cr_2O_3 and CrF_3.* Surf. Interface Anal., 1995. **23**: p. 887-891.
303. Kittaka, S., *Isoelectric point of Al_2O_3, Cr_2O_3 and Fe_2O_3. I. Effect of heat treatment.* J. Colloid Interface Sci., 1974. **48**: p. 327-333.
304. Bhattacharjee, S.J.J.o.C.R., *DLS and zeta potential–what they are and what they are not?* 2016. **235**: p. 337-351.
305. Clark, J.C., S. Dai, and S.H. Overbury, *Operando studies of desorption, reaction and carbonate formation during CO oxidation by Au/TiO2 catalysts.* Catal. Today, 2007. **126**: p. 135-142.
306. Phillip, N.D., C. Daniel, and G.M. Veith, In Preparation, 2019.
307. Shuttleworth, D., *Preparation of metal-polymer dispersions by plasma techniques. An ESCA investigation.* The Journal of Physical Chemistry, 1980. **84**: p. 1629-1634.
308. Jain, A., S. Agarwal, S. Kumar, S. Yamaguchi, H. Miyaoka, Y. Kojima, and T. Ichikawa, *How does TiF_4 affect the decomposition of MgH_2 and its complex variants?–An XPS investigation.* Journal of Materials Chemistry A, 2017. **5**: p. 15543-15551.
309. Giordano, L., T.M. Østergaard, S. Muy, Y. Yu, N. Charles, S. Kim, Y. Zhang, F. Maglia, R. Jung, and I.J.C.o.M. Lund, *Ligand-dependent energetics for dehydrogenation: Implications in Li-ion battery electrolyte stability and selective oxidation catalysis of hydrogen-containing molecules.* 2019.
310. Wang, C., L. Yu, W. Fan, J. Liu, L. Ouyang, L. Yang, and M.J.A.A.E.M. Zhu, *Lithium difluorophosphate as a promising electrolyte lithium additive for high-voltage lithium-ion batteries.* 2018. **1**: p. 2647-2656.
311. Hong, S., B. Hong, W. Song, Z. Qin, B. Duan, Y. Lai, and F.J.J.o.T.E.S. Jiang, *Communication—Lithium Difluorophosphate as an Electrolyte Additive to Improve the High Voltage Performance of LiNi0. 5Co0. 2Mn0. 3O2/Graphite Cell.* 2018. **165**: p. A368-A370.
312. Zhao, W., G. Zheng, M. Lin, W. Zhao, D. Li, X. Guan, Y. Ji, G.F. Ortiz, and Y.J.J.o.P.S. Yang, *Toward a stable solid-electrolyte-interfaces on nickel-rich cathodes: LiPO2F2 salt-type additive and its working mechanism for LiNi0. 5Mn0. 25Co0. 25O2 cathodes.* 2018. **380**: p. 149-157.

313. Karayaylali, P., R. Tatara, Y. Zhang, K.-L. Chan, Y. Yu, L. Giordano, F. Maglia, R. Jung, I. Lund, and Y.J.J.o.T.E.S. Shao-Horn, *Coating-Dependent Electrode-Electrolyte Interface for Ni-Rich Positive Electrodes in Li-Ion Batteries.* 2019. **166**: p. A1022-A1030.
314. Koerver, R., I. Aygün, T. Leichtweiß, C. Dietrich, W. Zhang, J.O. Binder, P. Hartmann, W.G. Zeier, and J. Janek, *Capacity Fade in Solid-State Batteries: Interphase Formation and Chemomechanical Processes in Nickel-Rich Layered Oxide Cathodes and Lithium Thiophosphate Solid Electrolytes.* Chem. Mater., 2017. **29**: p. 5574-5582.
315. Zhang, Z., S. Chen, X. Yao, P. Cui, J. Duan, W. Luo, Y. Huang, and X. Xu, *Enabling high-areal-capacity all solid-state lithium-metal batteries by tri-layer electrolyte architectures.* Energy Storage Materials, 2019.
316. Yoshinari, T., R. Koerver, P. Hofmann, Y. Uchimoto, W.G. Zeier, and J.r. Janek, *Interfacial stability of phosphate-NASICON solid electrolytes in Ni-rich NCM cathode-based solid-state batteries.* ACS applied materials & interfaces, 2019.
317. Wang, D., Q. Sun, J. Luo, J. Liang, Y. Sun, R. Li, K. Adair, L. Zhang, R. Yang, S.J.A.a.m. Lu, and interfaces, *Mitigating the Interfacial Degradation in Cathodes for High-Performance Oxide-Based Solid-State Lithium Batteries.* 2019. **11**: p. 4954-4961.
318. Koerver, R., W. Zhang, L. de Biasi, S. Schweidler, A.O. Kondrakov, S. Kolling, T. Brezesinski, P. Hartmann, W.G. Zeier, and J. Janek, *Chemo-mechanical expansion of lithium electrode materials–on the route to mechanically optimized all-solid-state batteries.* Energy & Environmental Science, 2018. **11**: p. 2142-2158.
319. Kim, Y., G.M. Veith, J. Nanda, R.R. Unocic, M. Chi, and N.J. Dudney, *High voltage stability of LiCoO2 particles with a nano-scale Lipon coating.* Electrochim. Acta, 2011. **56**: p. 6573-6580.
320. Eliaz, N. and E. Gileadi, *Physical Electrochemistry: Fundamentals, Techniques, and Applications*. 2018: Wiley-Vch.
321. Dahn, J., U. von Sacken, and C.J.S.S.I. Michal, *Structure and electrochemistry of Li1±yNiO2 and a new Li2NiO2 phase with the Ni (OH) 2 structure.* 1990. **44**: p. 87-97.
322. Erickson, E.M., F. Schipper, T.R. Penki, J.-Y. Shin, C. Erk, F.-F. Chesneau, B. Markovsky, and D. Aurbach, *Review—Recent Advances and Remaining Challenges for Lithium Ion Battery Cathodes.* J. Electrochem. Soc., 2017. **164**: p. A6341-A6348.
323. Fan, X., L. Chen, X. Ji, T. Deng, S. Hou, J. Chen, J. Zheng, F. Wang, J. Jiang, and K. Xu, *Highly fluorinated interphases enable high-voltage Li-metal batteries.* Chem, 2018. **4**: p. 174-185.
324. Liu, G., H. Zheng, X. Song, and V.S. Battaglia, *Particles and Polymer Binder Interaction: A Controlling Factor in Lithium-Ion Electrode Performance.* J. Electrochem. Soc., 2012. **159**: p. A214-A221.
325. Østergaard, T.M., L. Giordano, I.E. Castelli, F. Maglia, B.K. Antonopoulos, Y. Shao-Horn, and J.J.T.J.o.P.C.C. Rossmeisl, *Oxidation of Ethylene Carbonate on Li Metal Oxide Surfaces.* 2018. **122**: p. 10442-10449.
326. Zheng, L., T. Hatchard, and M.J.M.C. Obrovac, *A high-quality mechanofusion coating for enhancing lithium-ion battery cathode material performance.* 2019. **9**: p. 245-250.
327. Cui, X., L. Ai, L. Mao, Y. Xie, Y. Liang, N. Zhang, Y. Feng, S. Wang, and S.J.I. Li, *Enhanced electrochemical properties of LiNi 0.6 Co 0.2 Mn 0.2 O 2 cathode material by the diffusional Al 2 O 3 coating layer.* 2019. **25**: p. 411-419.
328. Liang, L., J. Jiang, F. Jiang, G. Hu, Y. Cao, Z. Peng, and K. Du, *An ordered olivine-type LiCoPO 4 layer grown on LiNi 0.6 Mn 0.2 Co 0.2 O 2 cathode materials applied to lithium-ion batteries.* J. Alloys Compd., 2017. **695**: p. 1993-1997.
329. Tebbe, J.L., A.M. Holder, C.B.J.A.a.m. Musgrave, and interfaces, *Mechanisms of LiCoO2 cathode degradation by reaction with HF and protection by thin oxide coatings.* 2015. **7**: p. 24265-24278.
330. Kim, Y., N.J. Dudney, M. Chi, S.K. Martha, J. Nanda, G.M. Veith, and C. Liang, *A Perspective on Coatings to Stabilize High-Voltage Cathodes: LiMn1.5Ni0.5O4 with Sub-Nanometer Lipon Cycled with LiPF6 Electrolyte.* J. Electrochem. Soc., 2013. **160**: p. A3113-A3125.

VITA

Nathan Phillip was born in Hinsdale, Illinois to the parents of Jeffrey and Christine Phillip. He has one older brother, Tyler, and always at least one dog in their home. He attended LaGrange Highlands Elementary, LaGrange Highlands Middle School, and Lyons Township High School in La Grange, Illinois. After graduation, he enrolled at Miami University of Ohio in August 2012 where he discovered research in energy materials and characterization. He earned a Bachelor of Science degree in Chemical Engineering from Miami University in May 2015 before continuing south for graduate school. He received a research fellowship from the Bredesen Center for Interdisciplinary Research and Graduate Education at the University of Tennessee, Knoxville for research in energy storage. Nathan graduated with a Doctor of Philosophy degree in Energy Science and Engineering in December 2019.